FEMUR SHAPE ANALYSIS SYSTEM USING MAXIMUM-MINIMUM CENTRE SKELETONIZATION

TS. SAW SEOW HUI

DOCTOR OF PHILOSOPHY

FACULTY OF INFORMATION AND COMMUNICATION TECHNOLOGY UNIVERSITI TUNKU ABDUL RAHMAN DECEMBER 2023

FEMUR SHAPE ANALYSIS SYSTEM USING MAXIMUM-MINIMUM CENTRE SKELETONIZATION

By

TS. SAW SEOW HUI

A Thesis submitted to the Department of Computer Science, Faculty of Information and Communication Technology, Universiti Tunku Abdul Rahman, in partial fulfilment of the requirements for the degree of Doctor of Philosophy in Computer Science DECEMBER 2023

IN LOVING MEMORY OF MY LATE FATHER, SAW TEIK LEONG, WHOSE ENDURING WISDOM AND UNCONDITIONAL SUPPORT GUIDED ME THROUGH EVERY STEP OF MY ACADEMIC JOURNEY. TO MY LATE MOTHER, LIM GII TEAI, WHOSE BOUNDLESS LOVE AND ENCOURAGEMENT WERE THE DRIVING FORCES BEHIND MY PERSEVERANCE. IN REMEMBRANCE OF MY LATE UNCLE, LEE MUN HEE, AND MY LATE AUNT, CHOY LAN YIN, WHOSE INSPIRATIONAL LEGACIES CONTINUE TO INFLUENCE MY PURSUIT OF KNOWLEDGE. LASTLY, A DEDICATED TRIBUTE TO MY LATE COUSIN SISTER, NICKIE LEE HUI MANG, WHOSE VIBRANT SPIRIT AND SHARED DREAMS ADDED AN IRREPLACEABLE WARMTH TO MY EDUCATIONAL ENDEAVOURS. THOUGH THEY ARE NO LONGER WITH US. THEIR PRESENCE RESONATES IN THE PAGES OF THIS THESIS, A HEARTFELT ACKNOWLEDGMENT OF THE PROFOUND IMPACT THEY HAD ON MY LIFE AND ACADEMIC PURSUITS.

ABSTRACT

FEMUR SHAPE ANALYSIS SYSTEM USING MAXIMUM-MINIMUM CENTRE SKELETONIZATION

Ts. Saw Seow Hui

The medical field covers an expansive expertise to serve the needs of a particular human body. The most competitive and rewarding medical specialities is the orthopaedic surgery, which is mainly focused on improving the lives of patients with mobility and disorder issues, such as arthritis, ligament sprains, femoral shaft fractures, etc.

Femoral shaft fractures are common, and it is correlated with frequent morbidity and mortality. It is a major musculoskeletal disorder caused by tremendous force applied to the femur. One of the most common surgical treatments for fixation is intramedullary nailing (IM) procedure, which utilises a specially designed metal rod and screws to be implanted into the medullary canal.

However, severe bowing of the femur and the increasing in the width of the medullary canal can result in a mismatch between the IM nail and the alignment of the femur. Such mismatch is a risk factor for anterior cortical perforation off the distal femur with subtrochanteric fractures and leg length discrepancy with fractures of the femoral shaft. Therefore, accurate three-dimensional (3D) preoperative planning is mandatory to facilitate the implant's design based on the obtained geometric data of the femur anatomy, especially for the bowed femur.

This thesis presents an automatic orthopaedic analysis system, namely, 3D femur shape analysis system (3D-FSA) based on the extracted skeleton of each individual patient to provide an accurate 3D preoperative simulation. Inspired by the theory defined in 3D skeletonization, we implemented a straightforward approach, namely the maximum-minimum centre approach for the skeleton extraction from the 3D femur in 3D-FSA.

The use of 3D skeletonization in statistical analyses of femur parameters and geometry is a relatively novel field. It has been shown that the skeleton of the 3D femur produced by 3D-FSA allows the orthopaedics to gain a better visualise anatomy, aid in analysis and planning for the complex surgery and implant measurements. This is mainly because the significant geometric and topological information of the 3D femur can be computed, by using the proposed maximum-minimum centre approach in 3D skeletonization module.

There are four (4) phases in the development of 3D-FSA. The first (1st) phase involves the creation of the 3D femur data files in .obj format from a set of cross-sectional CT images. These text files are created and shared by the researchers from South Korea and they are I. J. Jung (University of Ulsan College of Medicine, Seoul), E. J. Choi (Department of Orthopaedics, Asan Medical Centre, Seoul), B. G. Lee (Division of Computer Engineering, Dongseo University, Busan) and J. W. Kim (Department of Orthopedic Surgery, University of Ulsan College of Medicine, Asam Medical Centre, Seoul). The 3D femur is then constructed in the second (2nd) phase. The medial

axis (skeleton) is extracted in the third (3^{rd}) phase and finally the results are analysed in the fourth phase (4^{th}) .

3D-FSA has been utilised by the mentioned researchers for conducting the morphometric evaluation and anatomical analyses among Korean population. They have verified and validated the reliability of our system.

Extensions of the proposed approaches for 3D-FSA are discussed throughout this thesis.

ACKNOWLEDGEMENTS

As with any piece of research that results in the production of a thesis, on the cover there should be not only the name of the researcher, but also the names of all those who to varying degrees provided assistance, encouragement and guidance, and without whom I would not have succeeded. This research would not have been feasible without their support whose names would be impossible to list in these few paragraphs, to which I am deeply grateful nonetheless.

Firstly, I would like to express my sincere words of gratitude to my supervisors for their dedicated support and invaluable guidance throughout this research, especially to my main supervisor, Ir. Prof. Dato' Dr. Ewe Hong Tat (President/ CEO and the Senior Lecturer of Department of Electrical and Electronic Engineering (DEE), Lee Kong Chian Faculty of Engineering and Science (LKCFES), Universiti Tunku Abdul Rahman (UTAR)), for giving me the opportunity to do my research and his keen interest on me at every stage of the research. I can never feel lucky and be thankful enough to have met a mentor like him, who has never failed to show his kindness and offered help at needy times. His vision, sincerity and motivation have deeply inspired me to never give up in this long and challenging journey. It was a great privilege and honour to work and study under his supervision.

Secondly, I would like to extend my immeasurable appreciation and deepest gratitude to my external co-supervisor, Professor Lee Byung-Gook (Professor of Division of Computer Engineering (DCE) in Dongseo University (DSU), Busan, South Korea) for his continuous support, patience, valuable suggestions, and his immense knowledge to make this research

meaningful. He has taught me the technical skills and methodology plan to carry out this research and to present the research works as clearly as possible. I am extremely grateful for what he has offered me, his friendship, empathy, and great sense of humour. My heartfelt appreciation to him can never be expressed enough in words.

Thirdly, I thankfully acknowledge the support and dedication that I received from my internal co-supervisor, Prof. Dr. Leung Kar Hang (Professor of Department of Computer Science (DCS), Faculty of Information and Communication Technology (FICT) in UTAR). He has been playing an important role as a technical specialist and English critics, by checking my thesis thoroughly and constantly provides constructive feedback. If it wasn't for him, my thesis would be terrible. My deepest thanks to his valuable comments and suggestions during the final stage of this research.

I would also like to acknowledge the program of UTAR Scholarship Schemes for sponsoring my 5-years tuition fee during my candidature in UTAR, which greatly reduces the financial burden of my family.

Not forgetting the examiners, Ts. Dr. Khor Siak Wang (Head of Programme (HOP) for the Postgraduate Programmes, FICT in UTAR), Dr. Sayed Ahmad Zikri bin Sayed Aluwee (Assistant Professor of DCS, FICT in UTAR) and Dr. Goh Chuan Meng (Assistant Professors of DCS, FICT in UTAR) for letting my defence be an enjoyable moment, and for your brilliant comments and suggestions, thanks to all of you.

My sincere thanks to the professors in M. Kandiah Faculty of Medicine and Health Sciences (M. K. FMHS) in UTAR for sharing their knowledge and wisdom in the field of Orthopaedics. They are Dr. Simerjit Singh (Clinical Associate Professor of the Department of Surgery (DS)), Prof. Dato' Dr Oh Kim Soon (Adjunct Clinical Professor), Dr. Yan Naing Soe (Head of Department (HOD) of DS), Dr. Din Xin Jet (Head of Department (HOD) of Department of Population Medicine (DPM)). Furthermore, I would like to extend my thank you to Dr. Rajesh Singh (Orthopaedic Specialist of Regen Health Care) and Prof. Dr. David Ngo (Director of Research and Enterprise in Heriot-Watt University (HWU)).

It is tough as a part-time postgraduate student, and it is even tougher when I am trying to balance my full time job as a lecturer in FICT in UTAR, keeping up with family and friends all while taking care of my mental and physical health. It's not easy but it's definitely doable especially when I received a great deal of support understanding and positive comments from all my colleagues in FICT and Faculty of Science (FSc), UTAR during the different stages of my studies, in particular to:

- A. Administrators: Prof. Ts. Dr. Liew Soung Yue (Dean), Ts. Dr. Ooi Boon Yaik (HOD of DCS), Ts. Dr. Cheng Wai Khuen (Deputy Dean (DD)), Ts. Dr. Goh Hock Guan (DD), Ts. Dr. Chang Jing Jing (HOD of Department of Computer and Communication Technology (DCCT)), Ts. Lim Jit Theam (HOD of Department of Digital Economy Technology (DDET)) and Dr. Aun Yichiet (HOP of Master in Data Management and Analytics & Postgraduate Diploma in Data Management and Analytics (MDMA)).
- B. Buddies: Dr. Tan Joi San, Dr. Jasmina Khaw Yen Min and Ts Dr Tong Dong Ling.

- C. Assistant Professors: Ts. Dr. Lee Chen Kang, Dr. Lim Seng Poh, Dr. Lim Ean Heng, Dr Manoranjitham a/p Muniandy, Dr Mogana a/p Vadiveloo, Dr Ng Hui Fuang, Dr. Tan Hung Khoon, Ts Dr Ooi Joo On, Ts Dr Ooi Chek Yee, Ts Dr Gan Ming Lee, Dr Robithoh Annur, Dr Tse Siu Hong Savio, Ts Dr Chan Lee Kwun, Ts Dr Wong Pei Voon and Dr Kh'ng Xin Yi.
- D. Lecturers: Ts. Tan Teik Boon, Mr Tan Chiang Kang @ Thang Chiang Kang, Ts. Wong Chee Siang, Ts. Lai Siew Cheng, Ts Phan Koo Yuen, Ts Soong Hoong Cheng, Ts Sun Teik Heng @ San Teik Heng, Ms Tan Lyk Yin, Mr Teoh Shen Khang, Mr Tou Jing Yi, the Late Ms Yap Seok Gee and Ts Yong Tien Fui.
- E. Lab Officers: Mr Leong Yee Fee, Mr Tan Boon Ghee, Encik Mohd Azuan Bin Mat Nuri, Encik Mohamad Hafiq Bin Mohamad Nadzri, Encik Mohammad Firdaus Bin Zulkiflee and Puan Norshanini Amalina Binti Mahadzir.
- F. Faculty General Officers: Encik Abdul Rahman Bin Rashid, Cik Azlinda Binti Abdullah, Ms Chai Xue Fen, Ms Ng Shu Ting, Ms Ng Yen Yen, Cik Norashimah Binti Abdullah, Cik Siti Nurshafiqa Binti Sha'arani and Ms. Wan Mun Pik.
- G. Graduate Assistants: Ms Ang Yi Ling, Mr Ch'ng Chee Henn, Ms Ng Wan Qing and Mr Jason Lim Jing Wei.
- H. Department of Agricultural and Food Science (DAFS) in FSc: Dr.

Ooi Ai Lin and Dr. Kwong Phek Jin.

Thank you for making this voyage full of hardships a truly valuable experience.

I am so grateful and indebted to my former Monbukagakusho scholars, Prof. Dr Eric Lai Ngit Shin (Ketua Kampung), Prof. Dr Neoh Hui Min, Dr. Toh Gaik Theng (Captain), Dr. Lim Hui Wen, Prof. Dr Tee Kok Keng, Mr. Chua Chong Wei, Prof. Dr Nadia Tan Mei Lin, Mr Hoo Kuang Shan and his wife, Dr Ooi Xin-Yi, Dr. Jeffrey Tan Too Chuan, Ms. Connsynn Chye, and Fernando Javier Wong, Stefan Skudlarek, Franzi Dreke and her husband, Dr. Kim Juhoon, Oleg Chernov and his wife Olha Yeremenko for their invaluable advice and moral supports.

My utmost gratitude goes to my best friends and soul mates who never failed to be there for me at difficult moments, providing me shoulders to lean on. These people are none other than Prof. Dr Lee Yun Li, Ms. Janet Lee Yun Ti, Ms. Kaye Cheong, Mr. Kelby Cheong, Dr. Kwan Ban Hoe and his wife, Ms. Leong Sook Lai, Mr. Low Wai Leon and his wife, Ms Cheong Pei Fen. Life would have been different without you guys, and I thank God for the eternal friendship and great bond among us.

I also would like to give thanks to my relatives, my aunties: Mandy Lee Yee Fuan, Judy Lee Yee Han, my uncles: Uncle Vincent, Uncle KC and Uncle Chong; my cousins: Chong Hui Hui, Lee Lim Meng, Choo Kok Peng, Choo Siu Pig and Lee Sook Fang, who have always supported me all this time, especially after the sudden death of my late dad.

Last but not least, most important of all, an extra-large thank you to my

family and family, especially my twin sister, Dr. Saw Seow Hoon, who has been the best supporter, nurturing her trusts in my pursuits and morally providing me the invaluable support over these years, and thank you for being such a great and caring sister cum friend to me, saying encouraging words and cheering me up at difficult and stressful times. To my dearest late mom, who had been suffering from Dementia's disease, thank you is just too small a word to describe how much I appreciate you; your love and reassuring smile has made my life worthwhile. You are indeed my root and my foundation that I base my life on. Through life's rough patches, you still make me feel safe and secure; you have been nothing less than an angel for sure. Thank you, Mom, and may you find eternal peace. I love you, dearly!

Finally, this thesis is heartily dedicated to my dad who left for heaven before the completion of this work. Dad, we are no longer physically in touch, but I know you are watching me from above, showering me with blessings and making my wishes come true.

May you rest in peace, dad. You will be missed.

APPROVAL SHEET

This thesis entitled <u>"FEMUR SHAPE ANALYSIS SYSTEM US-ING MAXIMUM-MINIMUM CENTRE SKELETONIZATION"</u>

was prepared by SAW SEOW HUI and submitted as partial fulfilment of the requirements for the degree of Doctor of Philosophy in Computer Sciences at Universiti Tunku Abdul Rahman.

Approved by:

(Ir. Prof. Dato' Dr. Ewe Hong Tat)

Date: 3 January 2024

Senior Professor/Supervisor

Twe Horge lat

Department of Electrical and Electronic Engineering Lee Kong Chian Faculty of Engineering and Science Universiti Tunku Abdul Rahman

(Prof. Dr Leung Kar Hang)

Date: 3 January 2024

Professor/ Internal Co-Supervisor

Department of Computer Science

Faculty of Information and Communication Technology

Universiti Tunku Abdul Rahman

(Prof. Lee Byung-Gook)

Date: 2024.01.03

Professor/ External Co-Supervisor

Division of Computer Engineering

Dongseo University

South Korea

FACULTY OF INFORMATION AND COMMUNICATION TECHNOLOGY UNIVERSITI TUNKU ABDUL RAHMAN

Date:_	28/12/2023
	SUBMISSION OF THESIS
It i	s hereby certified that ${\color{red} {\bf SAW~SEOW~HUI}}$ (ID No: ${\color{red} {\bf 1403132}}$)
has co	ompleted this thesis entitled <u>"FEMUR SHAPE ANA-</u>
	S SYSTEM USING MAXIMUM-MINIMUM CENTRE
	ETONIZATION" under the supervision of Prof. Ir. Dr Ewe
	Tat (Supervisor) from the Department of Electrical and Elec-
	Engineering, Lee Kong Chian Faculty of Engineering and Sci-
-	Prof. Dr Leung Kar Hang (Internal Co-Supervisor) from the
_	ement of Computer Science, Faculty of Information and Com-
	ation Technology, and <u>Prof. Lee Byung-Gook</u> (External Corisor) from the Division of Computer Engineering, Dongseo Uni-
versity	,
versity	•
	aderstand that the University will upload soft-copy of my thesis
_	format into UTAR Institutional Repository, which may be made
accessi	ble to UTAR community and public.
You	ars truly,
	-04.5
	Chan.
(SAW	SEOW HUI)

DECLARATION

I, **SAW SEOW HUI** hereby declare that the thesis is based on my original work except for quotations and citations which have been duly acknowledged. I also declare that it has not been previously or concurrently submitted for any other degree at UTAR or other institutions.

(SAW SEOW HUI)

28/12/2023Date _____

Contents

\mathbf{A}	bstra	act			iii
A	ckno	wledge	ements		\mathbf{v}
$\mathbf{A}_{\mathbf{j}}$	ppro	val Sh	eet		xii
Su	ıbmi	ssion S	Sheet		xiii
D	eclar	ation			xiv
Co	ontei	\mathbf{nts}			$\mathbf{x}\mathbf{v}$
$\mathbf{G}^{]}$	lossa	ry		xx	xvii
A	crony	yms			xl
1	INT	rrod [°]	UCTION		1
	1.1	Hum	an Femur		2
	1.2	Thre	e-dimensional (3D) Skeletonization		11
		1.2.1	Comparison Criteria		
		1.2.2	Types of 3D Skeletonization Method		18
	1.3	3D F	emur Shape Analysis System (3D-FSA)		21
	1.4	Resea	arch Objectives		31
	1.5	Resea	arch Contributions		41
	1.6	Thes	is Organization		56
2	LIT	ERAT	TURE REVIEW		59
	2.1	Osteo	metric Analysis of Human Femur		59
		2.1.1	Conventional Method		61
		2.1.2	Lateral Radiographs		64
		2.1.3	Computer-aided Design Software		68
	2.2	Overv	view of 3D Skeletonization		78
		2.2.1	Distance-Transform Field Algorithms		78

		2.2.2	Voronoi Diagram Based Methods	81
		2.2.3	Thinning-Based	83
	2.3	3D Sk	eletonization in Human Femur	85
		2.3.1	Computer-aided Methods for Assessing Lower Limit	b
			Deformities in Orthopaedic Surgery Planning [1] .	86
		2.3.2	Anatomy-based 3D Skeleton Extraction from Femu	ır
			Model [2]	88
3	\mathbf{AL}	GORIT	THM OVERVIEW	93
	3.1	Pre-pr	rocessing	97
	3.2	3D Fe	mur Construction	99
	3.3	3D Sk	eletonization	101
		3.3.1	Maximum-Minimum Centre Approach	106
	3.4	Result	ts Evaluation	108
4	PR	E-PRC	OCESSING	110
	4.1	The Ir	nnovation of this Module	110
	4.2	Му Та	asks	111
	4.3	The S	tudy Subjects for 3D-FSA	111
	4.4	The C	Common Types of Diagnostic Imaging Device	112
	4.5	The D	Diagnostic of Femur Shaft Fracture	117
	4.6	3D Da	ata Files Collection	118
	4.7	Geom	etric Parameters (GP)	121
		4.7.1	Vector	121
		4.7.2	Normal	121
		4.7.3	Cross Product	122
		4.7.4	Magnitude (Length) of a Vector	125
		4.7.5	Magnitude (Length) of the Cross Product	125
		4.7.6	Area of Triangle	126
		4.7.7	Interpolation in Barycentric Coordinates	127
	4.8	The S	tructures for the 3D Data Files in .obj Format \dots	130
		4.8.1	Geometric Vertices	138
		4.8.2	Vertex Normals	139
5	3D	FEMU	JR CONSTRUCTION	146
	5.1	The Ir	nnovation of this Module	146
	5.2	Му Та	asks	147
	5.3	Modul	le Overview	150
	5.4	Modul	le Architecture	151
	5.5	Progra	am Designs and Implementations	154

	5.6	The F	Final Outputs	. 171
6	3D	SKEL	ETONIZATION	177
	6.1	The I	nnovation of this Module	. 177
	6.2	Му Та	asks	. 178
	6.3	The E	Basic Idea	. 179
	6.4	Media	d Axis Transform	. 181
		6.4.1	Axis Adjustment and Feature Detection	. 182
		6.4.2	Maximum-Minimum Centre Approach	. 196
		6.4.3	Maximum-Minimum Thickness Calculation	. 215
		6.4.4	Minimum Radius Angle Calculation	. 230
7	RE	SULTS	S & DISCUSSIONS	238
	7.1	Result	ts	. 239
	7.2	Verific	cation and Validation	. 251
	7.3	Comp	arative Results	. 253
		7.3.1	Constructed 3D Femurs	. 254
		7.3.2	Computed Medial Axis (Skeleton)	. 261
8	CO	NCLU	SION	274
	8.1	Summ	nary of the Thesis	. 274
	8.2	Futur	e Work	. 275
		8.2.1	Data Loss Criteria: Measurement Approaches	. 277
		8.2.2	3D Mesh Segmentation	. 278
\mathbf{A}	Cul	oe.obj	3D File	326
В	Exp	erime	ntal Results	335

List of Tables

1.1	Skeletonization properties that are used in our comparative
1 -	results
1.5	Generated geometric parameters and the respective figures 45
2.1	List of studies that have employed specific Computer-aided
	Design (CAD) software and 3D construction program for
	morphometric evaluations
2.2	A comparison table for the related 3D skeletonization
	research in human femur
4.1	The overview of three (3) common types of diagnostic
	imaging devices extracted from $[3, 4, 5]$
4.2	The six (6) 3D files in Object File (.obj) format for the left
	femurs
4.3	The six (6) 3D files in .obj format for the right femurs 119
4.4	The vertex coordinates defined for the 3D cube extracted
	from $cube.obj$ as illustrated in Fig. A.1 in Appendix A 139
4.5	The vertex normals defined for the 3D cube extracted from
	cube.obj as illustrated in Fig. A.1 in Appendix A 144
4.6	The vertex indexes and the index for the vertex normals
	that are used to define the triangle face of the $cube.obj$ as
	illustrated in Fig. A.1 in Appendix A
5.1	The six (6) 3D files in .obj format for the left femurs 155
5.2	The six (6) 3D files in .obj format for the right femurs 155
7.1	Generated geometric parameters and the respective figures 240
7.2	Skeletonization properties that are used in our comparative
	results
7.3	The computational scalability comparison between our
	algorithm and the Thinning-based algorithm271

8.1	The tested equations of the length term and curvature term
	for max-flow and min-cut algorithm
B.1	Time complexity measurements for ten (10) times of the
	3D femur meshes using our algorithm. The average
	and the standard deviation are calculated based on these
	measurements

List of Figures

1.1	The n	nain keywords in our research	1
1.2	An ex	cample of human femur (Right femur and left femur)	
	source	ed from the website [6]	2
1.3	The a	natomy of a right femur	4
	1.3a	(Posterior View) The femur is divided into three	
		parts: proximal, shaft and distal	4
	1.3b	The anatomy of the femur for proximal and distal	
		parts in anterior view and posterior view respectively.	4
1.4	Femor	ral shaft fracture can occur in some motor vehicle	
	accide	ents	5
1.5	Femor	ral shaft fracture can also occur in a lower-force accidents.	5
	1.5a	Falls from ladder and landing on foot	5
	1.5b	Older people with weaker bones or osteoporosis	5
1.6	Two ((2) types of treatments for femoral shaft fractures	7
	1.6a	The nonsurgical treatment with cast	7
	1.6b	The surgical treatment with a specially designed	
		metal rod known as an IM nail is inserted into the	
		medullary canal and passes across the fractured bone	
		to maintain its position	7
1.7	The e	examples of bowed knees and bowed femur	8
	1.7a	My cousin brother is suffering from the bowed knee	8
	1.7b	Anteroposterior (AP) view of the bowed femur in a 2	
		years old child with rickets sourced from the website	
		[7]	8
1.8	Radiu	s of Curvature (ROC)	12
	1.8a	1. Femur Length, 2. Femur Shaft Length	12
	1.8b	Femur Width	12
	1.8c	Anteroposterior (AP) Length	12
	1.8d	The femoral isthmus, medullary canal and the	
		compact bone	12

1.8		parameters are significant for decision making in	
	surgery	y planning	13
	1.8e	The femoral isthmus, medullary canal and the	
		compact bone	13
1.9	The M	edial Axis (skeleton) (MA) and Medial Axis Transform	
	(MAT)) obtained from the YouTube video available at $[8]$	14
	1.9a	The $MA(\Omega)$ and the maximal inscribed circle B_i of	
		the 3D mesh Ω	14
	1.9b	By adding the radii r of the corresponding circles	
		to the set of the medial centres p , the $MAT(\Omega)$ is	
		acquired	14
1.10	MAT i	is mainly composed of MA and radius function	14
1.11	The M	IA or skeleton of a 3D mesh can be known as several	
	equiva	lent definitions: (i) Maximally inscribed circles, (ii)	
	Grassfi	ire analogy, (iii) Maxwell set, (iv) Symmetry set	15
1.12	The th	aree (3) major groups for existing 3D skeletonization	
	metho	$\operatorname{ds.}$	19
1.13	Our p	roposed approach for 3D skeletonization namely,	
	maxim	um-minimum centre approach	20
1.14	The 3I	D human femur can be displayed in faces view, edges	
	view, a	and vertices view in our system, 3D-FSA	25
	1.14a	3D left femur in vertices view	25
	1.14b	3D left femur in edges view	25
	1.14c	3D left femur in faces view	25
	1.15a	The User Interface (UI) of the starting window when	
		the program is executed. The left rectangle provides	
		the information about the structure and status of a	
		loaded 3D mesh, whereas the right rectangle provides	
		the information of the cylindrical slider. We called	
		these rectangles as the information dialog boxes. The	
		reference lines of (x, y, z) – axes are located in the	
		middle part of the window	26
	1.15b	The reference lines of (x, y, z) – $axes$: The red line	
		represents the $x - axis$, green line represents the	
		y - axis, and the blue line represents the $z - axis$;	
		The menu bar consists of four (4) essential functions,	
		which consists of: File, Edit, View and About	26
1.16	The G	raphical User Interface (GUI) for the File menu in	
	3D-FS	A	27

	1.16a	The File menu consists of: New, Open, Save, Save	
		As, Print, Print Preview, Print Setup, Recent File	
		and Exit commands. There are several commands	
		can be accessed via keyboard shortcuts	27
	1.16b	In order to compute a skeleton, a 3D mesh has to be	
		opened. Go to File menu, select the Open command	27
1.16	The G	UI for the File menu in 3D-FSA	28
	1.16c	A new window will pop out with the list of 3D femurs	
		in .obj format. Select a file, e.g.: $0123964_L_all.obj$	
		and press the Open button	28
	1.16d	The 3D femur of $0123964_L_all.obj$ is displayed in	
		the window	28
	1.16e	The size of a 3D femur can be enlarged or reduced	
		by using the mouse	29
	1.16f	The 3D femur can be rotated around the reference	
		lines	29
1.17	The E	dit menu consists of: Undo, Cut, Copy and Paste	
	comma	ands. These commands can be accessed via keyboard	
	shortc	uts	30
1.18	The V	iew menu consists of many commands that are related	
	to the	geometry and viewing transformation of the 3D mesh.	
	These	commands can be accessed via keyboard shortcuts	30
1.19	The A	bout menu consists of a short introduction related to	
	3D-FS	A	31
1.20	The be	oundary and the cylindrical slider s in 3D-FSA	32
	1.20a	The square boxes in pink colour located at both end	
		of the 3D femur represent the boundary boxes	32
	1.20b	The two (2) circles are called the cylindrical slider	
		s in 3D-FSA. It plays an important role to traverse	
		from the beginning of the 3D femur until the end of	
		the 3D femur for the skeleton computation	32
1.21	The us	sage of the spacebar key in 3D-FSA	33
	1.21a	The information dialog boxes can be hidden by	
		selecting the View menu or by just pressing the space	
		bar keyboard.	33
	1.21b	Press the space bar keyboard one more time, the	
		information dialog box on the right will be visible	33
1.21	The us	sage of the spacebar key in 3D-FSA	

	1.21c	Press the space bar keyboard again, the information	
		dialog box on the left will also be visible	34
1.22	The ex	xecution process of our proposed maximum-minimum	
	centre	approach in 3D-FSA	35
	1.22a	Then press zero (0) key on keyboard to perform	
		the 3D skeletonization based on the position of the	
		cylindrical slider s	35
	1.22b	There are two (2) planes during the 3D skeletoniza-	
		tion: The base plane and the projection plane. These	
		planes are described in Chapter 6	35
1.22	The ex	xecution process of our proposed maximum-minimum	
	centre	approach in 3D-FSA	36
	1.22c	The 3D skeletonization continues. As you can see,	
		only the faces within the cylindrical slider s are used	
		to calculate all the medial centres	36
	1.22d	The medial line (medial axis) is constructed by	
		connecting these obtained medial centres	36
1.22	The ex	xecution process of our proposed maximum-minimum	
	centre	approach in 3D-FSA	37
	1.22e	The 3D skeletonization continues	37
	1.22f	The 3D skeletonization continues	37
1.22	The ex	xecution process of our proposed maximum-minimum	
	centre	approach in 3D-FSA	38
	1.22g	The 3D skeletonization continues	38
	1.22h	The 3D skeletonization continues	38
1.22	The ex	xecution process of our proposed maximum-minimum	
	centre	approach in 3D-FSA	39
	1.22i	The 3D skeletonization continues	39
	1.22j	The 3D skeletonization continues	39
1.22	The ex	secution process of our proposed maximum-minimum	
	centre	approach in 3D-FSA	40
	1.22k	The 3D skeletonization continues	40
	1.22l	The 3D skeletonization continues	40
1.22	The ex	secution process of our proposed maximum-minimum	
	centre	approach in 3D-FSA	41
	$1.22 \mathrm{m}$	The 3D skeletonization continues until the cylindrical	
		slider s reaches the end	41
	1.23a	The 3D skeletonization for the 3D femur is completed.	42

	1.23b	Finally, the medial centres and the medial line	
		(medial axis) are constructed	42
1.24	The re	sults generated by 3D-FSA	46
	1.24a	The femur length	46
1.24	The re	sults generated by 3D-FSA	47
	1.24b	The femur shaft length	47
1.24	The re	sults generated by 3D-FSA	48
	1.24c	The generated MA	48
1.24	The re	sults generated by 3D-FSA	49
	1.24d	The medial centres are generated by the selected	
		portion of the cylindrical slider s on the base plane. $$.	49
1.24	The re	sults generated by 3D-FSA	50
	1.24e	The computed radius function for the MAT	50
1.24	The re	sults generated by 3D-FSA	51
	1.24f	The location of the medullary canal	51
1.24	The re	sults generated by 3D-FSA	52
	1.24g	The diameter of the medullary canal is obtained in	
		the projection plane	52
1.24	The re	sults generated by 3D-FSA	53
	1.24h	The thickness of the compact bone is also calculated. $\boldsymbol{.}$	53
1.24	The re	sults generated by 3D-FSA	54
	1.24i	The location of the isthmus and its diameter, the	
		femur width and the AP length	54
	1.24j	The ROC together with the minimum radius angle	55
	2.1a	The osteometric board used to measure the maximum	
		length of the bones [9]	65
	2.1b	The location of the three (3) reference lines and meas-	
		urement points are indicated using the conventional	
		method [10]	65
2.2	An exa	ample of the lateral radiographs approach involves	
	using a	an X-radiation (X-rays) machine sourced from the	
	website	e [11]	69
2.3	The po	opular medical 3D modelling, printing and biomedical	
	engine	ering softwares	71
	2.3a	An example of a UI for Materialise Mimics software	
		sourced from the website [12]	71
	2.3b	An example of a UI for AVIEW Modeler software	
		sourced from the website [13]	71

2.4	The examples for the CAD softwares approach to measure
	the femur's parameters
	2.4a An example of a coronal Computed Tomography
	(CT) image of a femur for measurements [14] 76
	2.4b An example of a constructed 3D model of the femora
	based on the CT scans [15]
2.5	The three (3) major groups for existing 3D skeletonization
	methods
2.6	The generated MA with disconnected, noisy and spurious
	branches in [1]
2.7	The generated MA with spurious branches in [2] 91
3.1	Overview of our proposed algorithm
3.2	We are responsible for the implementation of three (3)
	phases: 3D Femur Construction, 3D Skeletonization and
	Results Evaluations. Whereas, the researchers from South
	Korea [16] are responsible for the implementation of two (2)
	phases: Pre-processing and Shape Analysis 96
3.3	A concise overview of the initial phase, specifically the First
	Phase (1^{st}) , with a focus on the pre-processing stage 98
3.4	A succinct summary of the Second Phase (2^{nd}) , highlighting
	the stage dedicated to the construction of the 3D femur 100
3.5	The crucial development tools collectively contribute to the
	functionality of our 3D-FSA system
3.6	The 3D human femur can be displayed in faces view, edges
	view, and vertices view in our system, 3D-FSA 102
	3.6a 3D left femur in vertices view
	3.6b 3D left femur in edges view
	3.6c 3D left femur in faces view
3.7	The crucial development tools collectively contribute to the
	functionality of our 3D-FSA system
3.8	A brief overview of the Third Phase (3^{rd}) , emphasising the
	steps devoted to the skeletonization of the 3D femur 105
3.9	Weighted average vertex (green in colour), inner slice
	polygon Ω_s which consists of the projected centroids of the
	faces (triangles) in F_s (blue in colour), maximal inscribed
	circle $B_s(p,r)$ with radius r (green circle and radius) 107
4.1	The twelve (12) femur .obj files and its illustration 120

4.2	The in	mportant parameters that influence the appearance of
	3D me	esh in computer graphics
	4.2a	Vectors: \vec{A} and \vec{B} . The magnitude of \vec{A} is represented
		as $\ \vec{A}\ $, and same goes to magnitude of $\ \vec{B}\ $. A unit
		vector is when $\ \vec{A}\ $ is equals to 1 or $\ \vec{B}\ $ is equals to 1.123
	4.2b	Normal: An example of the normal \vec{N} that is
		perpendicular to the plane of a triangle at p
4.3	The r	esulting vector \vec{N} obtained from the cross product
	operat	tion $\vec{A} \times \vec{B}$
4.4	The n	nagnitude (length) of cross product $\ \vec{A} \times \vec{B}\ $ is also
		s to the area of the parallelogram determined by \vec{A} and
	\vec{B}	
4.5	The c	alculation for the area of the triangle
	4.5a	Trigonometry relation with the two sides and angle
		using Eq. (4.6)
	4.5b	Heron Formula with three sides using Eq. (4.8) 128
4.6	An example of barycentric coordinates defining a position	
	with r	respect to the positions of the vertices of a triangle 131
	4.6a	The point f_i at i^{th} -triangle is the internal v_0, v_1, v_2
		vertices, whose area is $A(f_i) = t_u + t_v + t_w$
	4.6b	In computer graphics, barycentric coordinates can
		be seen as the area of sub-triangles (v_1, v_2, p) for t_u ,
		(v_2, v_0, p) for t_v and (v_0, v_1, p) for t_w over the area of
		the triangle $\Delta(v_0, v_1, v_2)$ which is the reason it's also
		called areal coordinates
	4.7a	The position of the vertices represented as v , which
		are used in rendering
	4.7b	The vertex normals represented as vn , which determ-
		ine the visual softness or hardness between the faces
		of 3D mesh [17]
	4.7c	The indexes of vertex and vertex normal that define
		the faces of the 3D mesh represented as f 136
4.8	The 3	D human femur can be displayed in faces view, edges
	view,	and vertices view in our system, 3D-FSA 137
	4.8a	3D left femur in vertices view
	4.8b	3D left femur in edges view
	4.8c	3D left femur in faces view

4.9	These examples are sourced from the website [18] that		
	illustrates the difference between face normals and vertex		
	normals		
	4.9a	The normals are computed for every face of a 3D mesh	.141
	4.9b	The normals are computed for every vertices of a 3D	
		mesh and are using to interpolate smoothly across	
		the surface	141
4.10	These	examples are extracted from [18]	142
	4.10a	A 3D cylinder rendered with face normals	142
	4.10b	A 3D cylinder rendered with vertex normals	142
4.11	The ex	camples for face normals and vertex normals of a 3D	
	cube n	nodelled in Blender [19]	143
5.1	The GUI of our 3D-FSA System		148
5.2	The 3I	O human femur can be displayed in faces view, edges	
	view, a	and vertices view in our system, 3D-FSA	149
	5.2a	3D left femur in vertices view	149
	5.2b	3D left femur in edges view	149
	5.2c	3D left femur in faces view	149
5.3	A cond	ceptual model that describes the structure and beha-	
	viours	of multiple components of this module	152
5.4	The at	tributes for the respective 3D femurs	156
	5.4a	The attributes of the 3D femurs obtained from a	
		patient with the code number of 0123964 (Left femur	
		with intramedullary canal) which consists of the	
		number of vertices, the number of edges, and the	
		number of faces	156
	5.4b	The attributes of the 3D femurs obtained from	
		a patient with the code number of 0123964 (Left	
		femur without medullary canal) which consists of the	
		number of vertices, the number of edges, and the	
		number of faces	156
5.4	The attributes for the respective 3D femurs		
	5.4c	The attributes of the 3D femurs obtained from a	
		patient with the code number of 0123964 (Right	
		femur with intramedullary canal) which consists of	
		the number of vertices, the number of edges, and the	
		number of faces	157

	5.4d	The attributes of the 3D femure obtained from a
		patient with the code number of 0123964 (Right
		femur without intramedullary canal) which consists
		of the number of vertices, the number of edges, and
		the number of faces
5.4	The a	ttributes for the respective 3D femurs
	5.4e	The attributes of the 3D femurs obtained from a
		patient with the code number of 0346688 (Left femur
		with intramedullary canal) which consists of the
		number of vertices, the number of edges, and the
		number of faces
	5.4f	The attributes of the 3D femurs obtained from a
		patient with the code number of 0346688 (Left femur
		without intramedullary canal) which consists of the
		number of vertices, the number of edges, and the
		number of faces
5.4	The a	ttributes for the respective 3D femurs
	5.4g	The attributes of the 3D femurs obtained from a
		patient with the code number of 0346688 (Right
		femur with intramedullary canal) which consists of
		the number of vertices, the number of edges, and the
		number of faces
	5.4h	The attributes of the 3D femurs obtained from a
		patient with the code number of 0346688 (Right
		femur without intramedullary canal) which consists
		of the number of vertices, the number of edges, and
		the number of faces
5.4	The a	ttributes for the respective 3D femurs 160
	5.4i	The attributes of the 3D femurs obtained from a
		patient with the code number of 00486295 (Left
		femur with intramedullary canal) which consists of
		the number of vertices, the number of edges, and the
		number of faces
	5.4j	The attributes of the 3D femurs obtained from a
		patient with the code number of 00486295 (Left
		femur without intramedullary canal) which consists
		of the number of vertices, the number of edges, and
		the number of faces

	5.4k	The attributes of the 3D femure obtained from a	
		patient with the code number of 00486295 (Right	
		femur with intramedullary canal) which consists of	
		the number of vertices, the number of edges, and the	
		number of faces	
	5.4l	The attributes of the 3D femurs obtained from a	
		patient with the code number of 00486295 (Right	
		femur without intramedullary canal) which consists	
		of the number of vertices, the number of edges, and	
		the number of faces	
5.5	This	flow chart shows the defined functions, together with	
	the O	penGL Mathematics (GLM) that is used to achieve	
	the 31	D femur construction	
5.6	The c	outputs of this module: 3D Femur Construction in	
	3D-FS	SA	
	5.6a	This is the File menu that consists of: New, Open,	
		Save, Save As, Print, Print Preview, Print Setup,	
		Recent File and Exit commands. There are several	
		commands can be accessed via keyboard shortcuts 173	
	5.6b	When the user select "Open" command 173	
5.6	The outputs of this module: 3D Femur Construction in		
	3D-F	SA)	
	5.6c	A dialog box will be popped out and any femur in	
		.obj format can be selected	
	5.6d	Once the Open button is clicked, the 3D femur is	
		displayed in faces view by default	
5.6	The c	outputs of this module: 3D Femur Construction in	
	3D-FS	SA)	
	5.6e	When the key 'E' or 'e' is detected from the keyboard,	
		the 3D femur is displayed in edges view 175	
	5.6f	When the key 'V' or 'v' is detected from the keyboard,	
		the 3D femur is displayed in vertices view 175	
	5.6g	The user can also change the view of the 3D femur	
		by selecting the commands in the View menu 176	
6.1	The b	easic idea of our 3D skeletonization algorithm 180	
6.2	MAT	is mainly composed of MA and radius function. $$ 181	
6.3	The in	nvolved processes for 3D skeletonization 183	

6.4	The highlighted method, glmDimensions is written by Nate		
	Robins	s [20], and the obtained measurements are used to	
	form o	ur display components	
6.5	The pr	cocesses involved in $glmDimensions()$ 187	
	6.5a	The first (1^{st}) part of the processes which involves	
		looking for the maximum and minimum values among	
		all the coordinate of the vertices (x, y, z) 187	
	6.5b	The second (2^{nd}) part of the processes which involves	
		calculating the dimensions of the 3D femur, the	
		centre point of the 3D femur, and the transformation	
		of the 3D femur to fit on the display 187	
6.6	Our w	ritten program for drawing the axes, boundary, 3D	
	femur	(with vertices, edges and faces), the cylindrical slider	
	and th	e curvature of the MA, based on the measurements	
	return	ed by the glmDimensions method written by Nate	
	Robins [20]		
6.7	The ar	natomy of a right femur	
	6.7a	(Posterior View) The femur is divided into three	
		parts: proximal, shaft and distal 191	
	6.7b	The anatomy of the femur for proximal and distal	
		parts in anterior view and posterior view respectively. 191	
6.8	The ca	alculation of the dimensions and adjustment for the	
	axes in	3D based on the size of the 3D femur in the method	
	of glm.	Dimensions.	
	6.8a	Left femur: The (x,y) – $axis$ adjustment, bounding	
		box $(pink\ in\ colour)$ and the cylindrical slider $s\ (green$	
		in colour) is calculated by the width and height of	
		the left femur	
	6.8b	Left femur: The z – $axis$ adjustment extracted from	
		the length of the left femur	
6.9	The cy	vlindrical sliders s (The composition of two (2) green	
	circles), adjacent faces F_s (brown faces (triangles)) 195	
6.10	The in	nplementation steps involved for the maximum-	
		um centre approach in Section 6.4.2 197	
6.11	The simplex operators $\lfloor v \rfloor$ and $\lceil v \rceil$		
6.12		elationship between the area of parallelogram and the	
	area of	f the triangle enclosed by the two (2) vectors using the	
	_	oroduct	
	6.12a	The area of the parallelogram	

	6.12b	The area of the triangle which follows from the fact	
		that the parallelogram formed by u and v is being	
		cut into half.	201
6.13	The ex	camples of the calculations for each face i in F_s	202
	6.13a	The centroid \bar{f}_i of each face (triangle)	202
	6.13b	The area $A(f_i)$ for each face (triangle) i in F_s	202
6.13	The ex	camples of the calculations for each face i in F_s	
		The multiplication of both the area $A(f_i)$ and the	
	0.401	centroid \bar{f}_i	203
	6.13d	The weighted normal of a face (triangle) f_i as denoted	
		in Eq. (6.11)	203
6.14	-	vlindrical sliders s (The composition of two (2) green	
), the base plane (grey in colour) and the projection	
		$(peach\ in\ colour)$	207
6.15	Weight	ted average vertex (green in colour), inner slice	
	polygo	on Ω_s which consists of the projected centroids of the	
	faces (triangles) in F_s (blue in colour), maximal inscribed	
	circle I	$B_s(p,r)$ with radius r (green circle and radius)	209
6.16	The 31	D femur skeletonization result with the connected	
	edges l	between the weighted average vertices (green in colour).	213
6.17	The ou	iter diameter of the medullary canal (compact bone).	216
6.18	The inner slice polygon Ω_s obtained from Section 6.4.2. It		
	consist	s of the projected centroids (blue in colour) of the	
	faces (triangles) in F_s and it is used to determine the outer	
	diamet	ter of the medullary canal (compact bone)	217
6.19	Conto	urs detection.	220
	6.19a	The outer diameter of the medullary canal (compact	
		bone) is measured from the outer curve of the inner	
		boundary of <i>contour</i> 2, to the inner curve of the outer	
		boundary of <i>contour</i> 1	220
	6.19b	After the execution of Algorithm 2, contour 1 (green	
		in colour) and <i>contour</i> 2 (tangerine in colour) are	
		found and coloured	220
6.20	An exa	ample of the Chamfer Distance (CD) computation in	
		processing. These figures are sourced from [21]	222
	6.20a	Target image and the distance-transform's version	
	6.20b	Computation of the CD	
6.20		ample of the CD computation in image processing.	
J. _ U		figures are sourced from [21]	223

	6.20c Best match of template image in target image 223
6.21	The thickness calculation using our approach, namely
	maximum-minimum thickness approach
6.22	The maximum inscribed circle $B_s(p,r)$ (green circle) and the
	radius r , with the diameter (thickness) of the compact bone
	=2r. These parameters are computed using the approaches
	described in Section 6.4.2 and Section 6.4.3
6.23	The involved range for the calculation of the minimum ROC. 234
	6.23a After the calculation in Section 6.4.2, the results of
	sixty-eight (68) cylindrical sliders are generated and
	displayed in faces view
	6.23b The results from Section 6.4.2 are displayed in vertices
	view after the 'F' or 'f' key is pressed. Although sixty-
	eight (68) cylindrical sliders are generated, only the
	indices from six (6) (bottom margin is equal to
	0.08%) to fifty-four (54) (top margin is equal to
	0.18%) are used to calculate the minimum ROC 234
6.23	The involved range for the calculation of the minimum ROC. 235
	6.23c Another example from the indices from eight (8)
	(bottom margin is equal to 0.11%) to 54 (top margin
	is equal to 0.18%) are used to calculate the minimum
	ROC
6.24	The projected vertices for the calculation of the minimum
	ROC
	6.24a The projected angle of 0° to 180° 236
	6.24b Projected plane
6.24	The projected vertices for the calculation of the minimum
	ROC
	6.24c Resulting projection in faces view
	6.24d The weighted normal of a face (triangle) f_i as denoted
	in Eq. (6.11)
7.1	The results generated by 3D-FSA
	7.1a The femur length
7.1	The results generated by 3D-FSA
	7.1b The femur shaft length
7.1	The results generated by 3D-FSA
	7.1c The generated MA
7 1	The results generated by 3D-FSA 244

	7.1d	The medial centres are generated by the selected
		portion of the cylindrical slider s on the base plane 244
7.1	The re	esults generated by 3D-FSA
	7.1e	The computed radius function for the MAT 245
7.1	The re	esults generated by 3D-FSA
	7.1f	The location of the medullary canal 246
7.1	The re	esults generated by 3D-FSA
	7.1g	The diameter of the medullary canal is obtained in
		the projection plane
7.1	The re	esults generated by 3D-FSA
	7.1h	The thickness of the compact bone is also calculated 248
7.1	The re	esults generated by 3D-FSA
	7.1i	The location of the isthmus and its diameter, the
		femur width and the AP length
	7.1j	The ROC together with the minimum radius angle 250
7.2	The c	omparison results between using the other program
	[22] as	nd our program to construct 3D femurs
	7.2a	Constructed 3D femurs of 0123964 (Left femur) using
		the other program [22] and our program
7.2	The c	omparison results between using the other program
	[22] an	nd our program to construct 3D femurs 256
	7.2b	Constructed 3D femurs of 0123964 (Right femur)
		using the other program [22] and our program 256
7.2	The c	omparison results between using the other program
	[22] an	nd our program to construct 3D femurs
	7.2c	Constructed 3D femurs of 0346688 (Left femur) using
		the other program [22] and our program 257
7.2	The c	omparison results between using the other program
	[22] as	nd our program to construct 3D femurs
	7.2d	Constructed 3D femurs of 0346688 (Right femur)
		using the other program [22] and our program 258
7.2	The c	omparison results between using the other program
	[22] an	nd our program to construct 3D femurs
	7.2e	Constructed 3D femurs of 00486295 (Left femur)
		using the other program [22] and our program 259
	7.2f	Constructed 3D femurs of 00486295 (Left femur)
		using the other program [22] and our program 260

7.3	The comparison results between using the existing method			
		of Thinning-based 3D skeletonization and our method on		
		D femurs		
	7.3a	3D femure obtained from a patient with the code		
		number of 0123964 (Left femur), and the constructed		
		skeletons using the existing method and our method 263		
7.3	The c	The comparison results between using the existing method		
	of Th	of Thinning-based 3D skeletonization and our method on		
	the 3I	O femurs		
	7.3b	3D femurs obtained from a patient with the code		
		number of 0123964 (Right femur), and the construc-		
		ted skeletons using the existing method and our		
		method		
7.3	The c	omparison results between using the existing method		
	of Th	of Thinning-based 3D skeletonization and our method on		
	the 3I	D femurs		
	7.3c	3D femure obtained from a patient with the code		
		number of 0346688 (Left femur), and the constructed		
		skeletons using the existing method and our method 265		
7.3	The comparison results between using the existing method			
	of Thinning-based 3D skeletonization and our method on			
	the 3I	O femurs		
	7.3d	3D femure obtained from a patient with the code		
		number of 0346688 (Right femur), and the construc-		
		ted skeletons using the existing method and our		
		method		
7.3	The c	omparison results between using the existing method		
	of Thinning-based 3D skeletonization and our method on			
	the 3D femurs			
	7.3e	3D femure obtained from a patient with the code		
		number of 00486295 (Left femur), and the constructed		
		skeletons using the existing method and our method 267		
	7.3f	3D femure obtained from a patient with the code		
		number of 00486295 (Right femur), and the con-		
		structed skeletons using the existing method and our		
		method		

8.1	The 31	I mesh segmentation results on the obtained skeleton
	using v	various proposed weight functions in max-flow min-cut
	algorit	hm
	8.1a	Equation No. 1: Not successful 280
	8.1b	Equation No. 2: Not successful 280
8.1	The 31	O mesh segmentation results on the obtained skeleton
	using v	various proposed weight functions in max-flow min-cut
	algorit	hm
	8.1c	Equation No. 3: Not successful 281
	8.1d	Equation No. 4: Successfully partition the skeleton
		into two parts, the source and the sink 281
A.1	An ex	ample $cube.obj$ to illustrate the definition for the
	keywor	rds in .obj that are used in 3D-FSA 327
	A.1a	The constructed 3D cube based on the definition in
		cube.obj. There are three (3) types of information:
		vertex coordinates, vertex normals and face indexes
		that are used to construct this 3D cube. $\ \ldots \ \ldots \ 327$
A.1	An ex	ample $cube.obj$ to illustrate the definition for the
	keywo	rds in .obj that are used in 3D-FSA 328
	A.1b	The vertices of the cube are arranged according to
		the specified vertex coordinates. It begins with the
		first row of vertex coordinates: $v_1:(0.0,0.0,0.0)$,
		then followed by $v_2: (0.0, 0.0, 1.0), v_3: (0.0, 1.0, 1.0),$
		$v_4: (0.0, 1.0, 1.0), v_5: (1.0, 0.0, 1.0), v_6: (1.0, 0.0, 1.0),$
		$v_7: (1.0, 1.0, 0.0)$ and $v_8: (1.0, 1.0, 1.0)$. There are
		total of eight (8) vertices used to construct the 3D
		cube
A.1		ample $cube.obj$ to illustrate the definition for the
	keywo	rds in .obj that are used in 3D-FSA 329
	A.1c	The face indexes define the three vertices that are
		used to form the triangle face, and its vertex normal.
		The first row indicates the first triangle face, f_1
		that is formed by (v_1, v_7, v_5) . The vertex normal
		for this face is (vn_2, vn_2, vn_2) , which is equals to
		(0.0, 0.0, -1.0) that is located at the second row in
		the vertex normals part. Same goes to the second
		triangle face, f_2 that is formed by (v_1, v_3, v_7) with the
		same vertex normals as $f_1, \ldots, 329$

A.1	An ex	ample $cube.obj$ to illustrate the definition for the	
	keywo	rds in .obj that are used in 3D-FSA	
	A.1d	Triangle face f_3 is formed by (v_1, v_4, v_3) , with the	
		(vn_6, vn_6, vn_6) that is equals to $(-1.0, 0.0, 0.0)$.	
		Triangle face f_4 is formed by (v_1, v_2, v_4) , with the	
		same vertex normals as f_3	
A.1	An ex	cample $cube.obj$ to illustrate the definition for the	
	keywo	rds in .obj that are used in 3D-FSA	
	A.1e	Triangle face f_5 is formed by (v_3, v_8, v_7) , with the	
		(vn_3, vn_3, vn_3) that is equals to $(0.0, 1.0, 0.0)$. Tri-	
		angle face f_6 is formed by (v_3, v_4, v_8) , with the same	
		vertex normals as f_5	
A.1	An example $cube.obj$ to illustrate the definition for the		
	keywords in .obj that are used in 3D-FSA		
	A.1f	Triangle face f_7 is formed by (v_5, v_7, v_8) , with the	
		(vn_5, vn_5, vn_5) that is equals to $(1.0, 0.0, 0.0)$. Tri-	
		angle face f_8 is formed by (v_5, v_8, v_6) , with the same	
		vertex normals as f_7	
A.1	An ex	cample $cube.obj$ to illustrate the definition for the	
	keywo	rds in .obj that are used in 3D-FSA	
	A.1g	Triangle face f_9 is formed by (v_1, v_5, v_6) , with the	
		(vn_4, vn_4, vn_4) that is equals to $(0.0, -1.0, 0.0)$.	
		Triangle face f_{10} is formed by (v_1, v_6, v_2) , with the	
		same vertex normals as f_9	
	A.1h	Triangle face f_{11} is formed by (v_2, v_6, v_8) , with	
		the (vn_1, vn_1, vn_1) that is equals to $(0.0, 0.0, 1.0)$.	
		Triangle face f_{12} is formed by (v_2, v_8, v_4) , with the	
		same vertex normals as f_{11}	

Glossary

- t test Paired t test is used when we are interested in the difference between two (2) variables for the same subject. It is often the two (2) variables are separated by time.. 252
- **3D reconstruction** 3D reconstruction technology refers to converting multiple 2D medical image slices to a 3D anatomical model [23].. 70, 110
- centroid It is also known as geometric centre, which can be determined by the point of intersection of all the three (3) medians of a triangle. In other words, it is the centre point of three (3) masses that are placed at the three (3) vertices of a fixed reference triangle face.. xxxi, 127, 200, 202, 203, 204, 205, 210
- **compact bone** Compact bone forms the hard, dense outer layer of bones throughout the human body.. xx, xxi, xxiv, 11, 12, 13, 53
- contour A contour can be simply defined as a curve that joins a set of points enclosing an area having the same colour or intensity [24].. xxxi, 196, 208, 212, 215, 218, 219, 220, 221, 224, 225
- corticocancellous Referring to bony tissue containing both cortical and cancellous elements.. 110, 120
- **distance-transform** The distance transform provides a metric or measure of the separation of points in the image.. xxxi, 78, 79, 221, 222
- femoral isthmus Isthmus is the narrowest point of the femoral medullary canal. It lies approximately 8 to 12 cm below the lesser trochanter.. xx, xxi, 10, 12, 13
- forensic anthropology Forensic anthropology (the study of human remains) that involves applying skeletal analysis and techniques in archaeology to solving criminal cases.. 10, 59, 70

- human kinematics Human Kinetics is a discipline focused on the comprehensive study and practice of human movement and exercise, and its impact on health and physical performance.. 59
- ICA ICA stands for Intraclass Correlation Analysis. It is commonly used to quantify the degree to which individuals with a fixed degree of relatedness (e.g. full siblings) resemble each other in terms of a quantitative trait.. 277
- ICC ICC stands for Intraclass Correlation Coefficient. It is used to measure the reliability of ratings in studies where there are two (2) or more raters. The value of an ICC can range from zero (0) to one (1), with zero (0) indicating no reliability among raters, whereas one (1) indicating perfect reliability among raters.. xxxviii, 56, 252
- **IDE** It is stands for Integrated Development Environment that used to define the difference in measuring between observers.. 269
- intra-observer It is used to define the difference in measuring between observers.. 252
- **loci** Loci is a plural nount of locus. Locus can be defined as a set of vertices which satisfy a certain condition.. 18, 181, 208
- medullary canal Medullary canal is located in the central area of the bone, which contains the marrow.. xx, xxi, xxiv, 6, 7, 9, 10, 12, 13, 45, 51, 52, 59, 66, 240
- Microsoft Foundation Class (MFC) MFC is a C++ object-oriented library for developing desktop applications for Windows [25].. 99, 146, 148, 150, 165
- **OpenCV** OpenCV is a library of programming functions mainly for real-time computer vision.. 218
- OpenGL Mathematics (GLM) GLM is a header only C++ mathematics library for graphics software based on the OpenGL Shading Language (GLSL) specifications [26].. xxix, 99, 146, 148, 153, 164, 166
- orthopaedics Orthopaedics (also called orthopaedic surgery) is the medical specialty that focuses on injuries and diseases of the body's musculoskeletal system.. 21, 31, 44, 59, 60, 112, 117, 120, 178

- parametrisation Mesh parametrisation represents the mapping between two triangular mesh with similar topology. The surface that the mesh is mapped to is typically referred to as the parameter domain [27].. 110, 120
- **Pearson's correlation coefficients** Pearson's correlation is the most common way of measuring a linear correlation.. 252
- radii Radii is the plural of radius r.. xxi, 12, 14, 106, 181, 210
- **rendering** Rendering is the process using colour and shading in order to make the meshes appear solid and 3D.. xxvi, 134, 140, 143, 150, 153, 168, 192
- **shading** Shading is a process of adding values to create light and shadow of a 3D mesh in the scene [28].. 122, 139, 140
- **spurious** false or fake. xxv, 19, 56, 82, 87, 88, 91, 178, 261, 262, 270
- **square root** The square root of a number is the factor that we can multiply by itself to get that number.. 125, 210
- voxels Voxels stands for volume pixels. They are essentially 3D pixels, but instead of being squares, they are perfect cubes.. 19, 20, 79, 80, 81, 83, 84, 85, 178, 261

Acronyms

- .obj Object File. xviii, xxv, xxix, xxxv, xxxvi, 56, 57, 97, 99, 110, 111, 118, 119, 120, 121, 130, 132, 133, 136, 138, 139, 143, 144, 146, 147, 148, 150, 153, 154, 155, 162, 165, 168, 171, 172, 174, 326, 327, 328, 329, 330, 331, 332, 333, 334
- .stl Stereolithography. 110, 120
- **1D** One-dimensional. 18, 85, 87
- **2D** Two-dimensional. 18, 44, 62, 66, 67, 85, 115, 150, 179, 215
- **3D-FSA** 3D Femur Shape Analysis System. xv, xxi, xxii, xxiii, xxiv, xxv, xxvii, xxix, xxxii, xxxiii, xxxv, xxxvi, 1, 3, 21, 22, 24, 25, 26, 27, 28, 29, 31, 32, 33, 34, 35, 36, 37, 38, 39, 40, 41, 42, 44, 46, 47, 48, 49, 50, 51, 52, 53, 54, 55, 56, 93, 95, 99, 101, 102, 103, 110, 148, 173, 174, 175, 176, 230, 239, 241, 242, 243, 244, 245, 246, 247, 248, 249, 250, 251, 252, 254, 274, 275, 276, 278, 327, 328, 329, 330, 331, 332, 333, 334

AI Artificial Intelligence. 276

AP Anteroposterior. xx, xxiv, xxxiii, 10, 12, 45, 54, 108, 239, 240, 249

API Application Programming Interface. 150

CAD Computer-aided Design. xviii, xxv, 9, 60, 68, 70, 72, 73, 74, 75, 76, 77, 78, 80

CD Chamfer Distance. xxxi, 219, 221, 222, 223, 224

CPU Central Processing Unit. 269

CT Computed Tomography. xxv, 9, 10, 62, 67, 68, 70, 75, 76, 86, 89, 97, 110, 111, 112, 113, 114, 115, 116, 117, 118, 120, 121, 251, 278

DAFS Department of Agricultural and Food Science. ix

DCCT Department of Computer and Communication Technology. viii

DCE Division of Computer Engineering. vi

DCS Department of Computer Science. vii, viii

DD Deputy Dean. viii

DDET Department of Digital Economy Technology. viii

DEE Department of Electrical and Electronic Engineering. vi

DICOM Digital Imaging and Communications in Medicine. 75, 110, 120

DPM Department of Population Medicine. viii

DS Department of Surgery. viii

DSU Dongseo University. vi

ED Emergency Department. 118

FEA Finite Element Analysis. 68

FICT Faculty of Information and Communication Technology. vii, viii

FSc Faculty of Science. viii, ix

GPU Graphics Processing Unit. 84, 150

GUI Graphical User Interface. xxi, xxii, xxvii, 22, 26, 27, 28, 29, 148

HOD Head of Department. viii

HOP Head of Programme. vii, viii

HWU Heriot-Watt University. viii

IGS2019 International Geometry Summit. 253

IM Intramedullary Nailing. 6, 9, 196

LKCFES Lee Kong Chian Faculty of Engineering and Science. vi

LLD Leg Length Discrepancy. 6, 9

LSF Least Square Fitting. 230, 233

M. K. FMHS M. Kandiah Faculty of Medicine and Health Sciences. vii

MA Medial Axis (skeleton). xxi, xxiv, xxv, xxix, xxx, xxxii, 11, 13, 14, 15, 20, 24, 48, 82, 87, 88, 91, 101, 103, 177, 178, 179, 181, 188, 196, 208, 211, 243

MAT Medial Axis Transform. xxi, xxiv, xxix, xxxiii, 13, 14, 20, 50, 81, 101, 177, 181, 239, 245

MDMA Master in Data Management and Analytics & Postgraduate Diploma in Data Management and Analytics. viii

MIP Medical Image Processing. 120

MRI Magnetic Resonance Imaging. 62, 67, 68, 86, 112, 113, 114, 115, 116, 117, 118, 120

MS Multiple Sclerosis. 114

ORIF Open Reduction and Internal Fixation. 6

PC Personal Computer. 18

PCA Principle Components Analysis. 20, 89, 90

RGB Red, Green and Blue. 218

ROC Radius of Curvature. xx, xxiv, xxxii, xxxiii, 9, 11, 12, 45, 55, 108, 192, 230, 232, 234, 235, 236, 237, 239, 240, 250, 253

 $\textbf{S-CT}\,$ Spiral Computed Tomography. 44

 \mathbf{UI} User Interface. xxi, xxiv, 26, 70, 71, 150

UTAR Universiti Tunku Abdul Rahman. vi, vii, viii

X-rays X-radiation. xxiv, 64, 67, 69, 86, 112, 113, 114, 115, 116, 117, 278

Chapter 1

INTRODUCTION

There are two (2) main research questions that are required to be answered throughout our research as follows:

- A. How to perform 3D skeletonization on the given femur 3D mesh data?
- B. How is the resulting skeleton be used as an analysis study for the anatomical and geometrical parameters of the femur shaft?

Therefore, I have divided this research into three (3) main keywords as shown in Fig. 1.1 which consists of the human femur, followed by the 3D skeletonization and lastly, our femur analysis system namely 3D-FSA. These keywords are discussed in detail in the following sections.

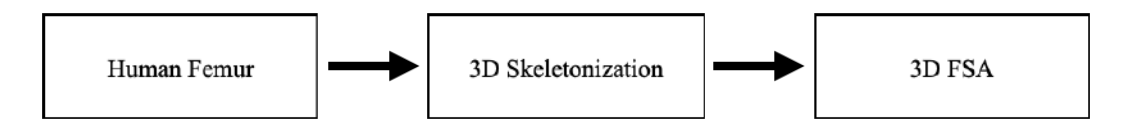


Figure 1.1: The main keywords in our research.

1.1 Human Femur

The human femur is the longest, heaviest and strongest bone in the human body as illustrated in Fig. 1.2. It acts as the site of origin and attachment of many muscles and ligaments, and can be divided into three parts: proximal, shaft and distal as illustrated in Fig. 6.7a. As shown in Fig. 6.7b, the proximal aspect of the femur articulates with the acetabulum of the pelvis to form the hip joint, which consists of a head and neck, and two bony processes - the greater and lesser trochanters [29].

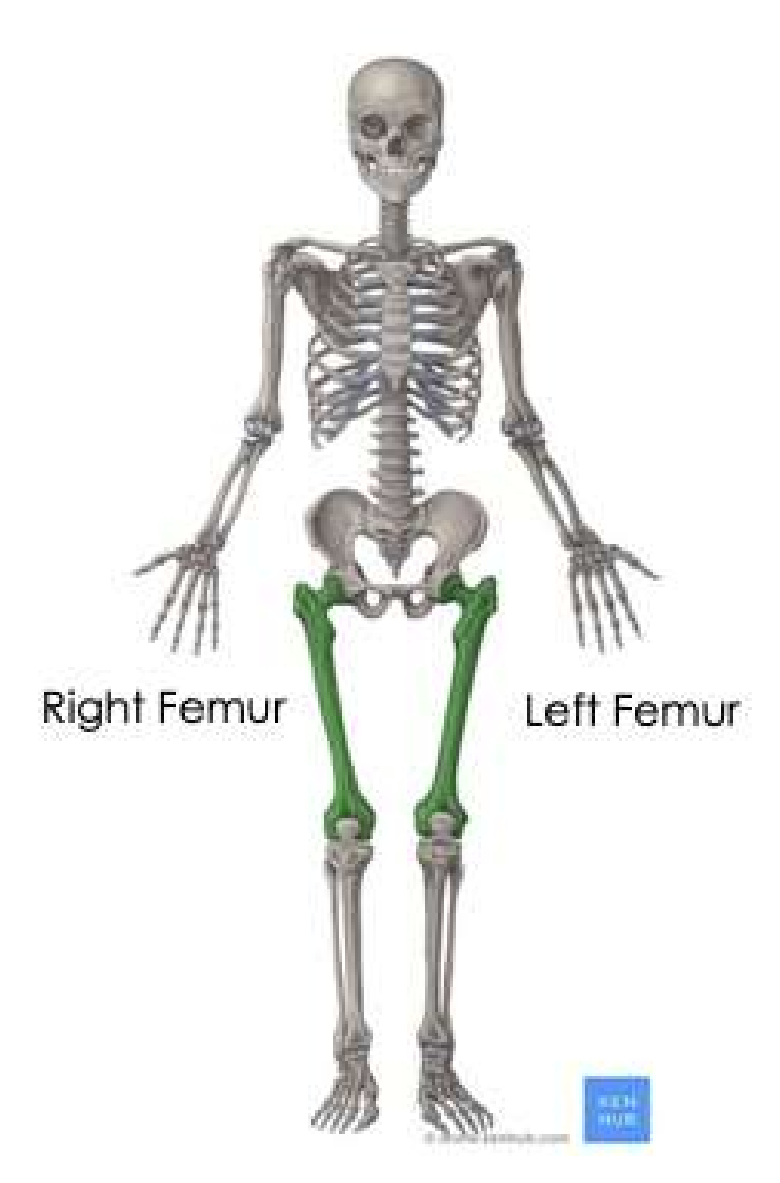
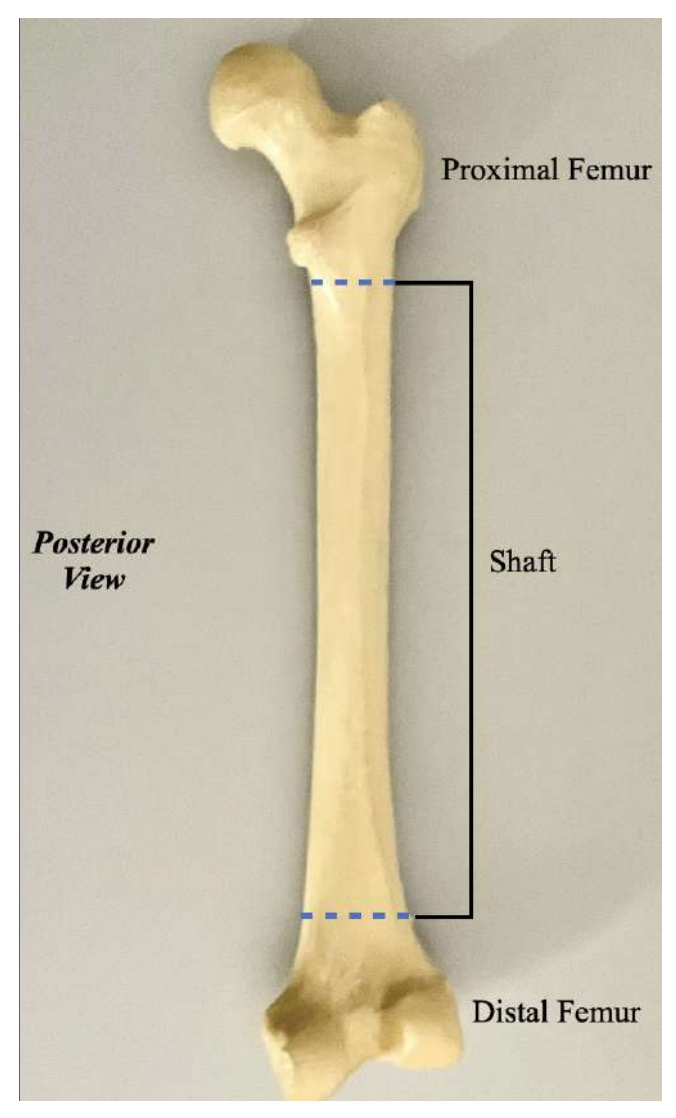


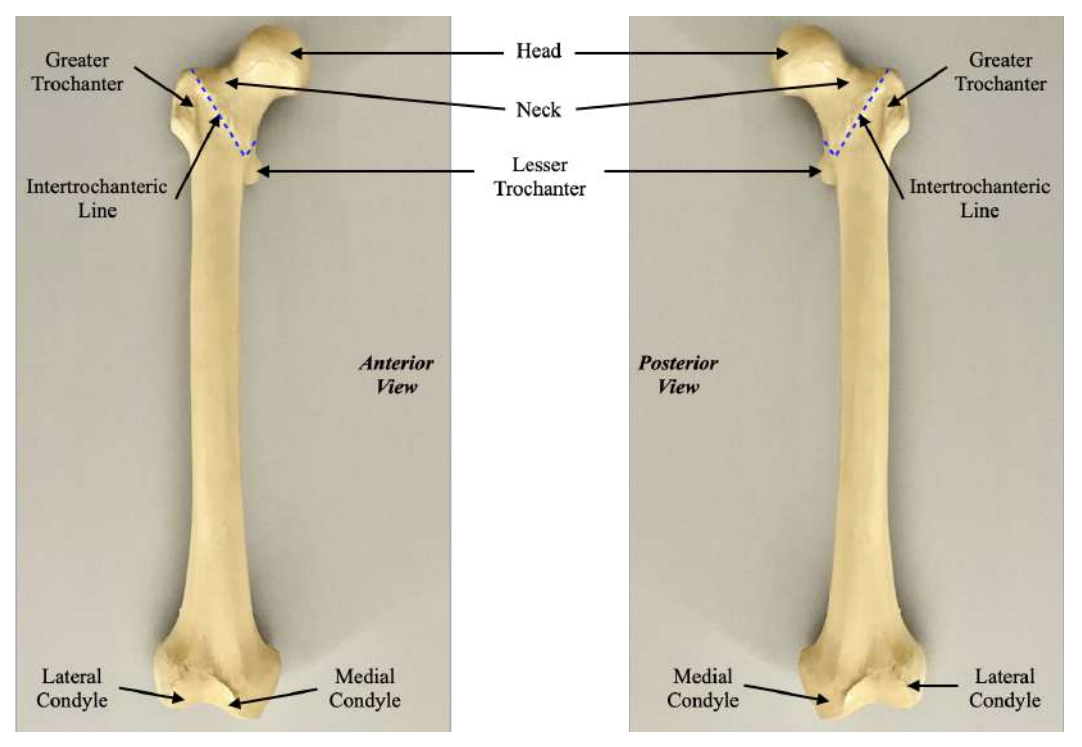
Figure 1.2: An example of human femur (Right femur and left femur) sourced from the website [6].

On the other hand, the distal end of the femur is characterised by the presence of the medial and lateral condyles, which articulate with the tibia and patella to form the knee joint. The third part is the shaft of the femur which descends in a slight medial direction. This brings the knees closer to the body's centre of gravity, increasing stability [29]. The femur shaft is our focused area in 3D-FSA.

There are times when there is a break anywhere along this length of bone, it is called a femoral shaft fracture [30]. Different kinds of trauma with many forces can result bone damage, such as in some motor vehicle



(a) (Posterior View) The femur is divided into three parts: proximal, shaft and distal.



(b) The anatomy of the femur for proximal and distal parts in anterior view and posterior view respectively.

Figure 1.3: The anatomy of a right femur.

accidents or motorcycle crashes as shown in Fig. 1.4, which causes over 1.3 million deaths worldwide and mostly involves a femoral shaft fracture [31]. The damage can also occur in a lower-force accidents, such as falls from slippery floors, and ladder landing on foot among the older people due to their weaker bones or osteoporosis as shown in Fig. 1.5. There are several types of femoral shaft fractures but these topics are beyond the scope of this research. Thus, the details of these topics will not be included in this thesis.

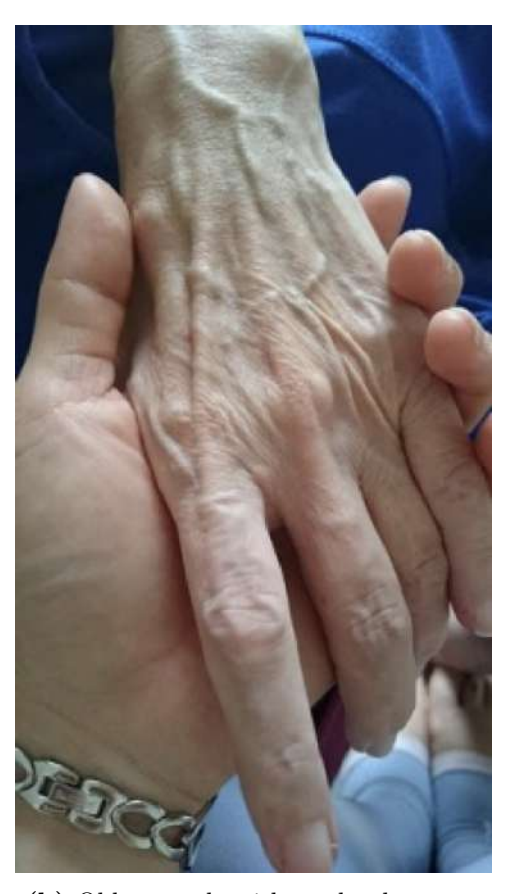
There are usually two (2) types of treatments for femoral fractures: non-surgical and the surgical (refer to Fig. 1.6). Nonsurgical treatment requires only a cast to heal as shown in Fig. 1.6a. This is mostly applicable to very young children. In contrast, surgical treatment requires surgery to repair and heal the broken bones within 24 to 48 hours. There are an approximately one in ten road injuries involves a femoral shaft fracture that is most effectively treated with surgery [31].



Figure 1.4: Femoral shaft fracture can occur in some motor vehicle accidents.



(a) Falls from ladder and landing on foot.



(b) Older people with weaker bones or osteoporosis.

Figure 1.5: Femoral shaft fracture can also occur in a lower-force accidents.

Open Reduction and Internal Fixation (ORIF) is a surgical treatment that consists of two procedures performed under anaesthesia [32, 33]. The first procedure is open reduction, in which the orthopaedic surgeon cuts the skin and adjusts the fractured bone to the normal position. The second procedure is internal fixation, where the bone fragments are held together with fixation devices such as plates, screws, stainless steel pins and wires until bone union [34, 35].

Intramedullary Nailing (IM) is the most common surgical treatment for certain diaphysial fractures of the femur [36]. During this procedure, a specially designed metal rod, also known as an IM nail as shown in Fig. 1.6b, is inserted into the medullary canal and passes across the fractured bone to maintain its position. Finally, screws are placed above and below the fracture to hold the femur in the correct alignment while the bone heals [37].

Nonetheless, orthopaedic surgeons often encounter severe problems such as iatrogenic fractures and complications during implant insertion due to exaggerated femoral bowing [10, 38, 39, 40, 41, 42]. Severe bowing of the femur as illustrated in Fig. 1.7 can result from a mismatch between the IM nail and the alignment of the femur. This mismatch occurs because most of the implants are designed for the typical femur, which does not usually match the atypical femur (the exaggerated bowing femurs).

Such mismatch is a risk factor for anterior cortical perforation off the distal femur with subtrochanteric fractures, and Leg Length Discrepancy (LLD) with fractures of the femoral shaft. LLD after IM nailing of femoral shaft fractures is common and is reported in 20% to 30% of cases [43]. Sev-



(a) The nonsurgical treatment with cast.



(b) The surgical treatment with a specially designed metal rod known as an IM nail is inserted into the medullary canal and passes across the fractured bone to maintain its position.

Figure 1.6: Two (2) types of treatments for femoral shaft fractures.



(a) My cousin brother is suffering from the bowed knee.



(b) Anteroposterior (AP) view of the bowed femur in a 2 years old child with rickets sourced from the website [7].

Figure 1.7: The examples of bowed knees and bowed femur.

eral techniques were proposed in [44, 45, 46, 47] to prevent intra-operative LLD during femoral fracture fixation. In addition, [48, 49] measured the LLD for several patients who had treated their femoral shaft fracture with IM nails for early intervention and repeat surgery.

Therefore, several morphological studies have been conducted on the differences in the magnitude of femoral bowing among the Asian population [50, 51, 52, 15] and Western populations [53, 54, 55, 56, 57, 58]. In addition, the other significant parameters of the human femur, such as femoral length, diameter of medullary canal, ROC, femur length and etc., were assessed using either roentgenogram [59, 60, 61], CT [62, 63, 14, 15], 3D spaces [64, 65, 52, 66, 51, 16] or 3D printed models [39]. These parameters obtained from all walks of life, various races and ages are used as a reliable frame of reference during the preoperative templating and preoperative design of custom-made implant devices [40].

Femoral bowing refers to the curvature or bending of the femur, which is the thigh bone. It is a natural variation in the shape of the femur that can be observed along its length. It can occur in different regions of the bone, such as the shaft of the neck. Femoral bowing can be determined by measuring of the angulation between the proximal and distal quarters of the femoral diaphysis, and the cut-off value was defined between 5.25° and 7.00° [67, 68, 56]. Thus, a preoperative planning template in orthopaedic surgery is an essential prerequisite to estimate the correct nail diameter and length for the success of the procedures. Conventionally, the detailed surgical plan and measurement are written down as blueprints and performed on hardcopy radiographs using various methods. This practice has become less practical because of a lack of consistency in radiographic magnification [69] and the rapid development of CAD software for deriving 3D meshes

from reconstructed lateral radiographs or images using CT images [52].

Therefore, a comprehensive anatomical study of human femurs by geometric computation is warranted to properly characterise the significant femur parameters and serve as a reference for physical and forensic anthropology as well as the design of medical devices suitable. Moreover, these studies are able to avoid potential malalignment, rotation, and abnormal stresses between the femur and implant.

These significant femur parameters including:

- The femur length from the upper pole of the femoral head to the bicondylar baseline as illustrated in Fig. 1.8a.
- The shaft length from the tip of the greater trochanter to the bicondylar line as illustrated in Fig. 1.8a.
- The femur width of the entire femur as illustrated in Fig. 1.8b.
- The AP length as illustrated in Fig. 1.8c.
- The diameter of the medullary canal as illustrated in Fig. 1.8e.
- The location and the width of the femoral isthmus as illustrated in Fig. 1.8e.

- The thickness of the compact bone as illustrated in Fig. 1.8e.
- The ROC as illustrated in Fig. 1.8d.

1.2 3D Skeletonization

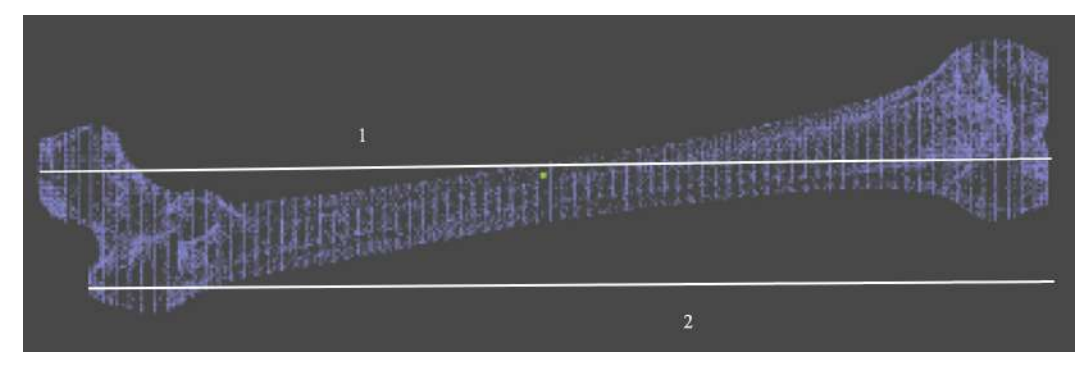
A 3D mesh is a raw, rich, complex and unmeaningful to be analysed. Furthermore, a high-resolution 3D mesh can be highly expensive in storage and processing terms. For that reason, 3D skeletonization is one such alternative representation that provides an effective and compact representation of objects.

3D skeletonization is a process of generating a skeleton, sometimes called the curve skeleton, which captures the inner structure of an overall complex 3D mesh. These computed skeletons consist of significant geometric and topological information that are used extensively to produce segmentation for various analyses and visualisations in medical imaging [70], robotics [71], reverse engineering [72] and video surveillance systems [73].

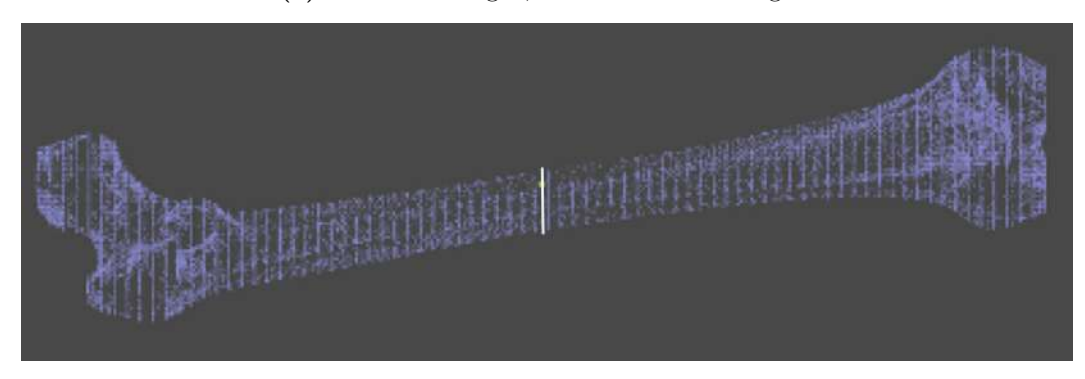
The resulting of 3D skeletonization is called the skeleton or the MA. For decades, many research efforts have focused on finding an optimal approach for generating skeletons or medial axes from these digital meshes. The concept of the MA was first presented by Blum [74] as a shape descriptor for computer vision applications in the year of 1967.

The concept was next extended to 3D shapes, yielding a wide family of variations and the state-of-art of 3D skeleton was published in the year of 2016 in Eurographics [75]. This paper defined the 3D mesh as Ω and

the medial axis of a 3D mesh as the locus of centres of maximal inscribed circles in the 3D mesh as shown in Fig. 1.9a. By adding the radii r of the



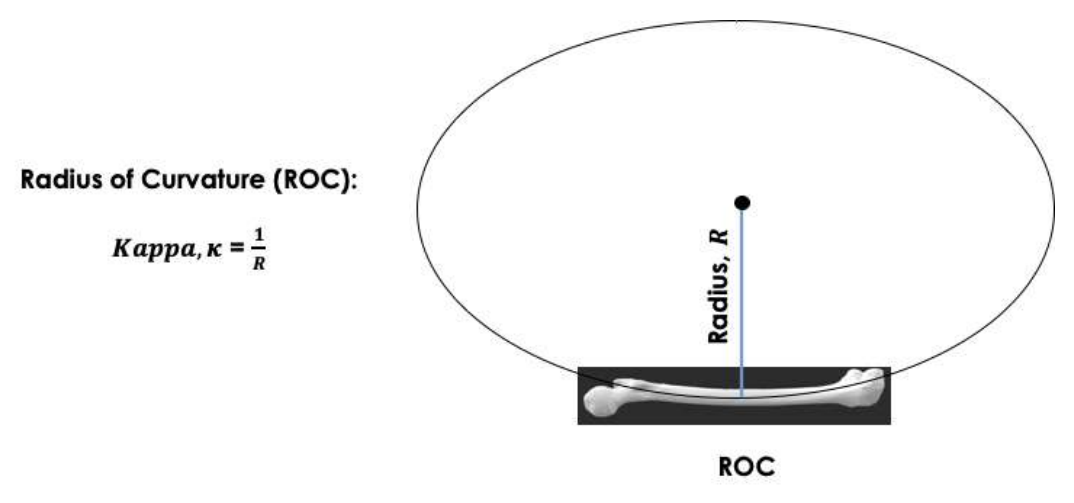
(a) 1. Femur Length, 2. Femur Shaft Length.



(b) Femur Width.

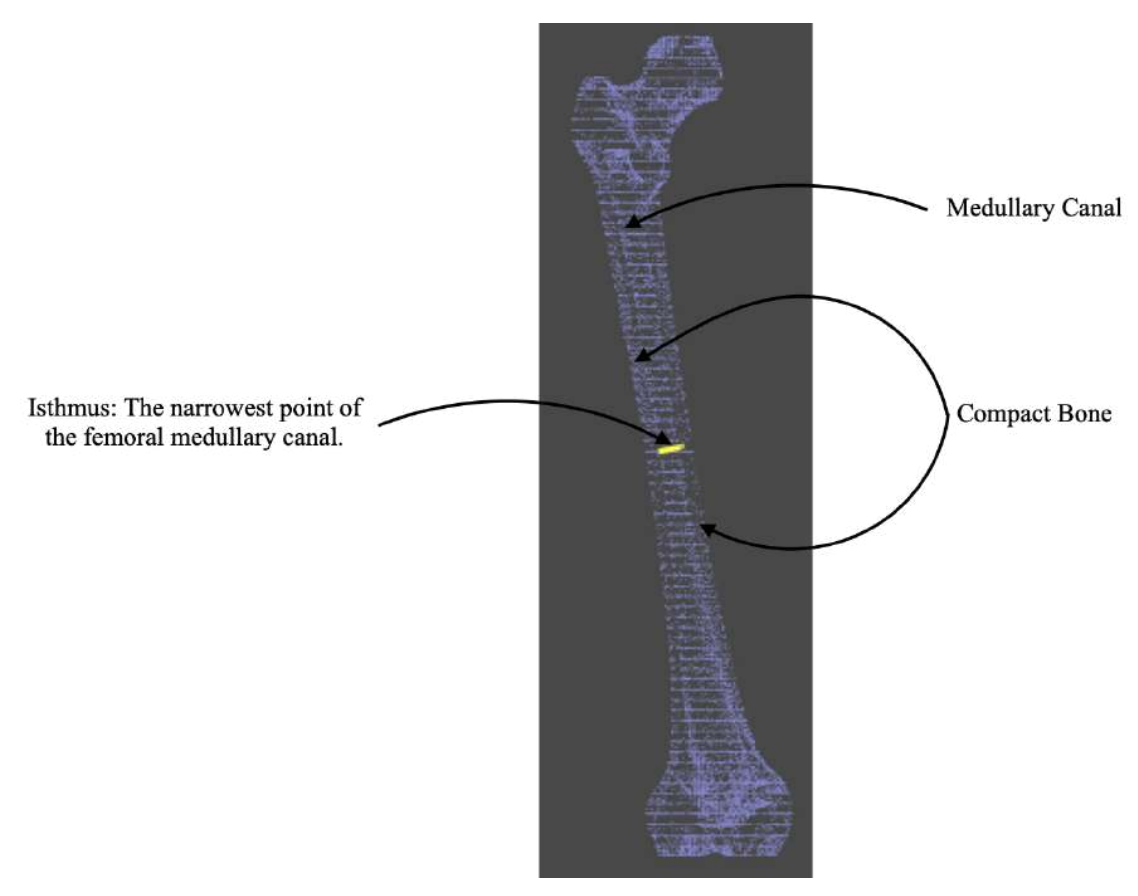


(c) AP Length.



(d) The femoral is thmus, medullary canal and the compact bone.

Figure 1.8: ROC.



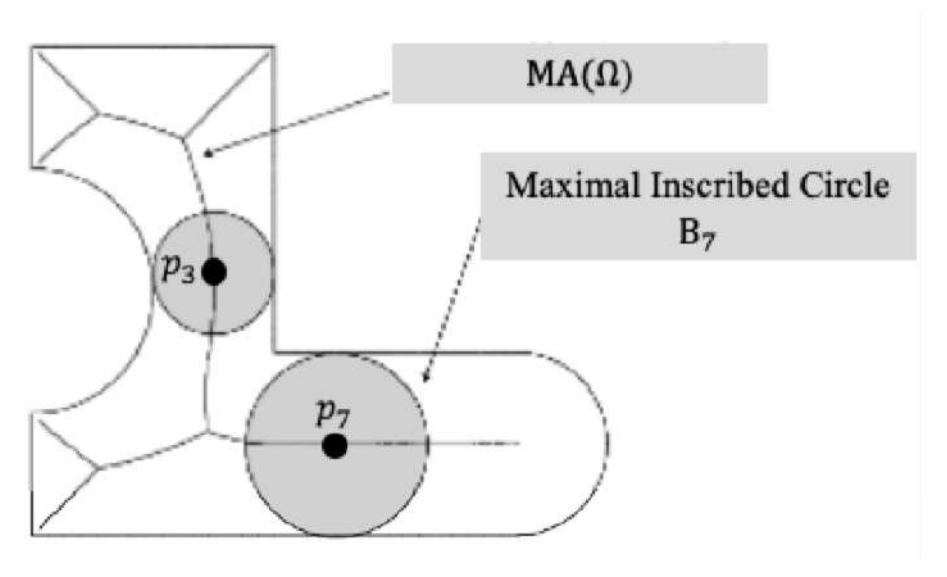
(e) The femoral isthmus, medullary canal and the compact bone.

Figure 1.8: These parameters are significant for decision making in surgery planning.

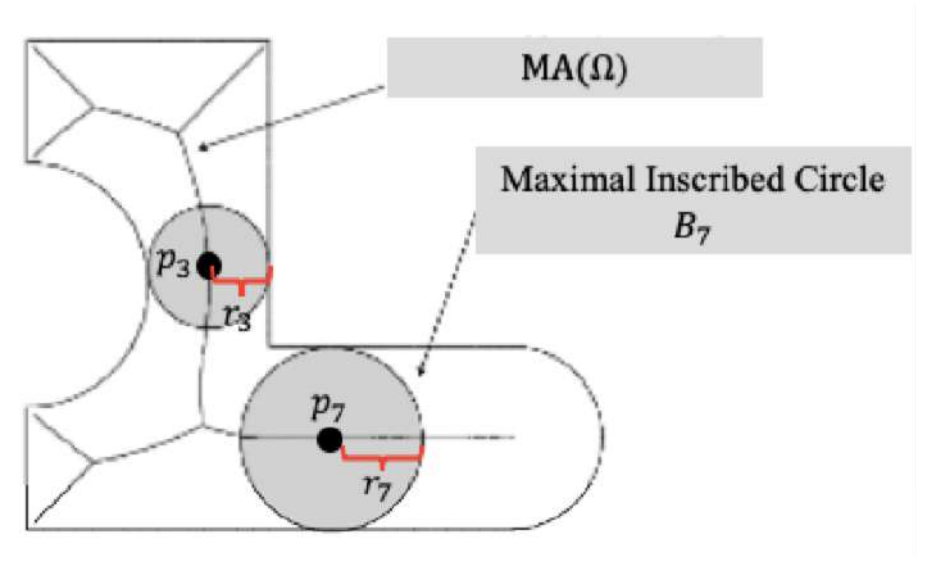
corresponding circles to the set of medial centres p, the MAT is obtained as shown in Fig. 1.9b. The corresponding circle $B_i(p_i, r_i)$ of centre p_i and radius r_i is also called a medial circle.

Hence, MA is based on MAT that is mainly composed of two (2) components as shown in Fig. 1.10. Apart from that, [75] concluded that the skeleton or the MA of a shape is known as several equivalent definitions, as shown in Fig. 1.11.

The main advantage of skeletons, thus, appears when they allow a simpler, more intuitive, and computationally effective way to analyse. There are several general properties that are used to define the efficiency and effectiveness of the generated skeletons [76]. Moreover, the proposed 3D skel-



(a) The $MA(\Omega)$ and the maximal inscribed circle B_i of the 3D mesh Ω .



(b) By adding the radii r of the corresponding circles to the set of the medial centres p, the $MAT(\Omega)$ is acquired.

Figure 1.9: The MA and MAT obtained from the YouTube video available at [8].

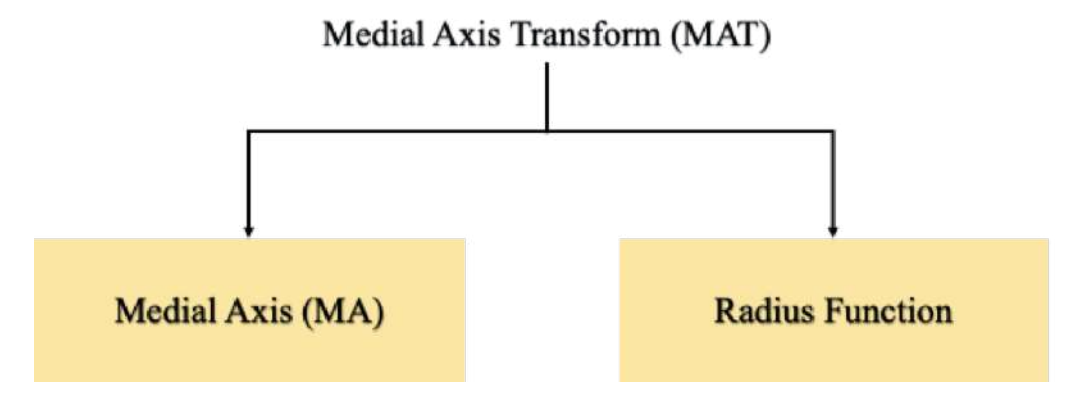


Figure 1.10: MAT is mainly composed of MA and radius function.

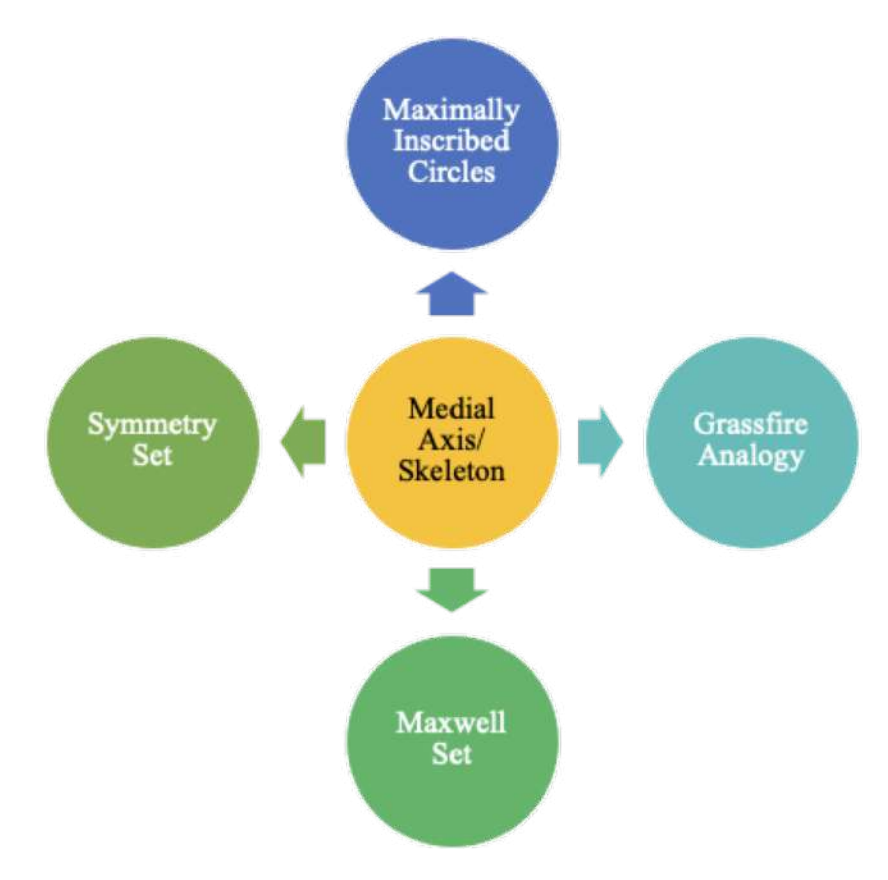


Figure 1.11: The MA or skeleton of a 3D mesh can be known as several equivalent definitions: (i) Maximally inscribed circles, (ii) Grassfire analogy, (iii) Maxwell set, (iv) Symmetry set.

etonization methods should comply with the desirable properties defined in [75]. Defining and assessing these properties are crucial for the performance verification and selection of a suitable skeletonization method for a specific application context.

As such, several desirable properties are selected to be discussed in Chapter 7 for the strengths and limitations of our methods and the existing method- Thinning-based method.

1.2.1 Comparison Criteria

This section describes the selected properties that we compare against, which are delineated in Table 1.1.

Table 1.1: Skeletonization properties that are used in our comparative results.

No.	Properties
1	Homotopy
2	Thinness
3	Centredness
4	Computational Scalability

Homotopy

Practical skeletons should maintain the homotopy property of the formal counterparts. The obtained skeleton should be topologically equivalent to the input shape such as the same number of connected components, cavities, and tunnels.

Thinness

The practical skeletons should be as thin as allowed by the space sampling used to model them. Mesh-based skeletons achieve the desired zero (0) thickness by construction.

The thickness of voxel-based skeletons is lower bound by the grid resolution, but the thickness conflicts with centredness.

Centredness

Each calculated skeleton point should be at equal distance from at least two (2) different points of the shape surface. There are mainly two (2) issues for the calculated skeletons with respect to centredness:

- A. The centredness is constrained by the spatial sampling used to represent the skeleton.
- B. Since there is no universally accepted definition thereof, it is very difficult to validate the centredness.

Voxel-based skeletons cannot always be perfectly centred, even for a simple 3D mesh. In practice, centredness is significant when using skeletons for shape reconstruction [77] and metrology [78]. It can be quantitatively assessed in absolute terms, by measuring distances from skeleton points to their closest surface points, or in relative terms, by comparing two or more skeletons produced by different methods against each other using Hausdorff distance metrics.

Computational Scalability

3D skeletonization have been used in many applications. In order to cope with the exponential growth of the number of triangles in a 3D mesh, a near-real-time, interactive and scalable 3D skeletonization methods are crucial [75, 79]. Thus, several approaches have been proposed to achieve this goal.

The computations of the Voronoi-based methods [80, 81, 82, 83, 84, 85] are time consuming process, whereas the Thinning-based methods [86, 87, 88, 89] are faster than the Voronoi diagram-based methods. Apart from that, [76] presented that the skeletonization methods should be able to extract skeletons of large, e.g.: 1024³ or similar voxel volumes in (tens of) seconds on a modern Personal Computer (PC) with 16 GB RAM.

1.2.2 Types of 3D Skeletonization Method

Based on the same article [75], the concept for 3D shapes can be either One-dimensional (1D) curves or Two-dimensional (2D) surfaces. Hence the existing methods for 3D skeletonization are divided into:

- Surface skeletonization methods: which the skeleton is the 2D manifolds which contain the loci of maximally inscribed balls in a 3D mesh.
- Curve skeletonization methods: which the skeleton is the 1D curves which are locally centred in the 3D mesh (Our method falls in this category due to well suited to describe tube-like anatomical structures, e.g.: our 3D human femur).

On the other hand, [88] grouped the major existing methods of 3D skeletonization into three (3) various groups as depicted in Fig. 1.12.

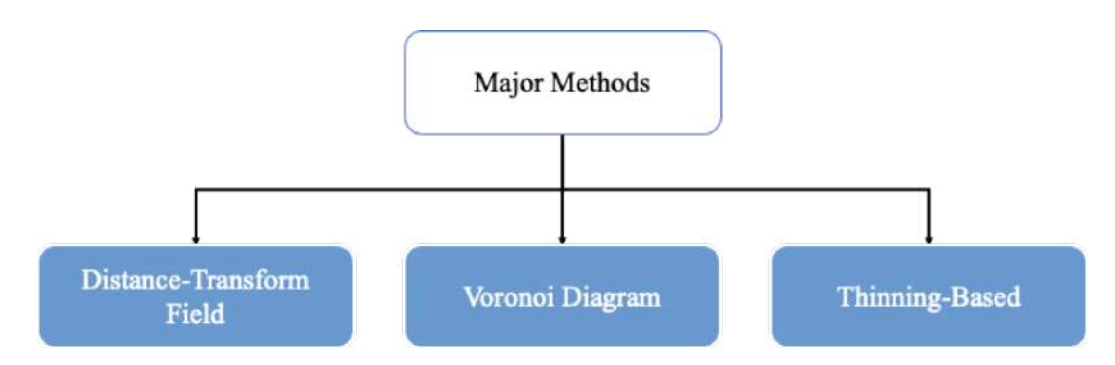


Figure 1.12: The three (3) major groups for existing 3D skeletonization methods.

However, these existing methods are unable to preserve the connectivity of the skeletons for the 3D meshes, and they are difficult to implement.

The first major methods are the distance-transformed field methods, also known as distance map or distance field, with the following articles [90, 91] in the year of 2007 and [77] in the year of 2011 respectively. These are the derived representation of digital images and the data structure are mostly in voxels. The main drawback of these methods is that the extracted skeleton tends to miss some branches, and some of the structures are usually disconnected. Besides that, these existing methods are quite sensitive to boundary noise.

The second major methods are the Voronoi-diagram based [80, 81, 84, 82, 85, 83]. A voronoi diagram is a partition of a plane into regions close to each of a given set of objects. However, these methods extract a great number of spurious skeletal branches that are not essential for compact representation of the models. Moreover, the computations of Voronoi-diagrams are time-consuming processes.

Lastly, the third major methods are the Thinning-based methods [86, 87, 88, 89]. Thinning methods iteratively peel off the boundary voxels (also called simple points) whose deletion sometimes alter the 3D mesh topology. In addition, these methods are not able to preserve the connectivity of the skeletons of 3D meshes.

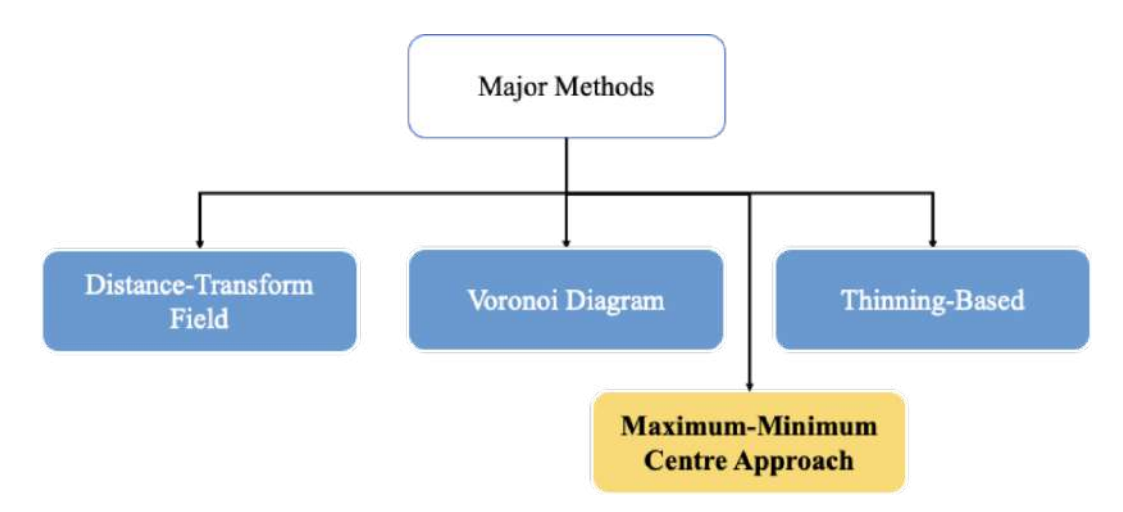


Figure 1.13: Our proposed approach for 3D skeletonization namely, maximum-minimum centre approach.

On the other hand, in the field of extracting skeletons from 3D human femurs, two (2) notable papers published in 2010 [1] and 2014 [2] have explored the application of 3D skeletonization techniques. In their respective studies, [1] employed a Thinning-based method to compute the MAT of the femur, while [2] utilised Principle Components Analysis (PCA) to compute the MA.

However, it is important to note that these methods face certain limitations when it comes to preserving the connectivity of the extracted skeletons for 3D femurs. Due to the nature of the skeletonization process, both approaches struggle to fully capture and maintain the intricate connectivity patterns present in the femur structure. As a result, there is a risk of missing out on significant information and details that are crucial for a comprehensive analysis of the femur morphology.

Preserving the connectivity of the femur skeleton is of utmost importance, as it provides valuable insights into the structural integrity and functionality of the bone. Disruptions in the connectivity can lead to misinterpretations and incomplete representations of the femur's internal architecture. Therefore, researchers and practitioners need to be aware of these limitations when employing these methods in applications where accurate preservation of skeleton connectivity is essential for a thorough understanding and analysis of 3D femurs. Future advancements in skeletonization techniques may address these challenges and provide more robust solutions for preserving connectivity and capturing intricate details in the femur skeletons.

In this thesis, a simple and uncommon method based on the 3D femur is implemented, namely the maximum-minimum centre approach as shown in Fig. 1.13.

1.3 3D-FSA

Although the development of the 3D skeletonization is relatively well established in medical research, skeleton computation in 3D human femurs is relatively unexplored in the field of orthopaedics.

Therefore, we developed an automatic 3D skeletonization using our approach namely, maximum-minimum centre approach to facilitate the human femur shape analysis conducted by the orthopaedics. This femur shape analysis system is called 3D-FSA, which stands for 3D Femur Shape Analysis System.

Fig. 1.14 shows the interface of our system, 3D-FSA. The 3D human femur can be displayed as vertices view (Fig. 1.14a), edges view (Fig. 1.14b) and vertices view (Fig. 1.14c).

When the program is executed, the window with two (2) information dialog boxes are displayed as shown in Fig. 1.15a. These information dialog boxes are mainly provide the structure of the 3D mesh, e.g.: the number of vertices, the number of edges and the number of faces, the current status of the view position and the light mode, the overall dimension of the loaded 3D mesh and etc.

Besides that, these information dialog boxes can be either hidden or visible by pressing the space bar key on keyboard as illustrated in Fig. 1.21a, Fig. 1.21b, and Fig. 1.21c. The reference lines as illustrated in Fig. 1.15b represents the (x, y, z)-axes. The red reference line represents the x-axis, the green reference line represents the y-axis, and the blue reference line represents the z-axis.

The menu bar is a thin, horizontal bar containing the labels of menus in a GUI as exhibited in Fig. 1.15b. This menu bar provides the user with a place in a window to find program's essential functions, which consists of have four (4) functions as follows:

A. File (Fig. 1.16)

New	Open	Save
Save As	Print	Print Preview

Print Setup	Recent File	Exit

B. Edit (Fig. 1.17)

New	Open
Save As	Print

C. View (Fig. 1.18)

Initial View	Top View	Rotation ($-90 \ x \ axis$,
		+90 x axis, -90 y
		axis, +90 y axis, -90
		$z \ axis, +90 \ z \ axis)$
Scale (Zoom In, Zoom	zValue (Inc, Dec)	Message
Out)		
Projection	Lighting	Color
Reference	Boundary	SlidingBox
Face	Edge	Vertex
Sliding (Up, Down,	Height (Dec, Inc)	Step (Dec, Inc)
Save)		
Auto Sliding	Cal Curvature	Toolbar

Status Bar	

D. About (Fig. 1.19)

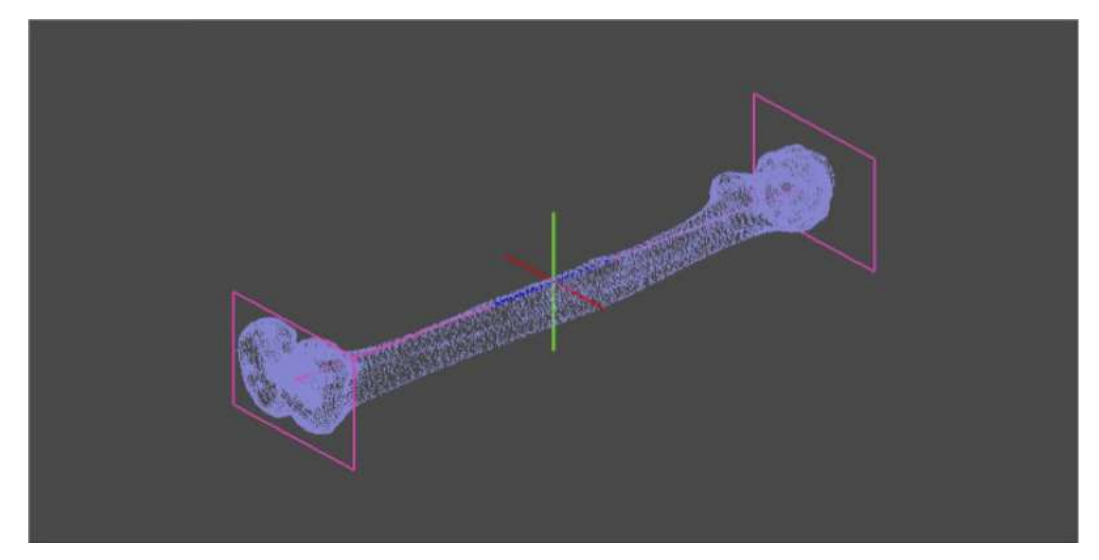
It displays an information dialog box that displays the version of the system, 3D-FSA.

Open any .obj file to load a 3D femur from the File menu (Fig. 1.16b, Fig. 1.16c), and then press zero (0) to execute the 3D skeletonization based on the maximum-minimum centre approach as illustrated from Fig. 1.22a to Fig. 1.22m.

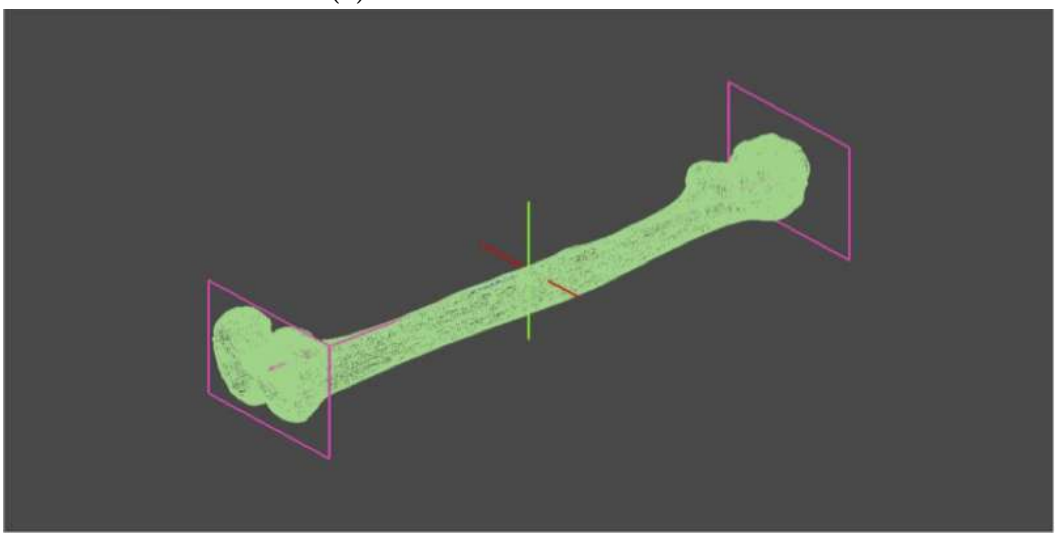
Fig. 1.20a renders a boundary for each end of the 3D femur. These boundaries are obtained from the maximum width and height values of the loaded 3D femur. When a 's' or 'S' key is pressed, the cylindrical slider s will be visible as shown in Fig. 1.20b. This slider plays a significant role for traversing along the femur, to compute the medial centres, and the medial line (MA) is constructed by connecting these medial centres.

Apart from that, two (2) planes are seen in Fig. 1.22b during the 3D skeletonization. The usage of these planes will be described in Chapter 6. The cylindrical slider s traverses from the distal femur until the proximal femur. In each traverse, a medial centre is calculated until the cylindrical slider s reaches the end of the femur. The medial line (MA) is constructed by connecting these obtained medial centres as shown in Fig. 1.22c until Fig. 1.22m.

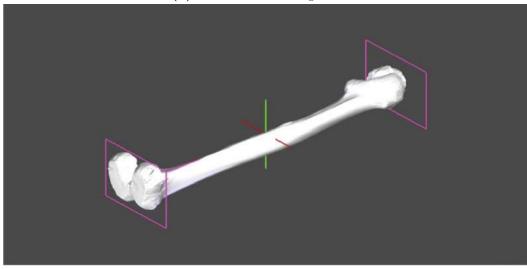
Finally, the skeleton (MA) of the 3D femur is extracted as shown in Fig.



(a) 3D left femur in vertices view.

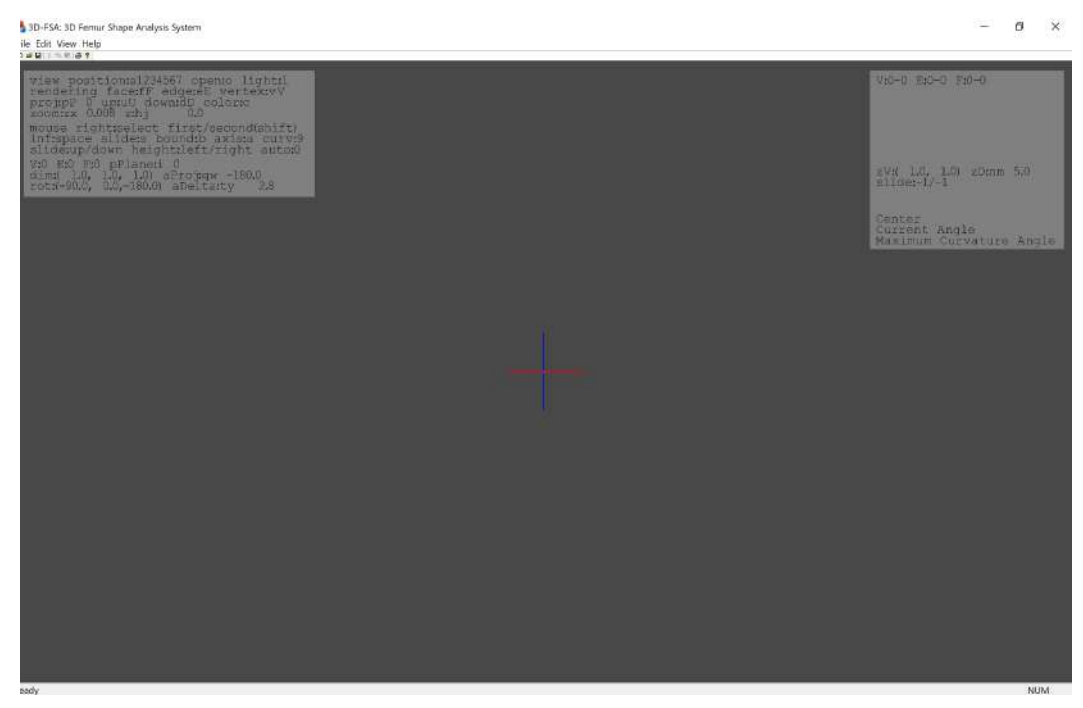


(b) 3D left femur in edges view.

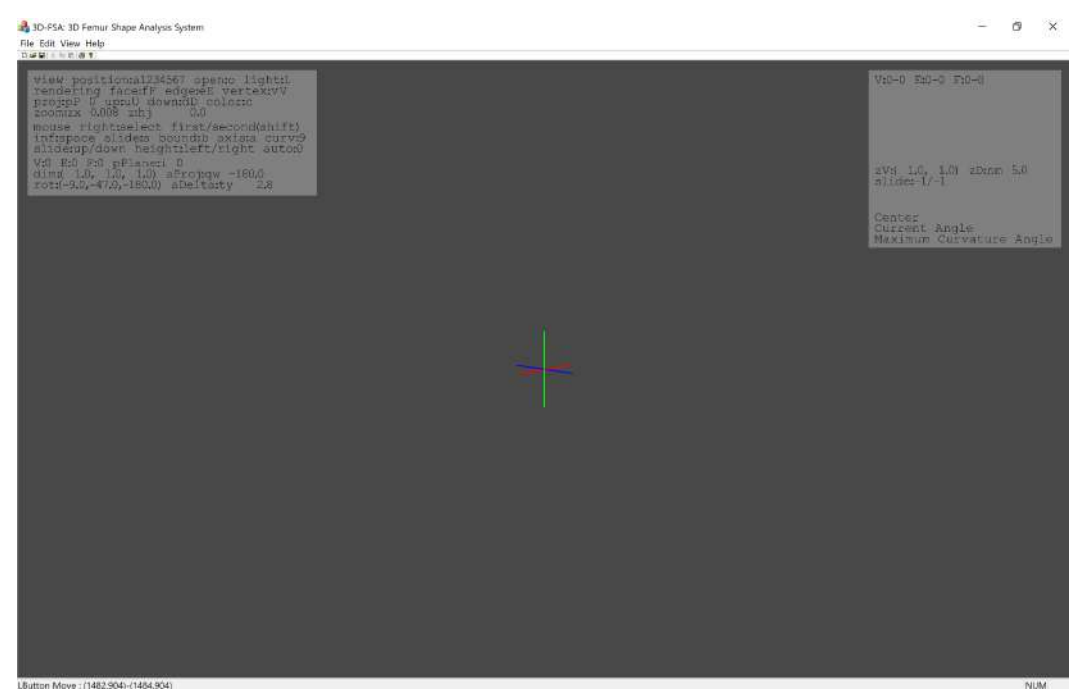


(c) 3D left femur in faces view.

Figure 1.14: The 3D human femur can be displayed in faces view, edges view, and vertices view in our system, 3D-FSA.

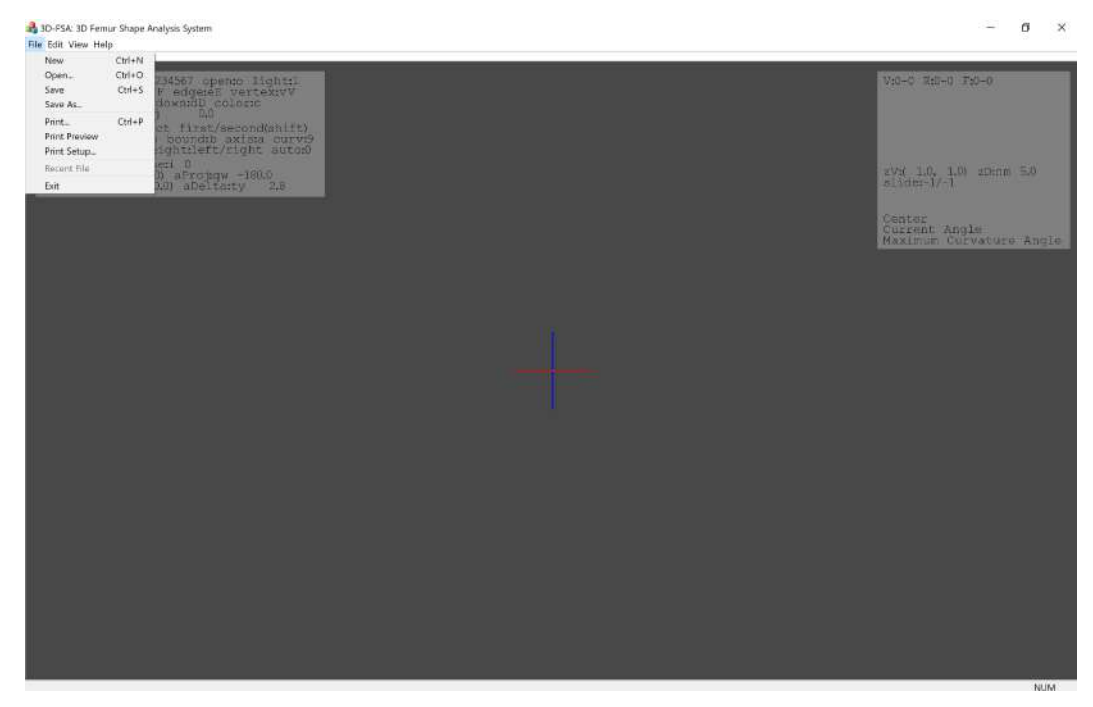


(a) The UI of the starting window when the program is executed. The left rectangle provides the information about the structure and status of a loaded 3D mesh, whereas the right rectangle provides the information of the cylindrical slider. We called these rectangles as the information dialog boxes. The reference lines of (x, y, z) - axes are located in the middle part of the window.

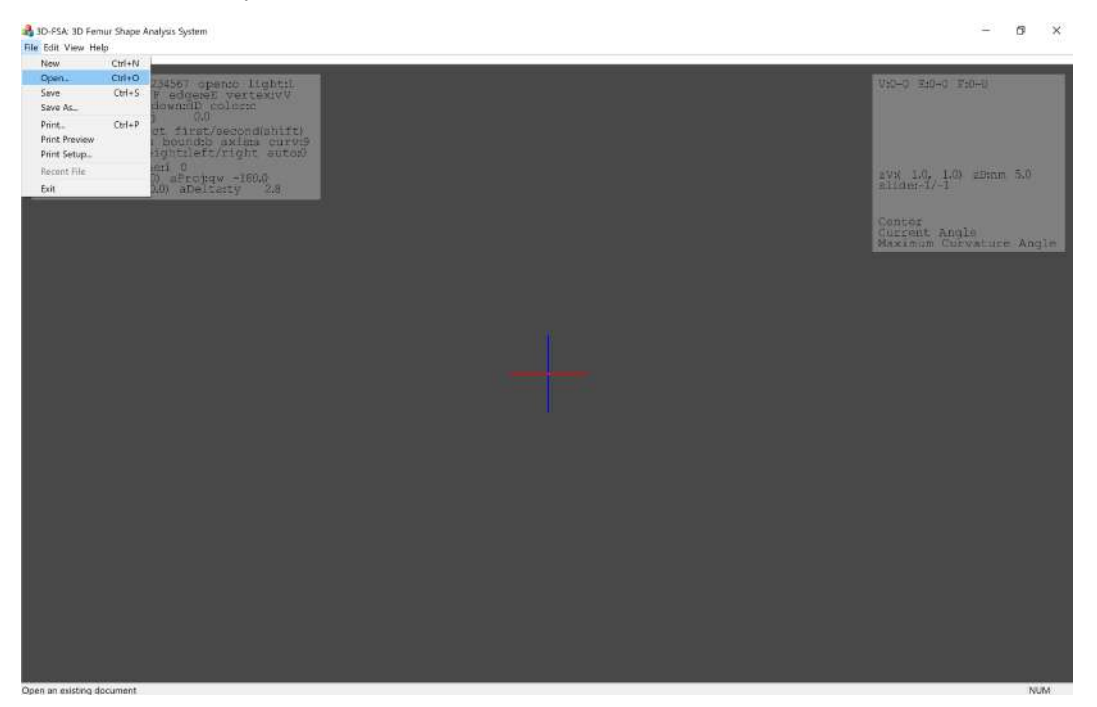


(b) The reference lines of (x, y, z) – axes: The red line represents the x – axis, green line represents the y – axis, and the blue line represents the z – axis; The menu bar consists of four (4) essential functions, which consists of: File, Edit, View and About.

Figure 1.15: The GUI of our 3D-FSA when the program is executed.

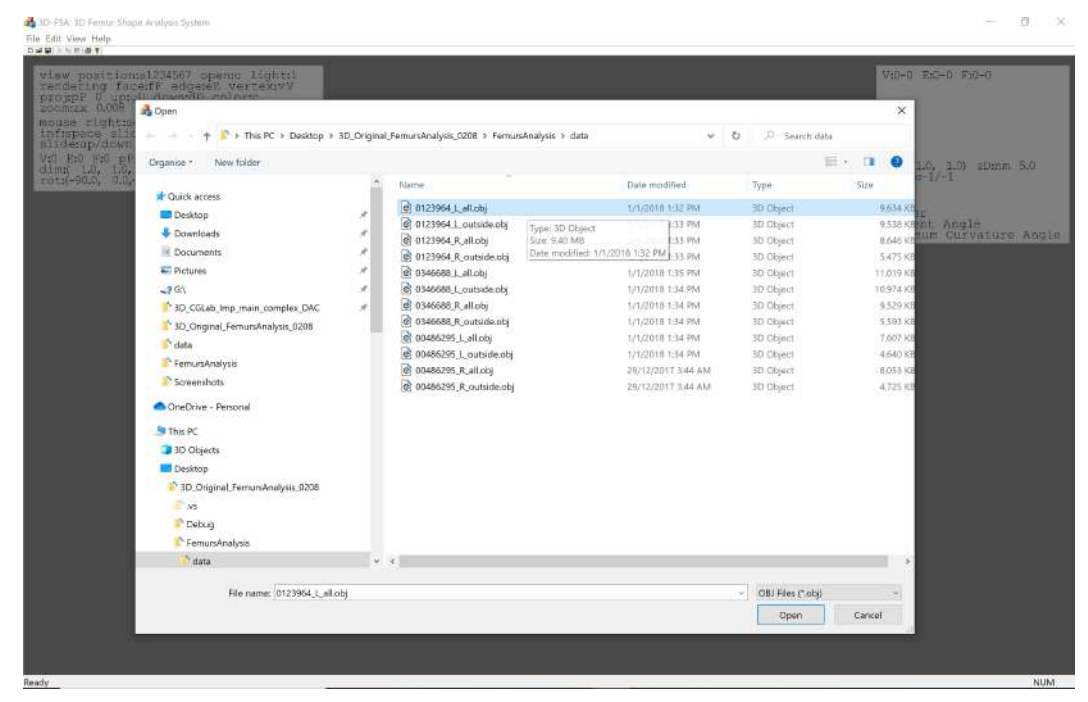


(a) The File menu consists of: New, Open..., Save, Save As..., Print..., Print Preview, Print Setup, Recent File and Exit commands. There are several commands can be accessed via keyboard shortcuts.

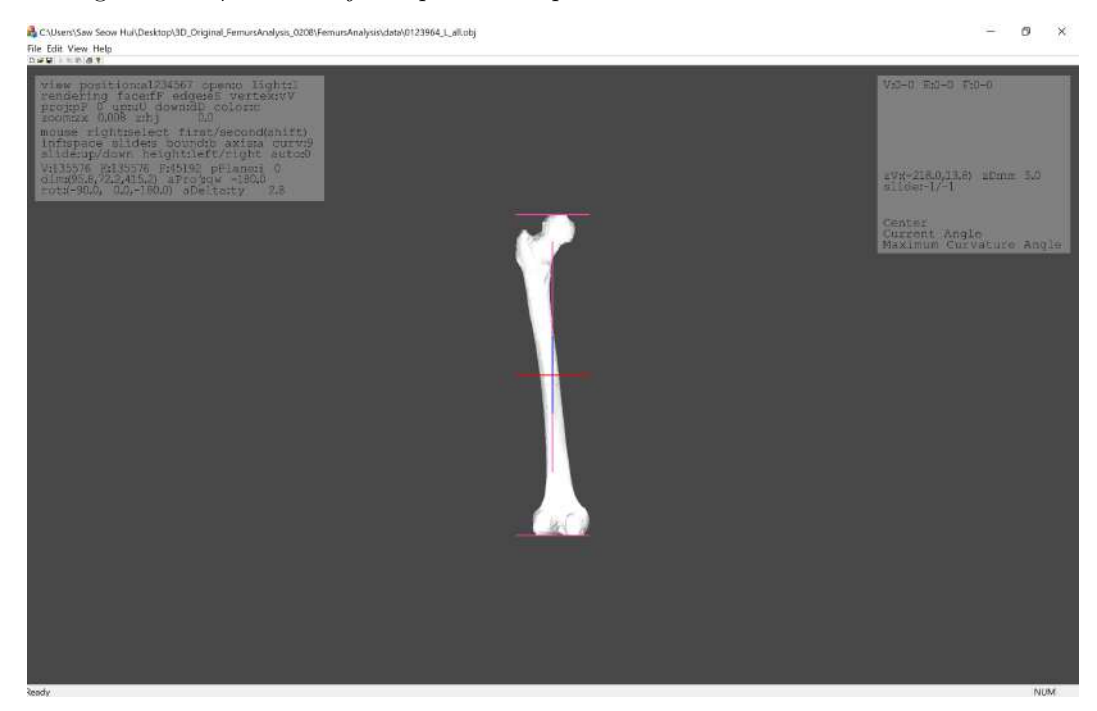


(b) In order to compute a skeleton, a 3D mesh has to be opened. Go to File menu, select the Open command.

Figure 1.16: The GUI for the File menu in 3D-FSA.



(c) A new window will pop out with the list of 3D femurs in .obj format. Select a file, e.g.: $0123964_L_all.obj$ and press the Open button.

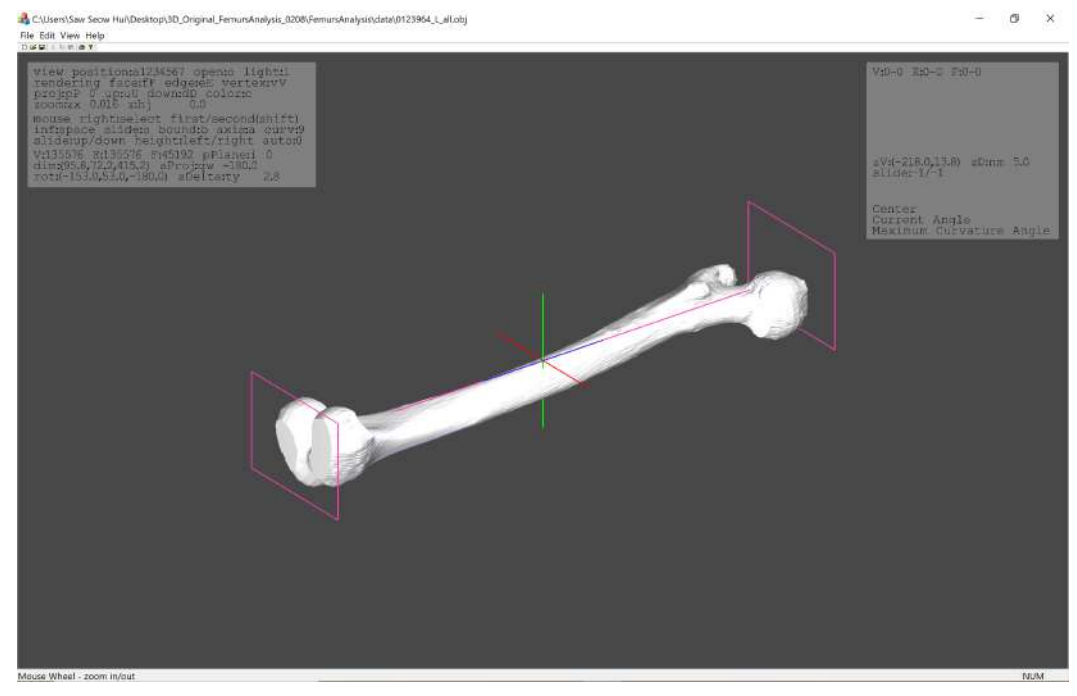


(d) The 3D femur of $0123964_L_all.obj$ is displayed in the window.

Figure 1.16: The GUI for the File menu in 3D-FSA.



(e) The size of a 3D femur can be enlarged or reduced by using the mouse.



(f) The 3D femur can be rotated around the reference lines.

Figure 1.16: The GUI for the File menu in 3D-FSA.



Figure 1.17: The Edit menu consists of: Undo, Cut, Copy and Paste commands. These commands can be accessed via keyboard shortcuts.

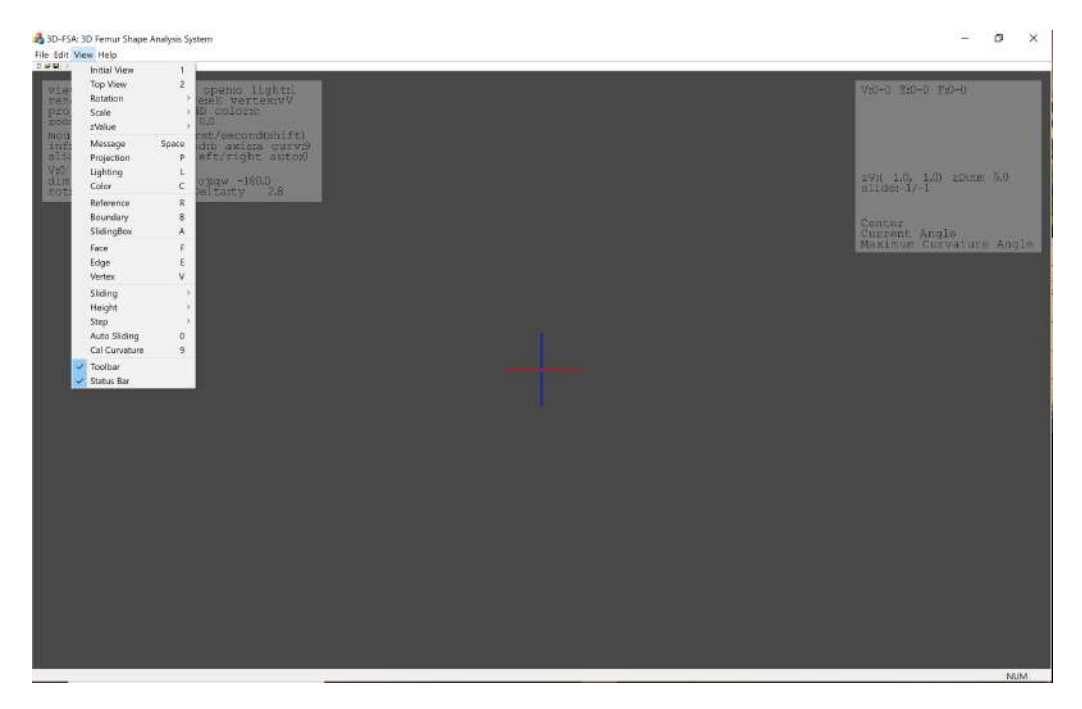


Figure 1.18: The View menu consists of many commands that are related to the geometry and viewing transformation of the 3D mesh. These commands can be accessed via keyboard shortcuts.

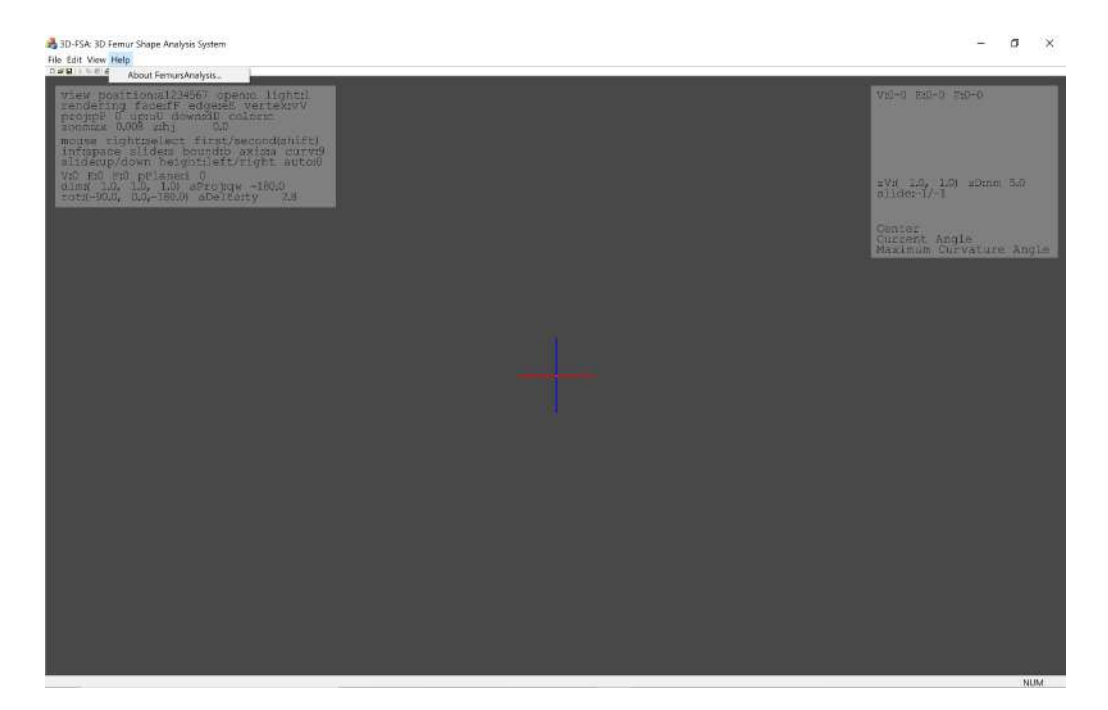


Figure 1.19: The About menu consists of a short introduction related to 3D-FSA.

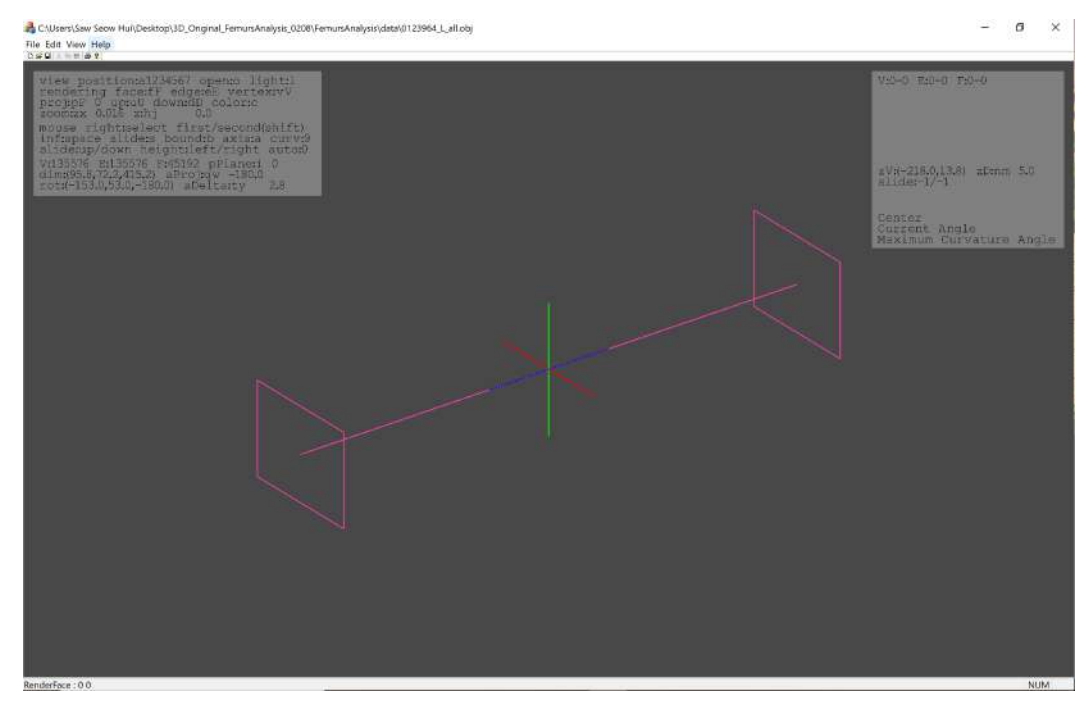
1.23a and Fig. 1.23a. All the details for each process is explained in the next Section.

As a results, our system, 3D-FSA is used to facilitate and support the orthopaedics for their morphological studies that deals with the differences of femoral geometric focus on the bowing and width [16].

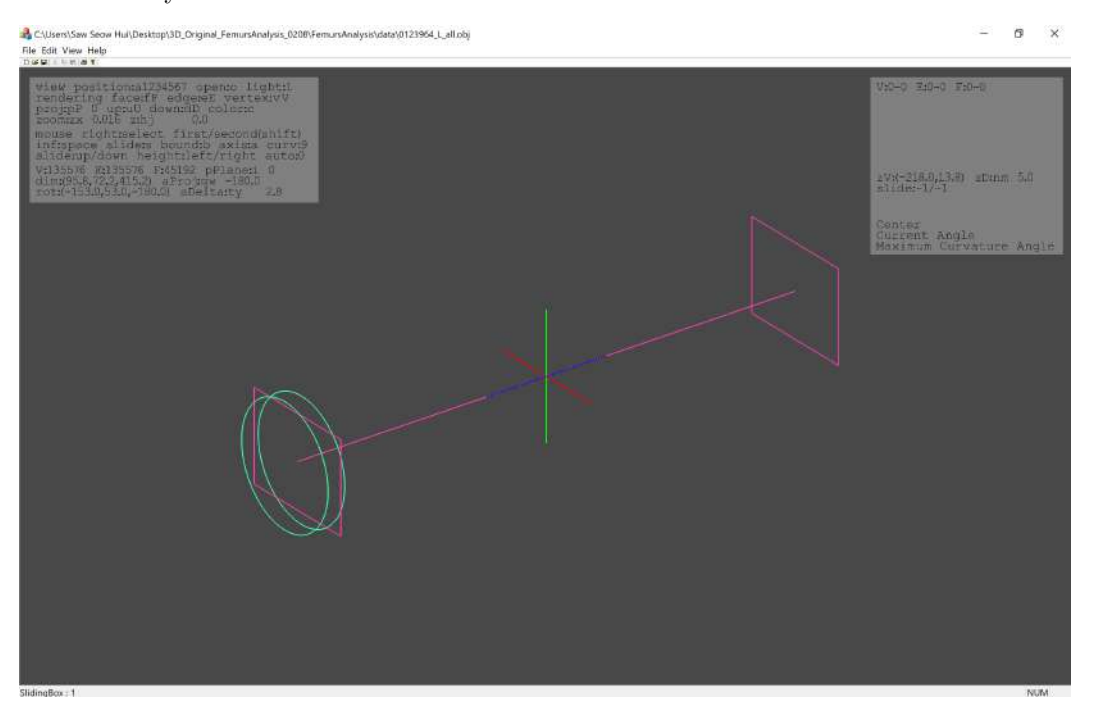
1.4 Research Objectives

This thesis presents an automatic 3D preoperative simulation called 3D-FSA that produces a skeleton of the 3D femur using the maximum-minimum centre approach for the analysis of femoral shaft geometry, which focuses on the femoral bowing and femoral width [16].

These parameters are very useful for orthopaedics to accurately perform preoperative evaluations and engineers in developing a new intramedullary

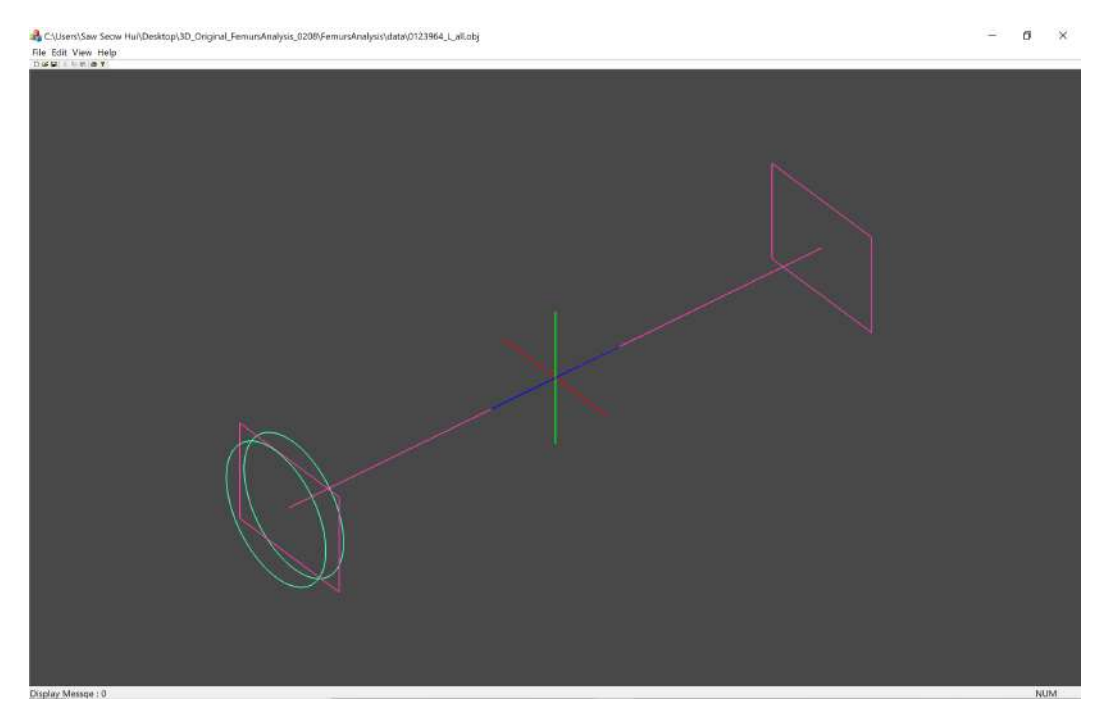


(a) The square boxes in pink colour located at both end of the 3D femur represent the boundary boxes.

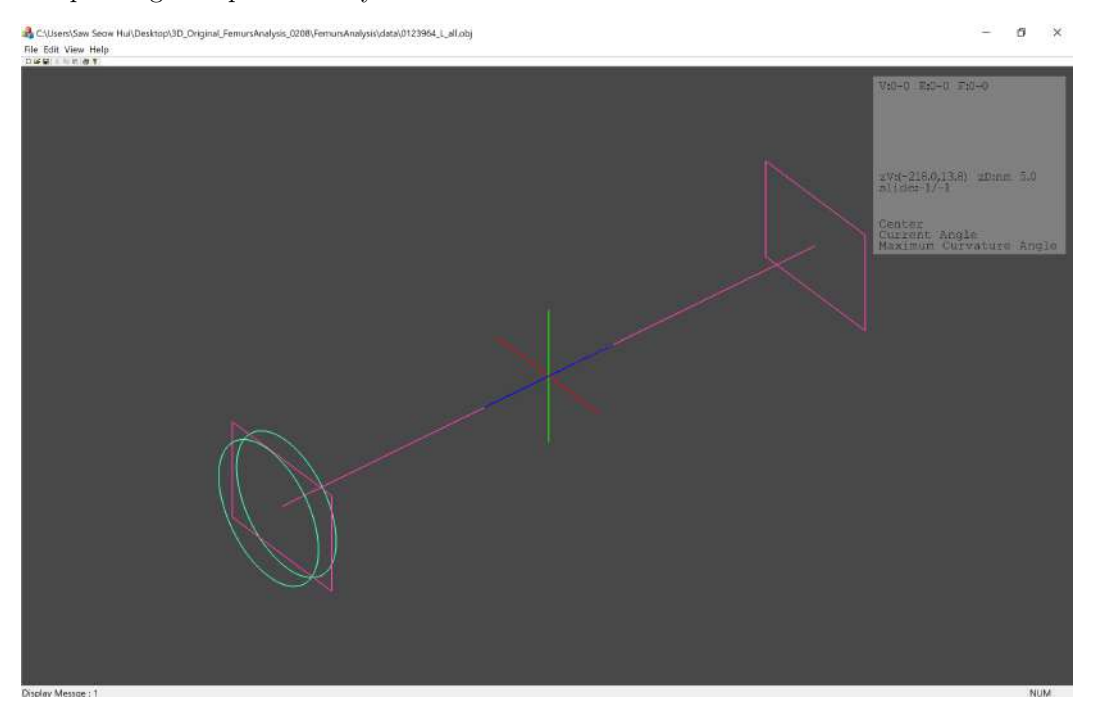


(b) The two (2) circles are called the cylindrical slider s in 3D-FSA. It plays an important role to traverse from the beginning of the 3D femur until the end of the 3D femur for the skeleton computation.

Figure 1.20: The boundary and the cylindrical slider s in 3D-FSA.

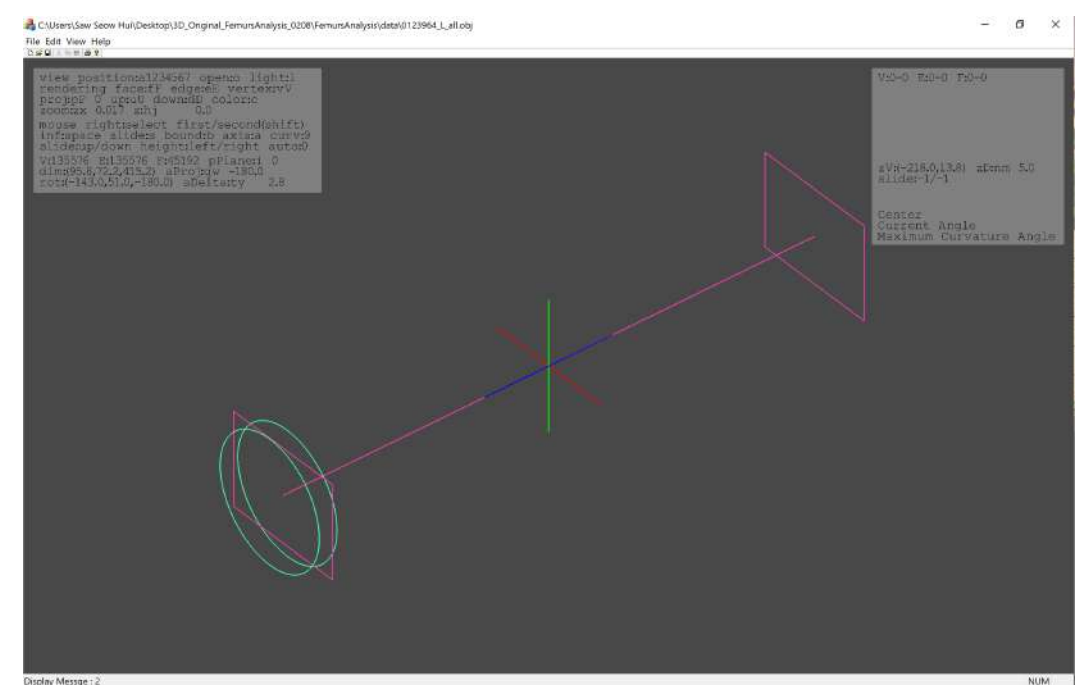


(a) The information dialog boxes can be hidden by selecting the View menu or by just pressing the space bar keyboard.



(b) Press the space bar keyboard one more time, the information dialog box on the right will be visible.

Figure 1.21: The usage of the spacebar key in 3D-FSA.



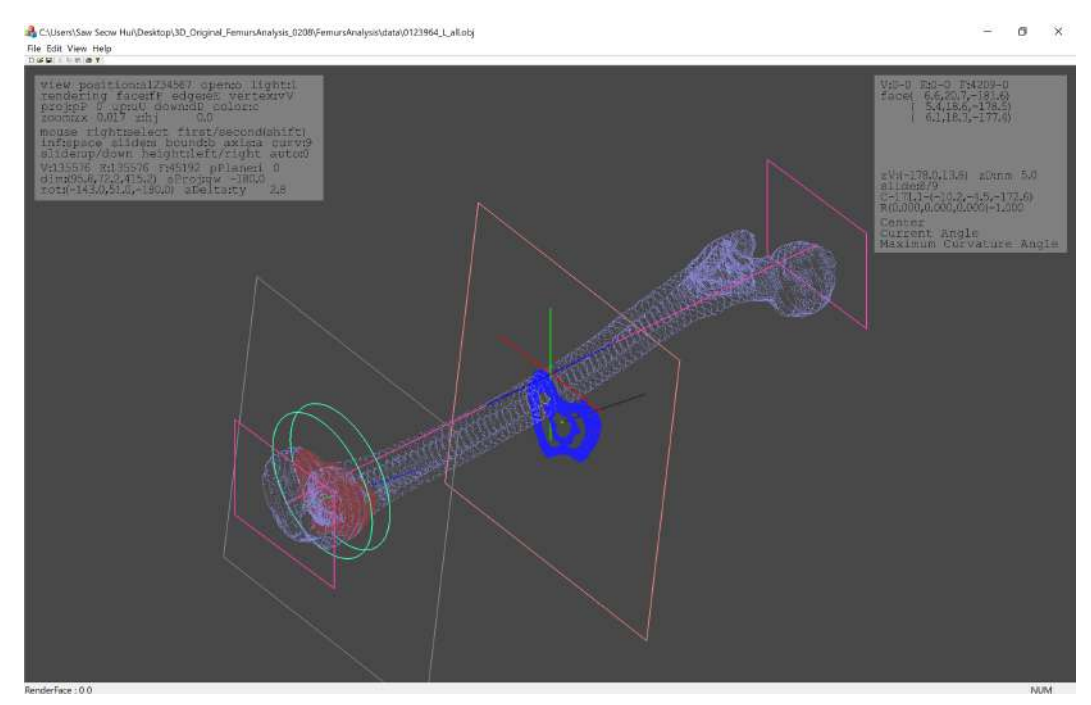
(c) Press the space bar keyboard again, the information dialog box on the left will also be visible.

Figure 1.21: The usage of the spacebar key in 3D-FSA.

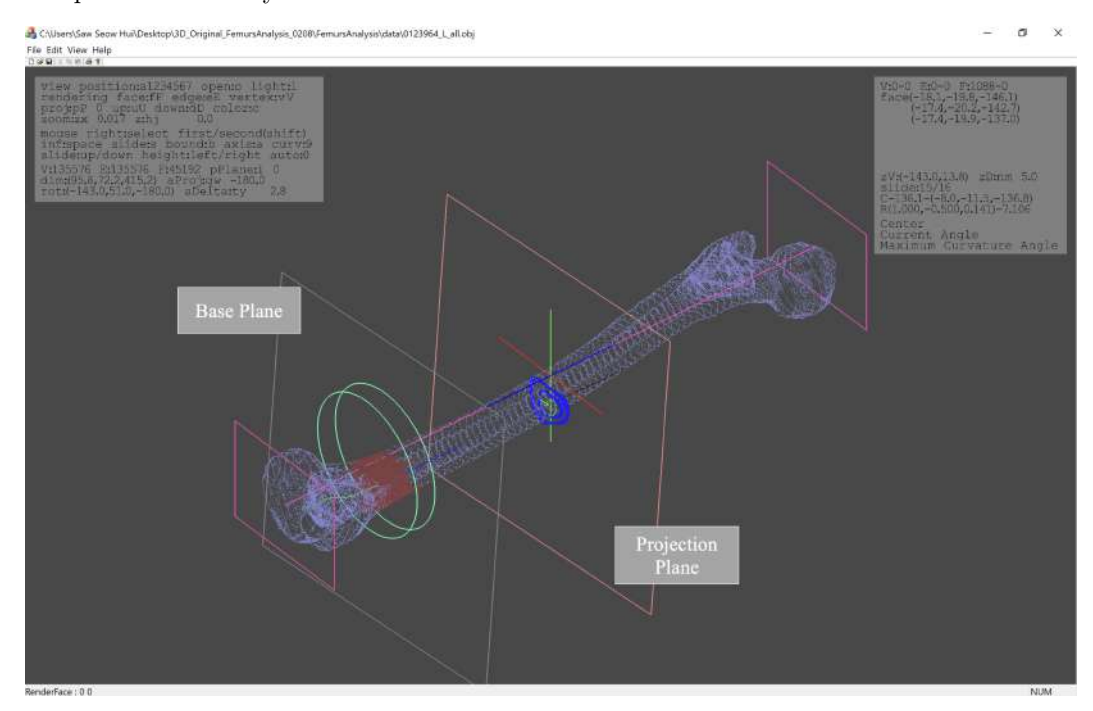
nailing system.

The followings are the rest of the objectives in this research:

- A. To design the framework of the 3D-FSA system.
 - A framework with four phases are created for 3D-FSA system.
 - An automatic femur shape analysis is designed to provide an accurate 3D preoperative simulation possible.
- B. To develop an optimised approach for performing 3D skeletonization based on the 3D mesh to our chosen application.

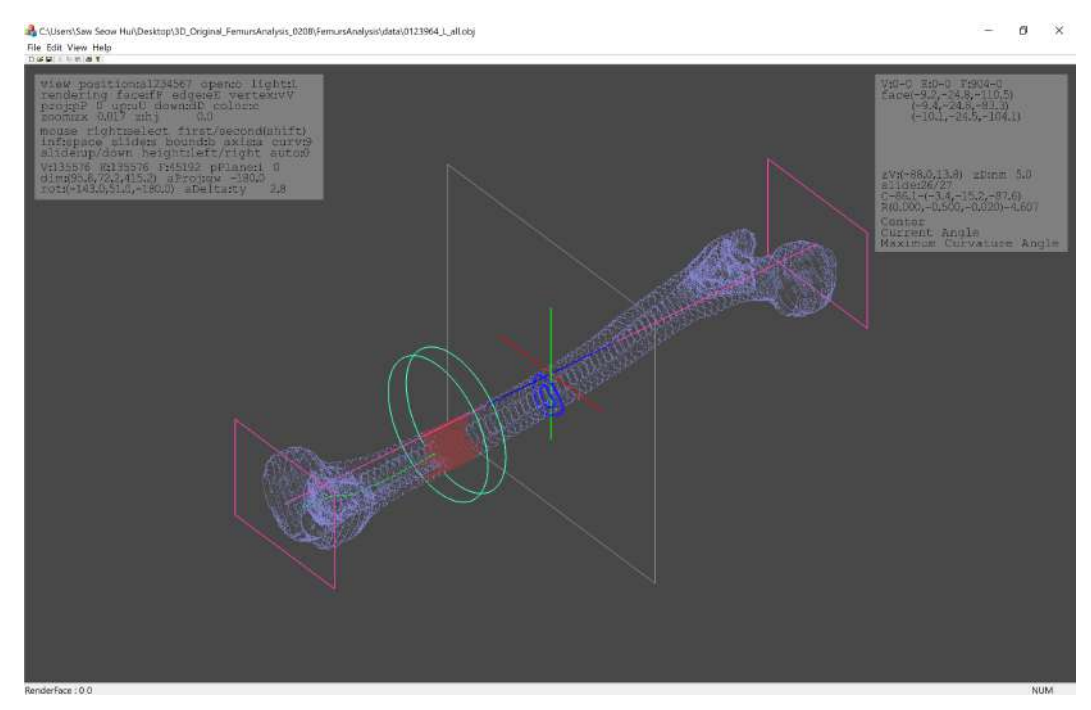


(a) Then press zero (0) key on keyboard to perform the 3D skeletonization based on the position of the cylindrical slider s.

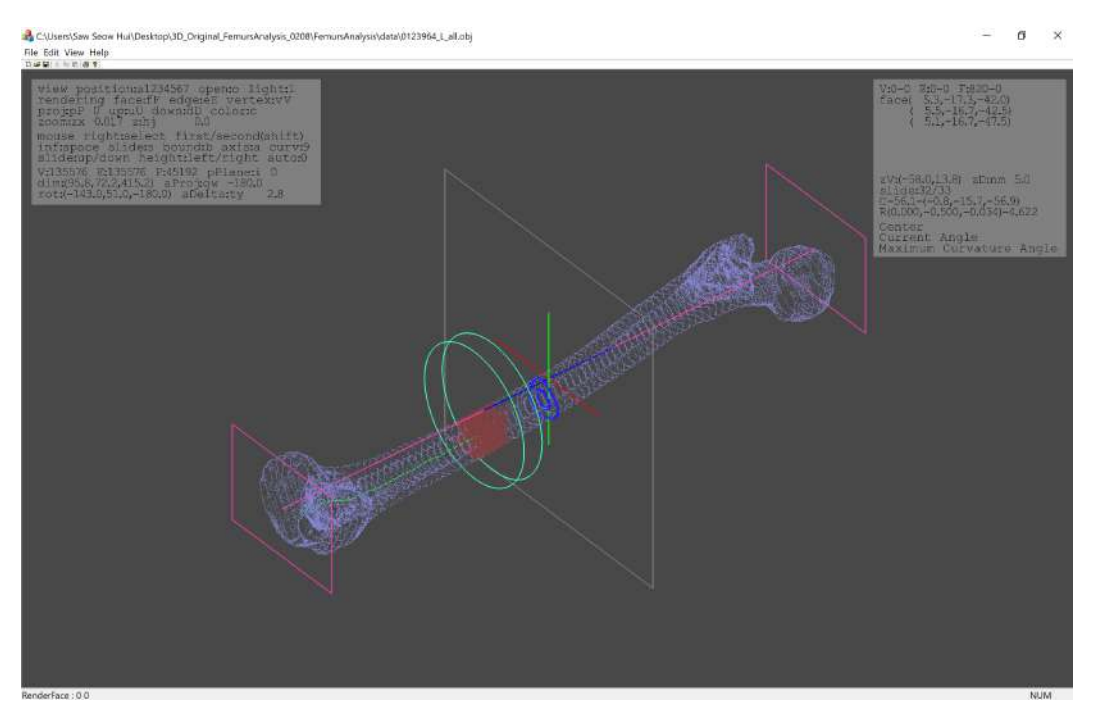


(b) There are two (2) planes during the 3D skeletonization: The base plane and the projection plane. These planes are described in Chapter 6.

Figure 1.22: The execution process of our proposed maximum-minimum centre approach in 3D-FSA.

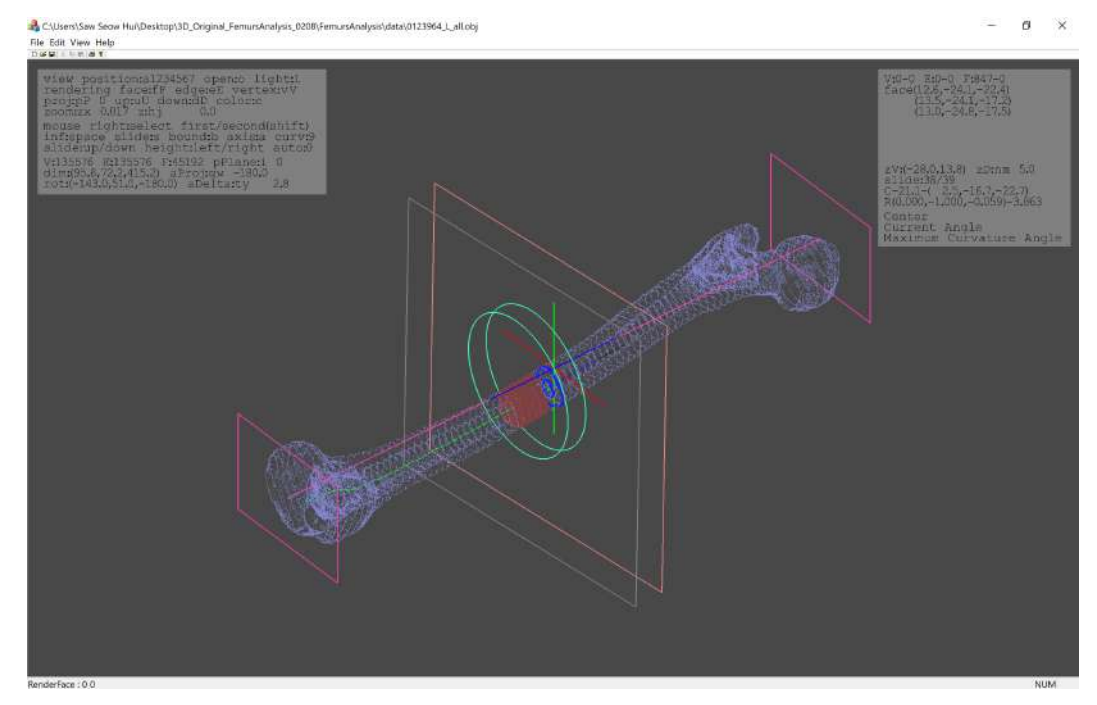


(c) The 3D skeletonization continues. As you can see, only the faces within the cylindrical slider s are used to calculate all the medial centres.

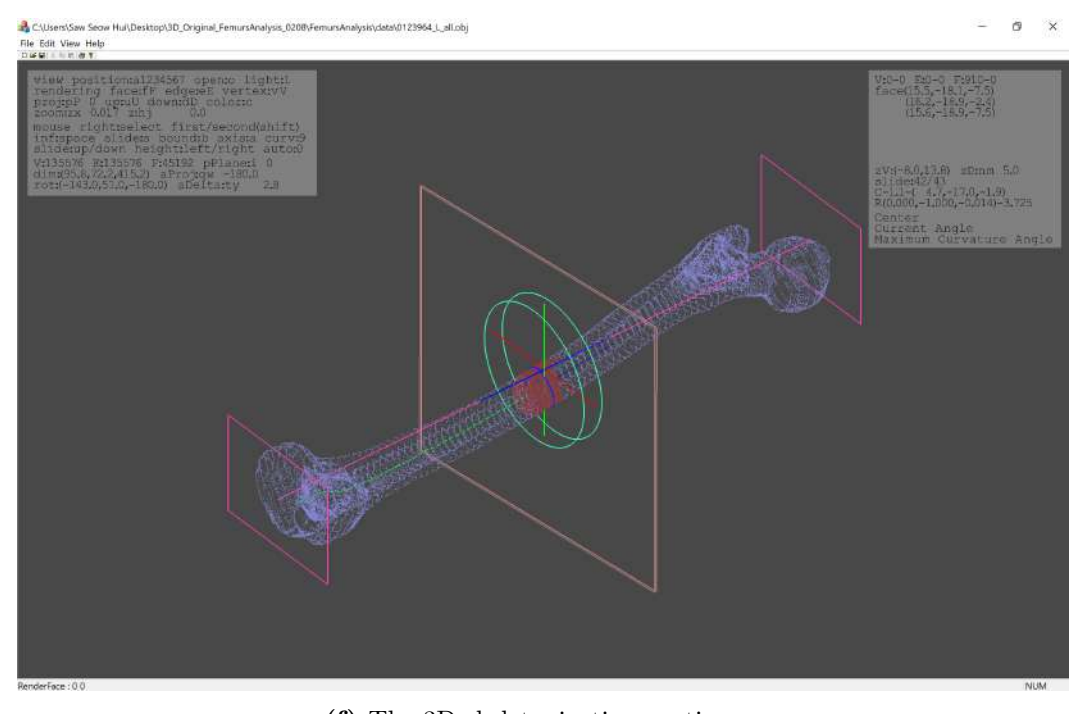


(d) The medial line (medial axis) is constructed by connecting these obtained medial centres.

Figure 1.22: The execution process of our proposed maximum-minimum centre approach in 3D-FSA.

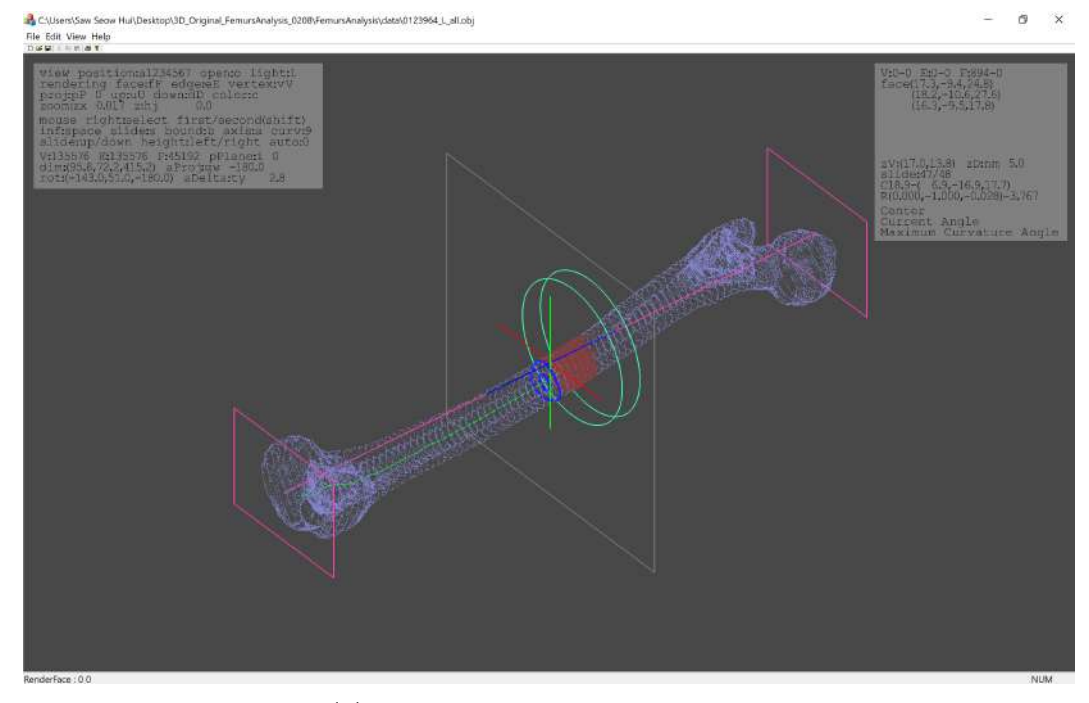


(e) The 3D skeletonization continues.

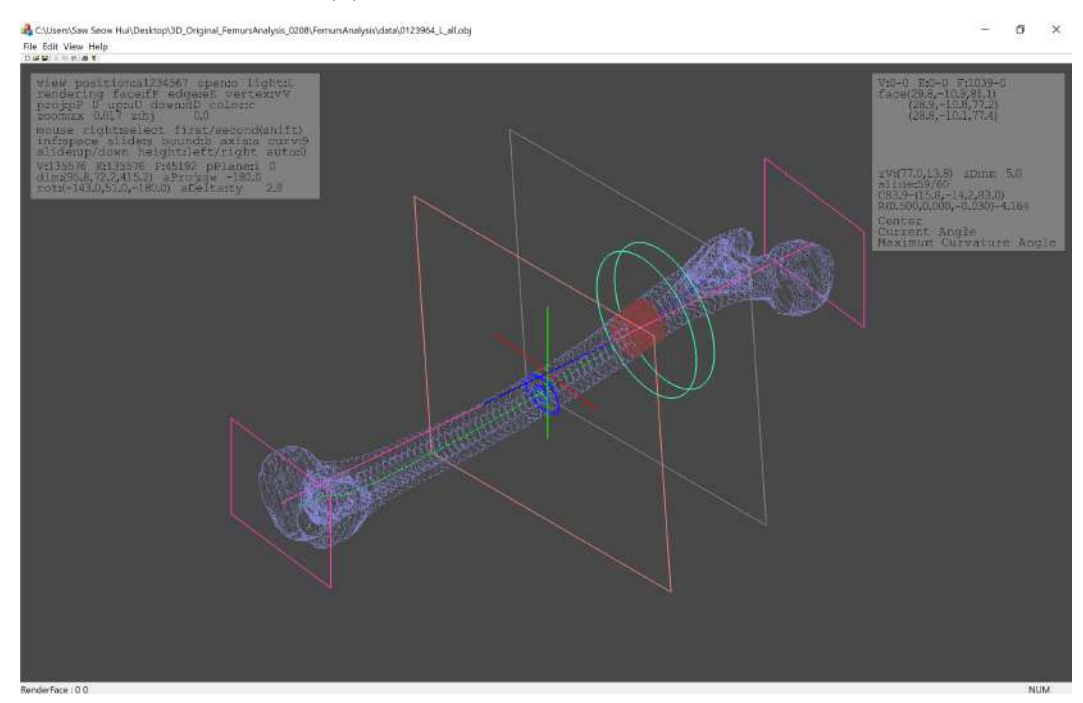


(f) The 3D skeletonization continues.

Figure 1.22: The execution process of our proposed maximum-minimum centre approach in 3D-FSA.

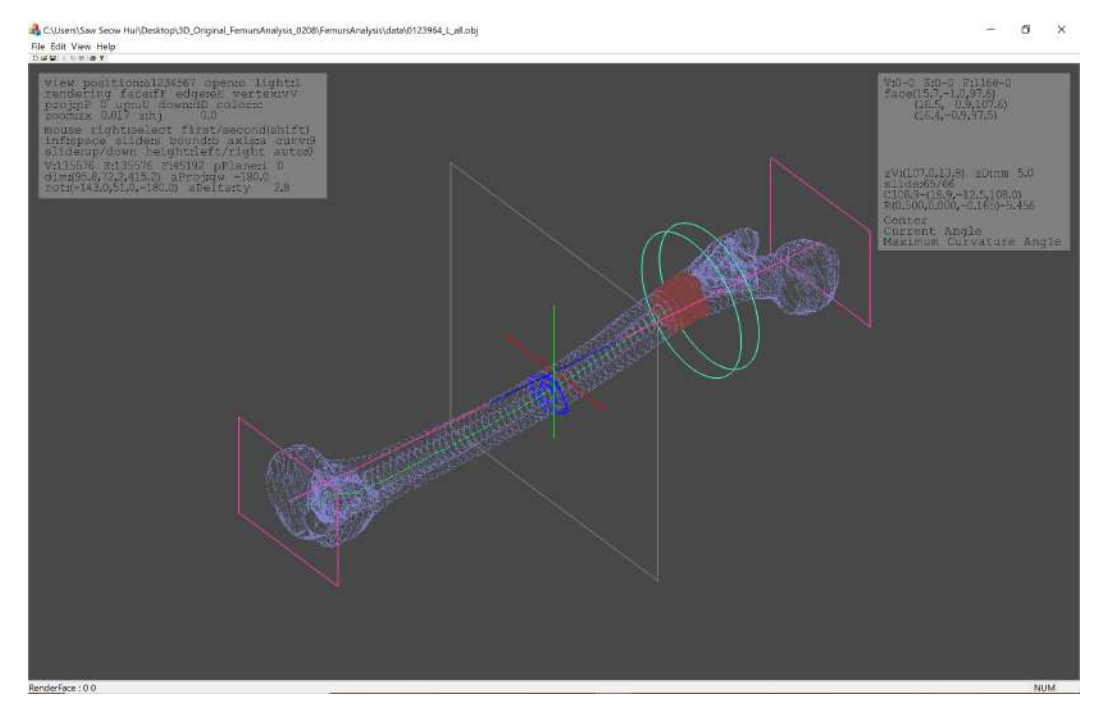


(g) The 3D skeletonization continues.

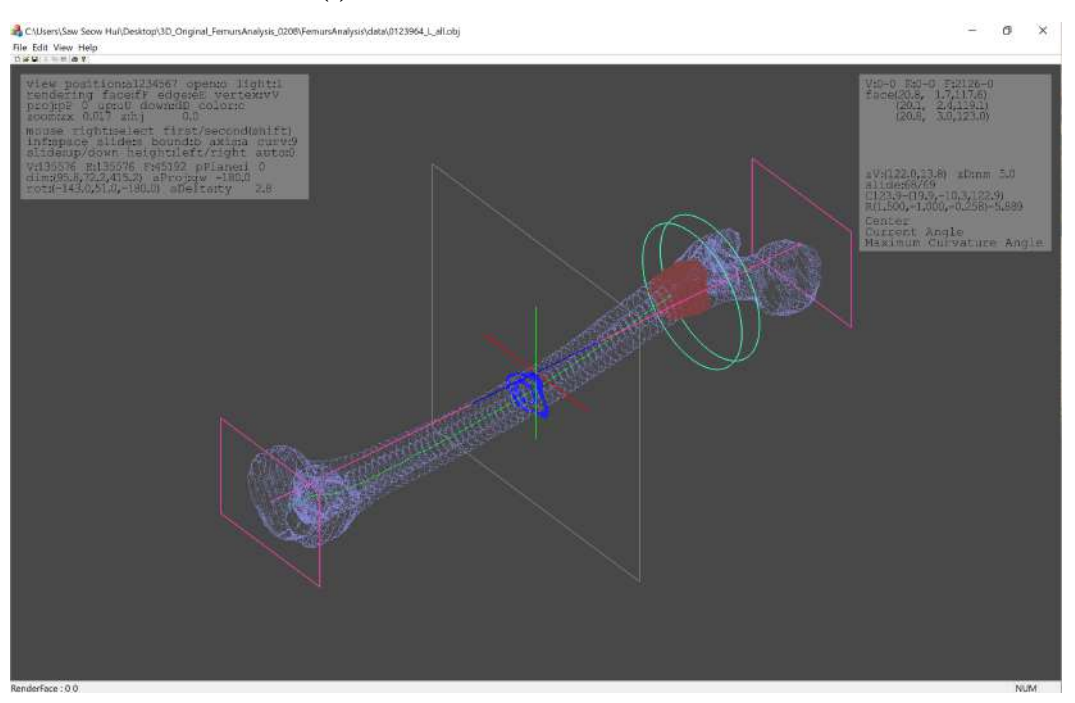


(h) The 3D skeletonization continues.

Figure 1.22: The execution process of our proposed maximum-minimum centre approach in 3D-FSA.

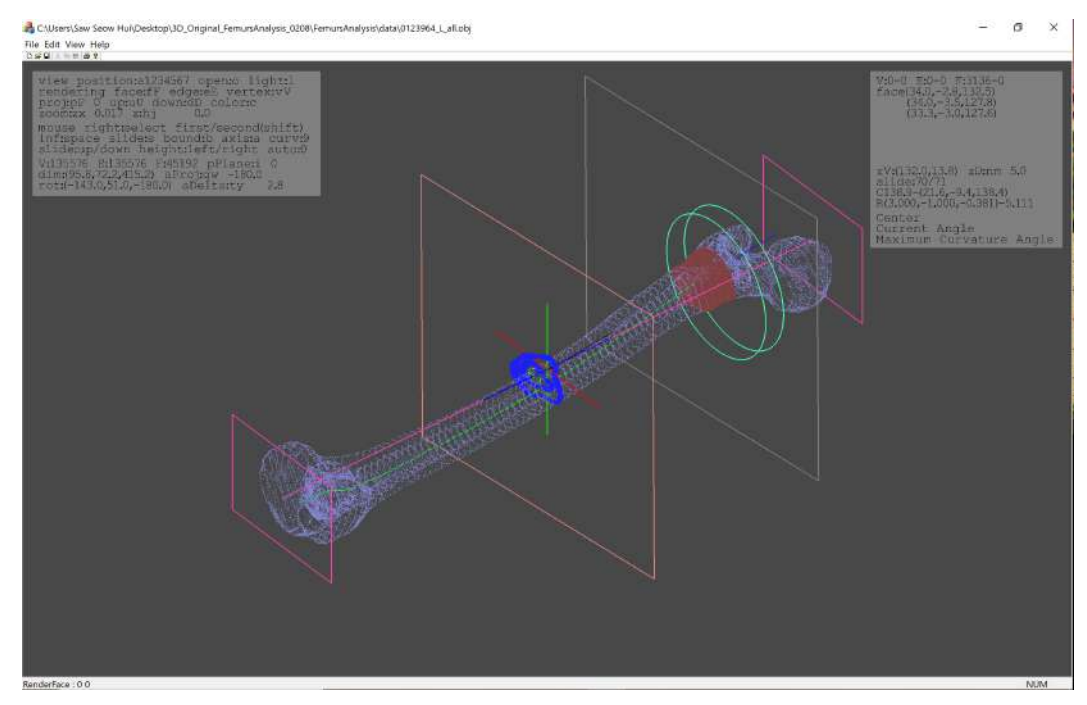


(i) The 3D skeletonization continues.

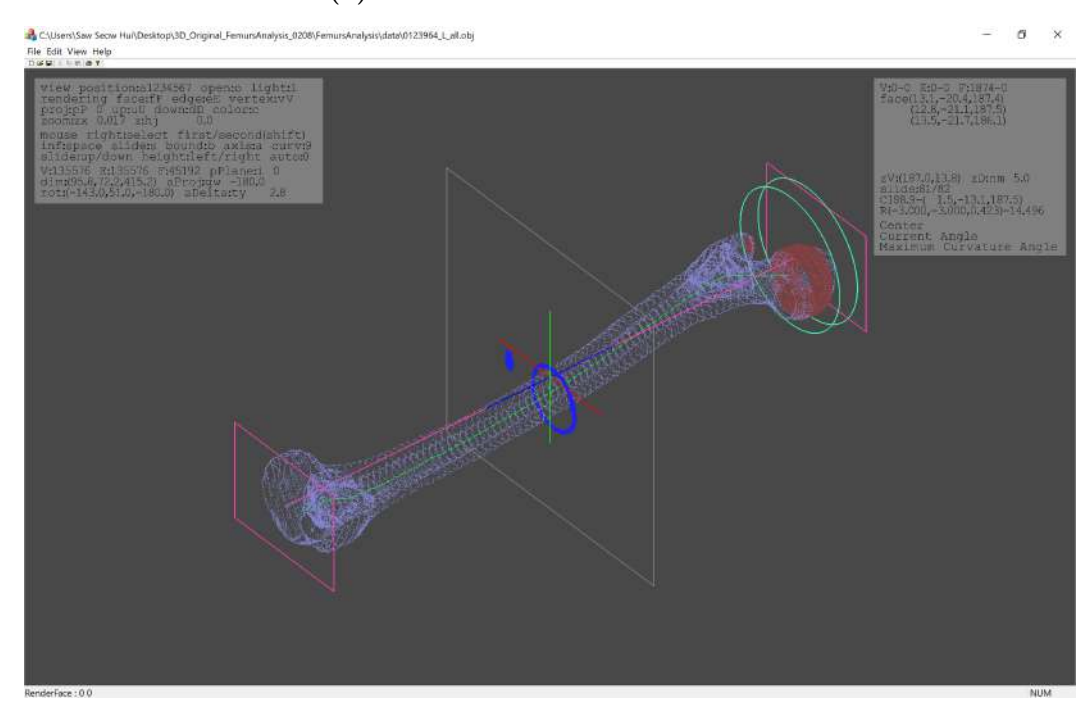


 (\mathbf{j}) The 3D skeletonization continues.

Figure 1.22: The execution process of our proposed maximum-minimum centre approach in 3D-FSA.

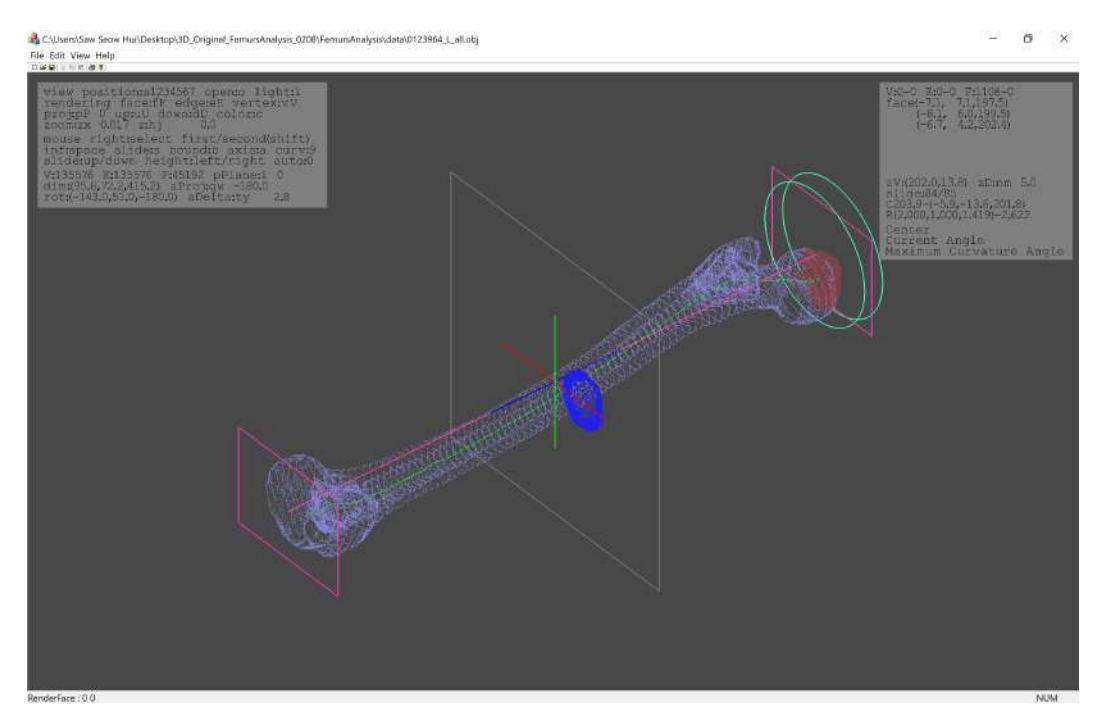


(k) The 3D skeletonization continues.



(1) The 3D skeletonization continues.

Figure 1.22: The execution process of our proposed maximum-minimum centre approach in 3D-FSA.



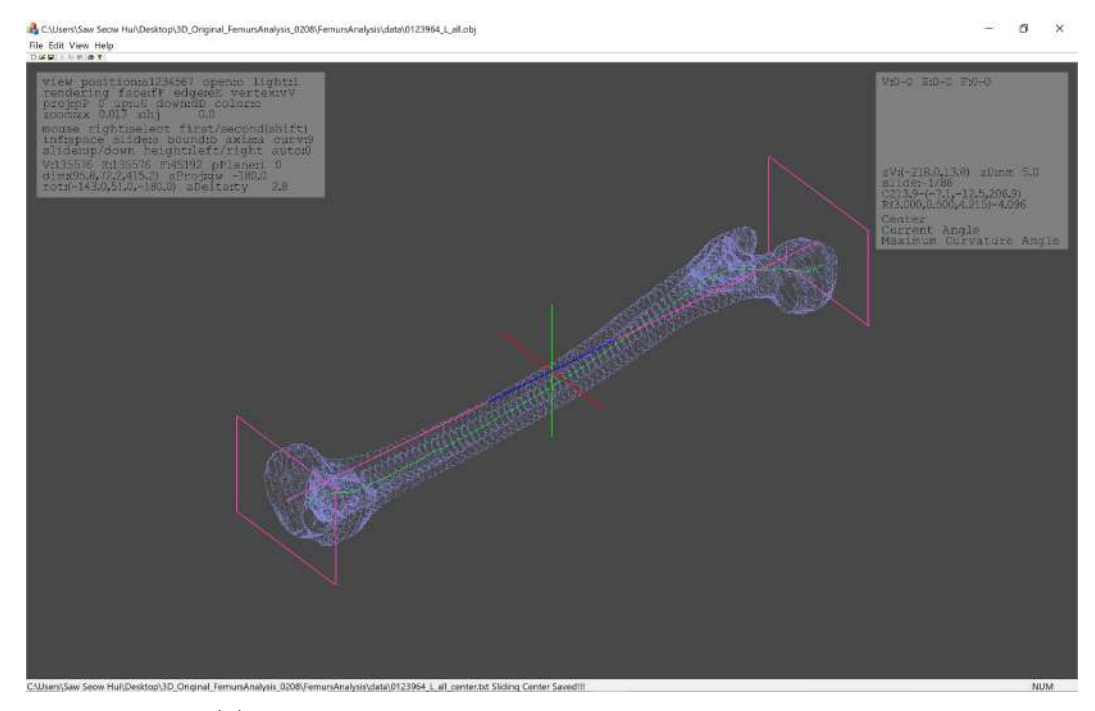
(m) The 3D skeletonization continues until the cylindrical slider s reaches the end.

Figure 1.22: The execution process of our proposed maximum-minimum centre approach in 3D-FSA.

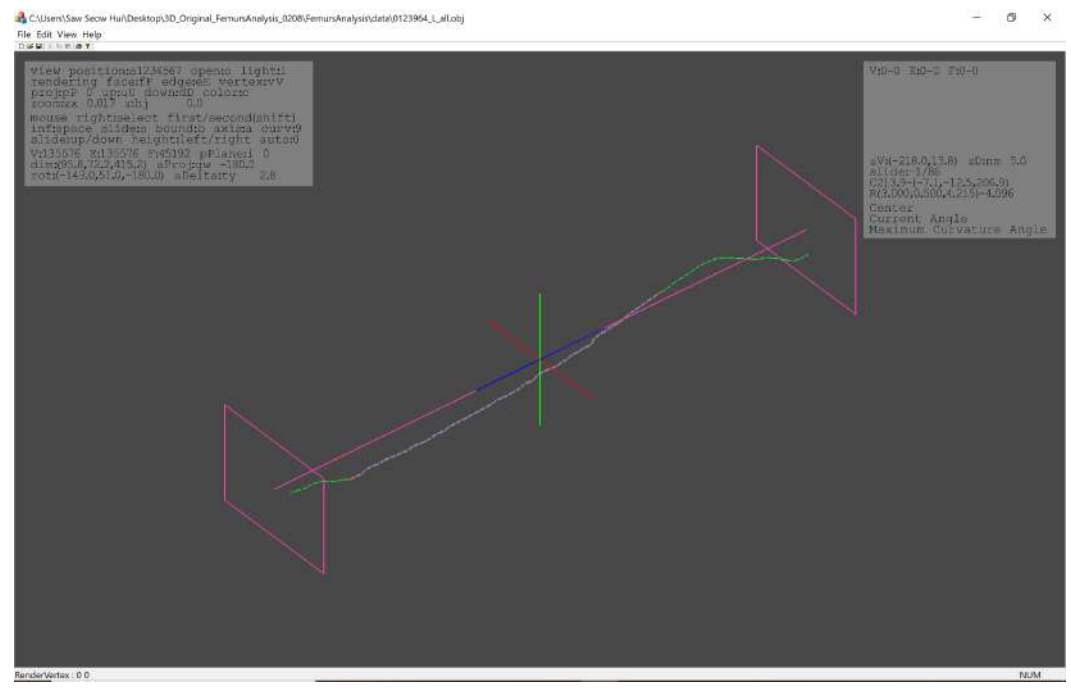
- An automatic approach is implemented to compute the skeleton from 3D femur, namely the maximum-minimum centre approach.
- C. To evaluate our results of the proposed approach against the desirable skeleton properties.
 - To check whether our extracted skeleton satisfies the desirable properties defined by [75].

1.5 Research Contributions

3D skeletonization is a process of reducing a 3D mesh to a simpler version that still retains the essential topology of the original 3D mesh. The thinned version of the 3D mesh is called the skeleton and it is referred as



(a) The 3D skeletonization for the 3D femur is completed.



(b) Finally, the medial centres and the medial line (medial axis) are constructed.

Figure 1.23: The results produced in 3D-FSA.

the medial axis when the skeleton is centred with respect to the boundaries of the original 3D mesh [92].

In the last several decades, there has been a great deal of interest in applying 3D skeletonization in various of applications such as:

- 3D mesh segmentation and 3D printing [93, 94, 95, 96, 97, 98, 99, 100, 101, 102].
- 3D reconstruction and point cloud [103, 78, 104, 105, 106].
- Action tracking and recognition [107, 108].
- Animal analysis [109, 110].
- Animation control [111, 112].
- Automatic navigation [113, 114].
- Image processing and medical analysis [115, 116, 117, 118, 119, 120, 121, 122, 123, 124, 125, 126, 127, 128, 129, 130, 131].
- Robotics [132, 133, 134].
- Shape abstraction and matching [135, 136].

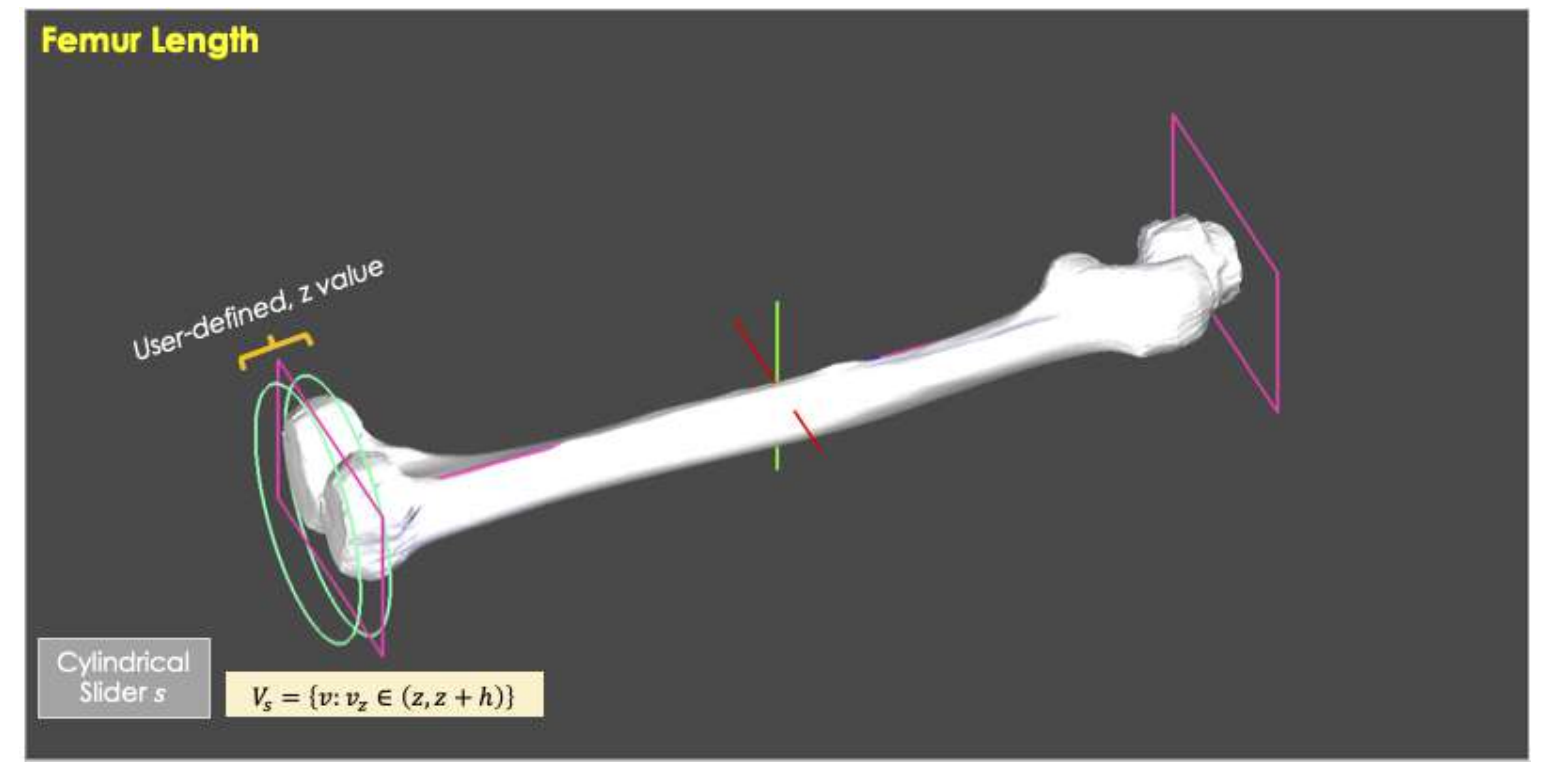
Furthermore, 3D skeletonization is particularly used in medical analysis research such as creating an interactive virtual colonoscopy for mass screening of patients for possible colon cancer in 2D space [115]. E. Sorantin et al. [117] presented a 3D assessment of tracheal-stenoses based on Spiral Computed Tomography (S-CT). Whereas, [122] demonstrated a method for automated central axis extraction from 3D segmented bronchial trees. [116] described a technique to represent relevant information of tree-like structures for volumetric vascular and [119] introduced a method for registering vascular images with sub-voxel consistency. In 2004, Y. Fridman et al. [121] extracted the branching geometry for blood vessels and other anatomic in the human body to be denoted as trees from 3D grayscale images.

However, none are known to have employed 3D skeletonization for producing the anatomical parameters of the femur especially the geometric for bowing and width of the femur except in [1, 137]. The authors in [137] introduced a strategy for extracting a compact skeleton from only ten (10) femurs. Whereas, [1] studied the anatomical deformed long bones of the lower limb. The approach used for the skeleton extraction in [137] and the characteristic of the sampled femurs [1, 137] are not specified, but they estimate sufficient number of femoral clinical parameters. Besides that, there are no proper validation for their results.

Therefore, this thesis provide a 3D analysis program, namely 3D-FSA3D for the orthopaedics in South Korea [16] to morphometrically evaluate seven (7) geometric parameters of 2800 femurs from Koreans from the age of twenty (20) to eighty-nine (89). These geometric parameters are illustrated in Fig. 1.24 respectively and listed in Table 1.5.

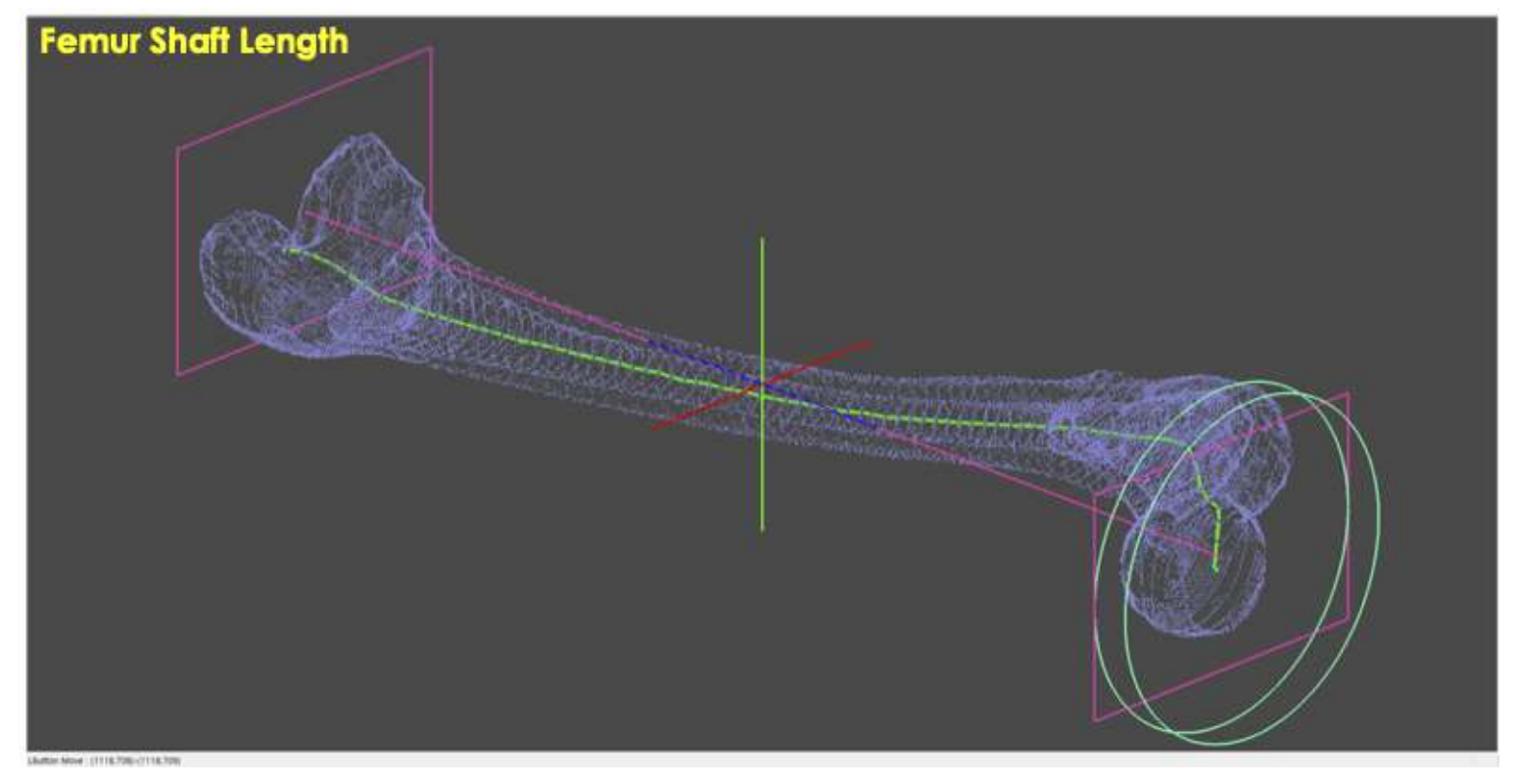
Table 1.5: Generated geometric parameters and the respective figures.

Generated Geometric Parameters	Figure No.
Femur Length	Fig. 1.24a
Femur Shaft Length	Fig. 1.24b
Femur Width	Fig. 1.24i
Femur AP Length	Fig. 1.24i
Diameter of medullary canal	Fig. 1.24f and Fig. 1.24g
Thickness of the Compact Bone	Fig. 1.24h
ROC	Fig. 1.24e and Fig. 1.24j



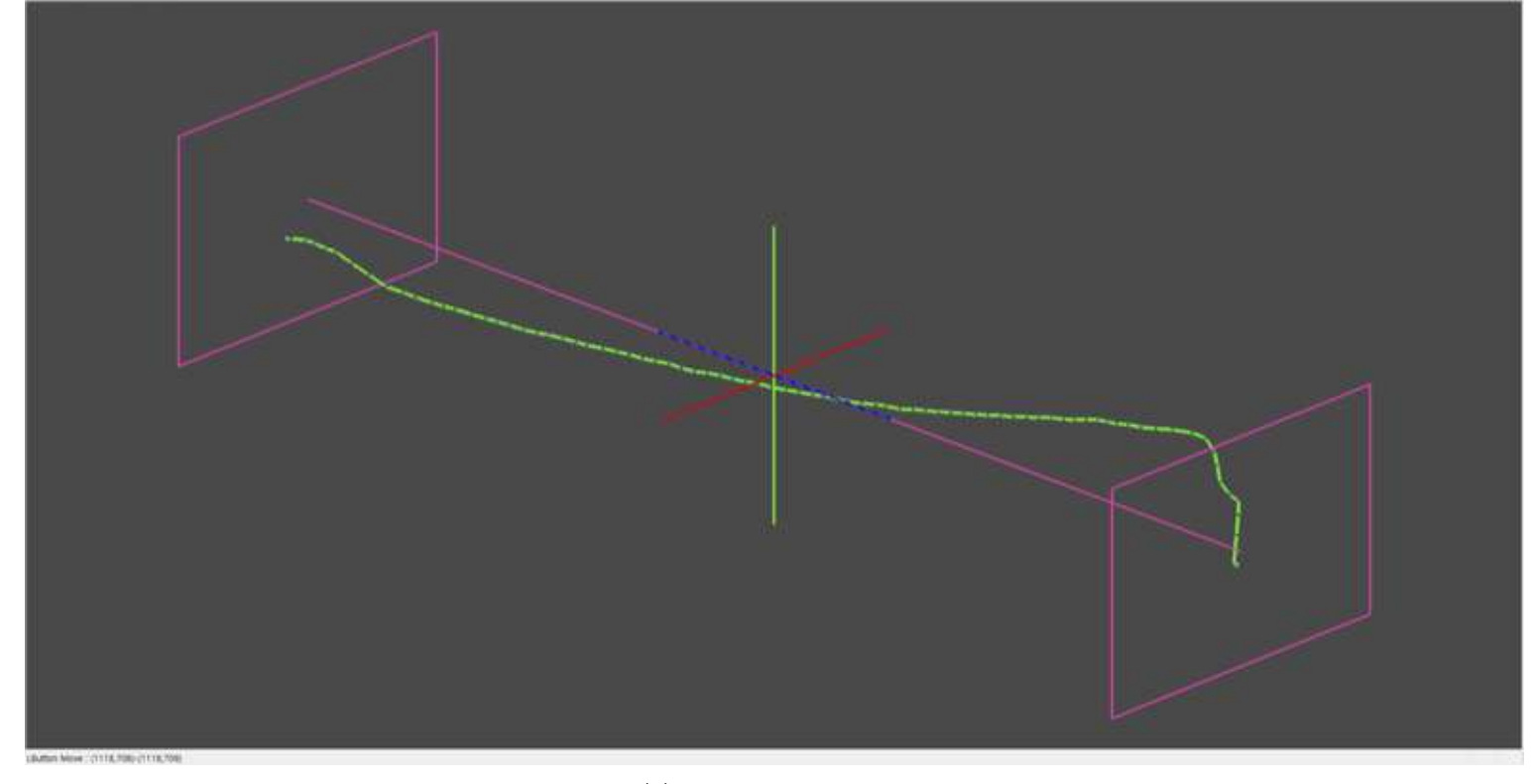
(a) The femur length.

Figure 1.24: The results generated by 3D-FSA.



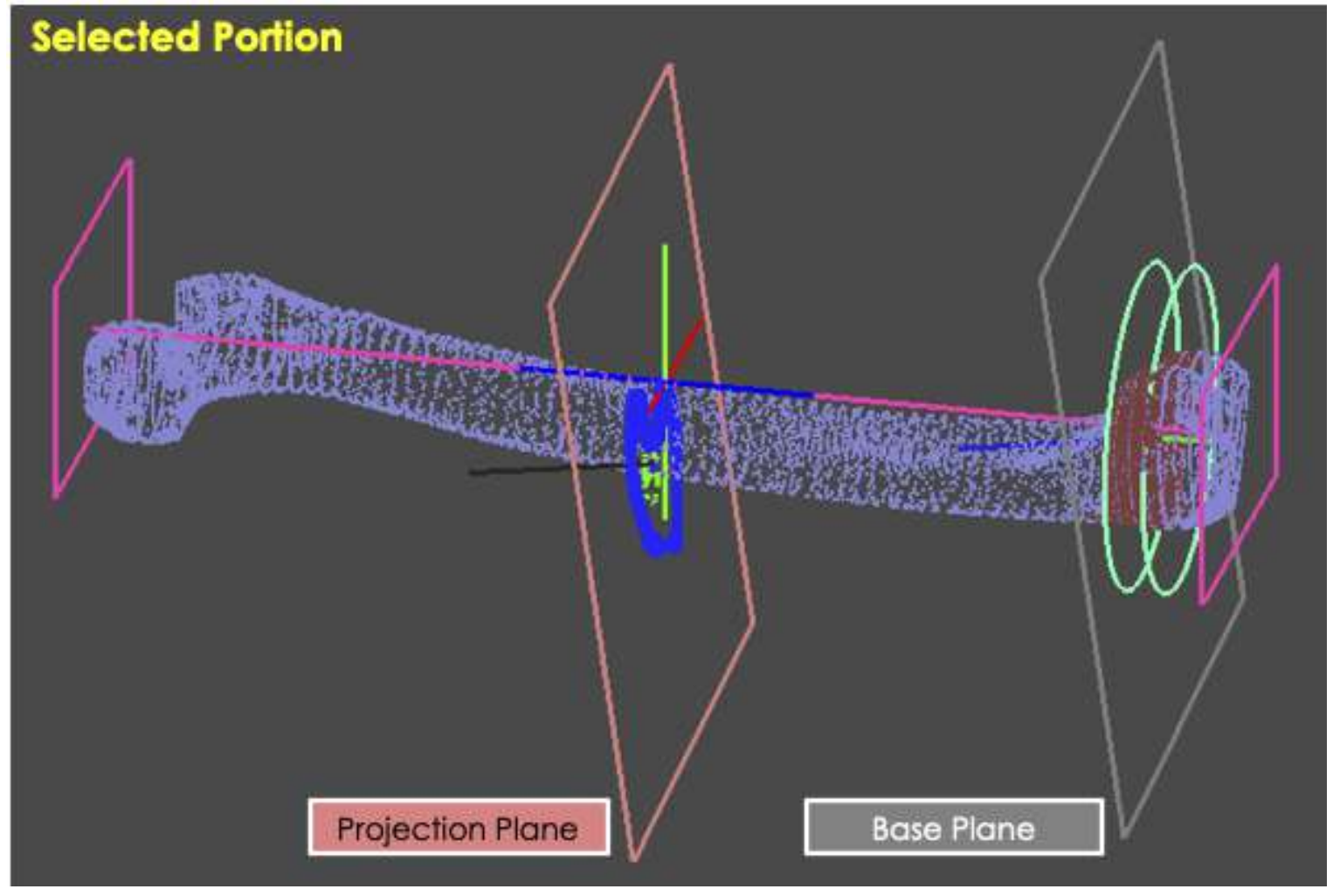
(b) The femur shaft length.

Figure 1.24: The results generated by 3D-FSA.



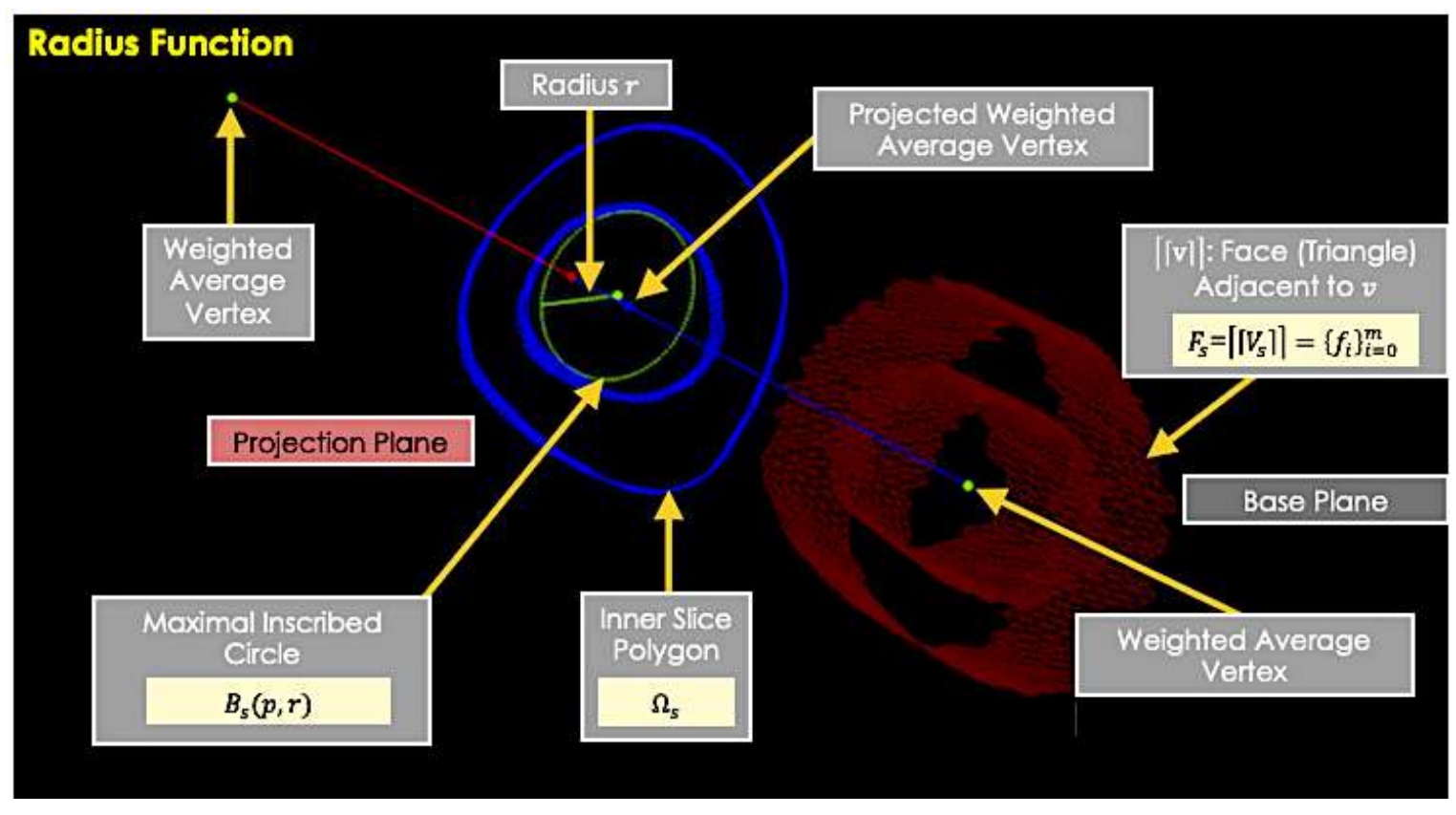
(c) The generated MA.

Figure 1.24: The results generated by 3D-FSA.



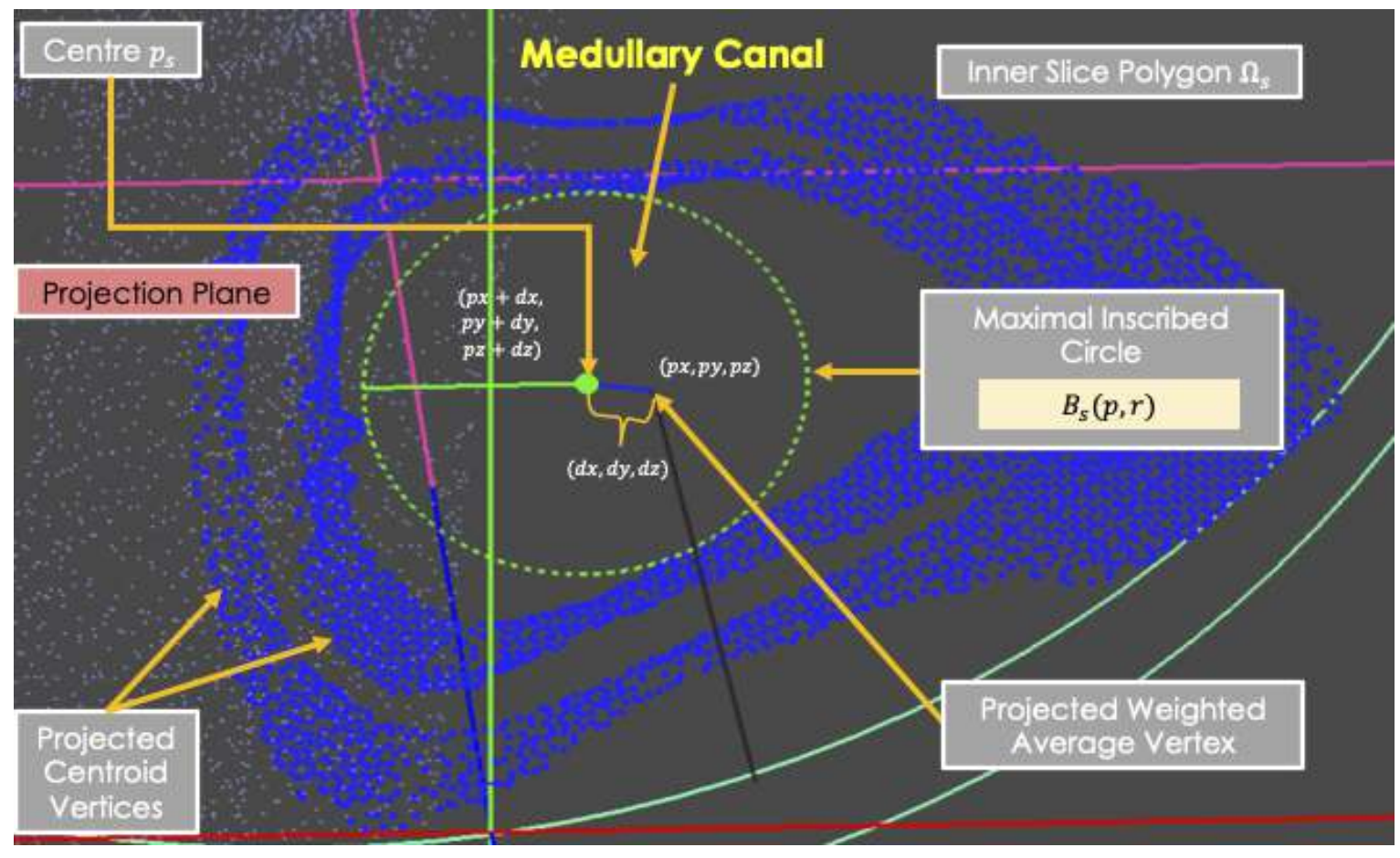
(d) The medial centres are generated by the selected portion of the cylindrical slider s on the base plane.

Figure 1.24: The results generated by 3D-FSA.



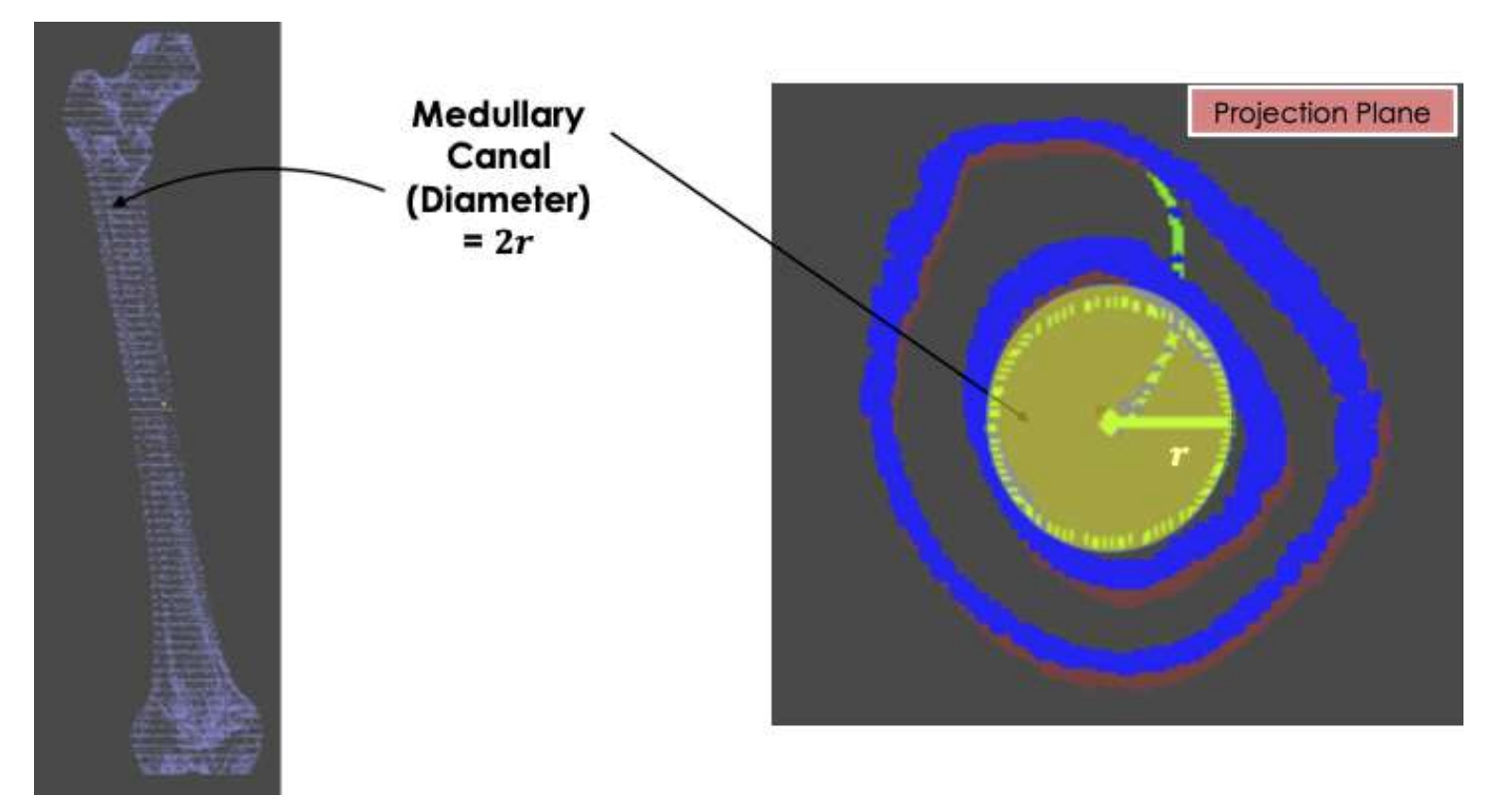
(e) The computed radius function for the MAT.

Figure 1.24: The results generated by 3D-FSA.



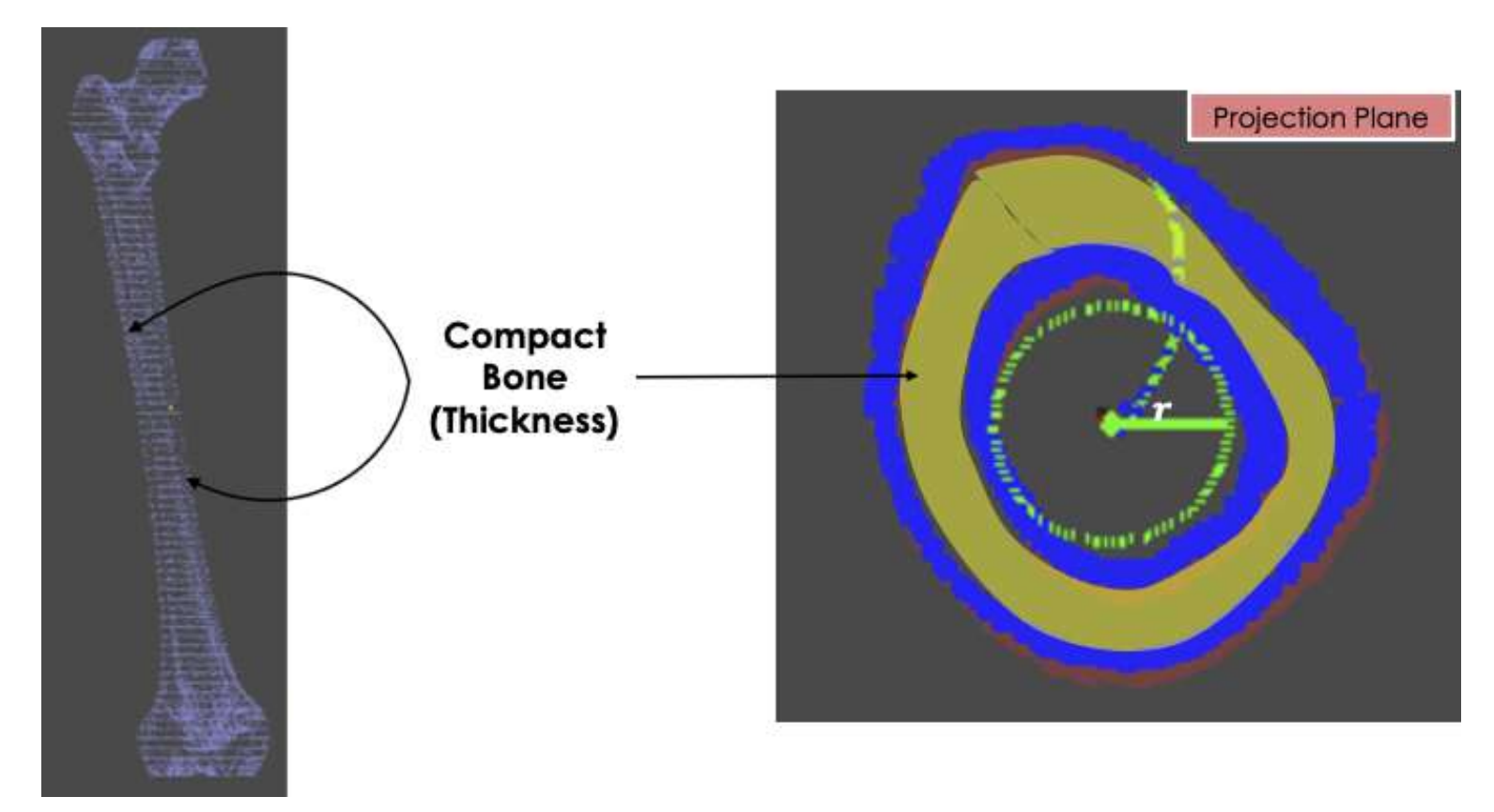
(f) The location of the medullary canal.

Figure 1.24: The results generated by 3D-FSA.



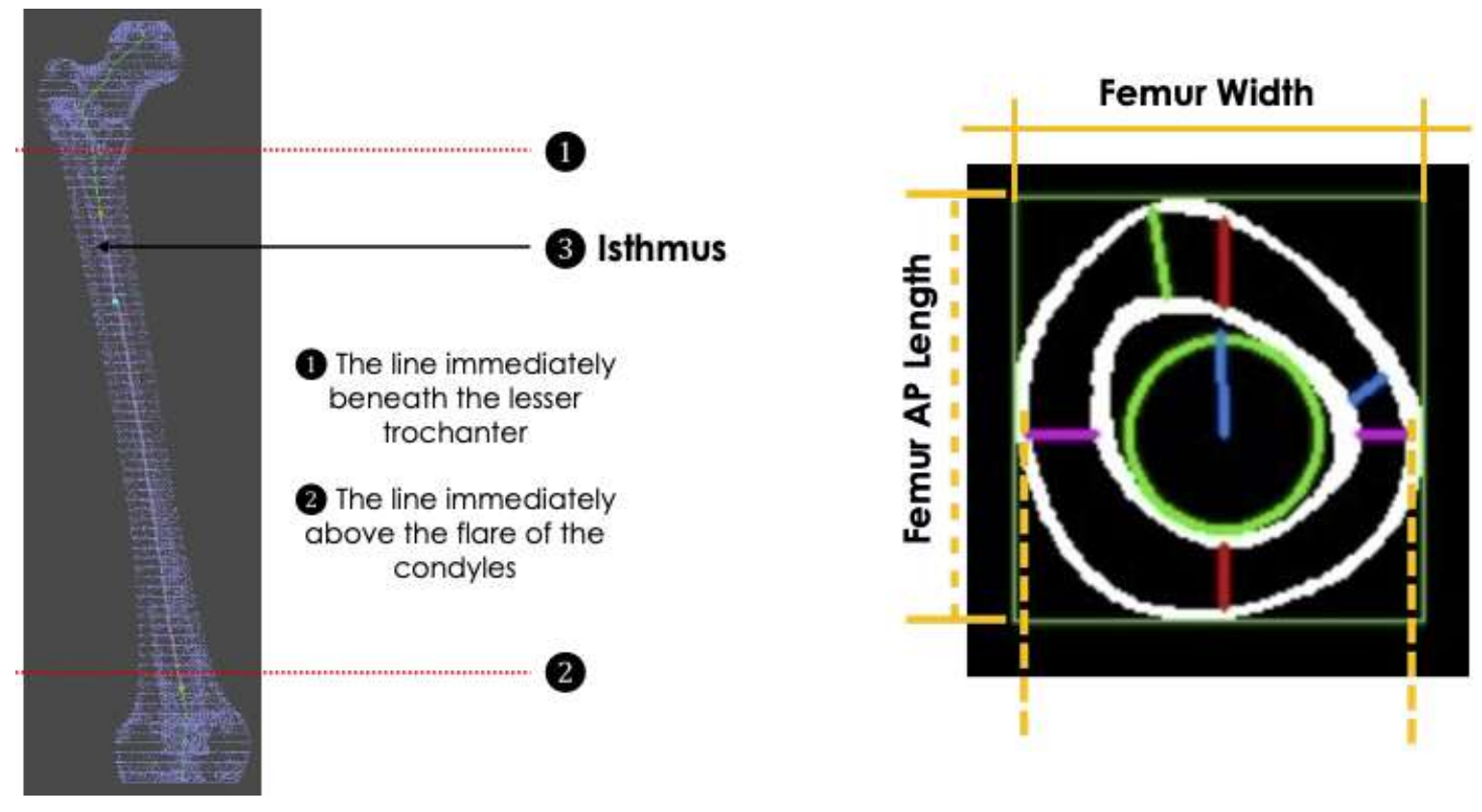
(g) The diameter of the medullary canal is obtained in the projection plane.

Figure 1.24: The results generated by 3D-FSA.



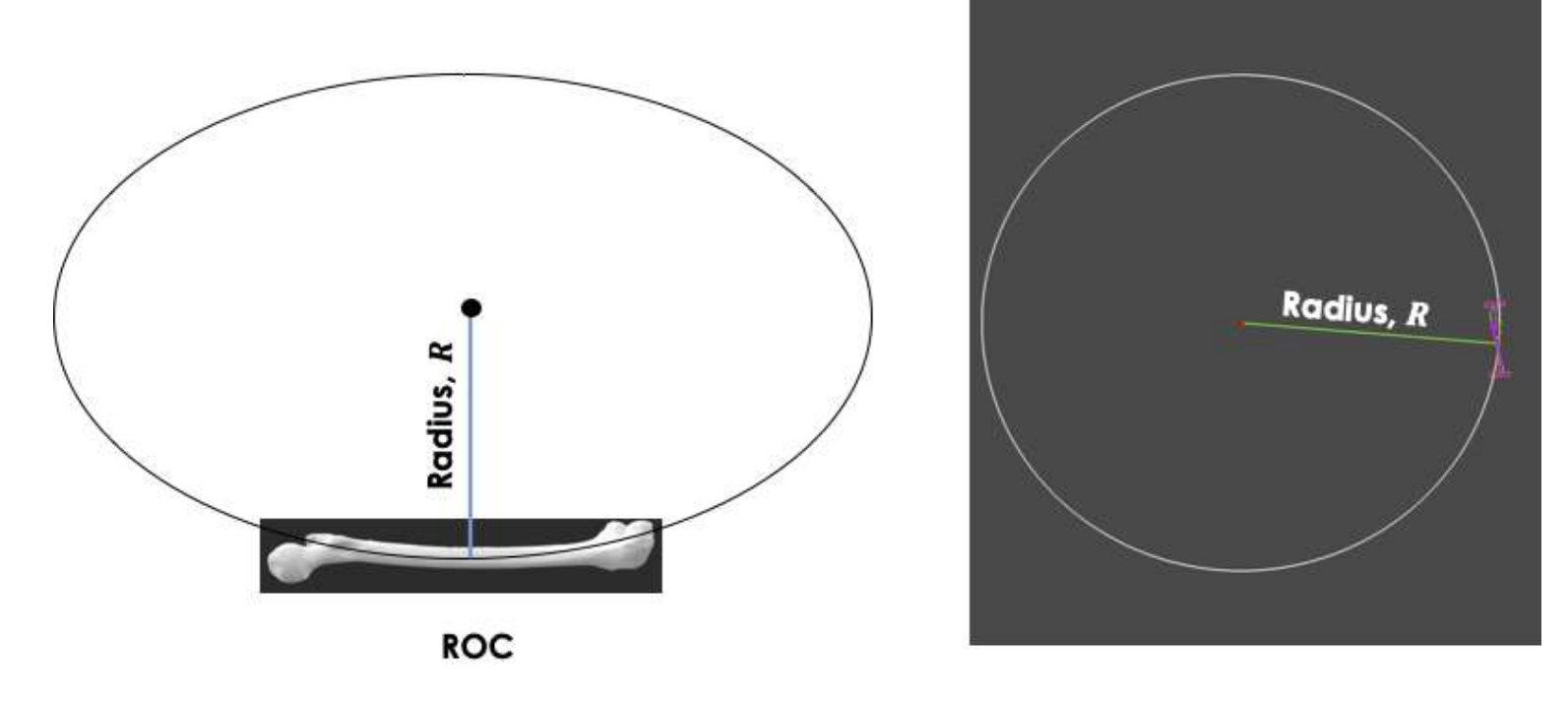
(h) The thickness of the compact bone is also calculated.

Figure 1.24: The results generated by 3D-FSA.



(i) The location of the isthmus and its diameter, the femur width and the AP length.

Figure 1.24: The results generated by 3D-FSA.



(j) The ROC together with the minimum radius angle.

Figure 1.24: The results generated by 3D-FSA.

Apart from that, the results produced by 3D-FSA has been validated using the ICC [138] and fits the excellent agreement based on the rules set by Cicchetti [139]. The rest of the contributions of this thesis are as follows:

- A simple, straightforward and low-cost 3D platform, namely 3D-FSA is implemented to perform analysis for the anatomical parameters (Refer to Table 1.5) of the femur especially bowing and the width of the femur.
- 2 A high-fidelity 3D femur from the input 3D data file that is in .obj format.
- 3 A new and straightforward algorithm is proposed to perform the 3D skeletonization, namely **maximum-minimum centre approach**.
- 4 Our computed medial axes (skeletons) satisfy the properties of 3D skeletonization, with no spurious branches. The comparisons between our method with the Thinning-based method are discussed in Chapter 7.

Most of the work presented in this thesis was previously presented in [140] and published in [141].

1.6 Thesis Organization

The contents of this thesis are structured into eight (8) topics. Chapter 2 familiarises the reader with the current advancements in analysing and

measuring the human femur. It explores different methodologies employed in this field, encompassing the utilisation of 3D skeletonization techniques. Chapter 3 serves as an introduction to the algorithm utilised in this thesis. It aims to familiarise the reader with the inner workings of the algorithm, offering a comprehensive overview of the four (4) key phases and its functionality of the system. Chapter 4 offers a comprehensive and detailed explanation of the pre-processing stage, which serves as the initial phase of the system. This chapter addresses various key aspects related to preprocessing, including the criteria of the steps involved in data acquisition, the criteria of the sampled data, the fundamental concepts underlying significant geometric parameters, and the structure of the 3D data employed in the implementation. It provides readers with a comprehensive understanding of the pre-processing stage, lying a solid foundation for subsequent chapters that delve into further stages and aspects of the system. Chapter 5 elucidates the second (2^{nd}) stage of the system, namely the 3D femur construction. This chapter provides additional details on the methodology employed to generate a 3D femur model from input 3D data files in the .obj format. It outlines the specific strategies, techniques, and algorithms utilised to accomplish this task effectively. By elaborating on the process of 3D femur construction, Chapter 5 aims to enhance the reader's understanding of the steps involved in transforming the input 3D data files into a comprehensive and accurate representation of the femur in 3D space. Chapter 6 represents a critical phase within the system, focusing on the essential process of 3D skeletonization. This chapter provides a comprehensive explanation of the proposed skeletonization algorithm specifically designed for the analysis of a 3D femur, known as the maximum-minimum centre approach. Within this chapter, intricate details of the skeletonization algorithm are discussed, aiming to provide a thorough understanding of its functioning and implementation. Chapter 7 presents the results obtained from applying the algorithm to the given 3D femurs. It serves as a comprehensive evaluation of the proposed maximum-minimum centre skeletonization algorithm, presenting the obtained results, the verification and validation procedures employed to ensure the algorithm's effectiveness and accuracy. A summary of this thesis, as well as concluding remarks and pointers to future work and research directions are provided in Chapter 8. This chapter serves as a conclusive chapter that encapsulates the main insights and conclusions of the study while also providing valuable directions for future research, inspiring further advancements and improvements in the field.

Chapter 2

LITERATURE REVIEW

In this chapter, an examination is conducted on the diverse methods used for analysing and measuring the human femur, commencing with the conventional method and concluding with the 3D skeletonization method.

2.1 Osteometric Analysis of Human Femur

As described in Chapter 1, the femur is the largest bone in the human body, which plays a significant role in the hip and knee joints [51]. As a result, extensive research is conducted on the femur in various fields such as physical and forensic anthropology, human kinematics, and orthopaedics. Physical and forensic anthropology [142, 143, 144, 58] studies involve the use of metric or non-metric methods to identify variations in the femur across different populations, sexes, and ages [142, 143, 145, 146, 147, 57, 148, 149, 150, 58, 50].

Additionally, orthopaedics research focuses on analysing specific areas of the femur, including the femoral head, neck, and the proximal part of the medullary canal, for the studies which are related to the hip joint [59, 151, 152, 62, 153, 154, 155, 156, 157, 158, 159, 160, 161, 162, 163,

164, 165, 166, 167, 168, 169, 170, 171]. Similarly, the shape of the distal part of the femur is also examined for the studies concerning the knee joint [172, 173, 174, 175, 176, 177, 178, 179, 180, 181, 182, 183, 184].

Several complications have been reported resulting from a mismatch between the curvatures of the femur and the implant [10]. These complications include nail impingement against the anterior or lateral cortex [185, 186, 187], encroachment or penetration of the anterior cortex [188, 189, 190, 191], and fractures of the anterior cortex [192].

Therefore, the anterior curvature of the femur is yet another important anatomical characteristic that has been extensively studied by the anthropologists and orthopaedics [142, 143, 144, 58]. The intramedullary nail insertion, revision prosthesis design, and biomechanics of the proximal femur are influenced by the anterior curvature of the femur.

This literature review aims to provide an overview of these established categories of methods employed for morphometric analysis and measurement of the human femur:

A. Conventional Method

B. Lateral Radiographs

C. CAD Software

By examining the existing body of research, this review explores the techniques, tools, and applications of each category. Furthermore, it discusses the strengths and limitations of these methods in enhancing our understanding of the human femur's morphology and dimensions.

2.1.1 Conventional Method

Conventional methods have long been employed for morphometric analysis and measurement of the human femur. These methods involve direct physical measurements using callipers, rulers, and osteometric boards as illustrated in Fig. 2.1.

The use of a calliper for measuring the femur on an osteometric board has been a common practice prior to the emergence of the technology [142, 143, 57]. Osteometric boards are tools used to measure skeletal remains, and a calliper is a measuring instrument that allows for precise measurements of bone lengths and other dimensions.

Additionally, they typically include measuring dimensions such as femoral length [9], head diameter, mid-shaft diameter [10], neck width, shaft circumference, and condylar dimensions.

These methods are widely used in anthropology and forensic sciences to determine age, sex, and population affinity. They provide reliable baseline data for population comparisons, as well as the assessment of growth and development patterns.

However, the conventional methods used in morphometric analysis and measurement of the human femur, have several disadvantages that should be taken into account. These disadvantages include:

• Subjectivity and Inter-Observer Variability

Manual calliper measurements and visual assessments in radiographs images rely on human judgment and interpretation. This subjectivity can introduce variations and inconsistencies in measurements between different observers. Inter-observer variability can affect the reliability and reproducibility of the results. Inter-observer variability can affect the reliability and reproducibility of the results, particularly in cases where multiple measurements or comparisons are required.

• Lack of Precision and Resolution

Conventional methods may lack of the precision and resolution required for accurate morphometric analysis. Manual calliper measurements are limited by the instrument's accuracy and the skill of the operator, which can result in measurement errors. Radiograph techniques, while providing more detailed information, are still subject to limitations in image resolution and the potential for foreshortening or projection distortions.

• Incomplete Representation of 3D Anatomy

The conventional methods typically capture measurements in a 2D plane or focus on specific dimensions, neglecting the comprehensive 3D anatomy of the femur. Complex parameters such as femoral head offset or femoral curvature cannot be adequately assessed with conventional methods alone. The complete understanding of femur morphology often requires advanced imaging techniques, such as CT or Magnetic Resonance Imaging (MRI).

• Limited Access to Internal Structures

Conventional methods primarily provide external measurements and do not directly capture information about the internal structures of the femur. Assessing features like cortical thickness, or internal bone geometry is not feasible with manual calliper measurements or radiographic images. These internal structures play a crucial role in bone strength, pathology, and surgical planning.

• Time and Labor Intensive

Conventional methods can be time-consuming and labor-intensive, particularly when dealing with large sample sizes or complex measurements. Manual calliper measurements require meticulous positioning and repeated measurements to ensure accuracy, which can be time-consuming. Radiographic techniques involve image acquisition, processing, and manual assessments, adding to the overall time and effort required for analysis.

• Limited Standardisation

Conventional methods often lack standardised protocols and guidelines for measurement procedures. This can lead to variations in measurement techniques across different studies or institutions, making it challenging to compare and combine results.

• Invasiveness and Patient Discomfort

In some cases, conventional methods may involve invasive procedures, such as bone biopsies or surgical measurements. These procedures can be uncomfortable for the patients and carry additional risks, making them less suitable for routine or non-invasive analysis.

Therefore, it's worth noting that technological advancements have introduced digital tools and 3D scanning techniques that can also be used for femur measurements and analyses. These technologies provide alternative methods for assessing the important anatomical characteristic of the femur accurately and precisely, but may not entirely replace this traditional method.

2.1.2 Lateral Radiographs

Lateral radiographs, particularly X-rays, have been widely used for the morphometric analysis and measurement of the human femur, especially among the meedical researchers who commonly utilise this measurement methods predominantly relying on the lateral radiographs or images of the femur.

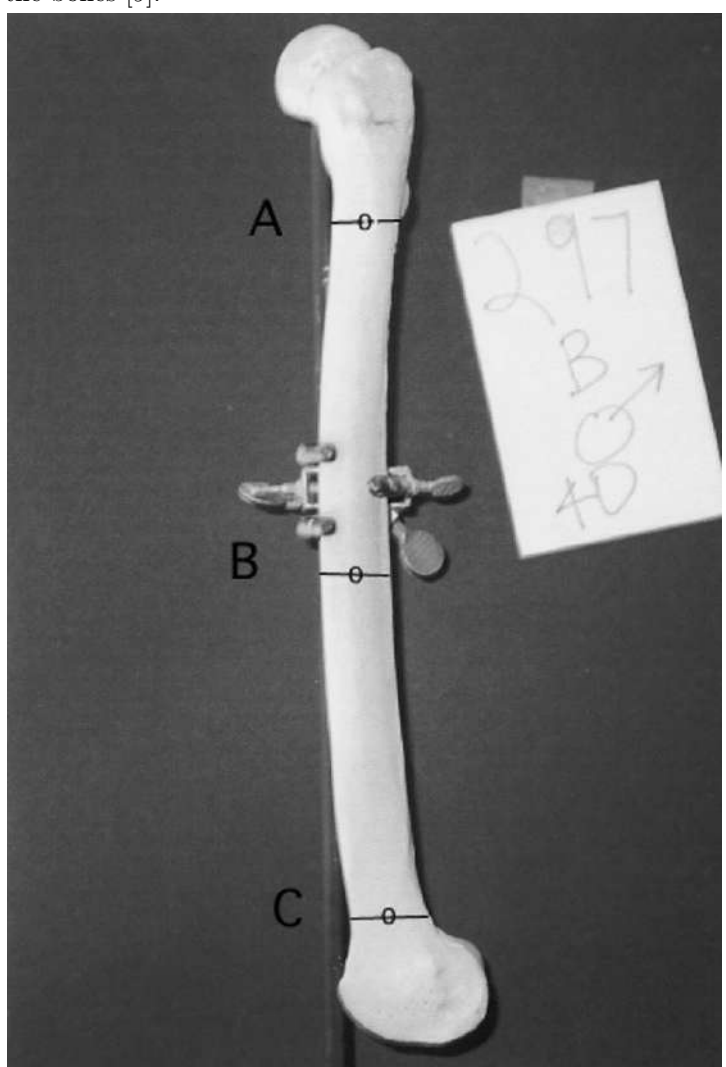
Lateral radiographs, also known as lateral X-rays or lateral views, are diagnostic imaging techniques that provide a side view of the body or a specific body part as shown in Fig. 2.2. In the case of the femur, a lateral radiograph captures an image of the femur from the side, allowing for visualising the bone structure including the hip and knee joint and assessing any abnormalities or measurements of interest.

These techniques enable accurate assessment of femoral length, cortical thickness, bone mineral density, and joint angles. They provide non-invasive and easily repeatable measurements, making them valuable in clinical settings for preoperative planning, fracture evaluation, and monitoring disease progression.

[193, 10] have conducted the analyses and measurements of the femoral



(a) The osteometric board used to measure the maximum length of the bones [9].



(b) The location of the three (3) reference lines and measurement points are indicated using the conventional method [10].

Figure 2.1: The examples for the conventional approach involves using a calliper to measure the femur on the osteometric board.

curvature using the outer surfaces of the femurs, whereas other researchers [194, 192] have determined the curvature of the femoral medullary canal by utilising lateral radiographs.

Lateral radiographs are also useful in anthropological studies, as they allow for the estimation of femoral dimensions in archaeological remains.

While lateral radiographs are commonly used in morphometric analysis and measurements of the human femur, they have certain disadvantages that should be considered. These represtn disadvantages include:

• Projection and Foreshortening Effects

Lateral radiographs provide a 2D representation of a 3D structure, which can introduce projection and foreshortening effects. This can lead to inaccuracies in measurements, especially when assessing parameters such as length, curvature, and angles of the femur. The distortion caused by projection can make it challenging to obtain precise and reliable measurements.

• Limited View and Anatomical Coverage

Lateral radiographs capture a specific view of the femur, typically in a single plane. This limited view may not provide a comprehensive representation of the entire bone, particularly for complex anatomical features and variations. Critical regions of interest, such as the femoral head, neck, and distal condyles, may be partially or poorly visualised, leading to incomplete measurements and potential diagnostic oversights.

Difficulty in Assessing 3D Parameters

Lateral radiographs are primarily designed for assessing 2D measurements, such as bone length and angles. Extracting accurate 3D parameters, such as femoral head offset, from lateral radiographs alone can be challenging. Specialised imaging techniques, such as CT or MRI, are often required for more precise assessment of these parameters.

• Variability in Patient Positioning

Patient positioning during radiographic imaging can vary, leading to inconsistencies in the orientation and alignment of the femur in lateral radiographs. Differences in limb rotation, pelvic tilt, and knee flexion can impact the accuracy and reproducibility of the measurements. Standardisation of patient positioning in essential to minimise these sources of variability.

• Reliance on Calibration and Scaling

Accurate measurement on lateral radiographs relies on proper calibration and scaling of the image. Any errors or inconsistencies in the calibration process, such as variations in X-rays magnification or incorrect scaling factors, can lead to significant measurement inaccuracies. Calibration procedures must be carefully performed and regularly validated to ensure reliable measurements.

• Radiation Exposure

Lateral radiographs involve exposure to ionising radiation, which poses potential health risks, particularly in cases where repeated imaging is required. Minimising radiation exposure is crucial, especially for vulnerable populations such as children or individuals undergoing serial

measurements.

Despite these disadvantages, lateral radiographs remain a valuable tool in the initial assessment and screening of femur morphometry due to their relatively low cost, widespread availability, and ease of used. However, for more detailed and accurate measurements, complementary imaging techniques like CT or MRI should be considered. Integration of multiple imaging modalities can provide a more comprehensive understanding of femur morphology and aid in clinical decision-making.

2.1.3 Computer-aided Design Software

With advancements in technology, CAD software has emerged as a powerful tool for morphometric analysis and measurement of the human femur. It allows for the creation of 3D digital models of the femur of the physical objects based on medical imaging data, such as CT, MRI scans, or ultrasound images. These models can be manipulated to accurately measure various dimensions, angles, and volumes of interest, and commonly used in the field of medical 3D modelling, printing, and biomedical engineering.

CAD software also enables the generation of virtual simulations, such as Finite Element Analysis (FEA) [195, 196], to assess the mechanical behaviour of the femur under different loading conditions.

As CAD software advances and its integration in digital medical imaging progresses, several authors have employed simulated (reconstructed lateral radiographs) or images through the utilisation of 3D femoral models derived



Figure 2.2: An example of the lateral radiographs approach involves using an X-rays machine sourced from the website [11].

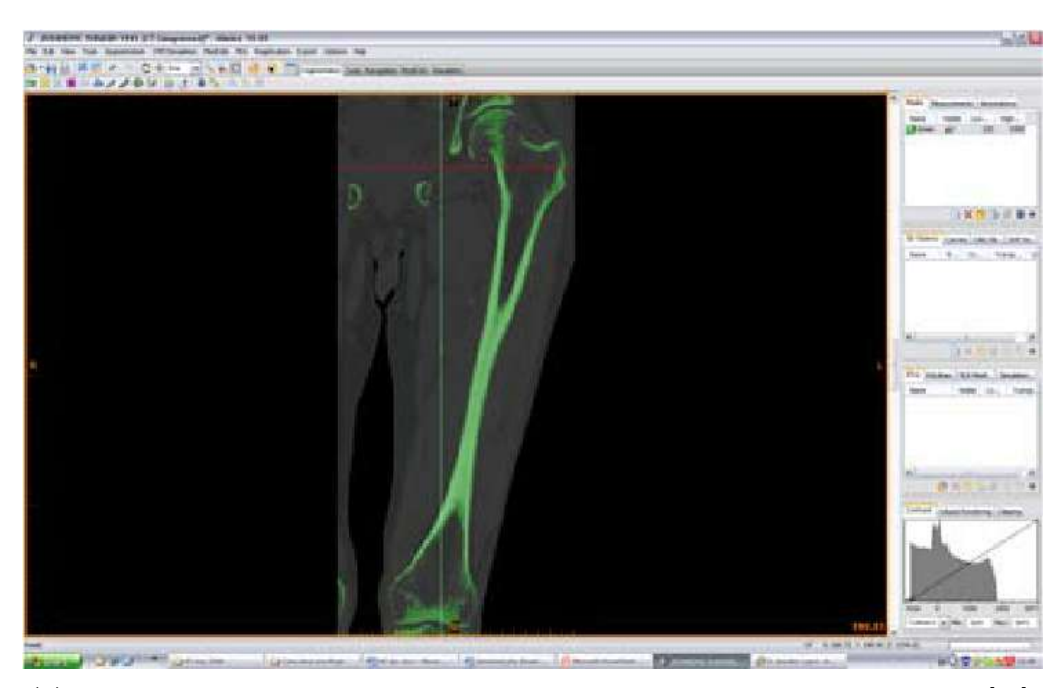
from CT. Subsequently, measurements of femoral curvature have been obtained using these models [185, 197, 198, 199, 200, 201, 202].

The most popular medical softwares are the Materialise Mimics and the AVIEW Modeler as illustrated in Fig. 2.3. Materialise Mimics is developed by a Belgian company, whereas AVIEW Modeler is developed by a Korean company, named Coreline. The UI for both softwares are shown in Fig. 2.3a and Fig. 2.3b respectively.

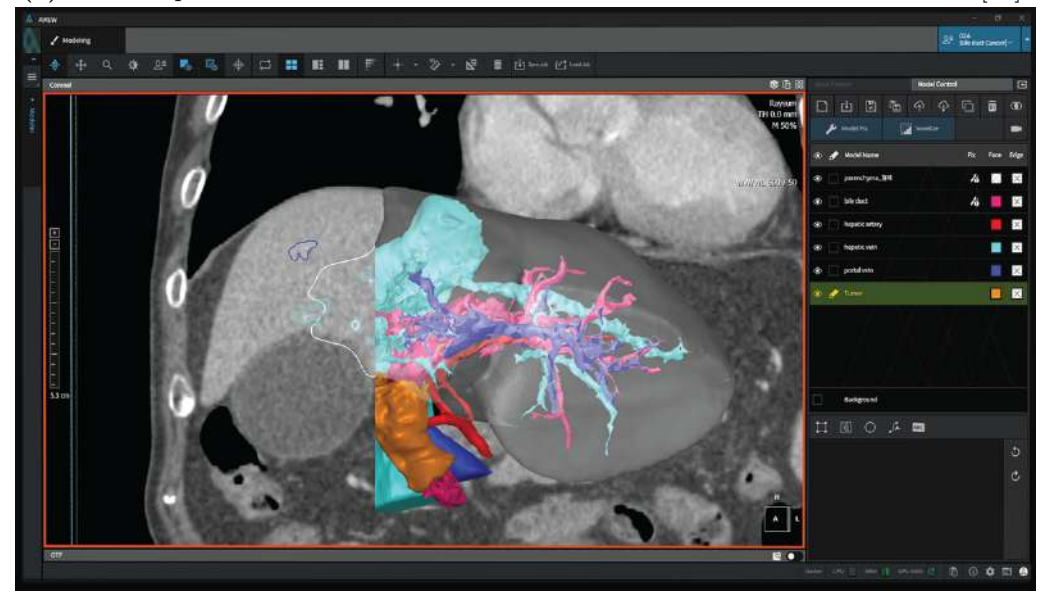
[14] conducted an investigation on sex differences in resected distal femoral morphology in Chinese osteoarthritic knees using CT scans as shown in Fig. 2.4a. Whereas, [51, 203] conducted a morphometric evaluation on 202 femurs from Korean individuals and on 426 femurs from the Chinese population respectively. These evaluations were carried out using a 3D reconstruction program, specifically using Mimics software by Materialise from Belgium [12], which utilised 3D models generated from CT images.

All the studied measurement parameters were selected with reference to physical and forensic anthropology studies as well as orthopaedic implant design studies.

Furthermore, the authors' findings in [15] revealed that femoral bowing is more pronounced among Japanese populations compared to other ethnic groups based on the constructed 3D model of the femora using a CAD software. This study holds significant importance in aiding orthopaedic surgeons in performing accurate preoperative evaluations of femoral bowing. By doing so, it helps to prevent potential issues such as malalignment, rotation, and abnormal stresses that may arise between the femur and implant during surgical procedures.



(a) An example of a UI for Materialise Mimics software sourced from the website [12].



(b) An example of a UI for AVIEW Modeler software sourced from the website [13].

Figure 2.3: The popular medical 3D modelling, printing and biomedical engineering softwares.

Table 2.1 provides a comprehensive list of studies that have employed specific CAD software and 3D construction programs for morphometric evaluations. These investigations highlight the growing utilisation of advanced digital tools in the field of femur analysis.

Table 2.1: List of studies that have employed specific CAD software and 3D construction program for morphometric evaluations.

Related Researchers	No. of Femurs & Focused Populations	urs & Focused Populations CAD Softwares Used				
[14]	130 Chinese	Mimics [12]				
[51]	202 Korean	Mimics [12]				
[203]	426 Chinese Mimics [12]					
[15]	132 Japanese AquariusNet Viewer [204					
[205]	31 Caucasian, 28 Japanese, 4 Thai	Amira Software [206] [207]				
[208]	The Specific Details were not Provided	Visual Studio [209] and Matlab [210]				
[211, 196]	The Specific Details were not Provided	Mimics [12]				
[212]	326 Koreans	AVIEW Modeller [13]				

 $continued\ on\ next\ page$

Table 2.1 – Continued from previous page

Related Researchers	No. of Femurs & Focused Populations	CAD Softwares Used			
[213]	46 Koreans	AVIEW Modeller [13]			
[214]	138 Koreans	AVIEW Modeller [13]			

Apart from that, several medical researchers [212, 214, 213, 215] obtained a collection of CT scans saved in the Digital Imaging and Communications in Medicine (DICOM) format. Subsequently, they utilised the AVIEW Modeler, a commercial 3D modelling software developed by Coreline in South Korea [13], to convert these CT images into the desired 3D data format.

While CAD software offers numerous benefits in morphometric analysis and measurement of the human femur, there are also several disadvantages to consider. These disadvantages include:

• Complexity and Learning Curve

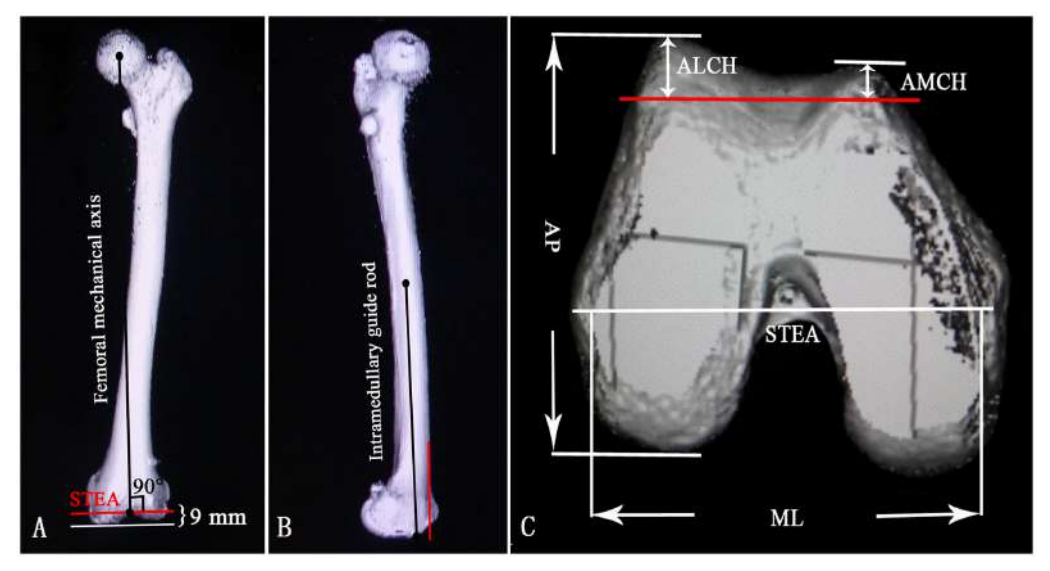
CAD software typically has a steep learning curve and requires specialised training to operate effectively. The complexity of the software and its advanced features may pose a challenge for users who are not familiar with CAD tools, leading to longer processing times and potential errors in measurement.

• Time and Resource Intensive

The process of creating accurate 3D models of the femur using CAD software can be time-consuming, especially when dealing with large datasets or complex shapes. Generating precise meshes, aligning and segmenting the bone, and refining the model often require significant computational resources and expert knowledge.

• Subjectivity in Model Creative

CAD software often relies on manual input for model creation and manipulation. This introduces a level of subjectivity, as the user's



(a) An example of a coronal CT image of a femur for measurements [14].



(b) An example of a constructed 3D model of the femora based on the CT scans [15].

Figure 2.4: The examples for the CAD softwares approach to measure the femur's parameters.

interpretation and judgement can influence the resulting model and measurements. Inconsistent interpretations and inter-observer variability can affect the reliability and reproducibility of the analysis.

• Data Processing and Limitations

CAD software may struggle with handling large datasets or complex geometries, resulting in difficulties in processing and analysing the femur models efficiently. Additionally, some CAD software may have limitations in accurately capturing intricate anatomical details or irregular bone shapes, potentially leading to measurement inaccuracies.

• Software Cost and Accessibility

High-quality CAD software often comes with significant costs, making it inaccessible for researchers or institutions with limited budgets. Licensing and maintenance fees, along with the need for powerful hardware, can further increase the overall expenses associated with using CAD software for morphometric analysis.

• Compatibility and Interoperability

CAD software may have compatibility issues with other software tools or file formats, making it challenging to integrate into existing workflows or collaborate with researchers using different software. Incompatibilities can hinder data sharing, collaboration, and reproducibility of the analysis.

• Lack of Standardisation

The absence of standardised protocols and guidelines for femur analysis using CAD software can lead to variations in measurement tech-

niques and data interpretation across different studies. This lack of standardisation makes it challenging to compare and combine results from different research groups, limiting the overall validity and reliability of the findings.

Despite these disadvantages, CAD software remains a powerful tool for morphometric analysis and measurements of the human femur. These drawbacks can be mitigated with proper training, careful data handling, and thorough validation of the results. Moreover, advancements in software development and improved standardisation efforts can address many of these limitations in the future.

2.2 Overview of 3D Skeletonization

In medical applications, 3D skeletonization refers to a computational technique that extracts a simplified representation of an object or structure within a 3D medical image. The goal of skeletonization is to derive a skeleton or central axis that captures the essential structure and connectivity of the 3D mesh.

Several existing skeletonization algorithms have been employed in medical applications. Here are three (3) commonly employed algorithms as illustrated in Fig. 2.5.

2.2.1 Distance-Transform Field Algorithms

The first major methods are the distance-transform field methods, also known as distance map or distance field with the following articles [90, 91]

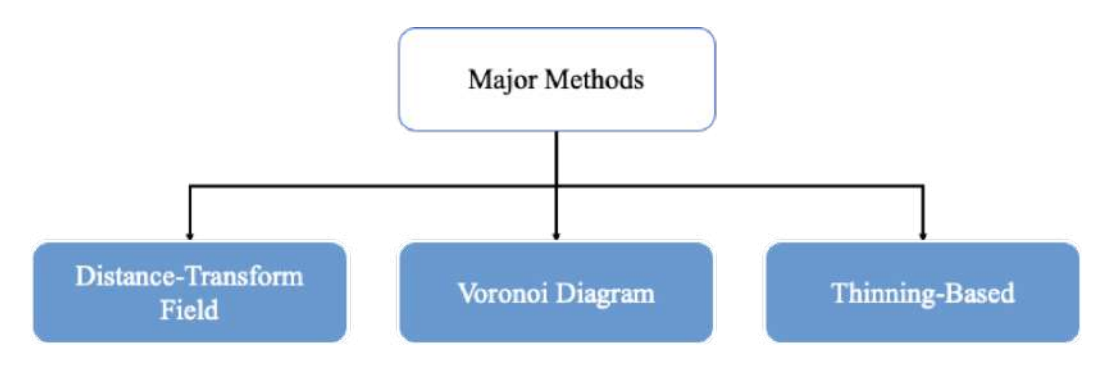


Figure 2.5: The three (3) major groups for existing 3D skeletonization methods.

in the year of 2007 and [77] in the year of 2011 respectively.

In the context of 3D skeletonization, distance-transform field refers to a method of extracting a simplified representation of a 3D mesh or structure within a 3D volume or mostly in voxels, using a distance transformation algorithm, such as Euclidean distance transform or the Chamfer distance transform (Refer to Chapter 6.4.3 for more details).

The basic concept for this algorithm is by calculating the distance from each voxel to the nearest points on the object's boundary, generating a distance-transform field. The resulting calculation is a scalar field where each voxel represents the shortest distance from that voxel to the 3D mesh's boundary.

The authors [90, 91] presented some techniques for precise skeleton extraction from 3D volumetric data using fast marching methods, by providing experimental evaluations using various volumetric datasets, including medical imaging data. These methods were effectively address the limitation of traditional approaches, which commonly exhibit voxel-level imprecision, leading to skeletons lacking sub-voxel accuracy.

Additionally, Arcelli et al. [77] introduced a method called "Distance-

Driven Skeletonization" for generating skeleton representation from voxel images, which are 3D images represented as a grid of voxels. Whereas, Milian et al. [216] have emphasised the generation of voxel models, which entails converting a surface into a volumetric representation where each voxel corresponds to a point within or in proximity to the surface.

These are the derived representation of digital images and the data structure are mostly in voxels. In a recent study, Vega et al. [217] conducted a comparative analysis, comparing CAD and voxel-based modelling methodologies, to simulate the mechanical behaviour of 3D printed scaffolds fabricated using extrusion-based techniques.

However, the distance-transform field method may encounter difficulties in accurately preserving the connectivity of complex structures. In cases where objects have thin or elongated regions, the method may struggle to capture the precise branching patterns or connectivity accurately. This can result in disconnections or inaccuracies in the skeleton representation.

Apart from that, the distance-transform field method is susceptible to noise and imaging artefacts present in the original volumetric data. These can introduce errors and distortions in the distance-transform field, affecting the quality and accuracy of the resulting skeleton.

These existing methods are also quite sensitive to boundary noise and can be influenced by the image resolution. Lower resolution images may result in lower precision and limited ability to capture fine details in the skeleton. Increasing the image resolution can help mitigate this issue, but it may also increase computational requirements.

2.2.2 Voronoi Diagram Based Methods

Voronoi diagram based methods in 3D skeletonization are techniques that utilise Voronoi diagrams to extract skeletons or centrelines from 3D volumetric data. Voronoi diagrams are geometric structures that divide a space into regions based on proximity to a set of input points or seeds.

In the context of 3D skeletonization, the Voronoi diagram is constructed using the voxels or points of interest within the volumetric data as seeds. It partitions the space into cells, where each cell represents the region that is closer to its associated seed point than any other seed point.

Various medical applications can benefit from these methods. For example, Naf et al. [80] discussed a technique for constructing 3D 3D Voronoi skeletons by representing anatomical structures as objects within a 3D grid. The Voronoi skeleton is generated by assigning seed points within the grid to represent organs or structures of interest. The resulting Voronoi diagram captures the spatial relationships and connectivity among the seed points.

In a different approach, Amenta and Bern [81] proposed an algorithm to construct the MAT of a given 3D point set. They utilised a union of ball technique, where each ball encompasses a subset of the input points. On the other hand, Siddiqi et al. [84] introduced a method for skeleton generation based on the Hamilton-Jacobi equation.

Tabb et al. [85] took advantage of two different skeletonization techniques, namely the Voronoi-based approach and the distance transformation method. By integrating these techniques, they aimed to achieve a balance between speed and accuracy in extracting skeletons from elongated objects encountered in real-world scenarios.

In their work, Ma et al. [82] presented a method for approximating the 3D MA points of an object. Their approach relied on utilising nearest neighbours and the normal field to achieve accurate approximation.

Lastly, Cheng et al. [83] proposed an approach to skeletonization that capitalises on the dual relationship between shape segmentation and skeleton extraction. They leveraged this duality to develop an effective method for skeletonization.

These methods are applied to various medical applications, such as analysing vascular structures, airways, neuronal pathways, and other anatomical features. By extracting skeleton using Voronoi diagram based methods, it becomes possible to quantify morphological characteristics, measure distances, analyse connectivity, and facilitate further analysis or simulations.

The Voronoi-based algorithm, however, has certain limitations that should be considered. Firstly, it can be sensitive to noise or irregularities present in the input data. When dealing with noisy or distorted data, the algorithm may generate spurious branches or incorrect skeleton topology, impacting the accuracy and reliability of the skeletonization process.

Additionally, the quality and accuracy of the Voronoi skeleton produced by this algorithm heavily rely on the placement of seed points within the 3D grid. Inadequate or improper selection of seed points can lead to incomplete or erroneous skeletonization, resulting in the loss of critical structural information.

Furthermore, the computational complexity of generating Voronoi dia-

grams in 3D should be taken into account. Particularly when working with large datasets or complex objects, the algorithm may require substantial computational resources and processing time. As a result, it may be less suitable for real-time or time-critical applications.

These limitations highlight the importance of considering the specific characteristics of the data and the application requirements when employing Voronoi-based algorithms for 3D skeletonization. Exploring alternative methods that address these challenges may be necessary in certain scenarios.

2.2.3 Thinning-Based

The Thinning-based skeletonization algorithm is a widely used technique in image processing and computer vision for extracting a simplified representation of objects or 3D meshes. This method aims to create a thin, centreline skeleton by iteratively reducing the width of the mesh until only a one-pixel wide skeleton remains. However, the removal of boundary voxels, known as simple points, during this iterative process can potentially impact the topology of the mesh.

Various studies have investigated different aspects of Thinning-based skeletonization. In the study by Roussopoulos et al. [218], the emphasis was on efficiently retrieving nearest neighbour information from a skeletonise image representation using graph-based algorithms. Telea et al. [86] employed a thinning process followed by level-set methods to extract centrelines from images, offering a means to capture the essential structure. Au et al. [87] proposed a technique that converts objects into mesh representations and applies contraction operations to extract a simplified and connected skeleton structure.

In the context of 3D objects represented by mesh models, Jin et al. [88] introduced an algorithm that combines a partial parallel 3D thinning algorithm with a 3D skeleton correcting algorithm. This approach allows for the extraction of skeletons with improved accuracy. Li et al. [219] proposed the Q-mat method, which involves fitting a quadratic function to sample points along the shape boundary. This technique was subsequently utilised by Lin et al. [89] in a 3D shape segmentation application, demonstrating its practical significance.

In their work, Ma et al. [82] presented a method that progressively reduces the radius of maximal tangent balls for each sample point and surface normal. This iterative process ensures that no other sample points are enclosed within the tangent balls. Building upon this work, Jalba et al. [220] introduced a Graphics Processing Unit (GPU)-based framework for extracting surface and curve skeletons from large meshes. Their approach, based on the ball shrinking algorithm proposed by Ma et al. [82], enables efficient skeleton extraction on GPU architectures, catering to the demands of processing substantial mesh data.

Overall, the Thinning-based skeletonization algorithm operate by iteratively removing the boundary voxels, or simple points, from a 3D mesh. This process involves peeling off these boundary voxels one by one. However, it is important to note that the removal of these boundary voxels can occasionally result in changes to the topology of the original 3D mesh. The altered topology may lead to the loss of structural information or introduce inaccuracies in the resulting skeleton representation.

Furthermore, another limitation of the Thinning-based methods is the

inability to preserve the connectivity of the skeletons of 3D meshes. As the thinning process proceeds and boundary voxels are removed, the connectivity between different parts of the skeleton may be compromised. This can result in disconnected or fragmented skeleton structures, where certain regions may become isolated from the main skeleton or lose their connectivity with other parts of the mesh.

Therefore, these limitations should be considered when applying Thinning methods in applications that require accurate preservation of topology and skeleton connectivity.

2.3 3D Skeletonization in Human Femur

3D skeletonization, also known as 3D thinning or 3D medial axis transformation, is a computational technique used to extract the skeletal structure or the central axis of a 3D mesh. It involves reducing the volumetric representation of a 3D mesh to its essential 1D or 2D skeleton while preserving its shape and connectivity.

The techniques for 3D skeletonization are constantly evolving, ranging from traditional algorithms based on distance maps, thinning, or graph-based methods to more recent approaches leveraging machine learning and deep learning methods. The choice of algorithm depends on the specific requirements of the application, the quality of the input data, and the desired accuracy and computational efficiency.

In the context of femur analysis and measurements, 3D skeletonization refers to the process of extracting the skeletal structure of the femur bone from its 3D representation obtained through imaging techniques such as CT or MRI or through implemented algorithm. Various skeletonization algorithm can be employed to extract the femur's skeletal structure. The resulting skeleton provides a simplified representation of the femur's central axis or core, which can be further analysed and measured for various purposes, including clinical diagnoses, surgical planning, anthropological studies, and forensic investigations.

To date, there have been two (2) noteworthy papers published in the realm of extracting skeletons from 3D human femurs, employing advanced 3D skeletonization techniques. Subburaj et al. presented a significant contribution in 2010 [1], while Gharenazifam et al. made another valuable contribution in 2014 [2]. These papers have significantly advanced the field by exploring effective methods for extracting skeletal structure from 3D representations of human femurs.

2.3.1 Computer-aided Methods for Assessing Lower Limb Deformities in Orthopaedic Surgery Planning [1]

The paper published in 2010 focuses on computer-aided methods used to assess lower limb deformities in orthopaedic surgery planning. It highlights the significance of accurate assessment and planning in orthopaedic surgeries, particularly for lower limb deformities. Traditional methods of assessment relied on manual measurements, which we were often subjective and prone to human error.

The paper introduced the use of computer-aided methods as a more reliable and objective approach. These methods involve the utilisation of advanced imaging techniques, such as X-rays and CT scans, to generate 3D models of the affected limb. These models can be analysed using specialised software to quantify and evaluate various parameters related to the deformity.

By employing computer-aided methods, orthopaedic surgeons can accurately measure and analyse deformities, including angular misalignments, leg length discrepancies, and joint orientations. Their proposed software facilitates precise measurements, allowing for a more comprehensive understanding of the deformity and enabling effective surgical planning.

The paper discusses several computer-aided techniques, such as image segmentation, landmark identification, and 3D reconstruction. It highlights their advantages over traditional methods, including increased accuracy, objectivity, and the ability to visualise complex deformities in three (3) dimensions.

In order to represent an anatomical axis in three (3) dimensions, it is necessary to have a 1D MA that resembles a line [79]. To achieve this, the researchers have devised a thinning skeletonization with distance control, which effectively generates the desired 1D MA of the bone [221]. This iterative process selectively eliminates the outermost surface layers of the object while maintaining its topological integrity, resulting in a slender medial structure.

However, as depicted in Fig. 2.6, we can observe that the extracted medial axis of the femur consists of spurious branches and additional artifacts that are not quite correspond to the true structure of the object. These spurious branches can complicate subsequent analysis or reconstruction tasks that rely on an accurate representation of the skeleton. Further-

more, this method has resulted in the loss of intricate features and fine details in the final output.

In conclusion, the paper emphasises the significance of computer-aided methods in the assessment and planning of lower limb deformities in orthopaedic surgery (Refer to Fig. 2.6). It highlights their ability to provide objective and accurate measurements, leading to improved surgical outcomes. The authors advocate for further research and collaboration to enhance these methods and their integration into routine orthopaedic practice.

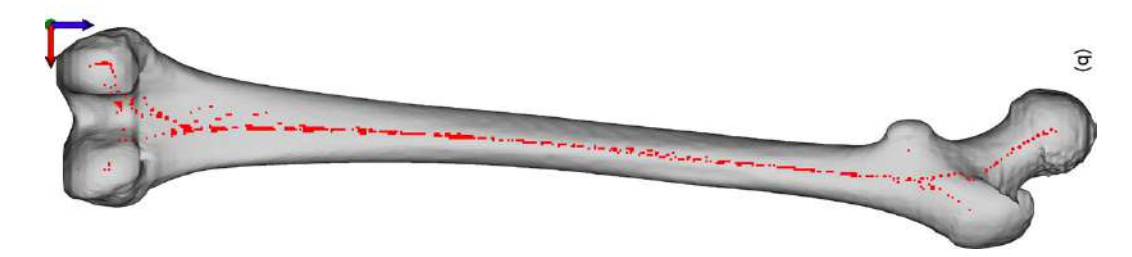


Figure 2.6: The generated MA with disconnected, noisy and spurious branches in [1].

2.3.2 Anatomy-based 3D Skeleton Extraction from Femur Model [2]

The paper published in 2014 focuses on the extraction of a skeleton from a femur model using anatomy-based approach. The researchers recognise the importance of accurately representing the skeletal structure of the femur for various medical applications and surgical planning.

The paper introduced a methodology that leverages anatomical knowledge to extract a reliable 3D skeleton from a femur model. The approach combines computational techniques with anatomical contraints to ensure the skeleton accurately reflects the underlying anatomical structure of the femur.

To extract the femur's skeleton, the authors employ a multi-step process. They begin by segmenting the femur model from medical imaging data, such as CT scans. Subsequently, they apply a series of algorithms to identify anatomical landmarks and determine the bone's principal axes and regions of interest.

The estimation of the femur shaft axis was achieved through the utilisation of PCA, which played a vital role in this process. PCA is a statistical technique used to identify the main directions of variation in a dataset. In the context of estimating the femur shaft axis, PCA analyses the geometric features of the femur model to determine the primary direction of variation, which corresponds to the axis of the femur shaft.

By applying PCA to the femur model, the algorithm identifies the principal components that capture the most significant variations in the data. These principal components represent orthogonal direction in the 3D space and are ranked based on the amount of variance they account for. The principal component associated with the highest variance is considered as the estimated femur shaft axis.

However, the drawback of PCA in the context of 3D skeletonization is its reliance on linear relationships between variables, as depicted in Fig. 2.7. PCA assumes that the relationships between the variables being analysed are linear, which may not hold true in the case of complex skeletal structures.

In 3D skeletonization, the goal is to extract a simplified representation of the skeletal structure from volumetric or point cloud data. PCA, being a

linear dimensionality reduction technique, may not adequately capture the intricate and non-linear relationships present in the 3D data.

The skeletal structure often exhibits complex geometry, with varying curvatures, branching patterns, and connectivity. These non-linear characteristics are not well-captured by PCA, which is more suited for linear transformations and variance maximisation.

Moreover, PCA does not explicitly consider the specific properties and constraints of the skeletal structure during the dimensionality reduction process. It treats all points or features equally and does not leverage the inherent structural information present in the skeleton.

Therefore, when applying PCA to 3D skeletonization, it's worth noting that the choice of a skeletonization algorithm for human femur analysis depends on factors such as the specific research objectives, characteristics of the data, desired accuracy, computational efficiency, and availability of labeled training data (in the case of deep learning-based methods). Researchers often compare and evaluate different algorithms to determine the most suitable one for their specific applications.

Overall, 3D skeletonization plays a vital role in femur analysis by providing a simplified representation of the femur's skeletal structure, enabling accurate measurements and detailed anatomical analysis that contribute to medical and scientific investigations.

Table 2.2 presents a summary table highlighting the strengths and weaknesses of existing skeletonization methods compared to our approach.

Upon examination of the table, it's evident that our approach excels in preserving both connectivity and topological information within the obtained skeleton.

Additionally, the implementation is simpler than the existing methods.

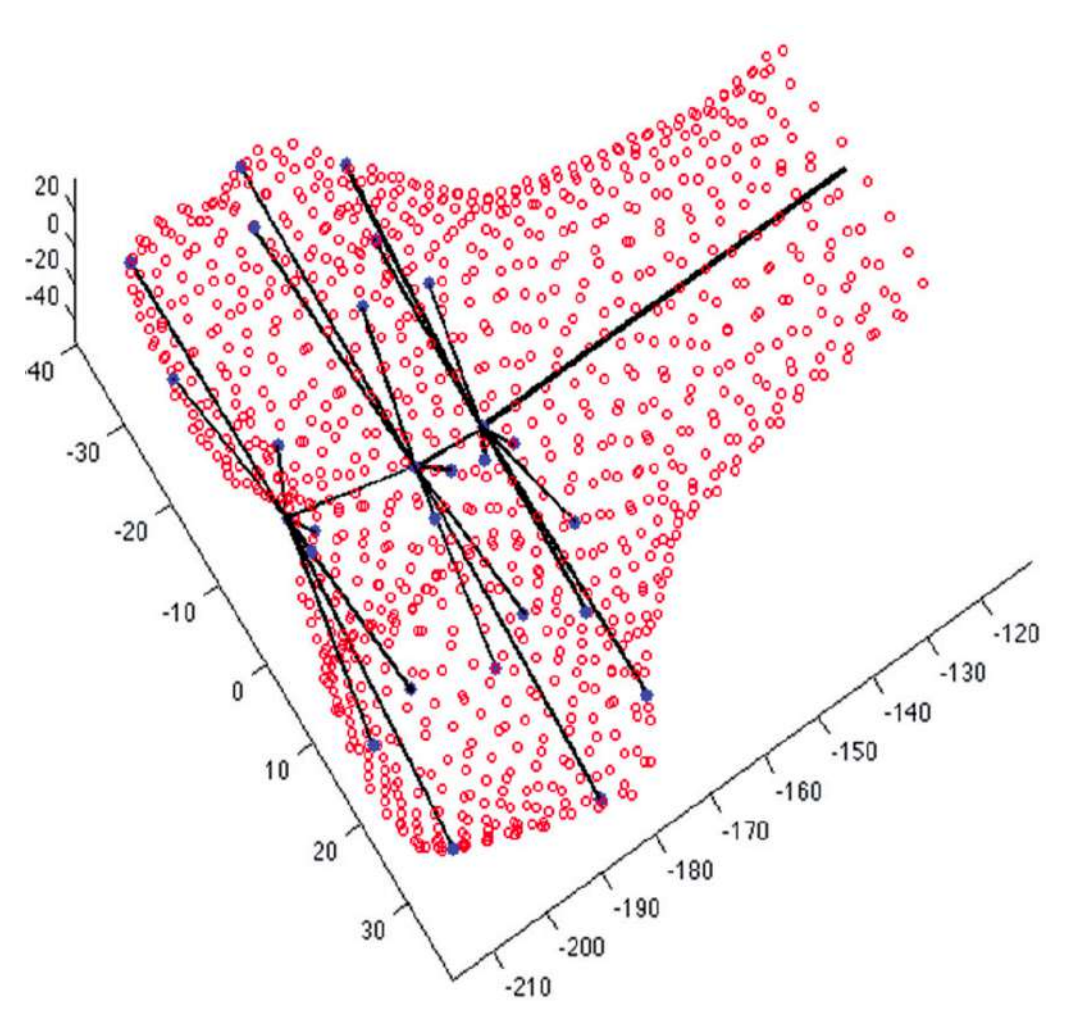


Figure 2.7: The generated MA with spurious branches in [2].

Table 2.2: A comparison table for the related 3D skeletonization research in human femur.

No.	A	ttributes	ributes Distance-Transform Field Voronoi		i Diagram	iagram Thinning-Based				PCA	MMCA (Our Approach)		
1	Paper		[90]	[77]	[80]	[82]	[86]	[87]	[88]	[1]	[2]	[140]	[141]
2	Year Published		2007	2011	1997	2012	2003	2008	2017	2010	2014	2019	2022
3	3 Focused Part		Aorta, renal and mesenteric arteries	2D Images	3D Organ Shape	Other 3D Meshes	Other 3D Meshes	Other 3D Meshes	Other 3D Meshes	Lower Limb	Human Femur	Human Femur	Human Femur
4	Strengths	Preserve Connectivity	×	×	✓	✓	×	✓	×	✓	~	~	✓
		Preserve Topological Information (avoid spurious skeletal branches)	Δ	Δ	Δ	Δ	Δ	Δ	Δ	×	Δ	~	✓
		Simple	×	×	×	×	×	×	×	×	×	~	✓

Chapter 3

ALGORITHM OVERVIEW

As highlighted in Chapter 1, this research aims to answer two (2) research questions. Our methodology aims to address the first question which is "How to perform 3D skeletonization on the given femur 3D mesh data?".

We named our system as 3D-FSA, which stands for 3D-FSA and there are four (4) key modules in the implementation as illustrated in Fig. 3.1:

- A. Pre-processing
- B. 3D Femur Construction
- C. 3D Skeletonization
- D. Results Evaluation

Since this is a collaborative research, the Pre-processing module was executed by researchers from South Korea and the results were shared with us for computation in the subsequent modules as shown in Fig. 3.2. Apart

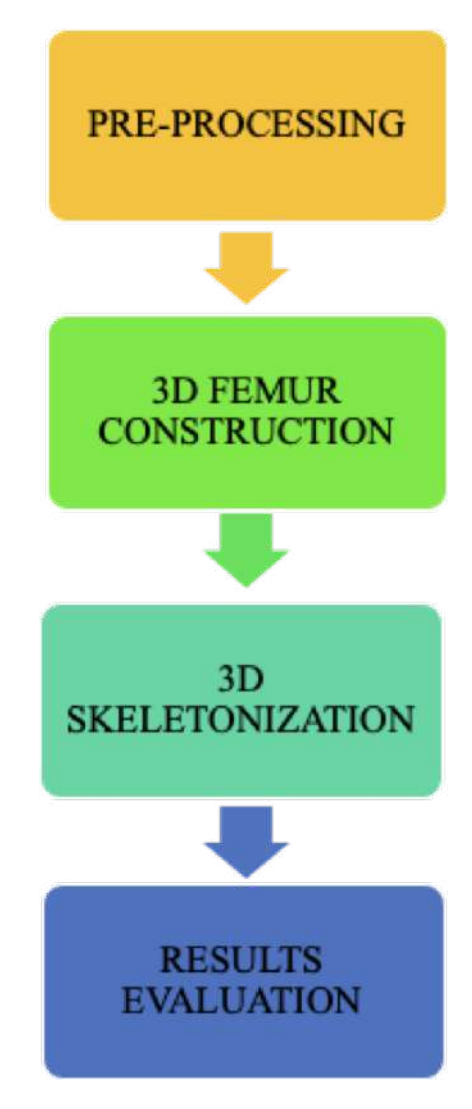


Figure 3.1: Overview of our proposed algorithm.

from that, they utilized our 3D-FSA system for aiding in shape and anatomical analyses of the human femur related to bowing and width throughout life [16].

For my contribution, I actively participated in implementing the second (2^{nd}) phase, third (3^{rd}) phase and fourth (4^{th}) phase. The brief overview of these modules will be explained in Chapter 3.1, Chapter 3.2 and Chapter 3.3 and Chapter 3.4.

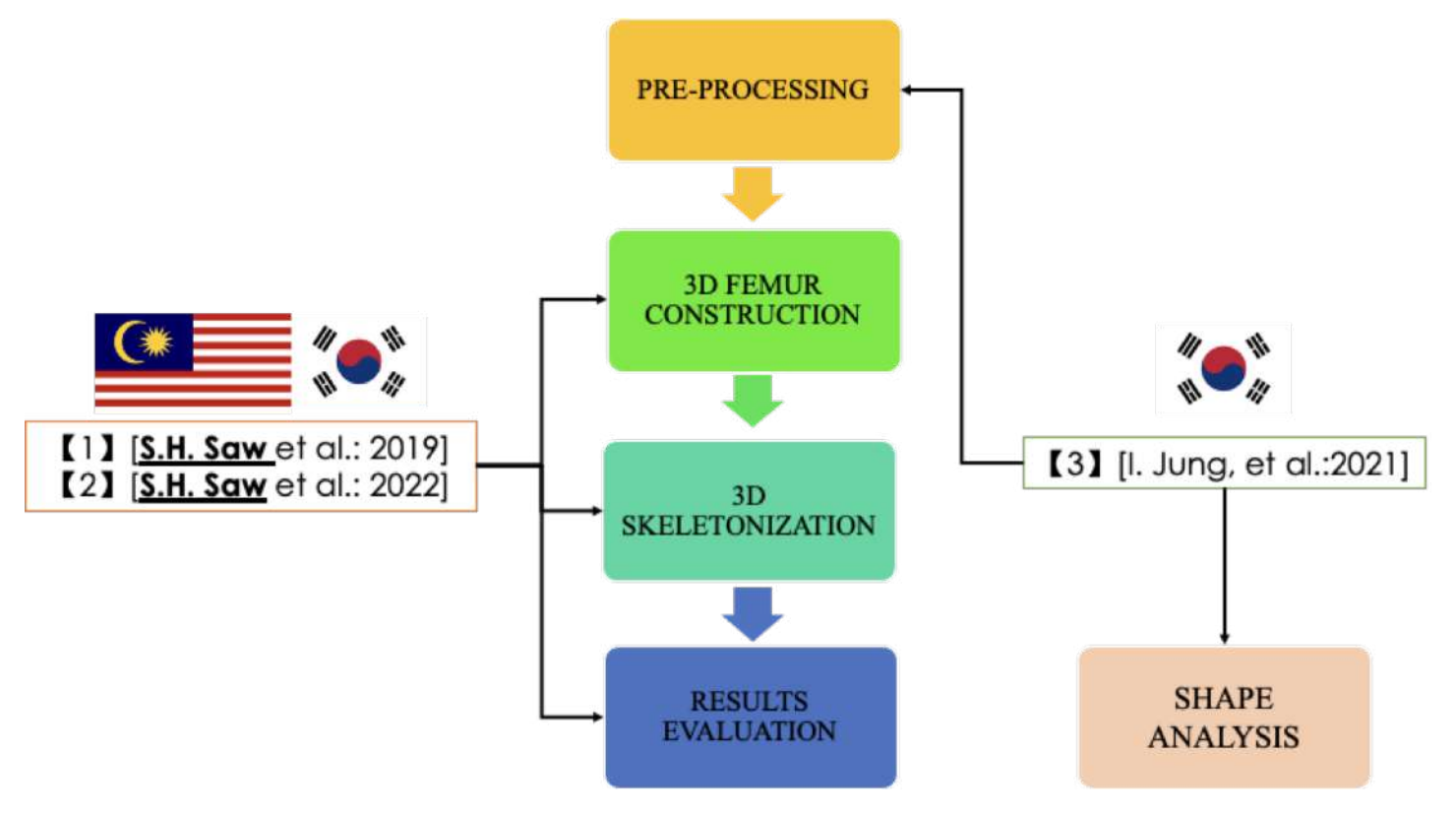


Figure 3.2: We are responsible for the implementation of three (3) phases: 3D Femur Construction, 3D Skeletonization and Results Evaluations. Whereas, the researchers from South Korea [16] are responsible for the implementation of two (2) phases: Pre-processing and Shape Analysis.

3.1 Pre-processing

In pre-processing phase involve a collection of of CT-scan images was introduced into AVIEW Modeler, which is a 3D modelling software, that generates 3D representations of anatomical features within the human femur.

By employing reconstruction and parametrisation on these datasets, structured data was segmented into .obj file format. These .obj file format encapsulate details about the geometry of 3D femurs.

The elaboration on the specifics will be provided in Chapter 4.

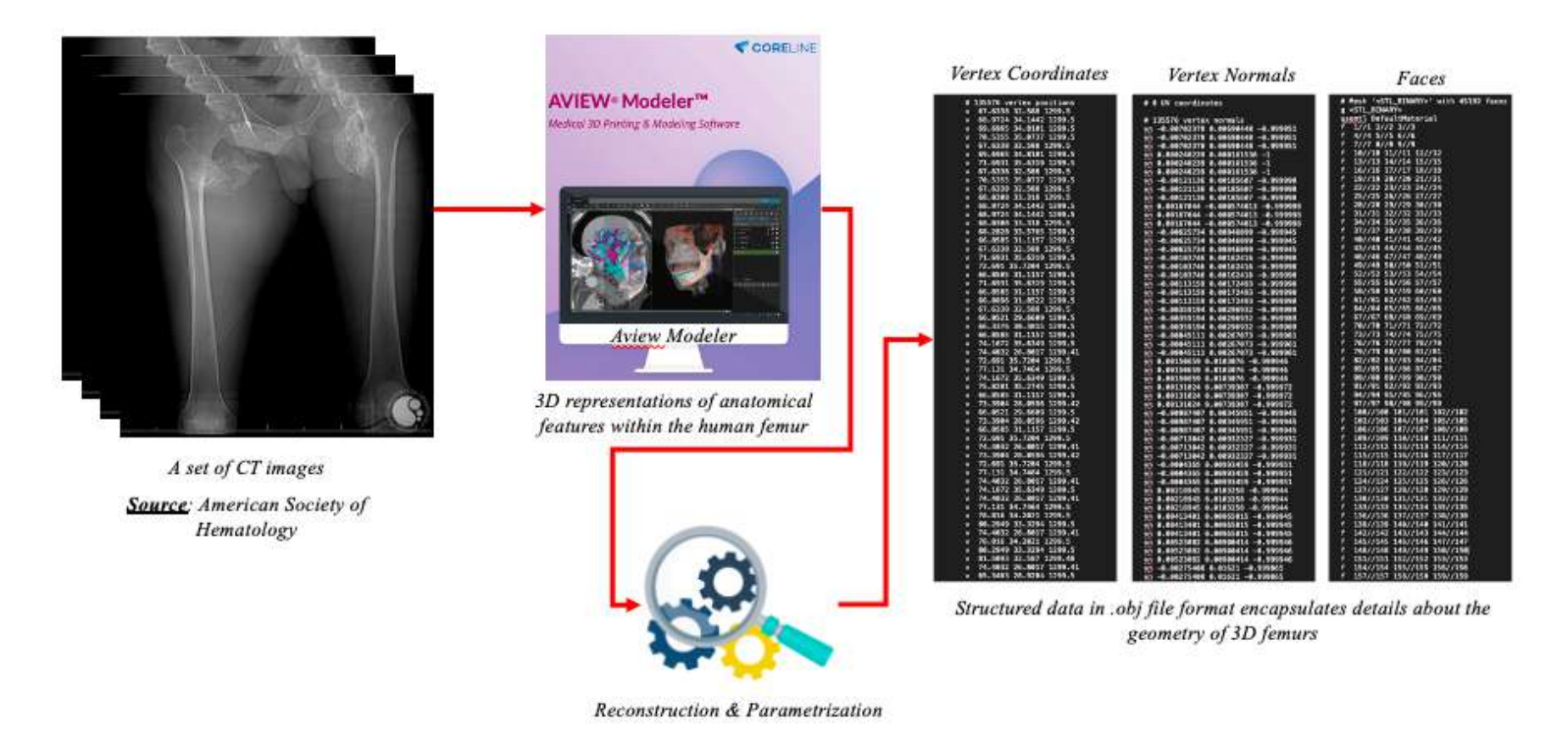


Figure 3.3: A concise overview of the initial phase, specifically the First Phase (1^{st}) , with a focus on the pre-processing stage.

3.2 3D Femur Construction

Subsequently, in the Second Phase (2^{nd}) , emphasis will be placed on the creation of the 3D femur, detailing the involved processes illustrated in Fig. 3.4.

We employed the .obj files obtained during the pre-processing phase. By adhering to the procedures outlined in Fig. 3.4, we have precisely rendered the 3D femur, showcasing its structural intricacies through vertices (Fig. 3.6a), edges (Fig. 3.6b), and faces (Fig. 3.6c).

Based on Fig. 3.5, the pivotal development tools that collaboratively contribute to the functionality of our 3D-FSA system include Visual Studio, OpenGL Mathematics (GLM), OpenGL, and Microsoft Foundation Class (MFC).

Details pertaining to this phase will be expounded upon in Chapter 5.

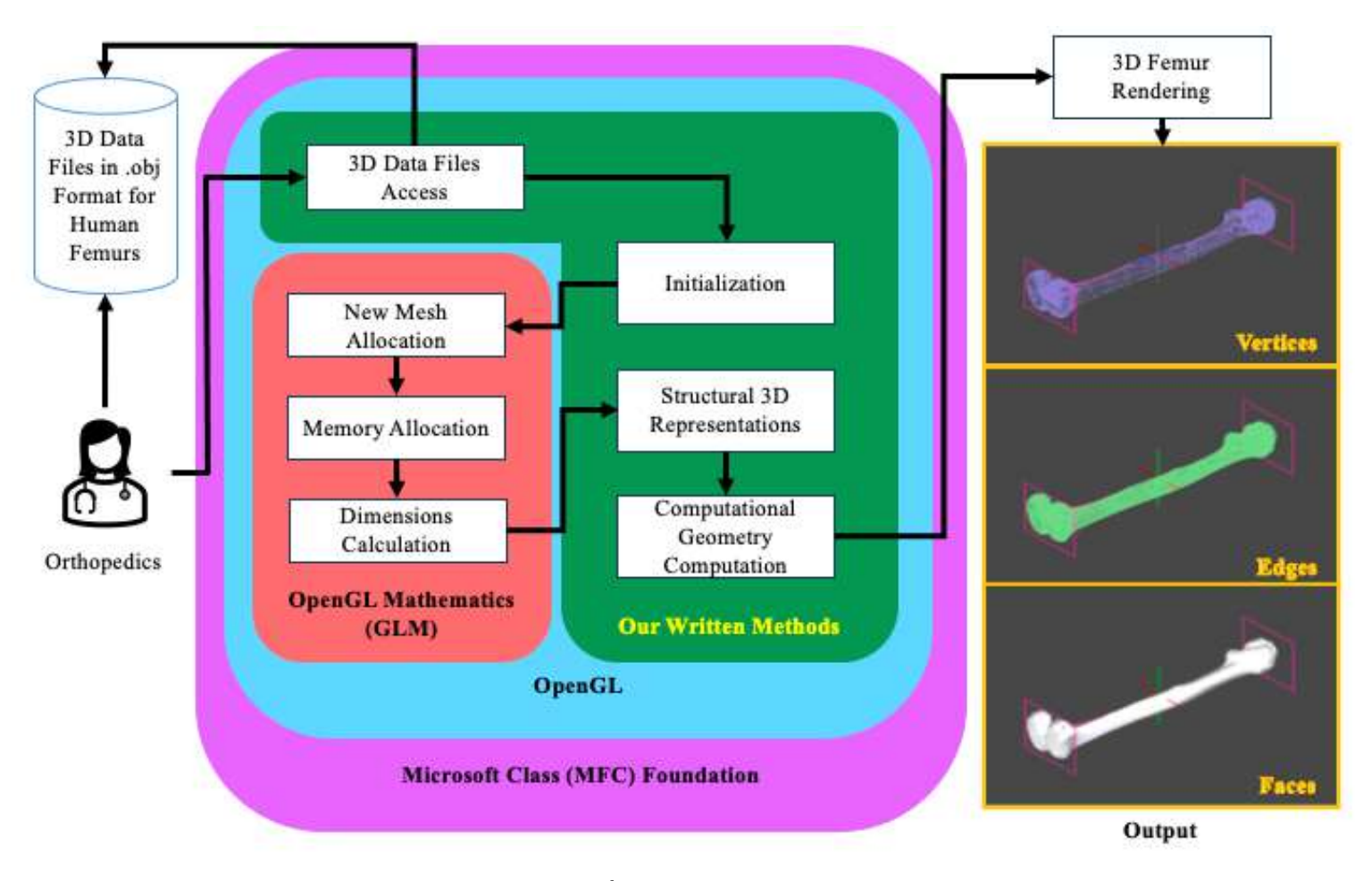


Figure 3.4: A succinct summary of the Second Phase (2^{nd}) , highlighting the stage dedicated to the construction of the 3D femur.



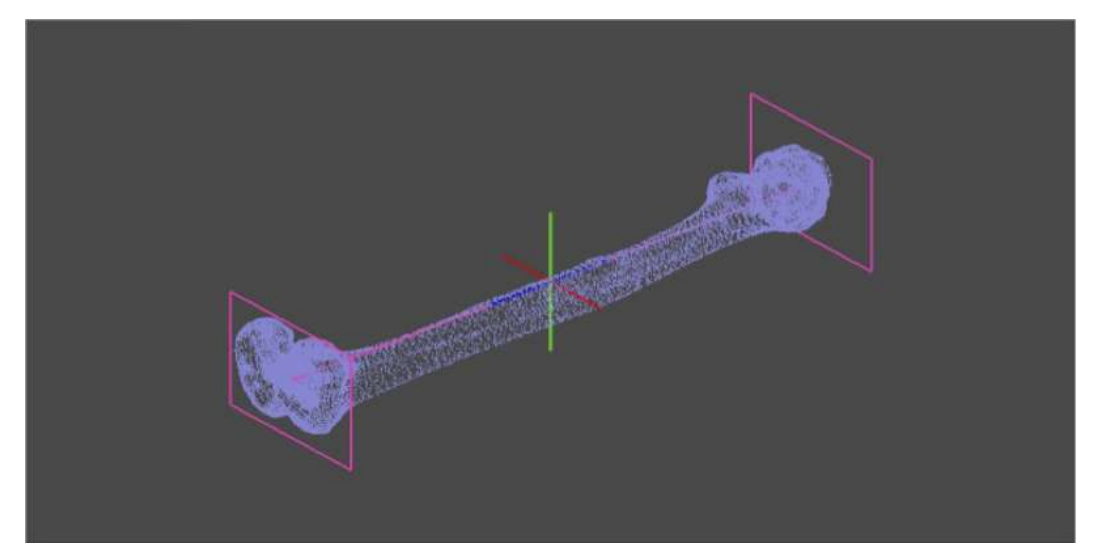
Figure 3.5: The crucial development tools collectively contribute to the functionality of our 3D-FSA system.

3.3 3D Skeletonization

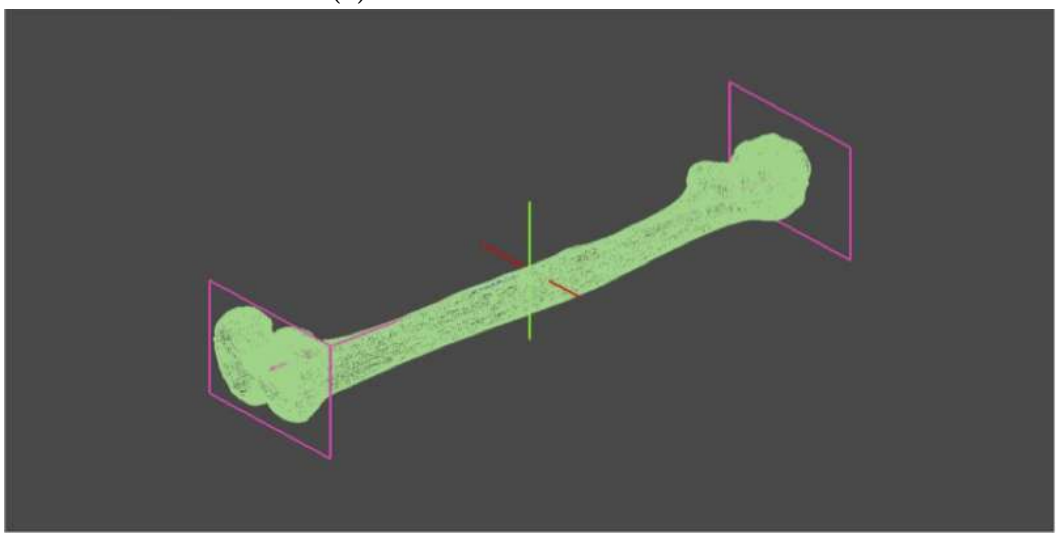
The subsequent step involves the 3D skeletonization phase. The outcome of this module is referred to as the skeleton or the MA as explained in Chapter 1.

The MA, based on the MAT, mainly includes the MA itself and the radius function.

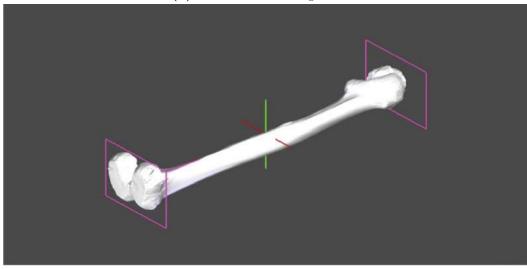
In this module, the fundamental concept is to build both a base plane and a projection plan as illustrated in Fig. 3.7.



(a) 3D left femur in vertices view.



(b) 3D left femur in edges view.



(c) 3D left femur in faces view.

Figure 3.6: The 3D human femur can be displayed in faces view, edges view, and vertices view in our system, 3D-FSA.

After constructing the 3D femur, cylindrical slider, s is introduced. This slider traverses the entire femur, processing specific data portions. The information contained within the slider will be projected onto the projection plane for additional computation.

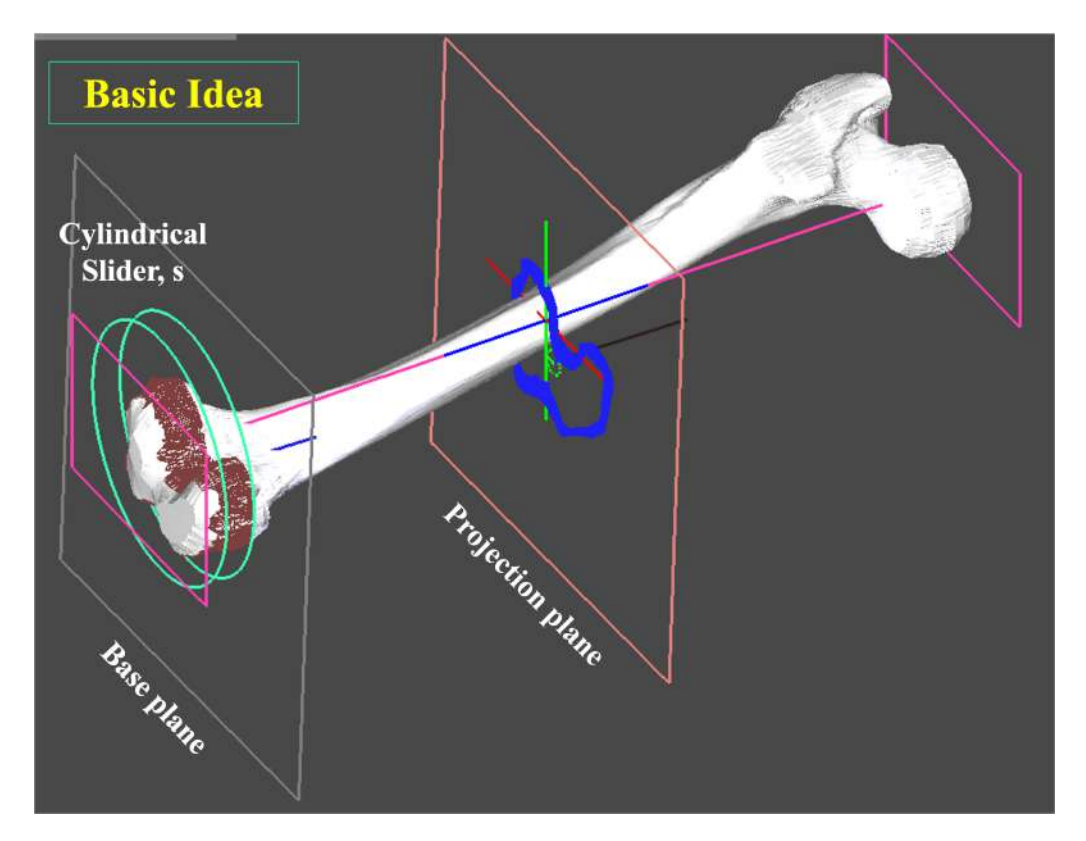


Figure 3.7: The crucial development tools collectively contribute to the functionality of our 3D-FSA system.

The concise elucidation of the internal processes is provided below, complemented by the visual representation in Fig. 3.8.

- A Faces within each cylindrical slider contribute to computing a weighted average vertex, which is equivalent to the medial centre. The MA takes form by connecting all these computed weighted average vertices.
- B Concurrently, the weighted normal of faces within the segment are used, employing the least square plane fitting, to compute the projec-

tion plane.

- C Simultaneously, the centroid of faces and the weighted average vertex are projected onto the projection plane, creating an inner slice polygon, Ω_S . With these data, our **maximum-minimum centre** approach (Summarized in Chapter 3.3.1) is applied to determine the optimal radius value and the maximal inscribed circle for that specific portion.
- D Additionally, the thickness of the outer medullary canal, or the compact bone, is computed using the Chamfer distance.
- E Finally, the minimum radius angle is calculated using the least squares fitting of the circle, providing the radius of curvature.

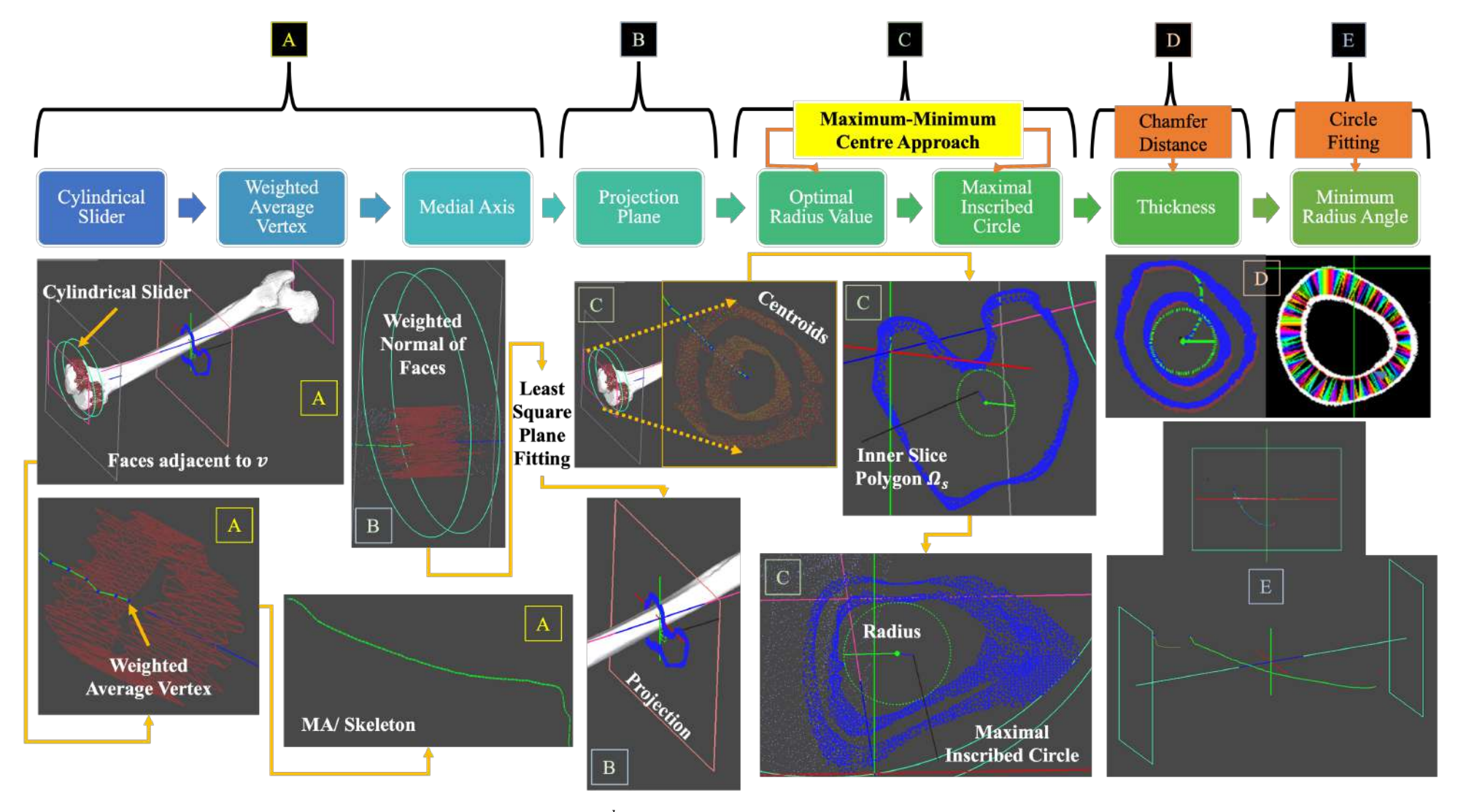


Figure 3.8: A brief overview of the Third Phase (3^{rd}) , emphasising the steps devoted to the skeletonization of the 3D femur.

3.3.1 Maximum-Minimum Centre Approach

The process involves calculating radii r, by generating a set of sample points forming a square shape. Starting from a sample point c_1 , our algorithm compares the distance from another sample point c_2 with the projected vertices in Ω_S , saving only the minimum distance minDist during each comparison. This iterative comparison continues for all projected vertices in Ω_S .

Subsequently, another sample point c_2 is chosen, and the maximum value maxDist is selected among the minDist values from the comparisons with all projected vertices.

In conclusion, maxDist represents the optimal distance from the projected weighted average vertex to the medullary canal boundary. The radius r of the square formed by the generated sample points is then calculated using a specific formula (Elaborated in detail in Chapter 6.4.2). This calculated r is utilised to render the medial circle what forms the maximal inscribed circle $B_s(p,r)$) within the selected portion of the cylindrical slider s.

Our methodology is labeled as the maximum-minimum centre approach for determining the maximum inscribed circle within the medullary canal contour, as illustrated in Fig. 3.9.

This phase will be elaborated upon in Chapter 6.

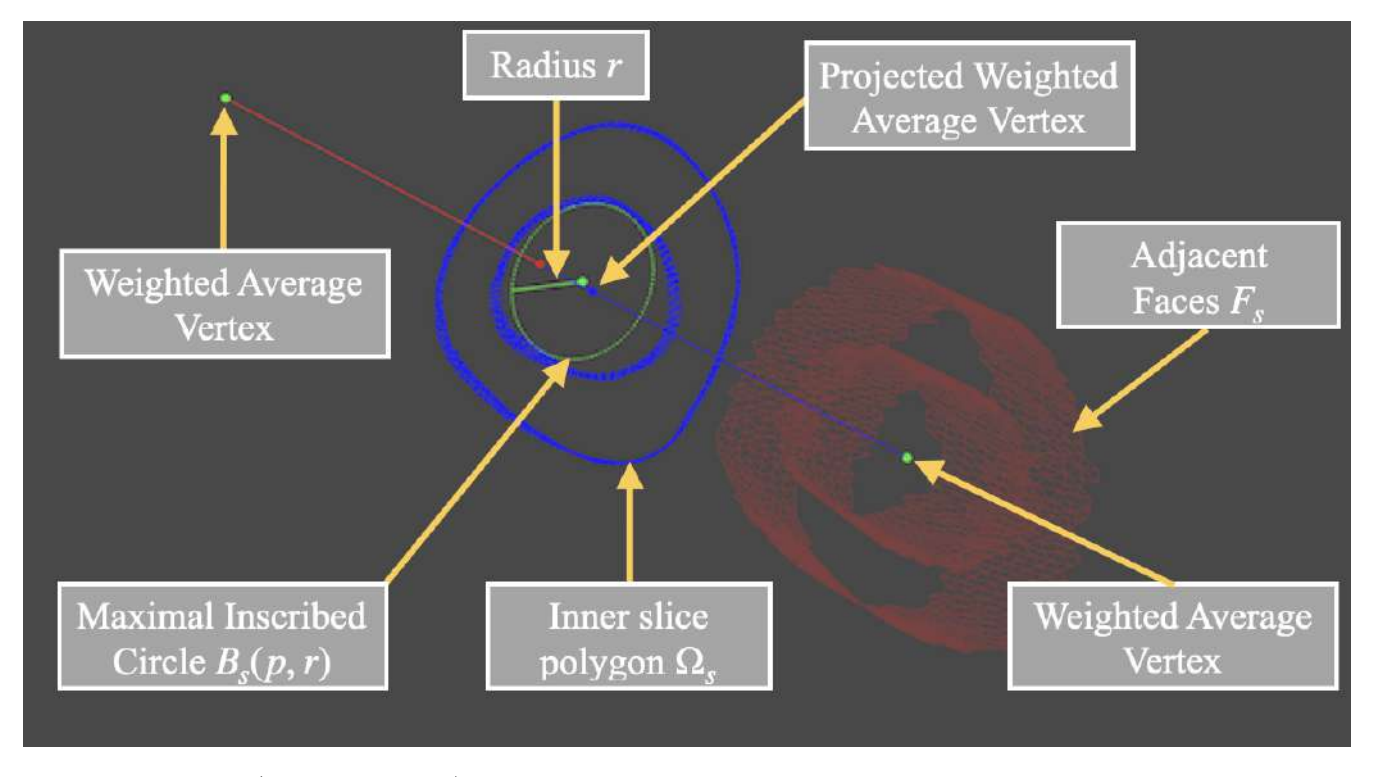


Figure 3.9: Weighted average vertex (green in colour), inner slice polygon Ω_s which consists of the projected centroids of the faces (triangles) in F_s (blue in colour), maximal inscribed circle $B_s(p,r)$ with radius r (green circle and radius).

3.4 Results Evaluation

This phase will provide insights to address the second research question which is "How is the resulting skeleton or medial be used as an analysis study for the anatomical and geometrical parameters of the femoral shaft?".

Our system generates seven (7) significant parameters, encompassing the following:

- A. Femur Length
- B. Femoral Shaft Length
- C. Femur Width
- D. Femur AP Length
- E. Diameter of Medullary Length
- F. Thickness of the Compact Bone
- G. ROC

Jung and his team from South Korea used our system in their study analysing femoral geometric differences related to bowing and width. Their results indicate good reliability based on the guidelines set by [139], and were published in the Osteoporosis International journal in 2021. For comprehensive information regarding their research, kindly refer to [16].

Apart from that, a comprehensive result evaluation was conducted by comparing the Thinning-based method [222, 22, 223] with our approach (MMCA) using the data obtained from the Korean side.

As depicted in Chapter 7, the skeleton generated by the Thinning-based method tends to exhibit numerous spurious branches, whereas our obtained skeletons are straight and simple. Therefore our method exhibited improved outcomes with better connectivity preservation and simplicity.

Further insights into this phase will be provided in Chapter 7.

Chapter 4

PRE-PROCESSING

This module plays an important role in preparing the 3D file formats for human femurs, in order to be read and processed in our 3D-FSA system.

4.1 The Innovation of this Module

The collected femur data in the form of 3D .obj file format requires two (2) conversion processes that deploy the theoretical innovation. The first conversion process acquired a list of CT scan that are saved in the DICOM format, then these files were imported into the commercially 3D modelling software namely, AVIEW Modeler by Coreline Soft Company in South Korea [13] to produce 3D samplings of anatomical elements of the human femur in Stereolithography (.stl) format.

These constructed datasets were then segmented and converted to the format of .obj files by applying the concept of 3D reconstruction [23] and parametrisation [27] to form a 3D femur mesh representing both the bone surface and the corticocancellous interface.

Although the existing research [212, 214, 215] consists of the first con-

version process by using AVIEW Modeler [13], but none of them includes the second conversion process. The results produced by this process have an impact in shape analysis and processing, especially to our system. This breakthrough in computer graphics was novel and useful in that it facilitates the prototype developments of 3D and computer graphics related projects.

4.2 My Tasks

Since this is a collaborative research project, my tasks in this module are as follows:

- To understand the basic concepts of data collection [16], imaging devices and the diagnostic of femur shaft fractures.
- To recognise the structures and the definitions of the obtained 3D data files in .obj format.

4.3 The Study Subjects for 3D-FSA

Researchers from South Korea [16] have collected a number of fully CT scan of both femurs from the participating centre that was approved by the Institutional Review Board of South Korea. These samples were randomly collected between 2015 and 2017 at a single centre with the following criteria:

• Total Participants: 1400 participants (2800 femurs)

• 20 years old \leq Age \leq 89 years old

• Femur Conditions: No implants, No deformity, or No surgical history

• Sex: Female or Male (100 participants were selected randomly)

• Ethnic: Korean (Asian)

Apart from that, the subjects with any implant, deformity, or surgical history of the femur were excluded. Among the 1400 participants, 100 participants were randomly selected for each decade and sex. The ethnic composition is 100% Korean which generally represents Asian.

4.4 The Common Types of Diagnostic Imaging Device

There are mainly three (3) common types of diagnostic imaging devices used by the doctors and orthopaedics for the diagnosis of fractures and the planning in surgery. There are the X-rays, CT scans and MRI tests. Each imaging test uses different technology to create images.

Table 4.1 provides the possible modalities, the purposes and etc for these imaging tests [3, 4, 5].

Table 4.1: The overview of three (3) common types of diagnostic imaging devices extracted from [3, 4, 5].

Modalities	X-rays	CT Scans	MRIs
Accessibility	Also called a radiographs, send radi-	CT Scans use a series of X-rays to cre-	MRIs use magnetic fields and radio
	ation through body. They are quick	ate cross-sectional images of the body,	waves to create detailed images of
	and painless tests that produce white	including bones, blood vessels, and soft	organs and tissues in the body.
	(soft tissues allow the radiation to pass	tissues.	
	through), grey and black (areas with		
	high levels of calcium, e.g., the bone		
	block the radiation) images.		

continued on next page

Table 4.1 – Continued from previous page

Modalities	X-rays	CT Scans	MRIs
Used to Diagnose	Patients with the following injuries:	Patients with the following severe	Patients with the following injuries:
	• bone fractures	injuries:	• aneurysms
	• arthritis	• injuries from trauma	• Multiple Sclerosis (MS)
	• osteoporosis	• bone fractures	• stroke
	• infections	• tumors and cancers	• spinal cord disorders
	• breast cancer	• vascular disease	• tumors
	• swallowed items	• heart disease	• blood vessel issues
	digestive tract problems	• infections	• joint or tendon injuries
		• used to guide biopsies	

continued on next page

Table 4.1 – Continued from previous page

Modalities	X-rays	CT Scans	MRIs
What to Expect	Patient will lie, sit or stand while the	Patient will lie on the a table that slides	Patient lie on a table that slides into
	X-rays machine takes images. He/ she	into the scanner, which looks like a	the MRI machine, which is deeper
	may be asked to move into several pos-	large doughnut. The X-rays tube ro-	and narrower than a CT scanner. The
	itions.	tates around the patient to take images.	MRI magnets create loud tapping or
			thumping noises.
Imaging Method	ionizing radiation	ionizing radiation	magnetic waves
Duration	10 - 15 minutes	10 - 15 minutes	45 minutes - 1 hour
Output Creation	2D images	3D images	3D images
Radiation Expos-	Yes	Yes	No
ure			

continued on next page

Table 4.1 – Continued from previous page

Modalities	X-rays	CT Scans	MRIs
Resolution (Level of Detail in the Images)	Low	Average	High
			N
Cost	Cheapest	Average	Most expensive
Not Recommended	Pregnant women has to handle with precautious.	Children or those who require multiple scans.	Patients with metal implants or pacemakers.

4.5 The Diagnostic of Femur Shaft Fracture

The diagnosis of the femur shaft fracture has to be acquired by the doctors and orthopaedics. It begins with the visual inspection by looking for bruises, an obvious deformity of the thigh or leg and tears in the skin. Then, they will check the tightness of the skin and muscles around the thigh. In order to learn in-depth about the injury, diagnostic imaging devices are used. X-rays are the most common imaging device to evaluate whether the femur is intact or broken. They can also show the type of fracture and the location of the fractured femur [37, 224].

Nevertheless, if the fractured femur is not spotted in X-rays due to its low sensitivity [225], but clinically suspicious by the doctors and orthopaedics, CT-scans are carried out to obtain valuable information about the severity of the fracture and preoperative surgery planning. It combines a series of X-rays images taken from different angles around your body and uses machine's computer to generate cross-sectional images, or "slices" of the bones, blood vessels and soft tissues inside your body. Once a number of successive slices are collected by the machine's computer, they can be digitally stacked together to form a 3D image of the patient [226]. CT scans provide more detailed information than plain X-rays do regardless of very thin fracture lines.

However, as mentioned in Section 1.1, femoral shaft fractures are beyond the scope of this research, hence, the details of these topics will not be included in this thesis.

Contrarily, MRI is carried out when the diagnosis of organs and tissues in the human body are required. It provides better soft tissue contrast and is able to differentiate among the fats, water, muscle, and other soft tissues. Although several studies suggested that MRI has a superior sensitivity for fractures, [227, 228, 229] proved that the use of CT scan has improved the detection accuracy of fractures among the elderly patients. [230, 231] also suggested that CT scan has the adequacy to rule out hip and pelvic fractures and it also be preferable to MRI based on decreased time spent in the Emergency Department (ED) due to the large percentage of elderly patients with contraindications to MRI.

4.6 3D Data Files Collection

I have received twelve (12) 3D files in .obj format from Professor Lee Byung-Gook (my external co-supervisor) which are related to human femurs in 3D structures for three (3) different patients, with three (3) respective codes as follows:

- 0123964
- 0346688
- 00486295

You may refer to Fig. 4.1, Table 4.2 and Table 4.3 for these files.

Table 4.2: The six (6) 3D files in .obj format for the left femurs.

	Left Femur	
Patient	With	Without
Code	Intramedullary	Intramedullary
	Canal	Canal
0123964	0123964_L_all.obj	0123964_L_outside.obj
0346688	0346688_L_all.obj	0346688_L_outside.obj
00486295	00486295_L_all.obj	00486295_L_outside.obj

Table 4.3: The six (6) 3D files in .obj format for the right femurs.

	Right Femur	
Patient	With	Without
Code	Intramedullary	Intramedullary
	Canal	Canal
0123964	0123964_R_all.obj	0123964_R_outside.obj
0346688	0346688_R_all.obj	0346688 _R_outside.obj
00486295	00486925_R_all.obj	00486925_R_outside.obj

The details of the .obj 3D file structures will be discussed in Section 4.8.

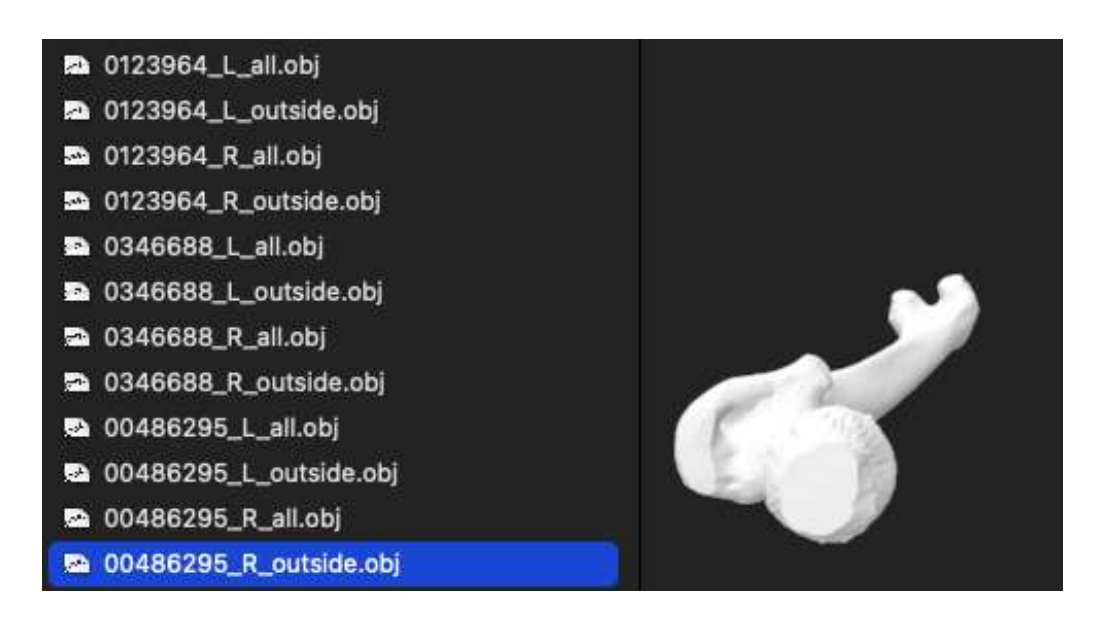


Figure 4.1: The twelve (12) femur .obj files and its illustration.

The researchers from South Korea [16] acquired a list of CT scans that are saved in DICOM format. CT scans are better at imaging bones and DICOM files is commonly used in 3D mesh reconstruction and computer graphics visualisation. It allows the doctors and orthopaedics acquire insight knowledge of the femura natomy and appropriate treatment for patients' injury [232].

The acquired CT scans are then imported into a commercially medical 3D imaging software (AVIEW Modeler by Coreline Soft, South Korea [13]) to produce a set of 3D samplings of anatomical elements of the human femur. By using the reconstruction and parametrisation methods on these datasets, the structure data of .stl format is formed and then converted into .obj formats that represents both the bone surface and the corticocancellous interface.

There are many software companies that have been established to specialise in Medical Image Processing (MIP), and AVIEW Modeler [13] is one of them and it is an all-in-one modelling software that models a desired part in CT or MRI images and convert into an .stl file for 3D printing. It has

been used by several medical researchers [212, 214, 215] for the conversion from CT-images to 3D data formats. Thus, the performance is satisfactory and reliable.

The researchers involved are from South Korea and they are I. J. Jung (University of Ulsan College of Medicine, Seoul), E. J. Choi (Department of Orthopaedics, Asan Medical Centre, Seoul), B. G. Lee (Division of Computer Engineering, Dongseo University, Busan) and J. W. Kim (Department of Orthopedic Surgery, University of Ulsan College of Medicine, Asam Medical Centre, Seoul).

4.7 Geometric Parameters (GP)

Before we explored further about this module, we are required to first understand the concepts of the geometric parameters, followed by the structures of .obj file, to enhance the understanding of the program implementation which is explained in Chapter 5.

4.7.1 Vector

Fig. 4.2a shows an example of two vectors, \vec{A} and \vec{B} . A vector is any quantity, such as force, that describes both a magnitude (length) and a direction. This parameter is critical in computer graphics and geometry.

4.7.2 Normal

A normal is the common term used in computer graphics and geometry. It is used to describe the orientation of a surface of a 3D mesh at a point on that surface. Technically, the surface normal to a surface at point p as shown in Fig. 4.2b. It can be seen as the face normal because the normal is the same for the entire face, regardless of any point on the triangle face.

Normals play a central role in shading [28], which are used to determine the brightness, and the amount of light it reflects from a 3D mesh surface, or the amount of light it reflects from the 3D mesh surface [233]. Thus, the effect of shading provides a more realistic and 3D quality.

For a 3D mesh that is made of triangles, each triangle defines a plane and the vector perpendicular to the plane is the normal of any point lying on the surface of that triangle. The vector perpendicular to the triangle plane can be easily be obtained with the calculation in Eq. (4.1) and Eq. (4.2).

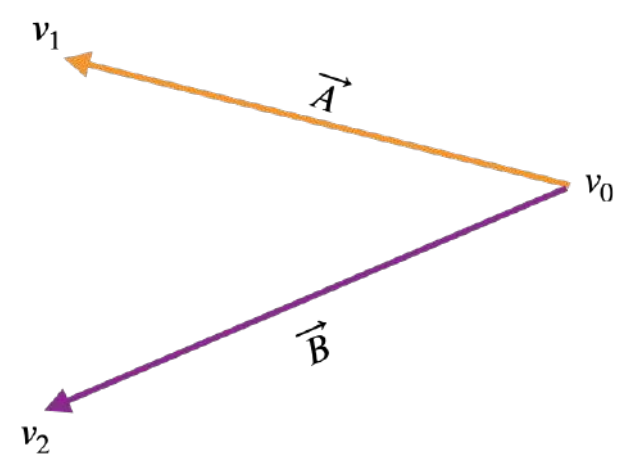
A unit normal vector is a vector with magnitude 1 that is perpendicular to the triangle plane (Refer to Eq. (4.4) for the formula).

4.7.3 Cross Product

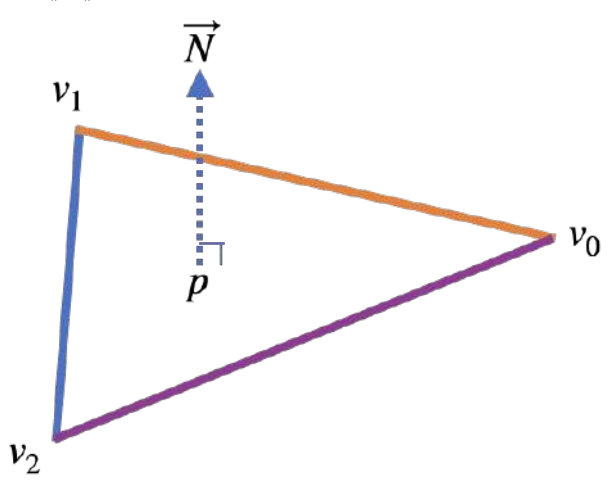
It is a binary operation on two vectors in 3D space. Two vectors are multiplied using the cross product operation denoted by, $\vec{A} \times \vec{B}$. The resulting vector is another vector \vec{N} that is perpendicular to both vectors as shown in Fig. 4.3. The followings defined the steps involved to calculate the cross product given the triangle points: v_0 , v_1 and v_2 :

A. Compute the two vectors for (v_0, v_1) and (v_0, v_2) :

$$\vec{a(x)} = v_1(x) - v_0(x), \ \vec{a(y)} = v_1(y) - v_0(y), \ \vec{a(z)} = v_1(z) - v_0(z)$$



(a) Vectors: \vec{A} and \vec{B} . The magnitude of \vec{A} is represented as $\|\vec{A}\|$, and same goes to magnitude of $\|\vec{B}\|$. A unit vector is when $\|\vec{A}\|$ is equals to 1 or $\|\vec{B}\|$ is equals to 1.



(b) Normal: An example of the normal \vec{N} that is perpendicular to the plane of a triangle at p.

Figure 4.2: The important parameters that influence the appearance of 3D mesh in computer graphics.

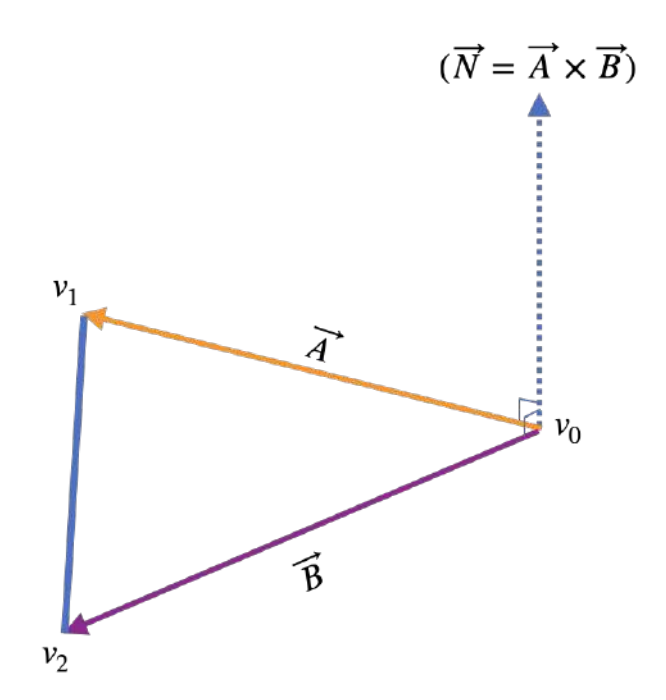


Figure 4.3: The resulting vector \vec{N} obtained from the cross product operation $\vec{A} \times \vec{B}$.

$$\vec{b}(x) = v_1(x) - v_0(x), \quad \vec{b}(y) = v_1(y) - v_0(y), \quad \vec{b}(z) = v_1(z) - v_0(z)$$

$$\vec{A} = \langle a(x), a(y), a(z) \rangle, \quad \vec{B} = \langle b(x), b(y), b(z) \rangle$$
(4.1)

B. Compute the cross product using computed two vectors in Eq. (4.1):

$$\vec{A} \times \vec{B} = \begin{vmatrix} \vec{i} & \vec{j} & \vec{k} \\ a(x) & a(y) & a(z) \\ b(x) & b(y) & b(z) \end{vmatrix}$$

$$= \begin{vmatrix} a(y) & a(z) \\ b(y) & b(z) \end{vmatrix} \vec{i} - \begin{vmatrix} a(x) & a(z) \\ b(x) & b(z) \end{vmatrix} \vec{j} + \begin{vmatrix} a(x) & a(y) \\ b(x) & b(y) \end{vmatrix} \vec{k}$$

$$= [a(y)b(z) - a(z)b(y)]\vec{i} - [a(x)b(z) + a(z)b(x)]\vec{j} + [a(x)b(y) - a(y)b(x)]\vec{k}$$

Then,

$$n(x) = \langle a(y)b(z) - a(z)b(y) \rangle$$

$$n(y) = -\langle a(x)b(z) + a(z)b(x) \rangle = \langle a(z)b(x) - \langle a(x)b(z) \rangle$$

$$n(\vec{z}) = \langle a(x)b(y) - a(y)b(x) \rangle$$

$$\vec{N} = \langle n(x), n(y), n(z) \rangle \text{ (Refer to Fig. 4.3)} \rangle \tag{4.2}$$

4.7.4 Magnitude (Length) of a Vector

The magnitude of a vector is the length of the vector and is denoted by \vec{A} . It is the square root of the sum of squares of the components of vector based on the Pythagorean theorem:

$$\|\vec{A}\| = \sqrt{a(x)^2 + a(y)^2 + a(z)^2}$$
 (4.3)

A unit vector is any vector whose magnitude is one, $\|\vec{A}\| = 1$ by using normalisation. Normalising refers to the process of making something standard, making the vector to point in the same direction and change its length to one. It is written as \hat{n} and is calculated as follows:

$$\hat{n} = \frac{\vec{A}}{\|\vec{A}\|} \tag{4.4}$$

In other words, to normalise a vector, simply divide each component by its magnitude. Since it describes a vector's direction without regard to its length, it's useful to have the unit vector readily accessible [234].

4.7.5 Magnitude (Length) of the Cross Product

As shown in Fig. 4.4, the magnitude (length) of the resulting vector from a cross product is equals to the product of the magnitudes of the two vectors: \vec{A} and \vec{B} , and the sine of the angle θ between them denoted as:

$$\|\vec{N}\| = \|\vec{A} \times \vec{B}\| = \|\vec{A}\| \|\vec{B}\| \sin\theta \tag{4.5}$$

The resulting \vec{N} is perpendicular to both \vec{A} and \vec{B} , hence, the distance of the \vec{N} based on the equation in (4.3) will yield to the area of a parallelogram.

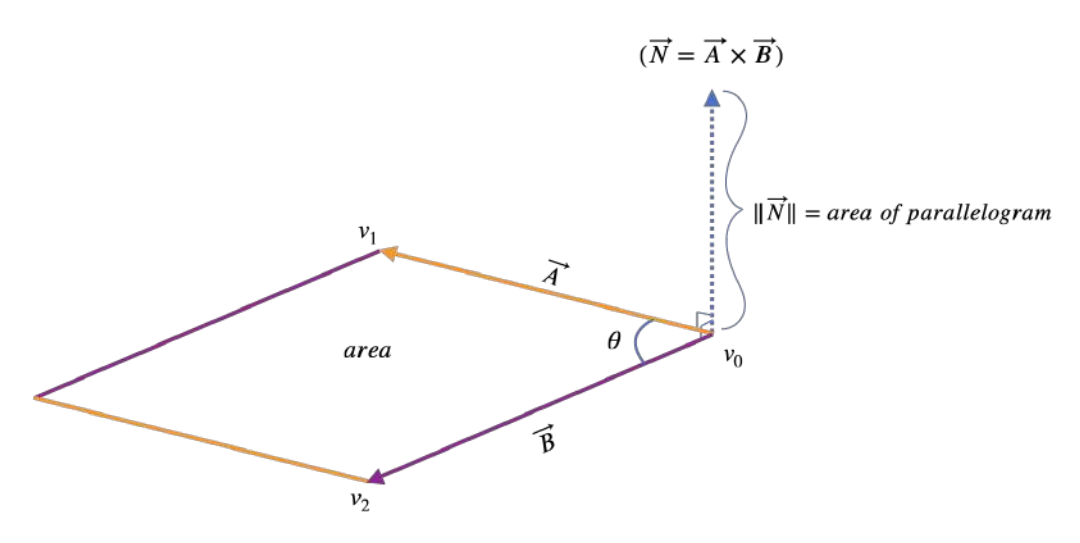


Figure 4.4: The magnitude (length) of cross product $\|\vec{A} \times \vec{B}\|$ is also equals to the area of the parallelogram determined by \vec{A} and \vec{B} .

4.7.6 Area of Triangle

• If an oblique triangle with two sides and the angle are known as shown in Fig. 4.5a, the areas can be found by the trigonometric relations:

Area,
$$A(f_i) = \frac{1}{2} \|\vec{A}\| \|\vec{B}\| \sin\theta = \frac{1}{2} \|\vec{A} \times \vec{B}\|$$
 (4.6)

where A and B are two sides of a triangle and θ is the angle between them. As one triangle is half the area of the parallelogram, thus, cross product can be used to determine areas. Moreover, if we define the following:

$$\frac{\vec{A} \times \vec{B}}{\|\vec{A} \times \vec{B}\|} = \hat{N} \tag{4.7}$$

where \hat{N} is the unit normal to the plane defined by \vec{A} , \vec{B} and has magnitude one.

• If a triangle with three sides are known as shown in Fig. 4.5b, Heron's Formula is used that allows the calculation of the area for the triangle:

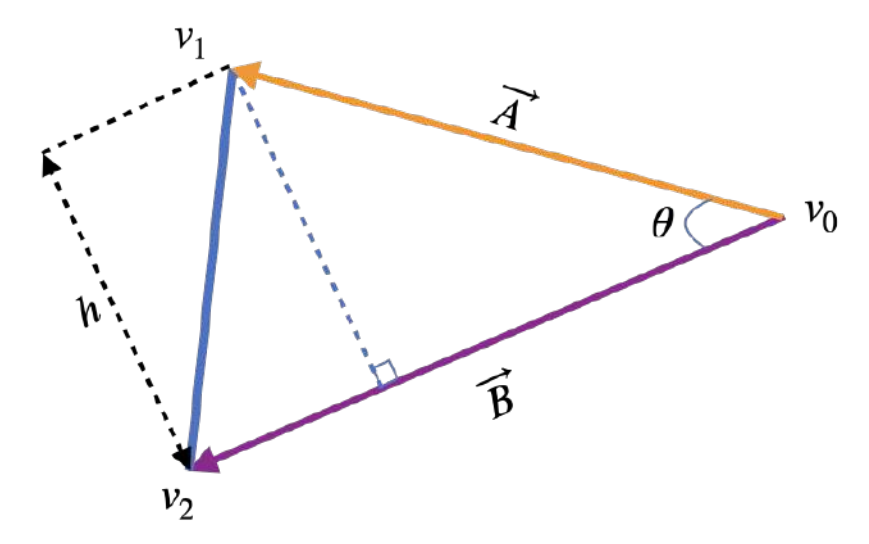
Area,
$$A(f_i) = \sqrt{s(s-\vec{A})(s-\vec{B})(s-\vec{C})}$$
 where $s = \frac{1}{2}(\vec{A} + \vec{B} + \vec{C})$ (4.8)

This formula is used for our calculation in this module of the 3D-FSA system analysis.

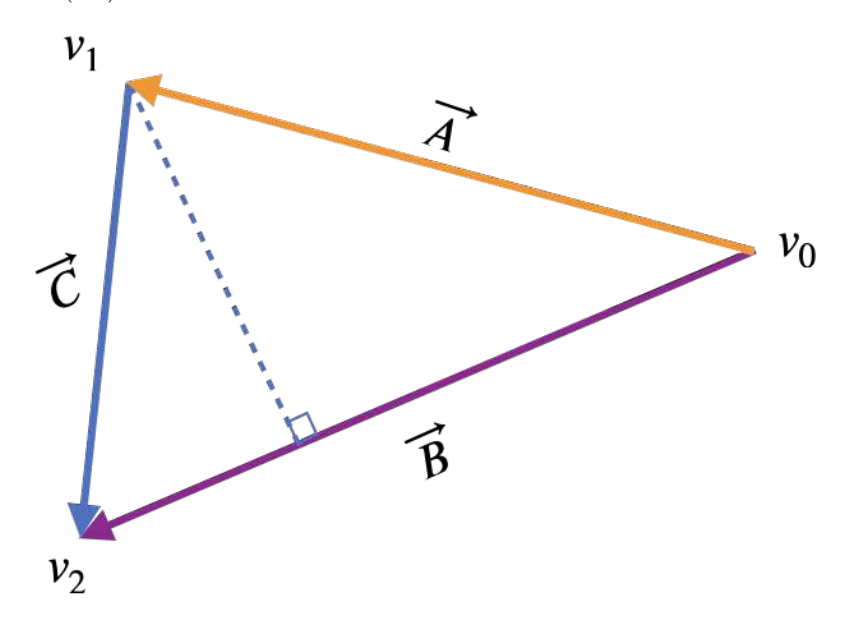
4.7.7 Interpolation in Barycentric Coordinates

Barycentric coordinates provide a measuring system that positions a point relative to the edges of the triangle, with a very simple scheme for converting from regular 3D spatial coordinates to barycentric coordinates, and from barycentric to 3D spatial coordinates. It is represented in triples of numbers (t_u, t_v, t_w) corresponding to masses placed at the vertices of a fixed reference triangle $\Delta v_0, v_1, v_2$. These masses then determine the point f_i at i^{th} -triangle, which is the geometric centroid of the three masses and is identified with coordinates (t_u, t_v, t_w) as illustrated in Fig. 4.6a. The barycentric coordinates of f_i are named t_u, t_v, t_w , and whose area is $A(f_i) = t_u + t_v + t_w$ are defined as follows:

$$u = t_u/A(f_i),$$



(a) Trigonometry relation with the two sides and angle using Eq. (4.6).



(b) Heron Formula with three sides using Eq. (4.8).

Figure 4.5: The calculation for the area of the triangle.

$$v = t_v/A(f_i),$$

$$w = t_w / A(f_i) = 1 - u - v$$

For example:

- if $f_i = v_0, u = 1, v = 0, w = 0$,
- if $f_i = v_1, u = 0, v = 1, w = 0,$
- if $f_i = v_2, u = 0, v = 0, w = 1$,
- if f_i is on the v_1, v_2 edge, u = 0
- if f_i is on the v_2, v_0 edge, v = 0
- if f_i is on the v_0, v_1 edge, w = 0

Given barycentric coordinates (u, v, w) and vertices v_0, v_1, v_2 for a triangle, it can be converted back to 3D coordinates by [235].

$$f_i = v_2 + u(v_0 - v_2) + v(v_1 - v_2) \tag{4.9}$$

Another way to see this is that u, v and w weight vertices to give the position of p. By rearranging the Eq. (4.9), the barycentric coordinates can be used to define any point on the triangle in the following manner:

$$p = v_2 + u(v_0) - u(v_2) + v(v_1) - v(v_2)$$

$$p = v_2(1 - u - v) + u(v_0) + v(v_1)$$

$$p = u(v_0) + v(v_1) + (1 - u - v)(v_2)$$

$$Since \ w = (1 - u - v),$$

$$\therefore \qquad p = u(v_0) + v(v_1) + w(v_2) \tag{4.10}$$

It can also be defined as weights for the triangle's vertices and defined as:

$$u + v + w = 1, \text{ for } p \in \Delta(v_0, v_1, v_2)$$
 (4.11)

This is a form of interpolation across the triangle using any quantity or variable that has been defined at triangle's vertices. Interpolation is a method of constructing new data points within range of discrete set of known data points [236]. For example, to find the colour at point p as shown in Fig. 4.6b, the colour of the three vertices (v_0, v_1, v_2) are interpolated across the surface of the triangle, defined as:

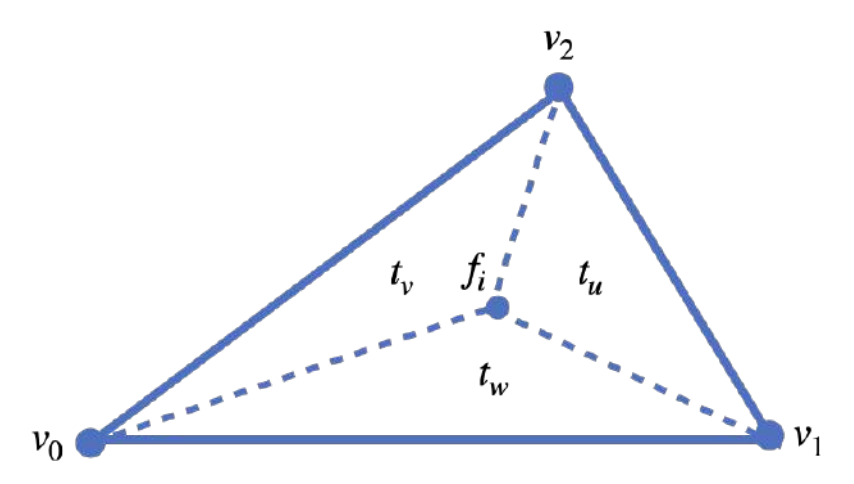
$$C_p = u(C_{v_0}) + v(C_{v_1}) + w(C_{v_2})$$
(4.12)

Besides colour attributes, normals and texture coordinates can be interpolated across the surface of the triangle.

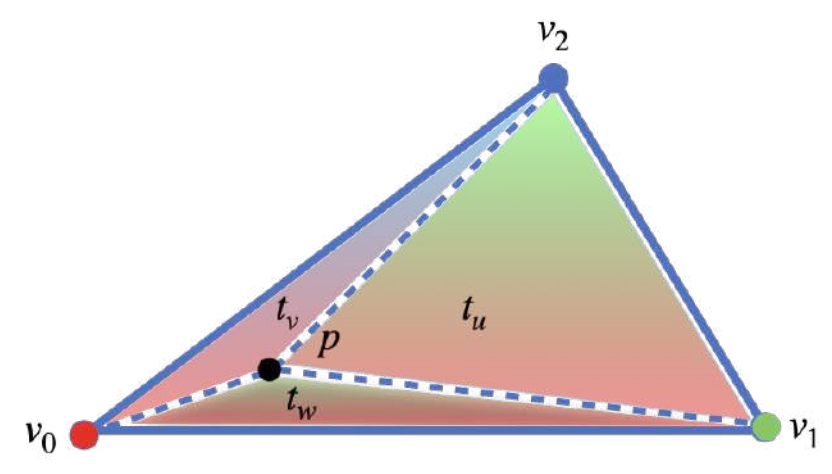
4.8 The Structures for the 3D Data Files in.obj Format

An .obj file contains information about the geometry of 3D meshes. The files are used for exchanging information, CAD (Computer Aided-Design), 3D printing, and 3D graphics applications [237, 238]. It is a vector file, which makes the defined 3D meshes scalable. There is no maximum file size.

Initially, this format was created in the 1980s by Wavefront Technologies for its Advanced Visualiser animation software application to store geometric objects composed of lines, polygons, and freeform curves and surfaces,



(a) The point f_i at i^{th} -triangle is the internal v_0, v_1, v_2 vertices, whose area is $A(f_i) = t_u + t_v + t_w$.



(b) In computer graphics, barycentric coordinates can be seen as the area of sub-triangles (v_1, v_2, p) for t_u , (v_2, v_0, p) for t_v and (v_0, v_1, p) for t_w over the area of the triangle $\Delta(v_0, v_1, v_2)$ which is the reason it's also called areal coordinates.

Figure 4.6: An example of barycentric coordinates defining a position with respect to the positions of the vertices of a triangle.

and until now it is able to store more data as follows:

- (1) Vertex data: geometric vertices, texture vertices, vertex normals, etc.
- (2) Elements: point, line, face, curve, etc.
- (3) Free-form curves/ surface body statements: parameter values, outer trimming loop, etc.
- (4) Connectivity between free-form surfaces: connect.
- (5) Grouping: group name, smoothing group, etc.
- (6) Display/ render attributes: colour interpolation, etc.

However, the scene information, such as the light position or animations, are not included in this file.

Overall, .obj file is simple and open format with wide export and import support among computer aided design (CAD) software. For example, the Autodesk 3Ds Max is used to convert the rendered 3D mesh into .obj file and read it using the Notepad in Windows or TextEdit in MacOS. Hence, it is getting famous as a file format for 3D meshes.

The .obj file that is used in 3D-FSA requires only the followings to construct a 3D femur:

(1) Vertex data: geometric vertices and vertex normals

(2) Element: face

As depicted in Fig. 4.7, the first part of the list is the definition of geometry vertices for the 3D femur. Then, followed by the vertex normals in the second part of the list. The face indexes with the vertex normals information are at the last part of the list. The resulting 3D mesh is shown in Fig. 4.8, with the vertices view (Fig. 4.8a), edges view (Fig. 4.8b) and faces view (Fig. 4.8c).

The .obj file does not require any sort of header, although it is common to begin with # symbol. 3D-FSA ignores anything after # until the next line, allowing developers to leave notes for themselves or others who may be viewing the codes [238] (e.g.: the number of vertices used for the construction of 3D femur).

Apart from that, blank space and blank lines can be freely added to the file to aid in formatting and readability. Each non-blank line begins with a keyword and followed on the same line with the data for that keyword. 3D-FSA reads the lines and processed until the end of the file [238, 239].

The following keywords are then read and processed in 3D-FSA. They are arranged by data type, and each is followed by a brief description and the format of a line:

(1) The geometric vertices represented as v in Fig. 4.7a:

 $v \quad x \quad y \quad z$

```
# 135576 vertex positions
   67.6338 32.588 1299.5
   68.9724 34.1442 1299.5
   69.6965 34.8101 1299.5
   70.5355 35.0737 1299.5
   67.6338 32.588 1299.5
   69.6965 34.8101 1299.5
v
   71.6931 35.6319 1299.5
           32.588 1299.5
   67.6338
   70.5355 35.0737 1299.5
   67.6338 32.588 1299.5
   68.0308 33.318 1299.5
v
   68.9724 34.1442 1299.5
   68.9724 34.1442 1299.5
   68.0308 33.318 1299.5
   68.2828 33.5765 1299.5
   66.8585 31.1157 1299.5
V
   67.6338 32.588 1299.5
   71.6931 35.6319 1299.5
   72.691 35.7204 1299.5
   66.8585 31.1157 1299.5
   71.6931 35.6319 1299.5
   66.8585 31.1157 1299.5
   66.8896 31.8522 1299.5
   67.6338 32.588 1299.5
   66.0521 29.6609 1299.5
   66.3376 30.3815 1299.5
   66.8585 31.1157 1299.5
74.1672 35.6349 1299.5
   74.4032 26.8017 1299.41
   72.691 35.7204 1299.5
   77.131 34.7464 1299.5
   74.1672 35.6349 1299.5
   75.8281 35.2745 1299.5
   66.8585 31.1157 1299.5
   73.3904 28.0596 1299.42
   66.0521 29.6609 1299.5
   73.3904 28.0596 1299.42
   66.8585 31.1157 1299.5
   72.691 35.7204 1299.5
   74.4032 26.8017 1299.41
   73.3904 28.0596 1299.42
   72.691 35.7204 1299.5
   77.131 34.7464 1299.5
   74.4032 26.8017 1299.41
   74.1672 35.6349 1299.5
   74.4032 26.8017 1299.41
   77.131 34.7464 1299.5
   78.816 34.2021 1299.5
   80.2949 33.3294 1299.5
   74.4032 26.8017 1299.41
   78.816 34.2021 1299.5
   80.2949 33.3294 1299.5
   81.5093 32.587 1299.48
   74.4032 26.8017 1299.41
   65.3463 28.9204 1299.5
```

(a) The position of the vertices represented as v, which are used in rendering.

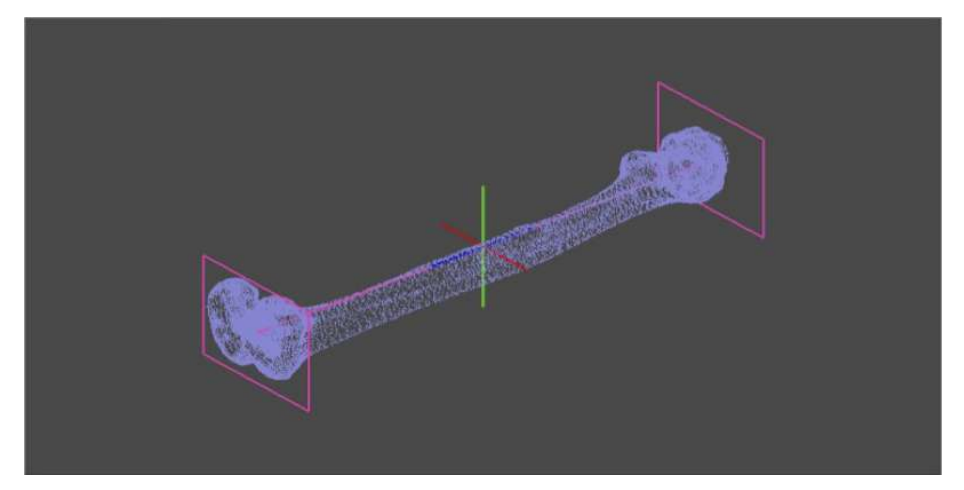
```
# 0 UV coordinates
# 135576 vertex normals
vn -0.00702378 0.00690448 -0.999951
vn -0.00702378 0.00690448 -0.999951
vn -0.00702378 0.00690448 -0.999951
vn 0.000240239 0.000161536 -1
  0.000240239 0.000161536 -1
Vn.
  0.000240239 0.000161536 -1
Vn
  -0.00121136 0.00185607 -0.999998
vn
  -0.00121136 0.00185607 -0.999998
  -0.00121136 0.00185607 -0.999998
  0.00167044 -0.000574013 -0.999998
νņ
  0.00167044 -0.000574013 -0.999998
  0.00167044 -0.000574013 -0.999998
  -0.00625734 0.00846099 -0.999945
  -0.00625734 0.00846099 -0.999945
  -0.00625734 0.00846099 -0.999945
vn
  -0.00103746 0.00162416 -0.999998
vn
   -0.00103746 0.00162416 -0.999998
VΠ
   -0.00103746 0.00162416 -0.999998
  -0.00113159 0.00172493 -0.999998
  -0.00113159 0.00172493 -0.999998
Vn.
  -0.00113159 0.00172493 -0.999998
VΩ
  -0.00359194 0.00296932 -0.999989
  -0.00359194 0.00296932 -0.999989
vn -0.00359194 0.00296932 -0.999989
  -0.00845111 0.00267073 -0.999961
  -0.00845111 0.00267073 -0.999961
   -0.00845111 0.00267073 -0.999961
vn
  0.00150659 0.0103076 -0.999946
vn
  0.00150659 0.0103076 -0.999946
  0.00150659 0.0103076 -0.999946
  0.00131024 0.00739307 -0.999972
  0.00131024 0.00739307 -0.999972
  0.00131024 0.00739307 -0.999972
  -0.00987407 0.00345951 -0.999945
-0.00987407 0.00345951 -0.999945
  -0.00987407 0.00345951 -0.999945
-0.00713042 0.00932327 -0.999931
vn
vn
   -0.00713042 0.00932327 -0.999931
VII
  -0.00713042 0.00932327 -0.999931
vn
  -0.0004365 0.00993459 -0.999951
  -0.0004365 0.00993459 -0.999951
  -0.0004365 0.00993459 -0.999951
  0.00218945 0.0103258 -0.999944
  0.00218945 0.0103258 -0.999944
  0.00218945 0.0103258 -0.999944
  0.00413401 0.00965815 -0.999945
  0.00413401 0.00965815 -0.999945
   0.00413401 0.00965815 -0.999945
   0.00523082 0.00900414 -0.999946
   0.00523082 0.00900414 -0.999946
  0.00523082 0.00900414 -0.999946
  -0.00275408 0.01621 -0.999865
   -0.00275408 0.01621 -0.999865
```

(b) The vertex normals represented as vn, which determine the visual softness or hardness between the faces of 3D mesh [17].

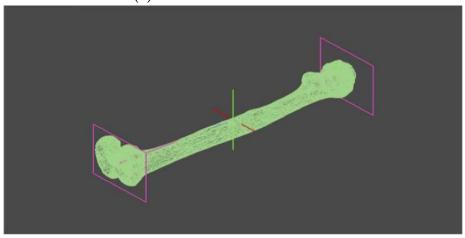
```
# Mesh '<STL_BINARY>' with 45192 faces
g <STL_BINARY>
usemtl DefaultMaterial
f 1//1 2//2 3//3
   4//4 5//5 6//6
   7//7 8//8 9//9
   10//10 11//11 12//12
   13//13 14//14 15//15
   16//16 17//17 18//18
   19//19 20//20 21//21
   22//22 23//23 24//24
25//25 26//26 27//27
   28//28 29//29 30//
   31//31 32//32
   34//34 35//35 36//36
   37//37 38//38 39//39
   40//40 41//41 42//42
   43//43 44//44 45//45
   46//46 47//47 48//48
   49//49 50//50 51//51
   52//52 53//53 54//54
   55//55 56//56 57//57
          59//59
   58//58
   61//61 62//62
   64//64 65//65 66//66
   67//67 68//68 69//69
   70//70 71//71 72//72
   73//73 74//74 75//75
   76//76 77//77 78//78
   79//79 80//80 81//81
   82//82 83//83 84//84
   85//85 86//86
   88//88 89//89 90//90
   91//91 92//92 93//
   94//94 95//95 96//96
   97//97 98//98 99//99
   100//100 101//101 102//102
   103//103 104//104 105//105
   106//106 107//107 108//108
   109//109 110//110 111//111
   112//112 113//113 114//114
   115//115 116//116
118//118 119//119
                      117//117
                      120//120
   121//121 122//122
   124//124 125//125
                      126//126
   127//127 128//128
                      129//129
   130//130 131//131
                      132//132
   133//133 134//134 135//135
   136//136 137//137 138//138
   139//139 140//140 141//141
   142//142 143//143
                      144//144
   145//145
            146//146
                      147//147
            149//149
                      150//150
   151//151
            152//152
   154//154 155//155 156//156
   157//157 158//158 159//159
```

(c) The indexes of vertex and vertex normal that define the faces of the 3D mesh represented as f.

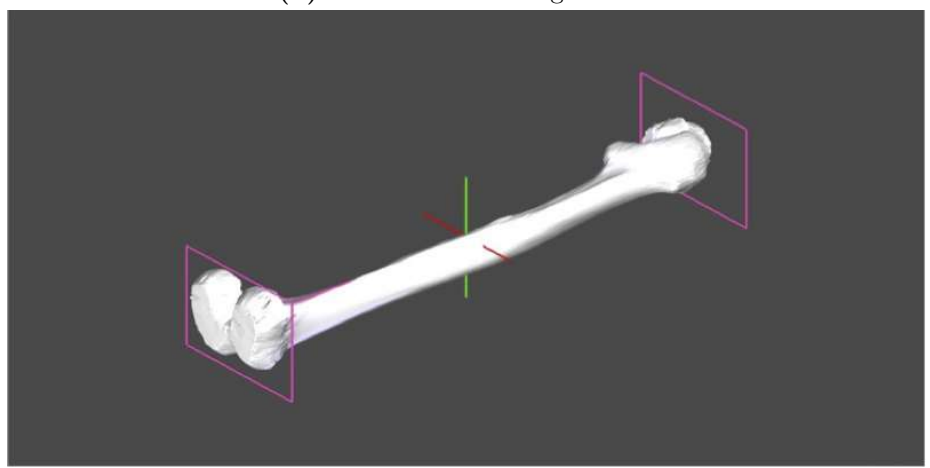
Figure 4.7: The structure for the 3D femur .obj text file.



(a) 3D left femur in vertices view.



(b) 3D left femur in edges view.



(c) 3D left femur in faces view.

Figure 4.8: The 3D human femur can be displayed in faces view, edges view, and vertices view in our system, 3D-FSA.

(2) The vertex normals represented as vn in Fig. 4.7b: vn dx dy dz

(3) The face with vertex indexes and the respective vertex normals represented as f in Fig. 4.7c:

$$f = v_i / / v n_m = v_j / / v n_m = v_k / / v n_m$$

Let's explore further for the meaning of these parameters that describes a .obj file. In order to facilitate our explanation, a simple *cube.obj* as illustrated in Fig. A.1 in Appendix A is used.

4.8.1 Geometric Vertices

Fig. 4.7a consists of all the geometric vertices that is used to define the position (floating point numbers) of the vertices of the 3D femur in (x, y, z) format.

The femur .obj file always begins with a # symbol representing notes to the developers or other users (e.g., the number of vertices used to form the 3D femur is 135576 vertices), and will be ignored by the program. Followed by the second line that starts with v, indicates the first vertex v_1 of the triangle. The three floating values after this alphabet v are the 3D coordinates (x, y, z) for v_1 .

These vertices are listed in counterclockwise order for the normal calculations and to decide the visual orientation of the triangle faces. The front face is characterised by a counterclockwise order around these vertices, whereas the back face is characterised by a clockwise order around

Table 4.4: The vertex coordinates defined for the 3D cube extracted from *cube.obj* as illustrated in Fig. A.1 in Appendix A.

Vertex Index	x-coordinate	y-coordinate	z – $coordinate$
v_1	0.0	0.0	0.0
v_2	0.0	0.0	1.0
_			
v_3	0.0	1.0	0.0
v_4	0.0	1.0	1.0
v_5	1.0	0.0	0.0
v_6	1.0	0.0	1.0
v_7	1.0	1.0	0.0
v_8	1.0	1.0	1.0

these vertices.

Table 4.4 shows the formed vertices for the 3D cube extracted from *cube.obj* (Refer to Fig. A.1 in Appendix A).

4.8.2 Vertex Normals

The second set of data in .obj file is the vertex normals as shown in Fig. 4.7b. As mentioned in Section 4.7.2, normal plays a central role in shading by describing the orientation of a surface of a 3D mesh. Basically, there are two types of normals:

• Face Normals (Refer to Section 4.7.2)

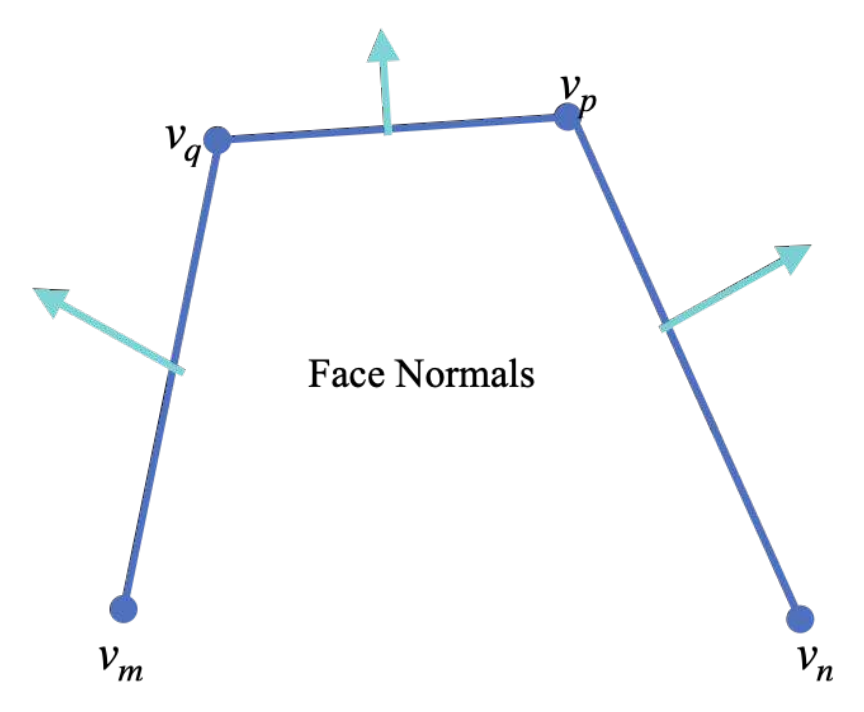
• Vertex Normals

Face normals are used to determine the orientation for the entire face. If it's pointing away from the camera, then that face will be ignored during the rendering. As shown in Fig. 4.9a, the calculation for face normals is required for every flat face of a 3D mesh by using the method described in Section 4.7.2. This approach is called the flat shading. However, by just using the face normals giving the 3D mesh a faceted appearance. An example of a 3D cylinder rendered with face normals can be seen in Fig. 4.10a.

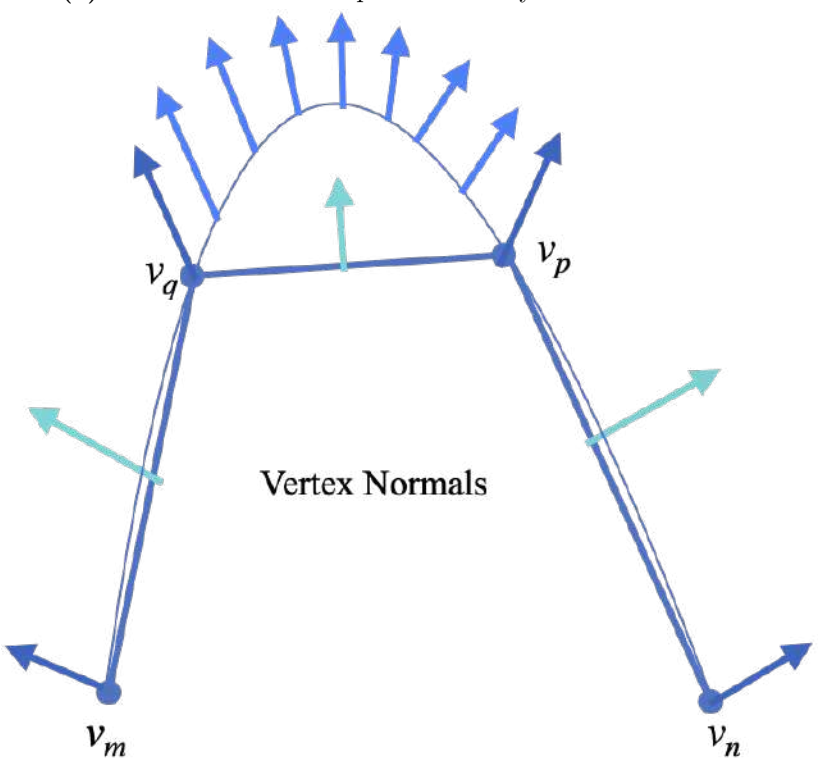
On the other hand, vertex normals are defined at the triangle vertices of 3D mesh and it is used to define smooth shading which adds the roundness to the 3D mesh. This concept is introduced by Henri Gouraud in 1971 namely, smooth shading or Gouraud shading [240], and then an improved shading method, namely Phong shading is introduced in 1975 by Bui Tuong Phong [241].

Since the vertex normals are stored at each vertex of the 3D mesh, they are oriented perpendicular to the smooth underlying surface of a 3D mesh as shown in Fig. 4.9b. These vertex normals can be generated automatically from 3D modelling softwares such as 3D Max, Maya or Blender by using their smooth shading feature.

Therefore, vertex normals and face normals are closely related. Sometimes, vertex normals are used as face normals due to flat surfaces. For example, the *cube.obj* file which consists of only flat faces, thus, the vector normals are used as the face normals which consists of six vector normals (two triangles at each side share the same vector normals) defined at every face of the 3D cube (Refer to Fig. A.1 in Appendix A). Fig. 4.11 shows

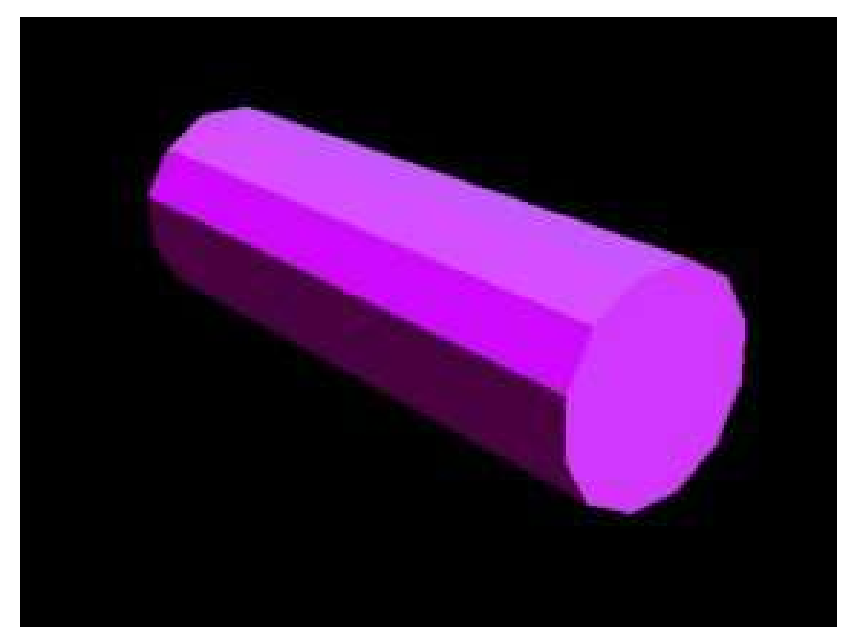


(a) The normals are computed for every face of a 3D mesh.

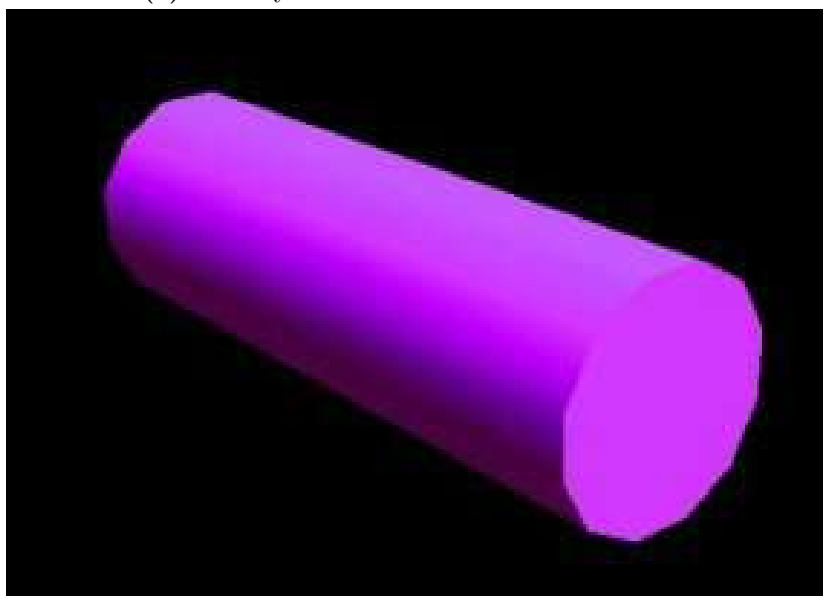


(b) The normals are computed for every vertices of a 3D mesh and are using to interpolate smoothly across the surface.

Figure 4.9: These examples are sourced from the website [18] that illustrates the difference between face normals and vertex normals.



(a) A 3D cylinder rendered with face normals.



(b) A 3D cylinder rendered with vertex normals.

Figure 4.10: These examples are extracted from [18].

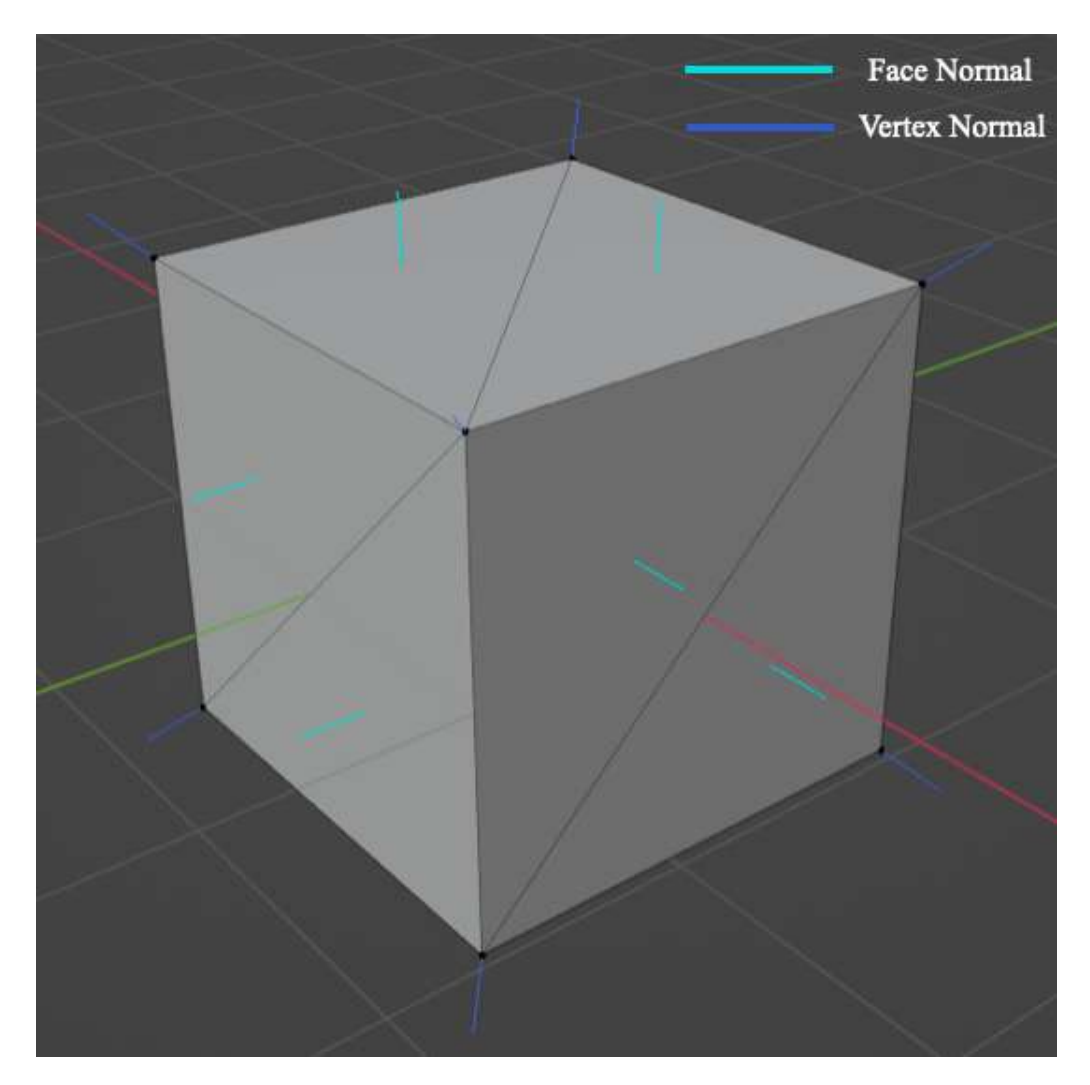


Figure 4.11: The examples for face normals and vertex normals of a 3D cube modelled in Blender [19].

the examples for face normals and vertex normals for a 3D cube drew using Blender [19].

Then during the rendering process, the smoothness of a 3D mesh is computed by interpolating the vertex normals that defined at each vertices. The calculation has been discussed in Section 4.7.7.

The .obj file for the 3D femur is created using a 3D modelling software, thus, the vertex normals have been calculated. Then, with the use of Microsoft Foundation Class (MFC) [25] and OpenGL Mathematics (GLM) libraries [242], a 3D femur is constructed based on the data file in .obj

Table 4.5: The vertex normals defined for the 3D cube extracted from *cube.obj* as illustrated in Fig. A.1 in Appendix A.

Index for Vertex Normal	dx	dy	dz
vn_1	0.0	0.0	1.0
vn_2	0.0	0.0	-1.0
vn_3	0.0	1.0	0.0
vn_4	0.0	-1.0	0.0
vn_5	1.0	0.0	0.0
vn_6	-1.0	0.0	0.0

format. This process is explained in detailed in Chapter 5.

Table 4.5 shows the formed vertex normals for the 3D cube extracted from *cube.obj* (Refer to Fig. A.1 in Appendix A for the illustrations).

Face Elements The last set of data in .obj file is the element of faces data. Each face is defined by three vertices and a vertex normal that acts as the face normal due to the flat surfaces with the following format:

$$f_n = v_i / |v n_m| = v_j / |v n_m| = v_k / |v n_m|$$

, where f_n is defined by three vertices (v_i, v_j, v_k) and the vertex normals for each vertices is defined by (vn_m, vn_m, vn_m) .

Table 4.6 shows the formed faces for the 3D cube extracted from *cube.obj* (Refer to Fig. A.1 in Appendix A for the illustrations).

Table 4.6: The vertex indexes and the index for the vertex normals that are used to define the triangle face of the cube.obj as illustrated in Fig. A.1 in Appendix A.

VertexIndex	Index for Vertex Normal
(v_1, v_7, v_5)	(vn_2, vn_2, vn_2)
(v_1, v_3, v_7)	(vn_2, vn_2, vn_2)
(v_1, v_4, v_3)	(vn_6, vn_6, vn_6)
(v_1, v_2, v_4)	(vn_6, vn_6, vn_6)
(v_3,v_8,v_7)	(vn_3, vn_3, vn_3)
(v_3, v_4, v_8)	(vn_3, vn_3, vn_3)
(v_5,v_7,v_8)	(vn_5, vn_5, vn_5)
(v_5, v_8, v_6)	(vn_5, vn_5, vn_5)
(v_1, v_5, v_6)	(vn_4, vn_4, vn_4)
(v_1, v_6, v_2)	(vn_4, vn_4, vn_4)
(v_2, v_6, v_8)	(vn_1, vn_1, vn_1)
(v_2,v_8,v_4)	(vn_1,vn_1,vn_1)
	(v_1, v_7, v_5) (v_1, v_3, v_7) (v_1, v_4, v_3) (v_1, v_2, v_4) (v_3, v_8, v_7) (v_3, v_4, v_8) (v_5, v_7, v_8) (v_5, v_8, v_6) (v_1, v_5, v_6) (v_1, v_6, v_2) (v_2, v_6, v_8)

Chapter 5

3D FEMUR

CONSTRUCTION

After a thorough investigation in pre-processing (Refer to Chapter 4), this module introduces the reader to strategies for generating 3D femur from input 3D data files in .obj format.

5.1 The Innovation of this Module

This module specialises in representing and manipulating surfaces for a 3D mesh especially both the human bone and the corticocancellous interface. It is thus an intuitive mesh viewer module, where a 3D mesh, stored in .obj file format, can be loaded and interactively inspected in an easy way, by simply dragging and clicking on the mesh itself. Once a mesh is loaded, the user can work on it by mean of a set of options and shortcuts as shown in Fig. 5.1 and Fig. 5.2.

Furthermore, the combination of Microsoft Foundation Class (MFC) [25] and OpenGL Mathematics (GLM) [26]. to form this module is novel and inventive.

This module has the capability of managing the hundred thousands or millions of primitives, which often consists of discrete amount of vertices, and these vertices are connected by edges, followed by forming the faces from the connected edges. A 3D femur is a 3D shape in which all the faces are triangles. Triangles are commonly used in many graphics software packages and hardware devices because of the following reasons:

- Triangles are atomic geometry.
- Triangles are primitive geometry.
- Triangles can operate more efficiently.
- Triangles are easy to handle.
- The mathematical calculation is straightforward.

Therefore, these benefits are adopted in this module for the use of 3D femur construction. More specifically, we propose a process for creating 3D femur based on the structures contained within a .obj file.

5.2 My Tasks

Since this is a collaborative research project, my tasks in this module are as follows:

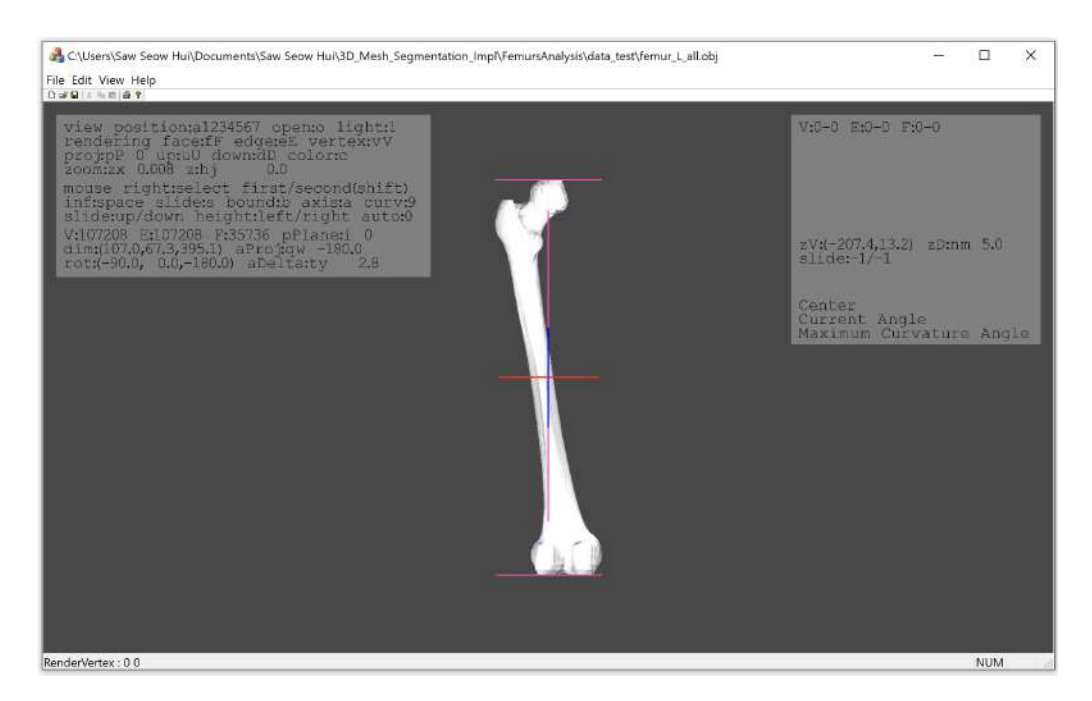
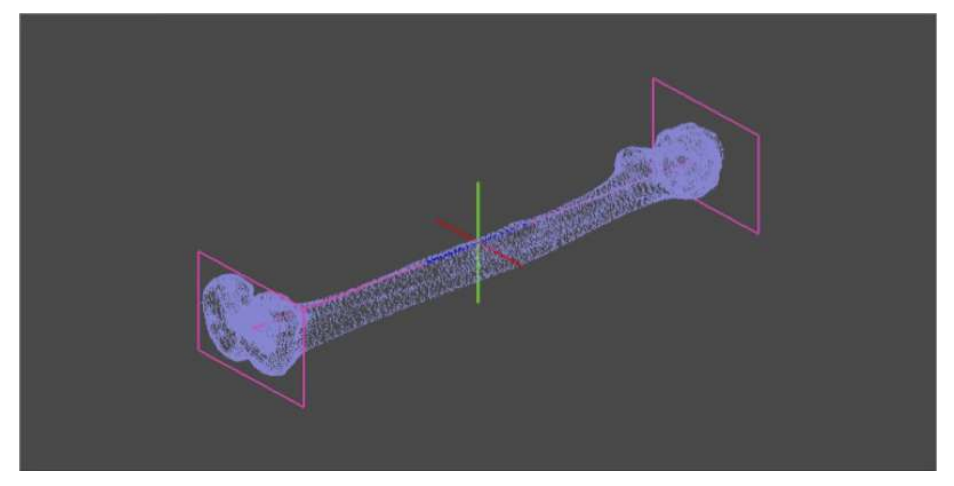
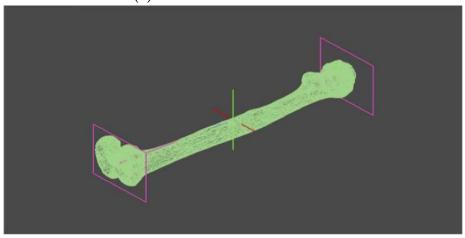


Figure 5.1: The GUI of our 3D-FSA System.

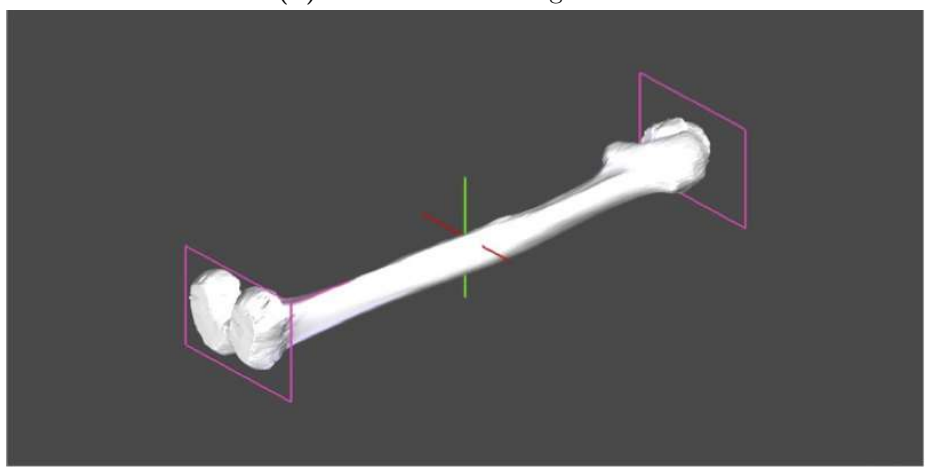
- To design the flowchart for the following features:
 - A. How to read the information from the .obj text files as shown in Fig. 4.7, that begins with the vertex positions, vertex normals and the faces?
 - B. How to construct the 3D femur based on the read data?
- To convert the designed flowchart into program implementations, incorporated with the Microsoft Foundation Class (MFC) and the OpenGL Mathematics (GLM) libraries.



(a) 3D left femur in vertices view.



(b) 3D left femur in edges view.



(c) 3D left femur in faces view.

Figure 5.2: The 3D human femur can be displayed in faces view, edges view, and vertices view in our system, 3D-FSA.

5.3 Module Overview

In order to facilitate the input process of the system, such as an easy access to the existing 3D data files in .obj format, a simple interface with minimum efforts is designed to showcase this module. Hence, the Microsoft Foundation Class (MFC) Libraries [25] are employed for the simple desktop applications creation. These libraries provide an object-oriented wrapper over much of the Win32 and COM Application Programming Interface (API)s, and consist of the most useful when the need of developing easier UI with multiple controls.

Additionally, on the creation of 3D structures that explicitly represent the human femurs, the work of Nate Robins on the 3D modelling method of Wavefront .obj file format is of particular interest [20]. The method written by the author consists of a complete data structure that represents a 3D mesh such as the number of vertices, number of normals, number of faces and other information of a 3D mesh that is based on the input data file. This method has seen a recent application in the production of high quality 3D meshes [243, 244, 245, 246].

OpenGL is used in this module to perform the rendering. It is a cross-language, cross-platform API for rendering 2D and 3D vector graphics. The API is typically used to interact with a GPU, to achieve hardware-accelerated rendering [247].

The combination of these tools are unique and hardly found in the state of art. The structure of this combination is defined in Section 5.4.

5.4 Module Architecture

Once the basic concepts has been developed as described in Chapter 4, the next step is to design the architecture for the 3D femur construction. Fig. 5.3 shows a visual representation of this module's architecture, that describes the structure and behaviours of multiple components.

The module of 3D femur construction consists of the following components:

- A. 3D Data Files Access
- B. New Mesh Allocation
- C. Memory Allocation
- D. Dimensions Calculation
- E. Structural 3D Representations
- F. Computational Geometry Processing
- G. 3D Femur Rendering
- H. Output

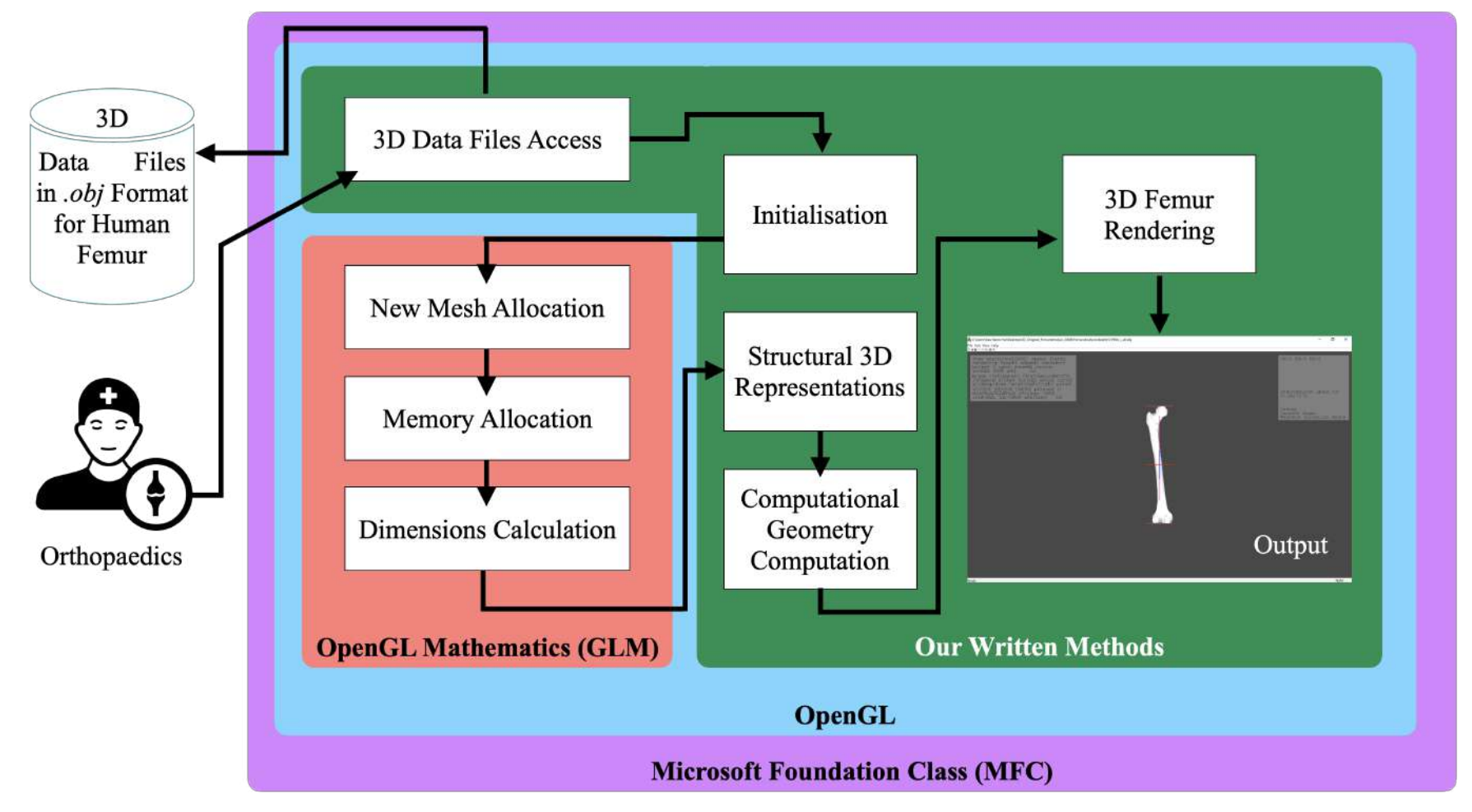


Figure 5.3: A conceptual model that describes the structure and behaviours of multiple components of this module.

The end user, especially the orthopaedic is able to select and access any 3D data files that are in .obj format from the storage. After a file is selected, all the necessary parameters for our program are initialised accordingly to be used in the rendering and 3D skeletonization later.

A new 3D femur is then allocated by clearing all the attributes to null. These attributes consists of the name of the file, the number of vertices, the number of normals, the number of faces, the position of x, the position of y, the position of z, etc. The "malloc" method is used to dynamically allocate a single large block of memory with the respective size for the vertices, triangles, normals, and the texture coordinates after the clearing is done.

Based on the input information, the dimensions which composed of the width, the height, and the depth of the 3D femur are calculated. Additional details on this component are provided in Section 6.4.1.

These three (3) components: New mesh allocation, memory allocation and dimensions calculation are written by Nate Robins [20] with OpenGL Mathematics (GLM) [26] and we incorporate these components in our system.

After executing the above mentioned components, a customised 3D structure based on the input file is created. This 3D structure is a structural build for the human femur comprises the significant elements: vertices, edges, and the faces.

With this 3D structure, we can compute the significant geometry attributes: the normal vectors and the centre point of each edge to be used later. At this point, we can begin to render these information to be displayed to the screen.

5.5 Program Designs and Implementations

In the previous section, we presented a system architecture for constructing a 3D femur based on the 3D data file that are in .obj format. At this stage, the system architecture is used as a guidance for designing the program which has successfully constructs 3D femurs that are illustrated in Fig. 5.4.

There are total of twelve (12) data files of three different patients of with the following codes:

- A. 0123964
- B. 0346688
- C. 00486295

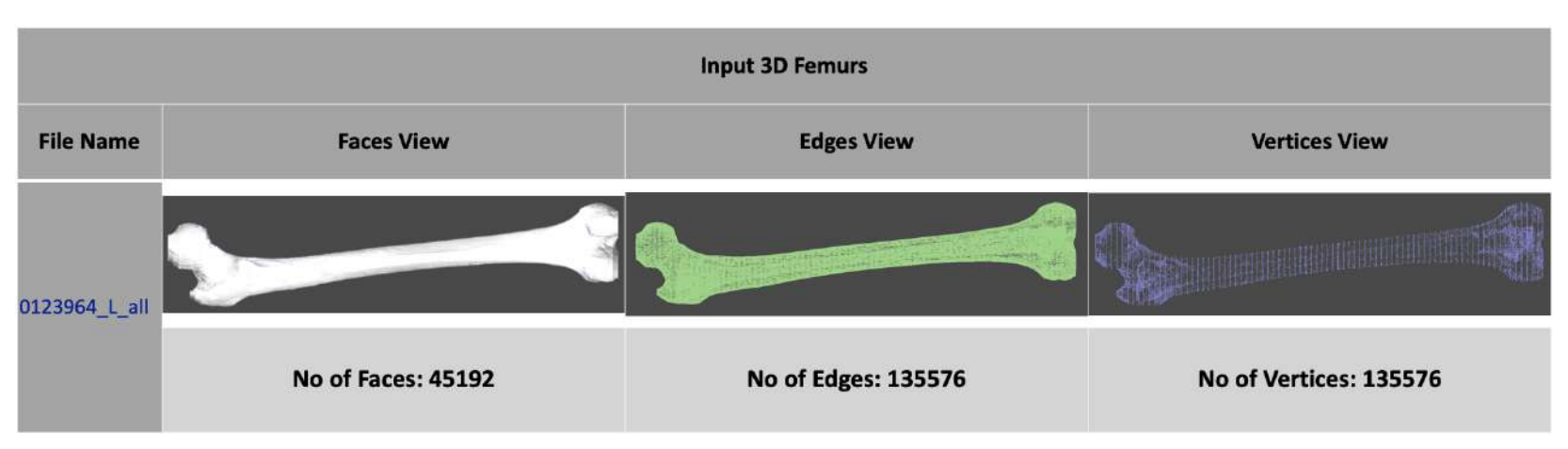
Each patient contributes four (4) set of .obj files with the left and right femurs, that includes the intramedullary canal and without intramedullary canal. Table 5.1 and Table 5.2 listed all the data files we received for the respective left and right 3D femurs.

Table 5.1: The six (6) 3D files in .obj format for the left femurs.

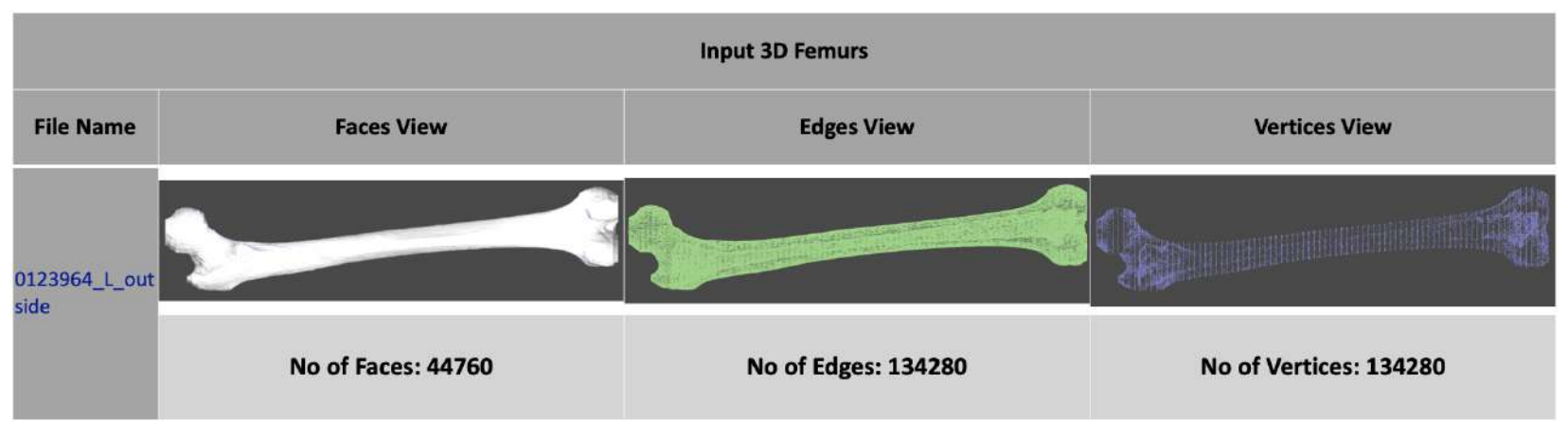
	Left Femur		
Patient	With	Without	
Code	Intramedullary	Intramedullary	
	Canal	Canal	
0123964	0123964_L_all.obj	0123964_L_outside.obj	
0346688	0346688_L_all.obj	0346688_L_outside.obj	
00486295	00486295_L_all.obj	00486295_L_outside.obj	

Table 5.2: The six (6) 3D files in .obj format for the right femurs.

	Right Femur		
Patient	With	Without	
Code	Intramedullary	Intramedullary	
	Canal	Canal	
0123964	0123964_R_all.obj	0123964_R_outside.obj	
0346688	0346688_R_all.obj	0346688_R_outside.obj	
00486295	00486925_R_all.obj	00486925_R_outside.obj	

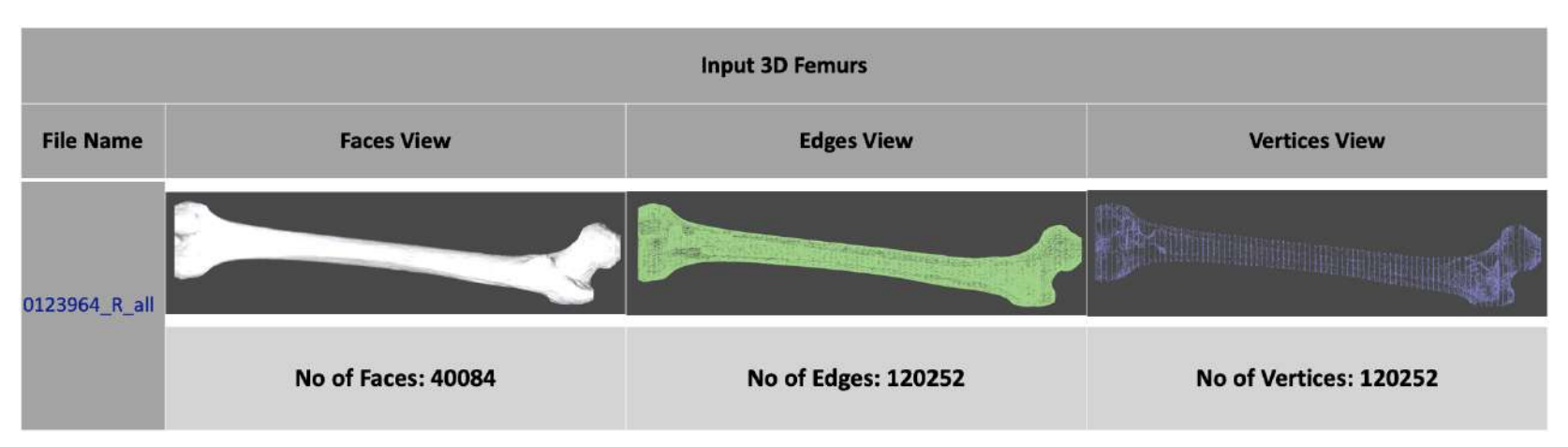


(a) The attributes of the 3D femurs obtained from a patient with the code number of 0123964 (Left femur with intramedullary canal) which consists of the number of vertices, the number of edges, and the number of faces.

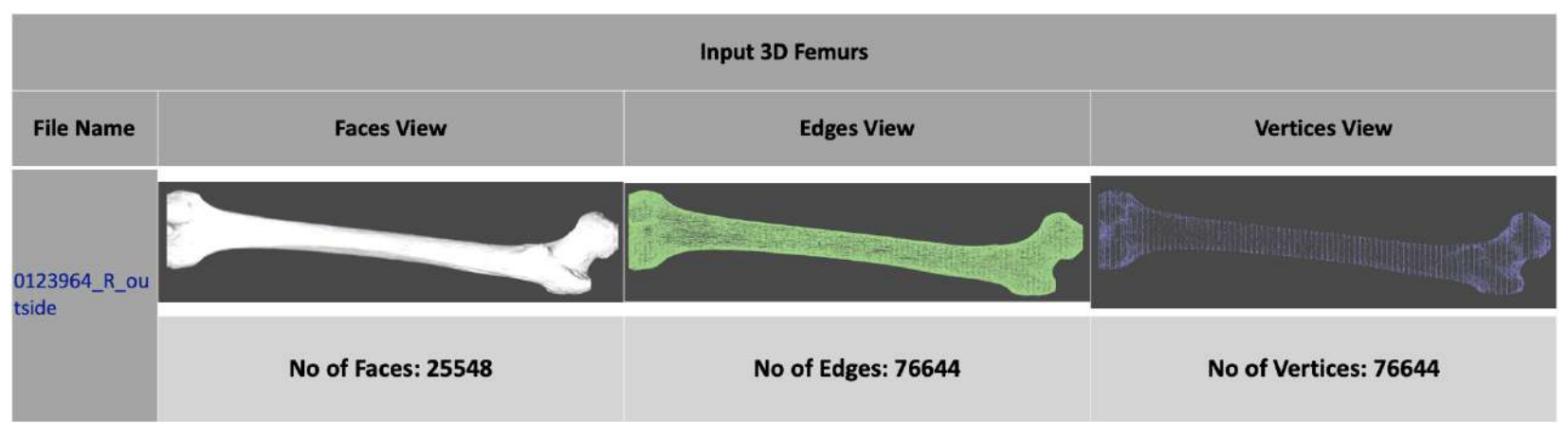


(b) The attributes of the 3D femure obtained from a patient with the code number of 0123964 (Left femure without medullary canal) which consists of the number of vertices, the number of edges, and the number of faces.

Figure 5.4: The attributes for the respective 3D femurs.

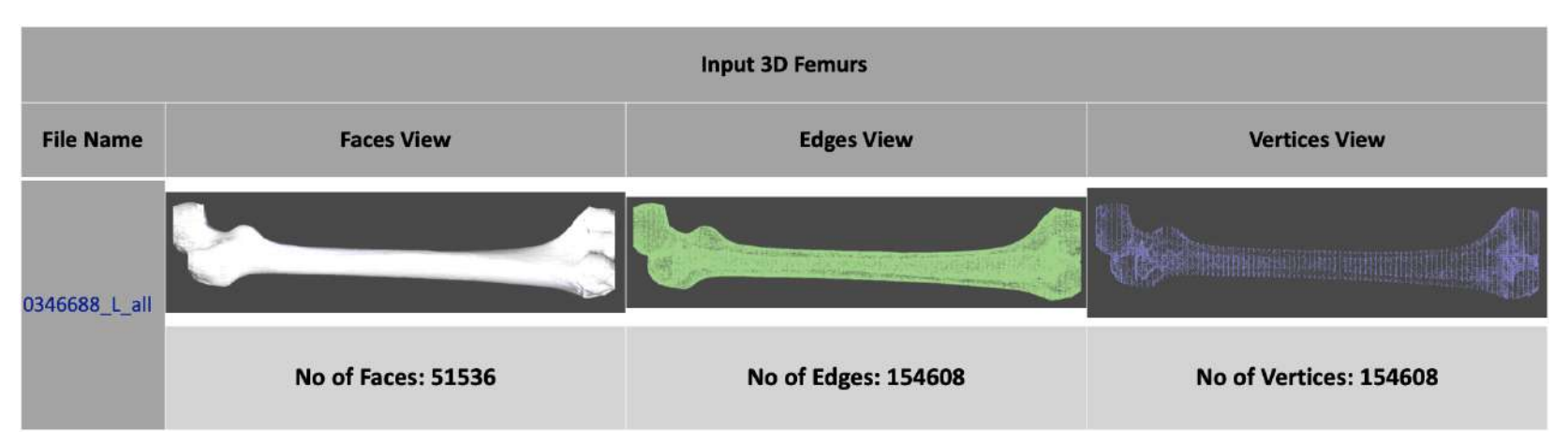


(c) The attributes of the 3D femurs obtained from a patient with the code number of 0123964 (Right femur with intramedullary canal) which consists of the number of vertices, the number of edges, and the number of faces.

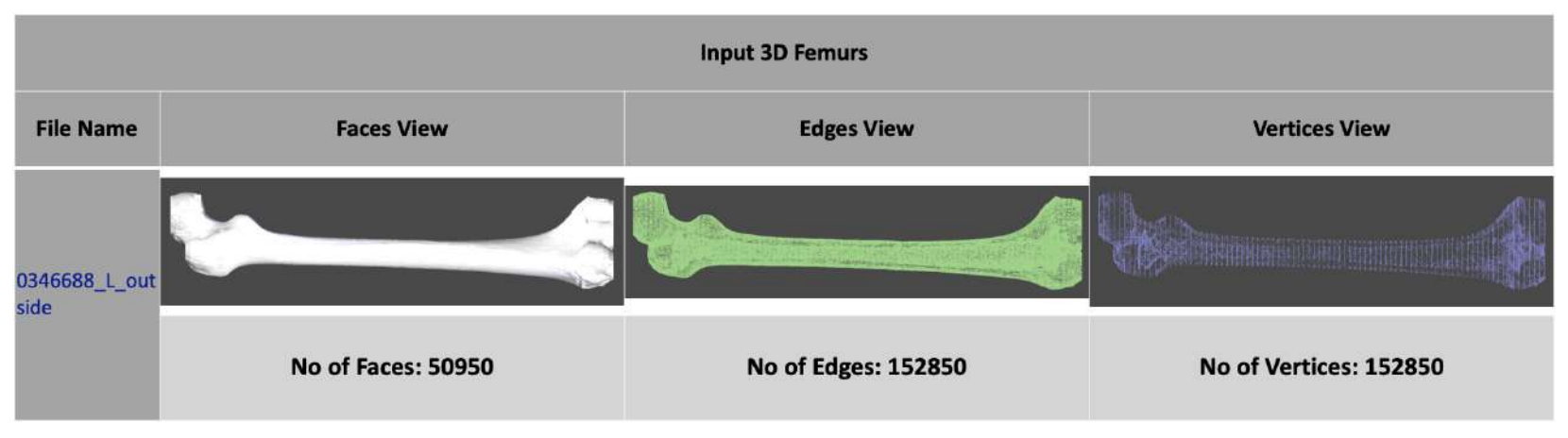


(d) The attributes of the 3D femure obtained from a patient with the code number of 0123964 (Right femur without intramedullary canal) which consists of the number of vertices, the number of edges, and the number of faces.

Figure 5.4: The attributes for the respective 3D femurs.

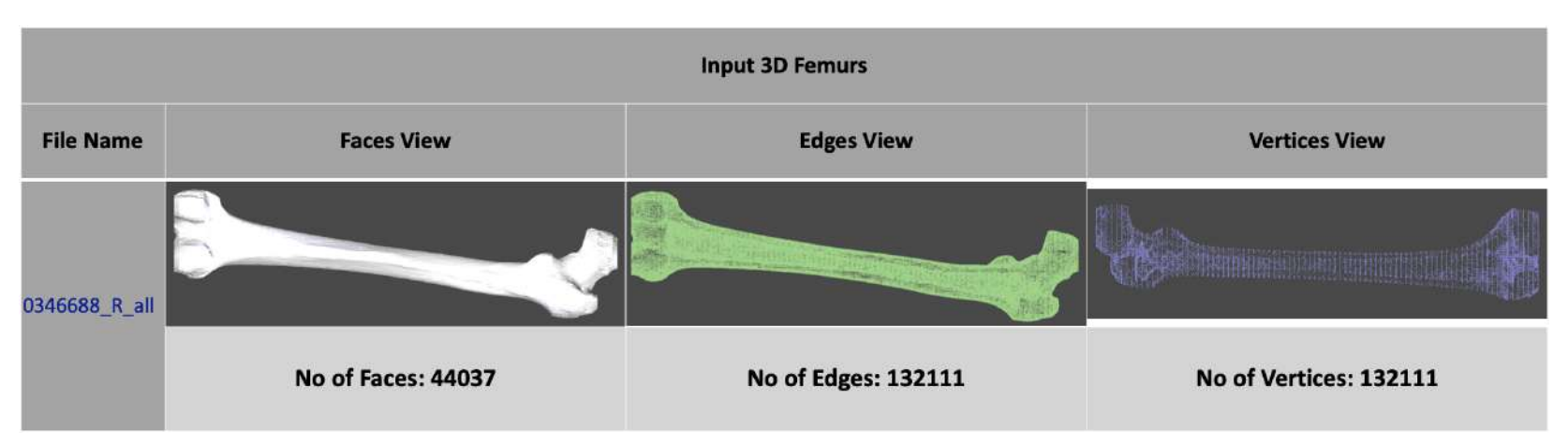


(e) The attributes of the 3D femurs obtained from a patient with the code number of 0346688 (Left femur with intramedullary canal) which consists of the number of vertices, the number of edges, and the number of faces.

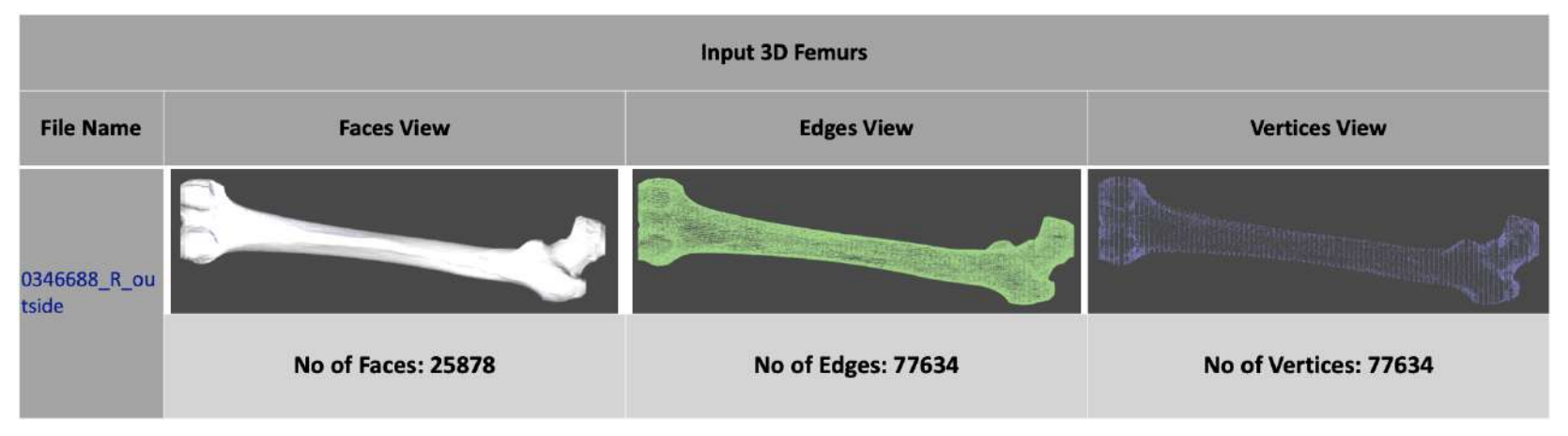


(f) The attributes of the 3D femure obtained from a patient with the code number of 0346688 (Left femure without intramedullary canal) which consists of the number of vertices, the number of edges, and the number of faces.

Figure 5.4: The attributes for the respective 3D femurs.

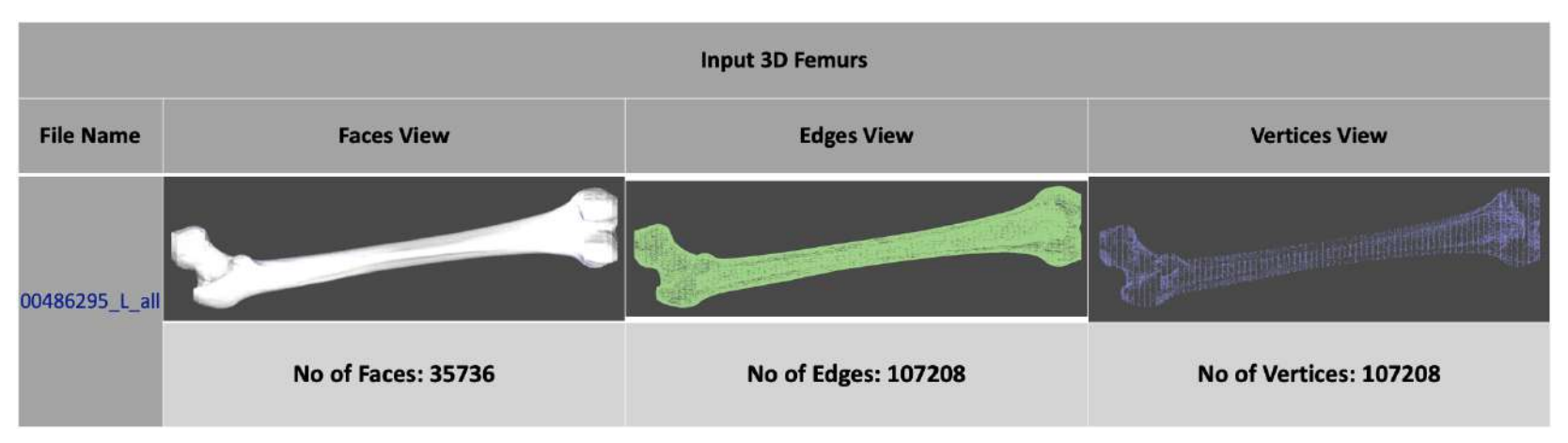


(g) The attributes of the 3D femure obtained from a patient with the code number of 0346688 (Right femur with intramedullary canal) which consists of the number of vertices, the number of edges, and the number of faces.

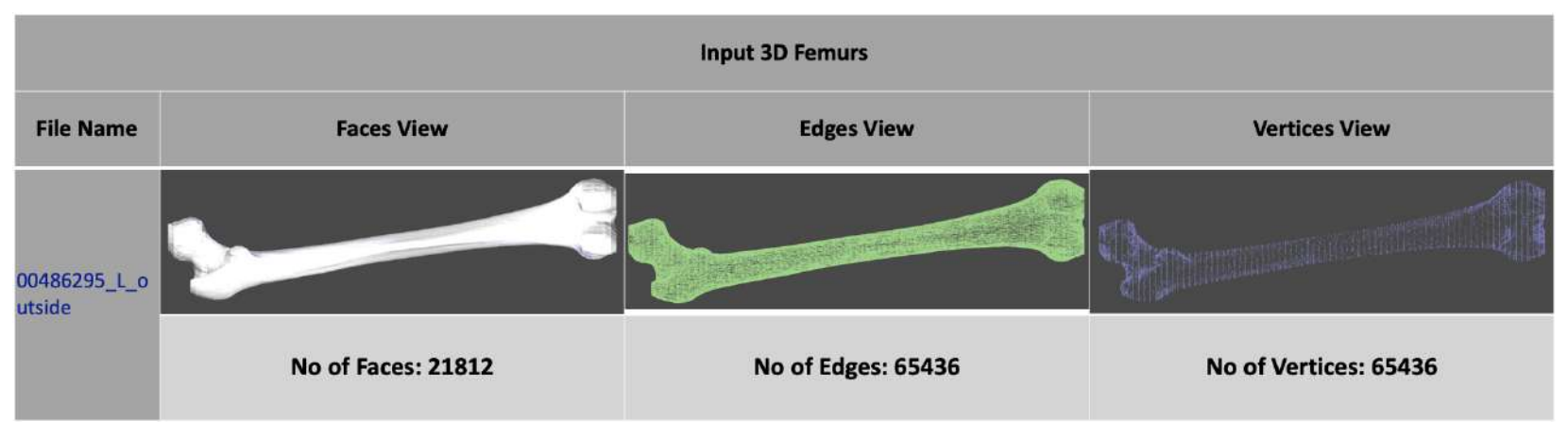


(h) The attributes of the 3D femure obtained from a patient with the code number of 0346688 (Right femure without intramedullary canal) which consists of the number of vertices, the number of edges, and the number of faces.

Figure 5.4: The attributes for the respective 3D femurs.

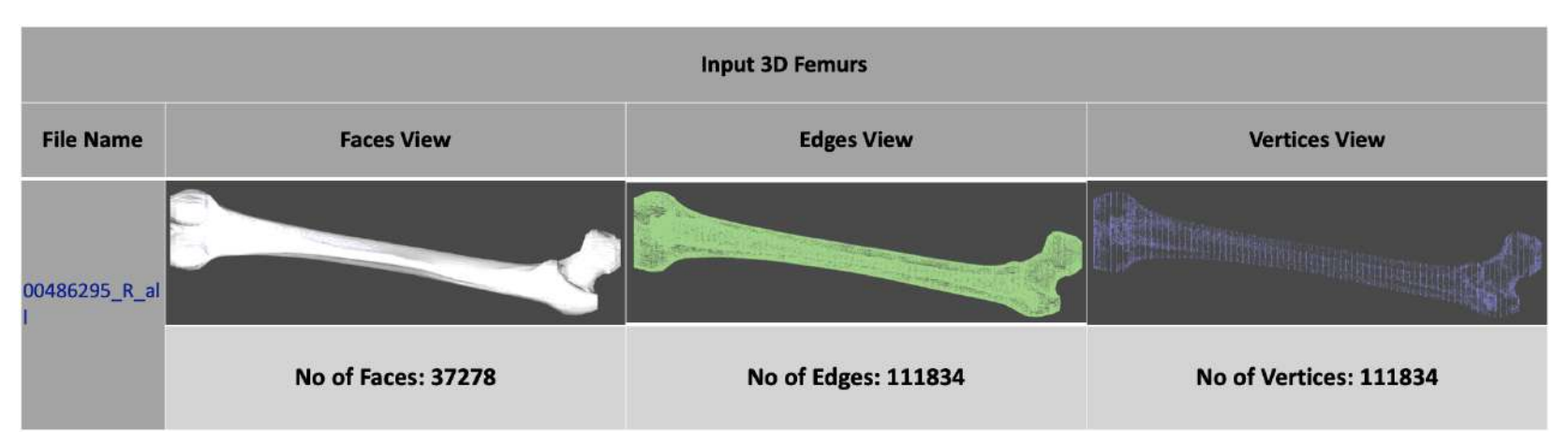


(i) The attributes of the 3D femurs obtained from a patient with the code number of 00486295 (Left femur with intramedullary canal) which consists of the number of vertices, the number of edges, and the number of faces.

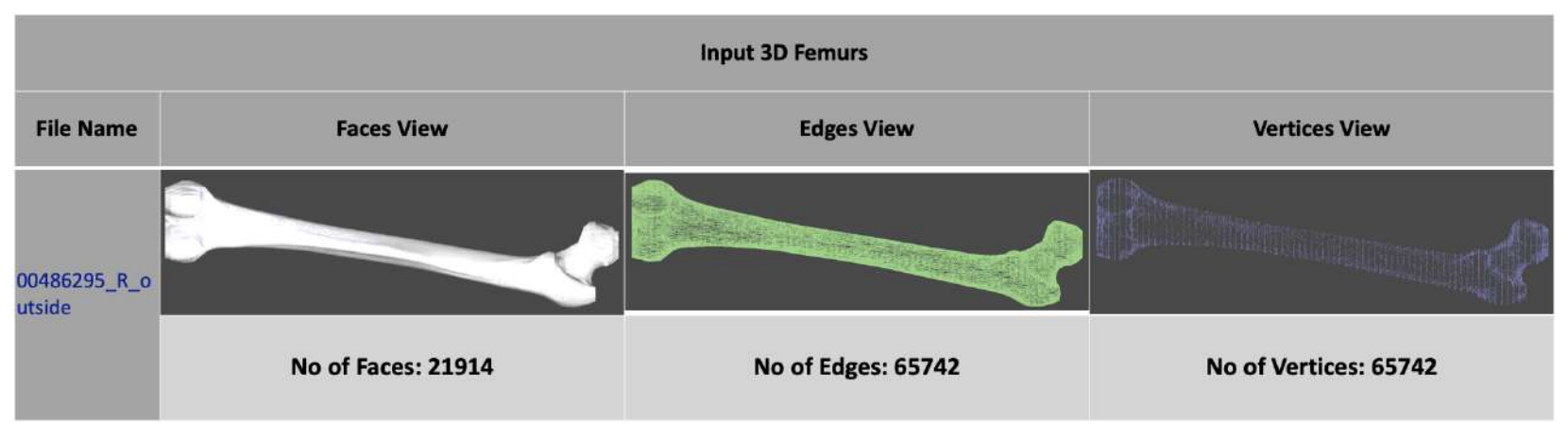


(j) The attributes of the 3D femure obtained from a patient with the code number of 00486295 (Left femure without intramedullary canal) which consists of the number of vertices, the number of edges, and the number of faces.

Figure 5.4: The attributes for the respective 3D femurs.



(k) The attributes of the 3D femure obtained from a patient with the code number of 00486295 (Right femur with intramedullary canal) which consists of the number of vertices, the number of edges, and the number of faces.



(1) The attributes of the 3D femure obtained from a patient with the code number of 00486295 (Right femure without intramedullary canal) which consists of the number of vertices, the number of edges, and the number of faces.

Figure 5.4: The attributes for the respective 3D femurs.

At this stage, a flowchart is designed to construct a 3D femur based on the input data as illustrated in Fig. 5.5. It is able to manage hundred thousands or even millions of vertices as long as the input data file is in .obj format. Our strategy for the 3D femur construction consists of the following steps:

- 1 OnFileOpen()
- 2 glmDelete(mesh)
- 3 mesh_structure.freeData()
- 4 fileName = GetPathName()
- 5 InitalValue()
- $6 \quad mesh = glmReadOBJ(\)$
- 7 glmDimensions(mesh, dimension)
- 8 Init3DStructOBJ()
- 9 meshFace.calNormalVectors()
- $10 \quad meshEdge.calCenter(\)$

- 11 RefreshDisplay()
- 12 3D Femur

Further details on how each of these steps are performed in our approach are provided throughout the following sections.

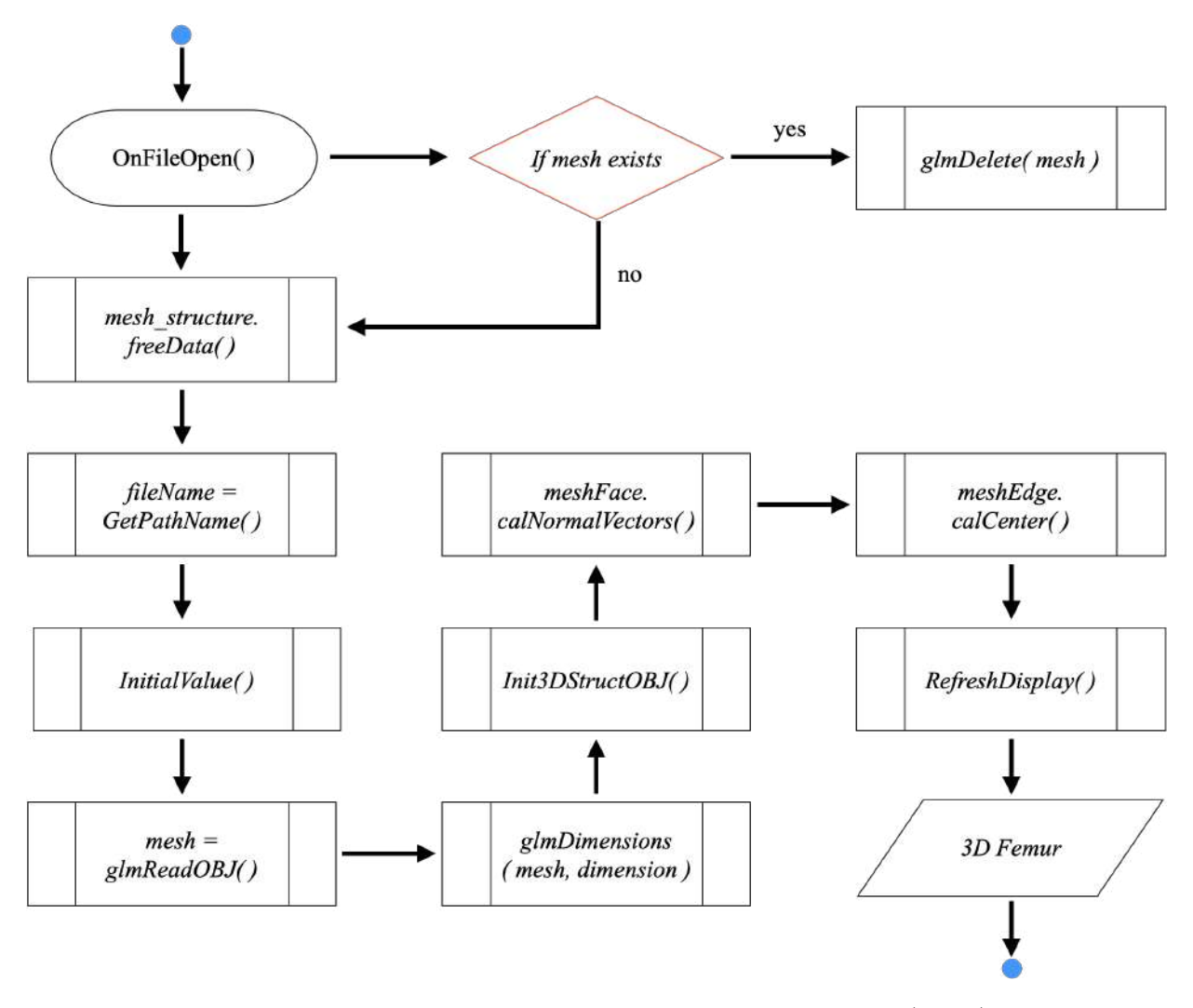


Figure 5.5: This flow chart shows the defined functions, together with the OpenGL Mathematics (GLM) that is used to achieve the 3D femur construction.

1 OnFileOpen()

Prior in constructing the 3D femur, the orthopaedics are required to select any existing human femur's file in .obj format. We utilised the Microsoft Foundation Class (MFC) messages of *CFileDialog* class to implement the file-selection dialog boxes, for example, Open File and Save As, in a manner that is consistent with Windows standards.

We derive our own dialog box class from *CFileDialog* and writes a constructor to suit our needs. It behaves like the standard Microsoft Foundation Class (MFC) dialog boxes. The windows messages for this class vary based on what operating system you are using [248].

Once the CFileDialog object is created by using the constructor, we initialise the values and states of the dialog box controls. Then, the method of CFileDialog :: DoModal method is called to display the dialog box so that the orthopaedic can select the files.

The CFileDialog :: DoModal returns whether the orthopaedic clicked the OK (IDOK) or the Cancel (IDCANCEL) button. All the tasks below can be continued when the returned value of CFileDialog :: DoModal is equals to (IDOK).

2 glmDelete(mesh)

Once a data file is selected and the IDOK is returned, the next step is to check the existence of a 3D mesh. If there is an existing 3D mesh constructed, this step will delete it and initialise all the attributes in this 3D mesh structure. We deployed the libraries from OpenGL Mathematics (GLM) [20] to define the structure of a 3D mesh.

The structure of a 3D mesh in OpenGL Mathematics (GLM) libraries are defined with the some of the following attributes:

- Path name to a 3D mesh.
- Number of vertices in a 3D mesh.
- Array of vertices.
- Number of normals in a 3D mesh.
- Array of normals.
- Number of triangles in a 3D mesh.
- Array of triangles.
- Position of the vertices for a 3D mesh, (x, y, z).

3 mesh_structure.freeData()

Apart from using the structure of a 3D mesh from OpenGL Mathematics (GLM) [20], we customised our own 3D mesh structure that is

designed for the 3D femur. All attributes and all the related operations are defined in this structure, which consists of the following:

Attributes

- (a) Points: The coordinates of the vertices, pointers to the previous point, pointer to the neighbouring point, incident edges, incident faces, and etc.
- (b) Edges: Starting point, ending point, length of the edge, number of incident faces, pointer to the previous edge, pointer to the neighbouring edge, and etc.
- (c) Faces: The connecting three (3) points, normal vector components, cross product vectors, number of linked edges, pointer to the previous face, pointer to the neighbouring face, and etc.

Operations

- (a) Points: Constructors, edge formation, face formation, edge deletion, and face deletion.
- (b) Edges: Constructors, cross product calculations, face formation, and face deletion.
- (c) Faces: Constructors, normal vector calculation, edge formation, edge deletion, edge validation, and point validation.

4 fileName = GetPathName()

GetPathName() is one of the public method in CFileDialog class. It retrieves the full path of the selected data file entered in the dialog box. The path of the filename includes the file's title plus the entire directory path.

5 <u>InitalValue()</u>

We create this method to initialise all the attributes for the following purposes:

- (a) For drawing and rendering.
- (b) For 3D skeletonization.
- (c) For 3D transformations.

$6 \quad mesh = glmReadOBJ(\)$

This method reads a 3D mesh description from a Wavefront file in .obj format. It is written by Nate Robins [20]. It returns a pointer to the created 3D mesh which should be free with the *glmDelete()*.

After the data file is opened successfully, this method will first allocate a new 3D mesh by initialising all the attributes to null. Then, the data file will be passed to the glmFirstPass(mesh, filename) method

to obtain all the statistics of the 3D mesh such as the number of vertices, the number of normals and etc. The memory of these attributes will then be allocated accordingly.

The next method to be called is the glmSecondPass(mesh, filename). This method receives the same Wavefront data file for the details of the 3D mesh such as the vertex coordinates, vertex normals, face indexes and etc.

7 glmDimensions(mesh, dimension)

At this stage, all the details are collected from the Wavefront files and the dimensions of the 3D femur can be calculated. The dimensions are a measurable extend of a particular kind, such as length, breadth, depth, or height. In this step, the width, height and depth of the 3D femur are computed.

This measurement is crucial for defining the cylindrical slider that is used during the 3D skeletonization. Additional details on the usage are provided in Chapter 6.

$8 \quad \underline{Init3DStructOBJ(\)}$

Our created 3D mesh structures are initialised, and the collected details from the Wavefront files are assigned to all the attributes, including the vertices formation, edges formation and the faces formation. A complete 3D mesh structure will be setup at the end of this method.

9 meshFace.calNormalVectors()

This method is implemented to compute the normal vectors of a face of the 3D femur, by applying the cross products of two adjacent vectors. Further details on how these calculations are performed in our approach are provided in Chapter 6.

10 meshEdge.calCenter()

This method is implemented to calculate the centre points for all the respective edges of a 3D femur.

11 RefreshDisplay()

This method is required to make the 3D femur visible on the screen. Furthermore, it consists of all the drawing operations for the following items:

- (a) Axes (x, y, z),
- (b) Vertices,
- (c) Edges,
- (d) Faces,

- (e) Cylindrical Slider,
- (f) Selected faces within the cylindrical slider,
- (g) Messages.

12) 3D Femur

Finally, a 3D femur is constructed based on the .obj data files and displayed on the screen as shown in Fig. 5.4. These methods have provided the answers for the following:

- (a) How to read the information from the .obj text files as shown in Fig. 4.7, that begins with the vertex positions, vertex normals and the faces? ✓
- (b) How to construct the 3D femur based on the read data? ✓

5.6 The Final Outputs

The final outputs for this module are illustrated in Fig. 5.6. The main goal in this module is to allow the user to select any .obj files to be displayed in 3D format based on the input data.

Therefore, we defined the following experiences a user would go through in sequence when interacting with this module:

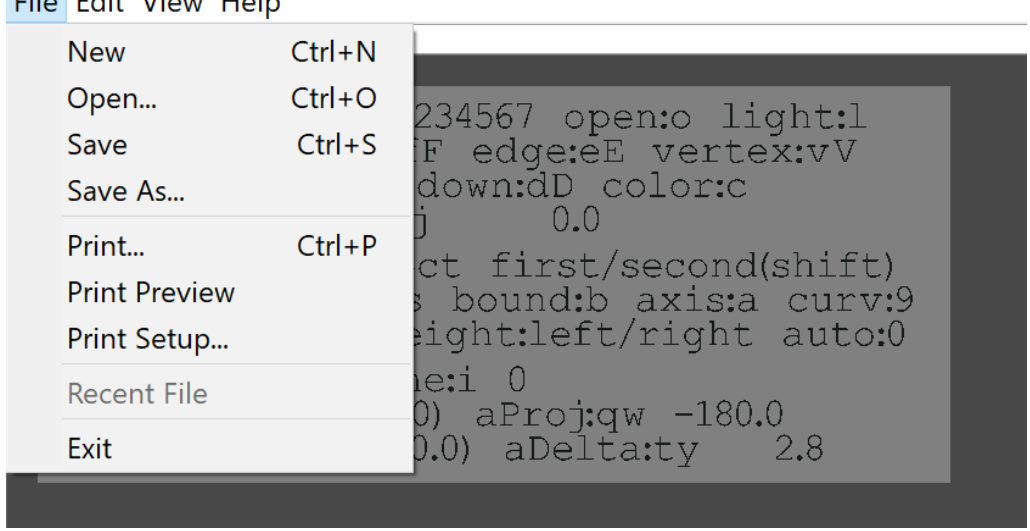
- A. Select File menu when the program is executed (Refer to Fig. 5.6a).
- B. Select the "Open..." command from the File menu (Refer to Fig. 5.6b).
- C. Select any desire 3D files in .obj format from the popped up dialog box (Refer to Fig. 5.6c).
- D. The 3D mesh is then constructed accordingly and display in faces view by default in the program canvas (Refer to Fig. 5.6d).

In order to change the view of the 3D femur, the user can perform the following actions on the keyboard:

- Press 'E' or 'e' key to change to edges view.
- Press 'V' or 'v' key to change to vertices view.
- Press 'F' or 'f' key to change to faces view.

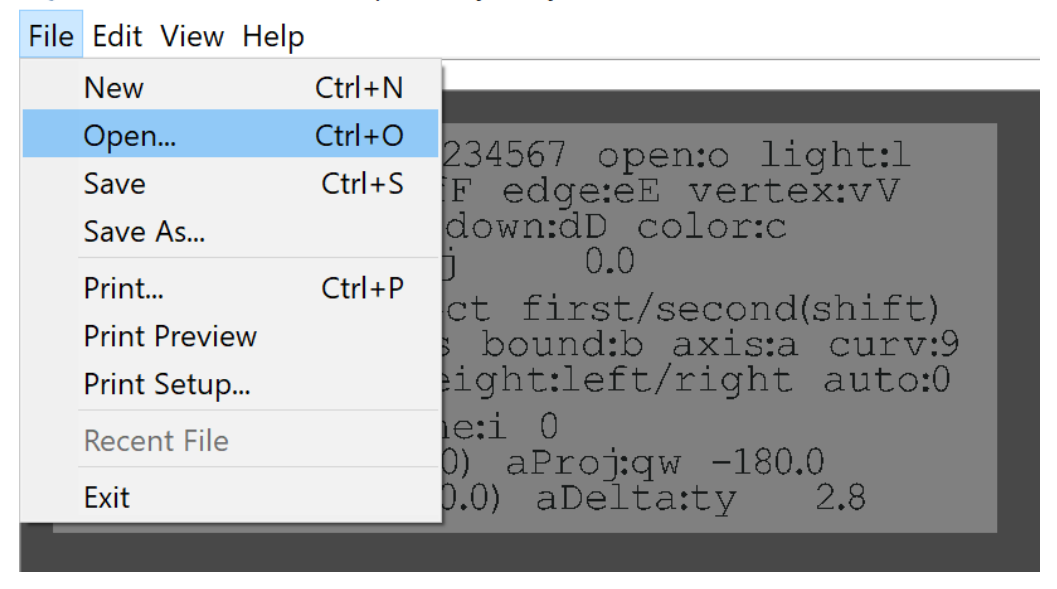
Alternatively, the view can be changed using the selections in the View menu as shown in Fig. 5.6g.





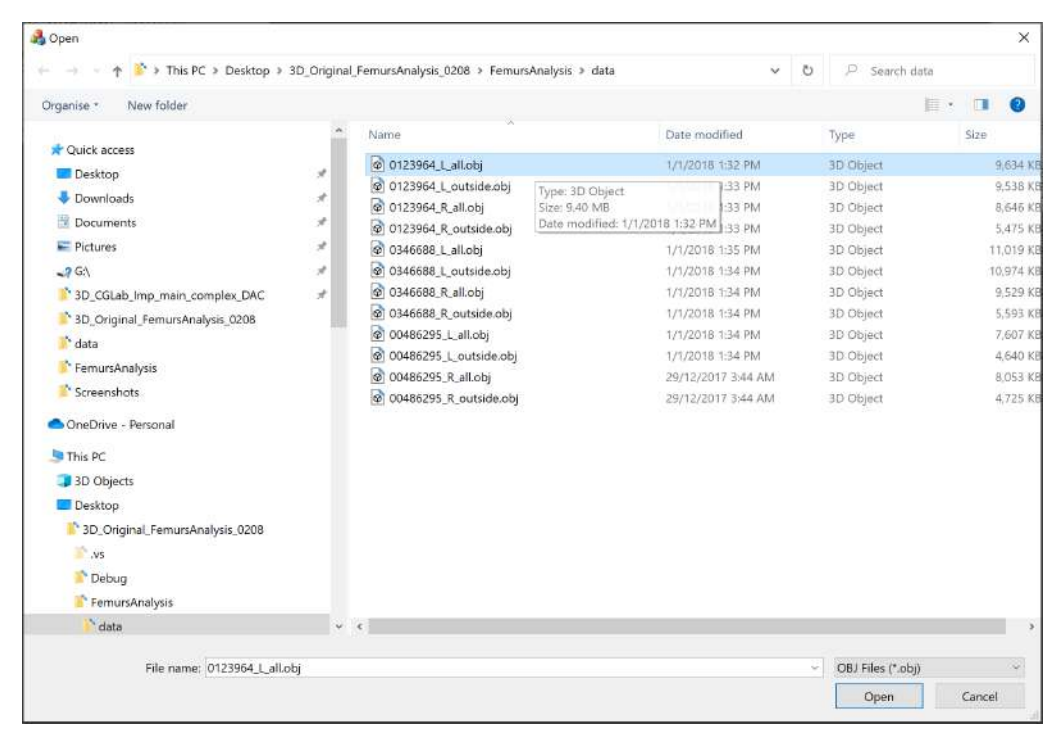
(a) This is the File menu that consists of: New, Open..., Save, Save As..., Print..., Print Preview, Print Setup, Recent File and Exit commands. There are several commands can be accessed via keyboard shortcuts.

<page-header> 3D-FSA: 3D Femur Shape Analysis System

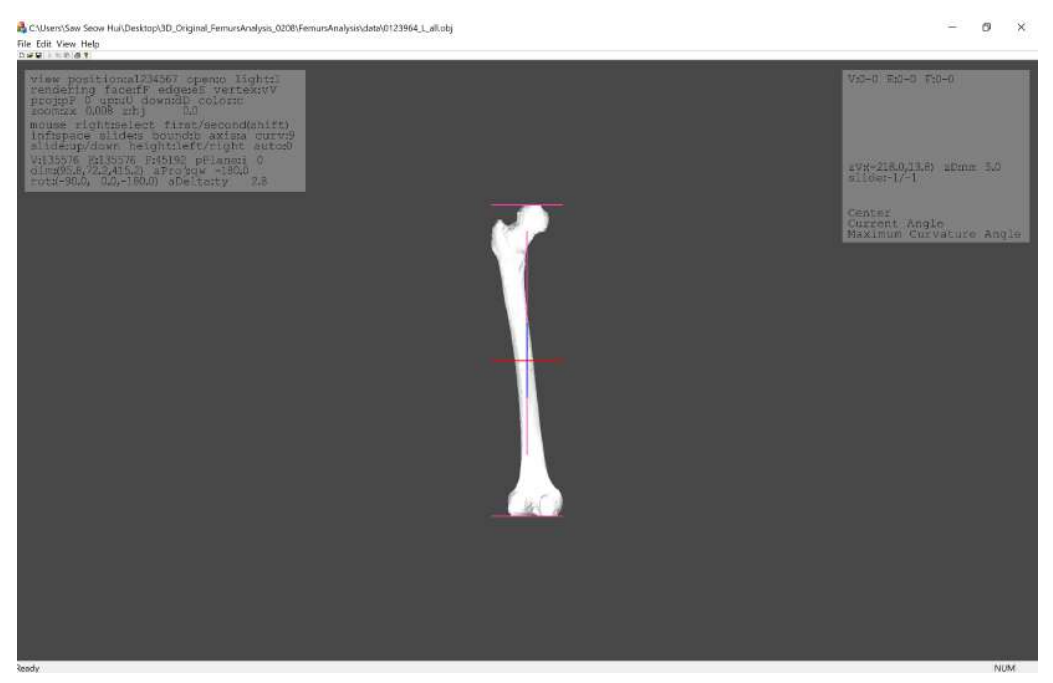


(b) When the user select "Open..." command.

Figure 5.6: The outputs of this module: 3D Femur Construction in 3D-FSA.

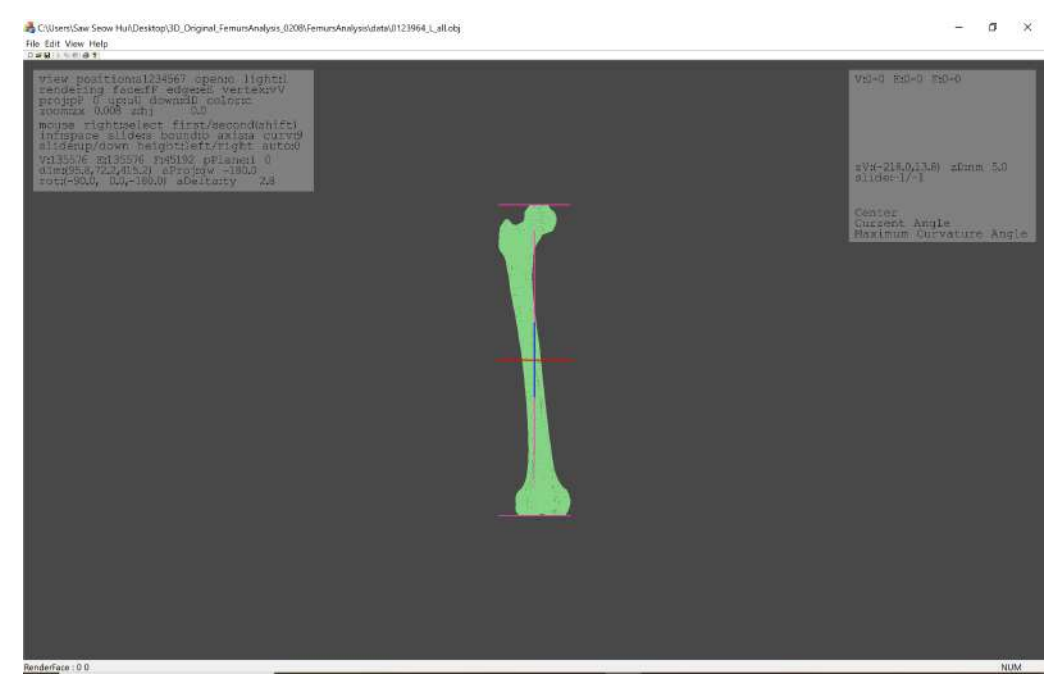


(c) A dialog box will be popped out and any femur in .obj format can be selected.

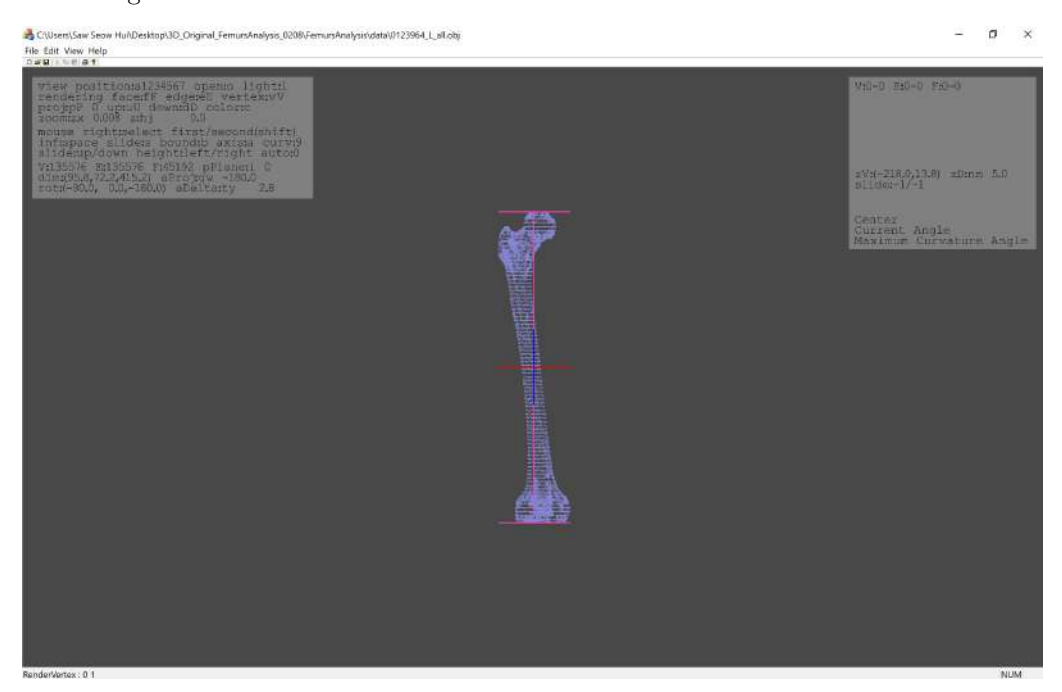


(d) Once the Open button is clicked, the 3D femur is displayed in faces view by default

Figure 5.6: The outputs of this module: 3D Femur Construction in 3D-FSA).

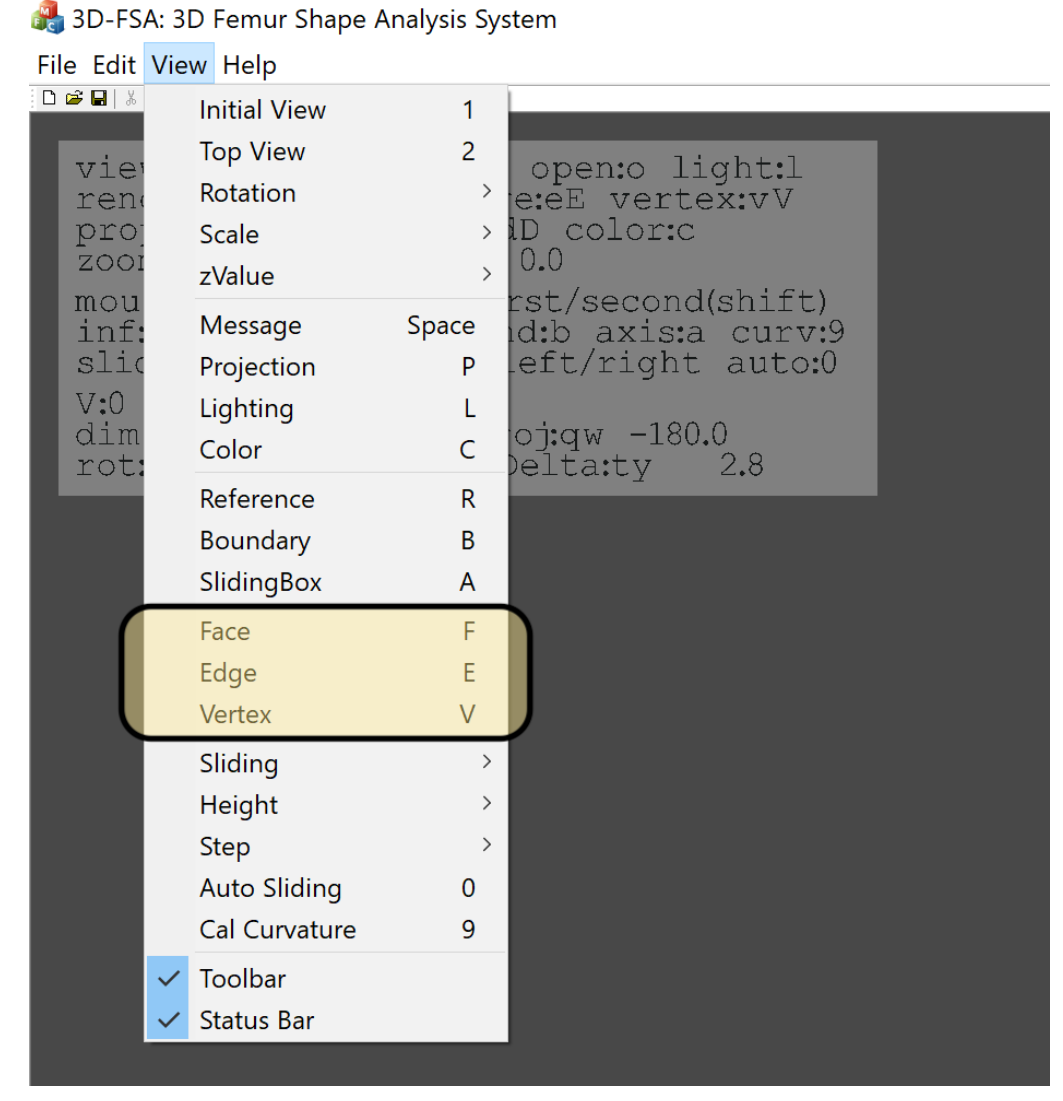


(e) When the key 'E' or 'e' is detected from the keyboard, the 3D femur is displayed in edges view.



(f) When the key 'V' or 'v' is detected from the keyboard, the 3D femur is displayed in vertices view.

Figure 5.6: The outputs of this module: 3D Femur Construction in 3D-FSA).



(g) The user can also change the view of the 3D femur by selecting the commands in the View menu.

Figure 5.6: The outputs of this module: 3D Femur Construction in 3D-FSA.

Chapter 6

3D SKELETONIZATION

This chapter introduces the reader to strategies for generating the MA that is based on the MAT from the constructed 3D femur in the previous Chapter 5. This phase plays a significant component employed later on by our proposed maximum-minimum centre approach.

6.1 The Innovation of this Module

This module is innovative both in the proposed 3D skeletonization and the thickness calculation for the compact bone (outer diameter) of the medullary canal. Concerning the proposed 3D skeletonization algorithm, although it is aligned with a general framework introduced by Lien et al. [249], new approaches have been introduced for the implementation of distinct stages of the framework leading to improved accuracy and robustness as has been verified by an experimental evaluation.

The two (2) most significant contributions of our 3D skeletonization algorithm is the straightforward centroids computation and the utilisation of the projection method [86, 250] to compute the thickness of the compact bone (outer diameter) of a femur's medullary canal based on the portions

covered by the user-defined cylindrical slider. Both of these approaches differ significantly from these existing approaches [249, 86, 250].

The centroids computation in our algorithm is able to construct a MA that represents the shape of the 3D femur, without the use of other expensive computation such as the principal axis which used by Lien et al. [249]. Apart from that, the utilisation of the projection method in a 3D femur and for the thickness calculation is a novel and radically different approach in 3D skeletonization. Whereas [86, 250] presented the projection methods to locate voxels [86] and other types of 3D mesh [250] to be centred with respect to three orthogonal slicing directions.

The major advantage of our approach is that the computed MA of a 3D femur does not produce spurious branches, which avoid unnecessary noises to facilitate the anatomical analysis by the orthopaedics. Additional details on each of the processes are provided throughout the rest of this section.

6.2 My Tasks

Since this is a collaborative research project, my tasks in this module are as follows:

- To design the flowchart for the following features:
 - A. How to compute the MA for the constructed 3D femur?
 - B. How to provide the measurements for the thickness of a compact bone (outer diameter) of a femur's medullary canal?

• To convert the designed flowchart into program implementation, incorporated with our written program.

6.3 The Basic Idea

Fig. 6.1 illustrates the basic idea of our 3D skeletonization. The medial centres are computed with respect to the user-defined cylindrical sliders which will describe further in Section 6.4.2. The MA is then constructed by connecting all these medial centres.

Besides that, we have divided the display space into two (2) planes:

- Base Plane: A plane that is parallel to the lateral z axis.
- Projection Plane: A flat plane which the objects created by the line of sight is projected. In effect, 3D object is transformed into a 2D representation, also called projections.

Both the medial centres and media axis are located in the base plane. However, the computed medial centres are also projected to the projection plane to be used in the radius function calculation. Once the radius function was retrieved, the maximal inscribed circle can be formed on the projection plane. The details are explained in the following sections.

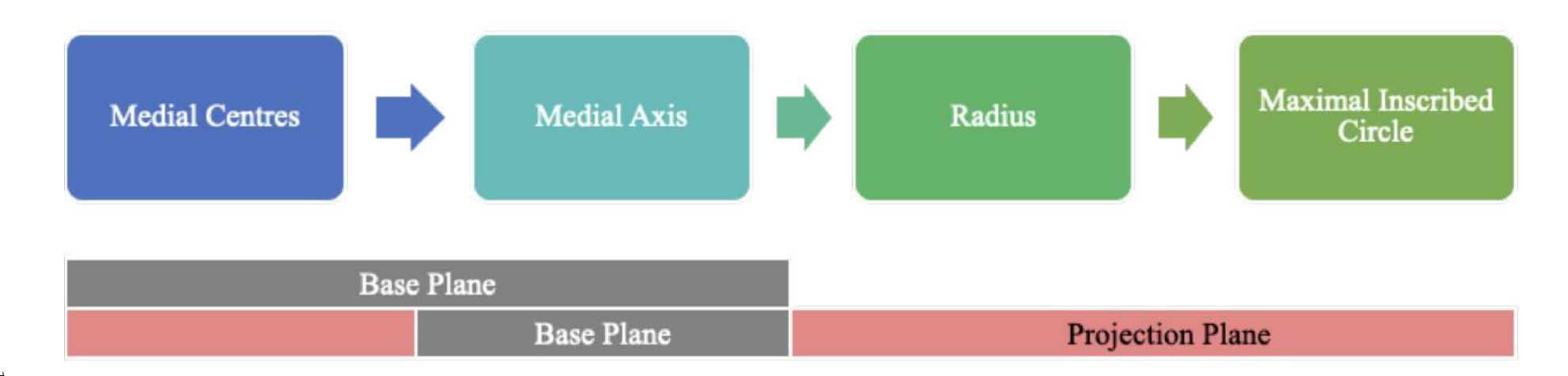


Figure 6.1: The basic idea of our 3D skeletonization algorithm.

6.4 Medial Axis Transform

MAT was introduced by Blum [74] and is mainly composed of two (2) properties: the MA and the radius function as shown in Fig. 6.2 (refer to Eq. (6.1)).

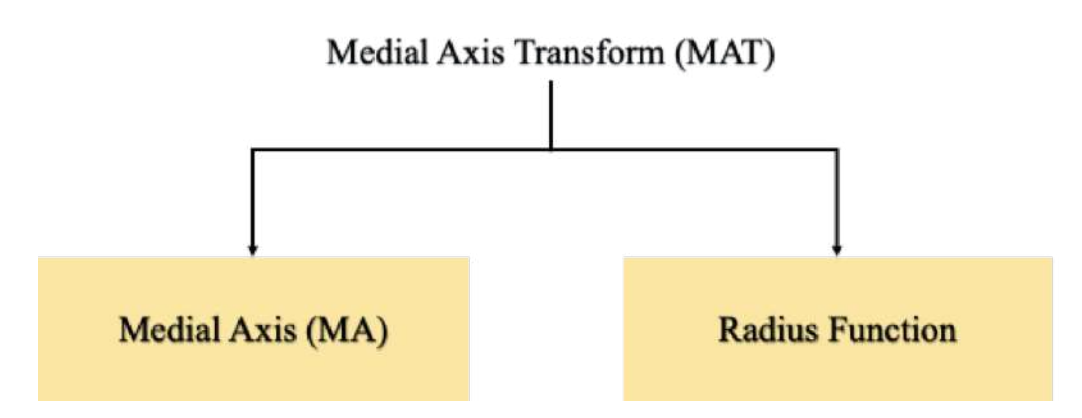


Figure 6.2: MAT is mainly composed of MA and radius function.

Let Ω be a connected bounded domain in \mathbb{R} with n-dimensions (3D femur with boundaries), and let B to be the loci of all maximal inscribed disks that meet two (2) or more boundary points without crossing any of the boundaries in Ω . We define MA, denoted by $MA(\Omega)$, as the set of centre lines or disks obtained from B [251] as written in Eq. (6.2).

Each vertex p is defined as centre vertex in the $MA(\Omega)$ and the radius r_s of the s^{th} ball in $B_r(p) \in B$, which forms the medial circle, and the volume is enclosed by the surface in Ω , which is exactly the union of these circles, as presented in Eq. (6.2). In other words, this notation indicates the medical circles in B that is formed by a set of centre vertices p, together with the radii r.

$$MAT(\Omega) = \{(p, r) \in \mathbb{R}^n \times \mathbb{R} | B_r(p)$$
 (6.1)

is maximal ball in Ω }

Remark. $MAT(\Omega)$ is the combination of two (2) properties: i) $MA(\Omega)$, ii) Radii, r.

$$MA(\Omega) = \{ p \in \mathbb{R}^n | r \ge 0 \text{ s.t. } (p, r) \in MAT(\Omega) \}$$
 (6.2)

Therefore, to obtain the skeleton of the 3D femur, we determined the maximum radius r_s of each circle s (Refer to Eq. (6.16)) that is well suited for each slice (portion) of the irregular inner 3D femur. Then, an approach is introduced to find the reliable skeleton of the 3D femur, namely the maximum-minimum centre approach (Refer to Section 6.4.2).

Before further explanation, we review some basic facts regarding graphs in the context of 3D skeletonization. A bidirectional weighted graph $G = \{V, E\}$ consists of a set of vertices V and a set of bidirectional edges E that connect them. The 3D femur is composed of a large number of faces F that are made of three (3) connected edges each, or in other words, a triangle.

In this thesis, four (4) processes are involved, as depicted in Fig. 6.3, to compute a reliable and consistent skeleton from a 3D femur. A more detailed explanation is provided in the following sections.

6.4.1 Axis Adjustment and Feature Detection

After the second (2^{nd}) phase, namely the 3D femur construction (Chapter 5) has completed, the dimensions of the 3D femur are calculated which consists of the width, height and depth measurements as highlighted in Fig. 6.4.

The strategy for computing such dimensions basically consists of the

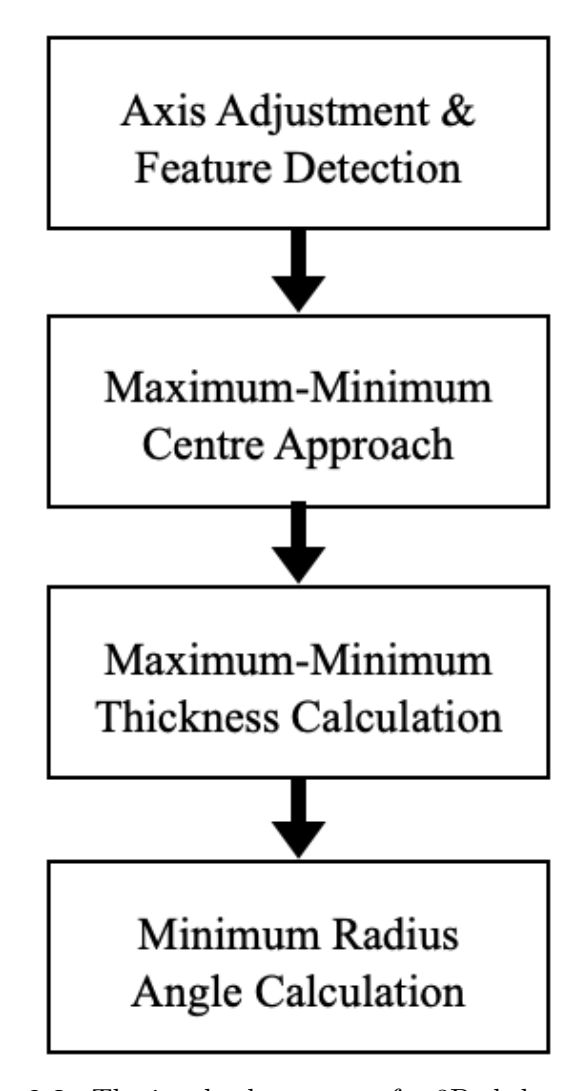


Figure 6.3: The involved processes for 3D skeletonization.

following steps:

- A. Obtain a set of maximum and minimum values among all the coordinate of the vertices (x, y, z) (Refer to the flowchart in Fig. 6.5a).
- B. Calculates the dimensions including the width (dimension[0]), height (dimension[1]) and depth (dimension[2]) of the 3D femur (Refer to the flowchart in Fig. 6.5b).
- C. Calculates the centre point of the 3D femur: (cx, cy, cz) (Refer to the flowchart in Fig. 6.5b).
- D. Transform the 3D femur so that it fits in the centre of the display using the above parameters (the centre points) (Refer to the flowchart in Fig. 6.5b).

We incorporate the method of *glmDimensions* in our program as shown in the highlighted flowchart in Fig. 6.4. This method is mainly obtain a pair of maximum and minimum values among all the vertices of a 3D femur, resulting a maximum coordinate (max_x, max_y, max_z) and a minimum coordinate (min_x, min_y, min_z), as shown in the flowchart of Fig. 6.5a.

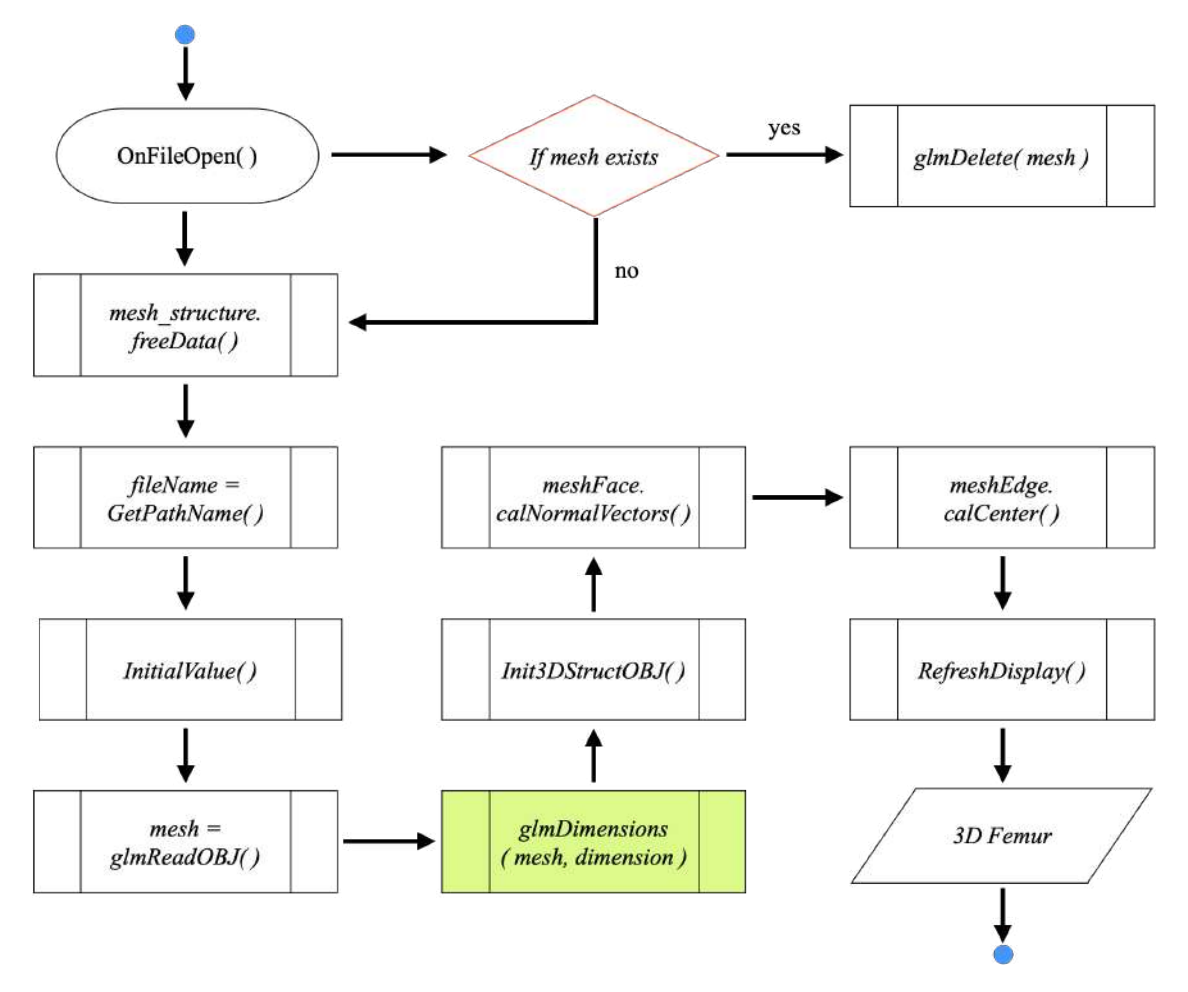
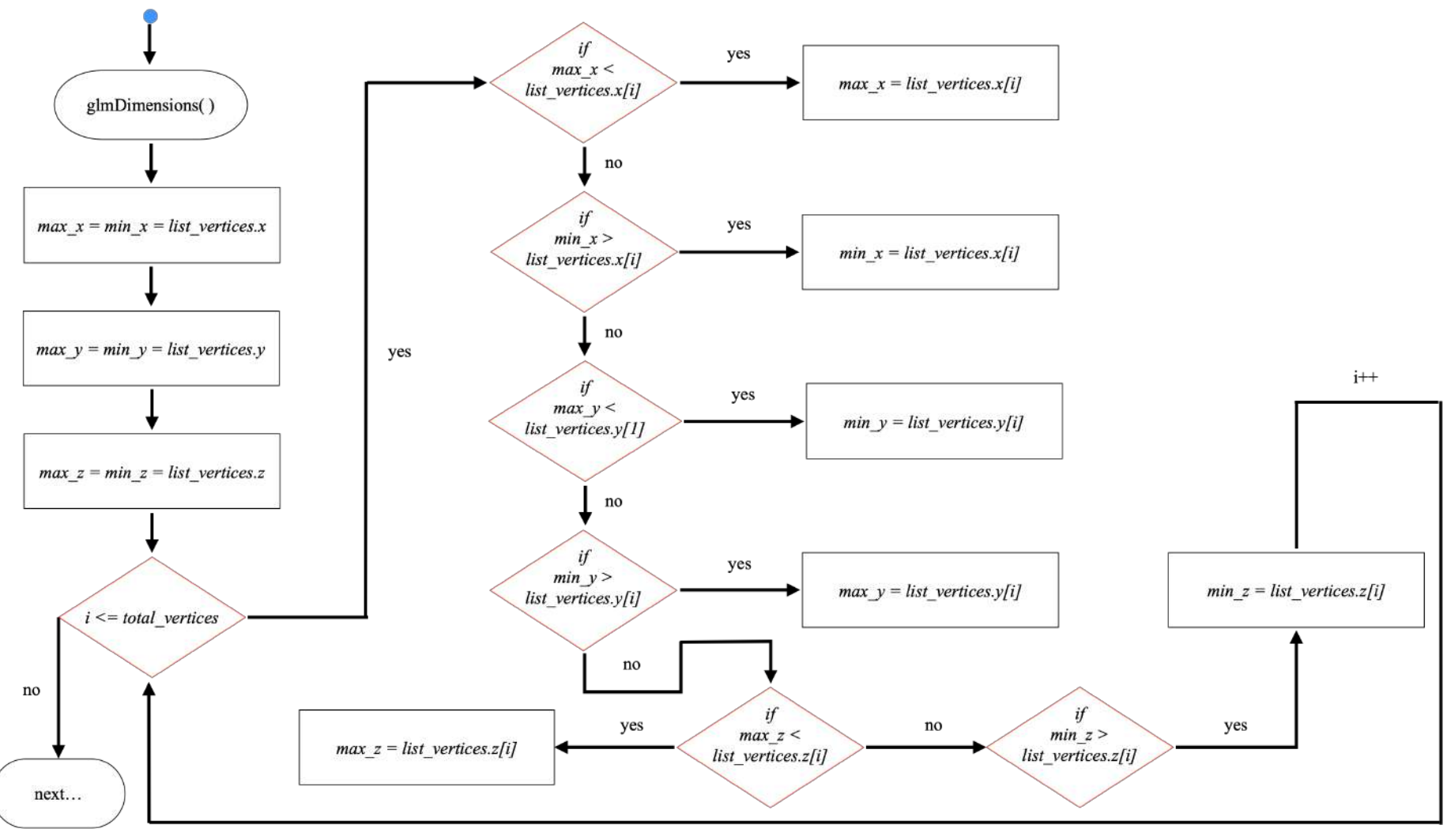
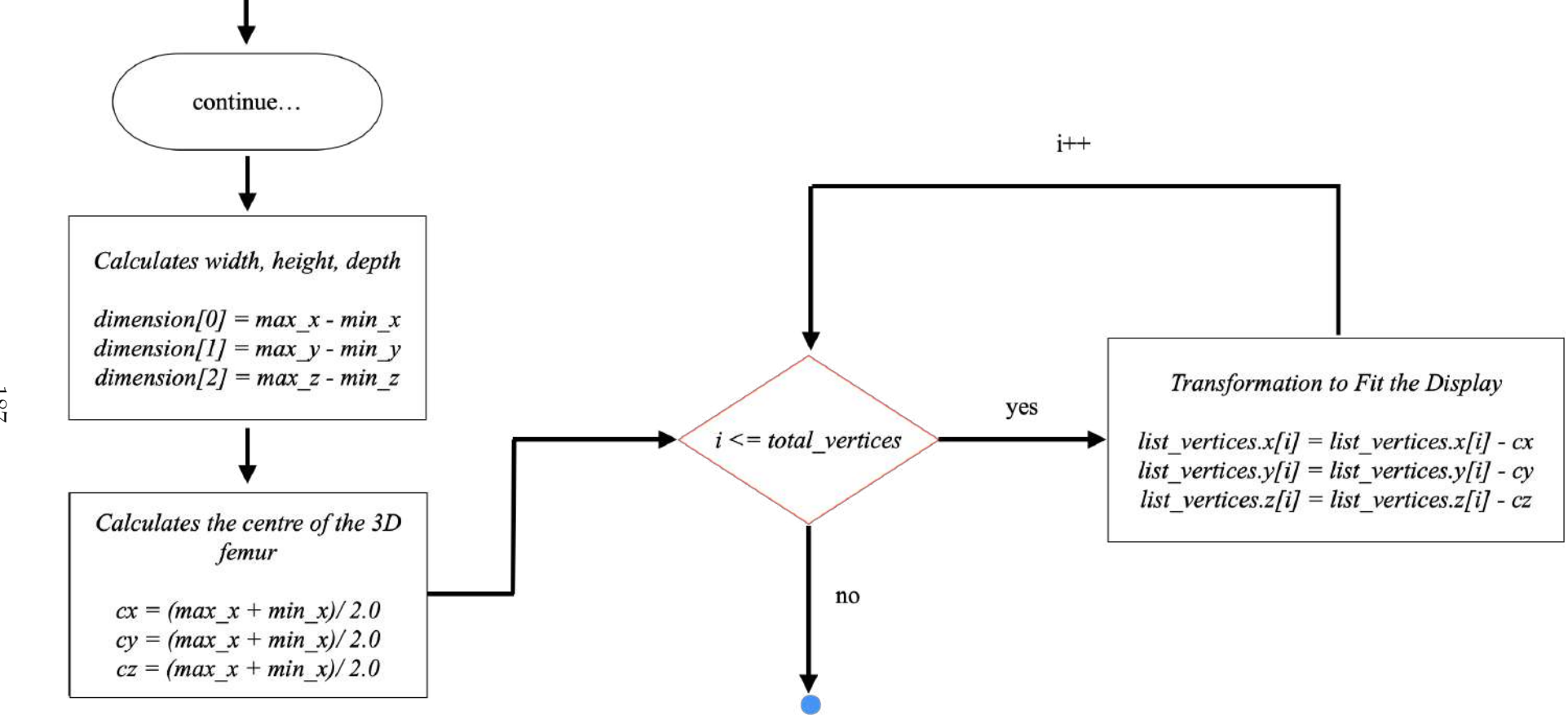


Figure 6.4: The highlighted method, *glmDimensions* is written by Nate Robins [20], and the obtained measurements are used to form our display components.



(a) The first (1^{st}) part of the processes which involves looking for the maximum and minimum values among all the coordinate of the vertices (x, y, z).



(b) The second (2^{nd}) part of the processes which involves calculating the dimensions of the 3D femur, the centre point of the 3D femur, and the transformation of the 3D femur to fit on the display.

Figure 6.5: The processes involved in glmDimensions().

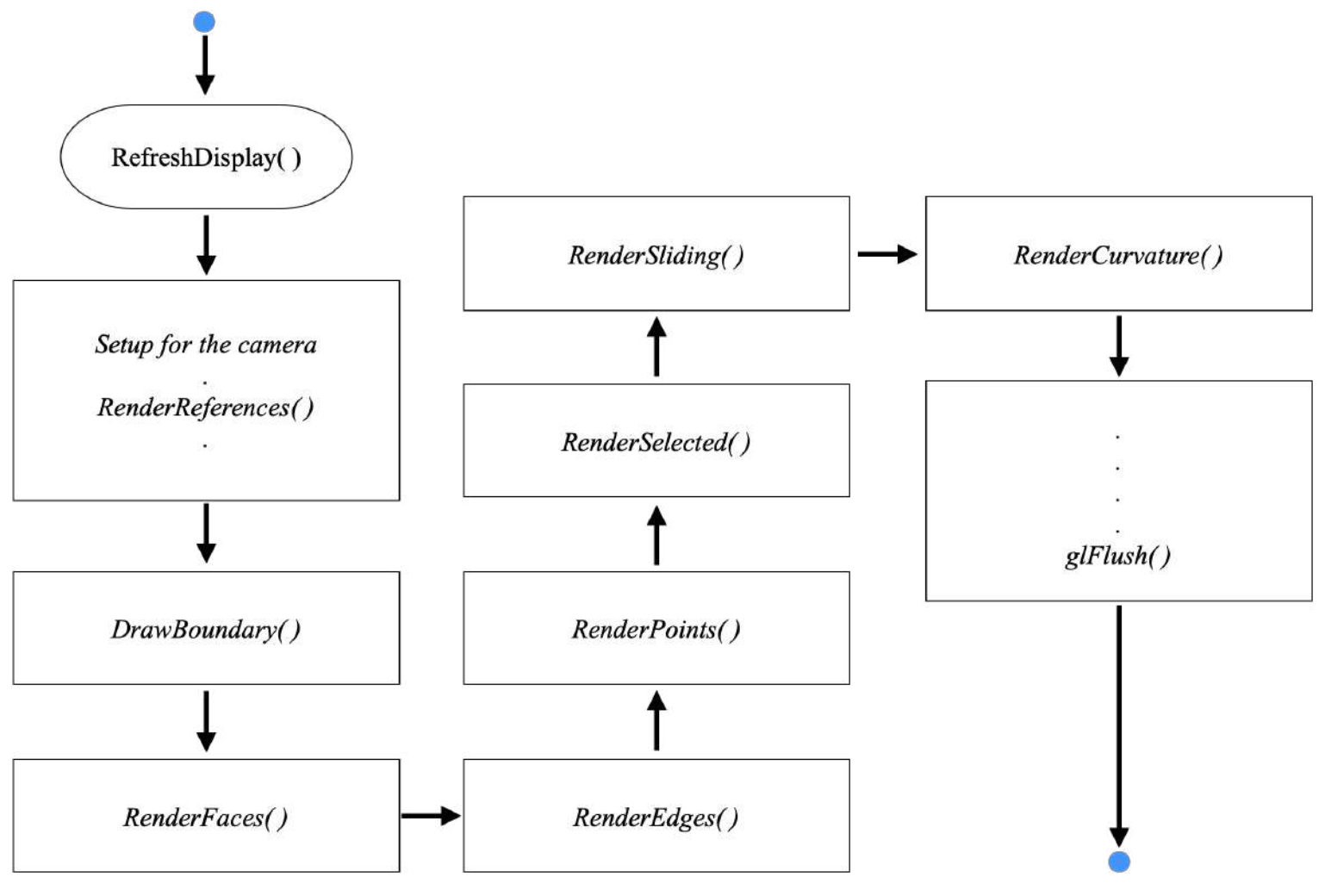


Figure 6.6: Our written program for drawing the axes, boundary, 3D femur (with vertices, edges and faces), the cylindrical slider and the curvature of the MA, based on the measurements returned by the *glmDimensions* method written by Nate Robins [20].

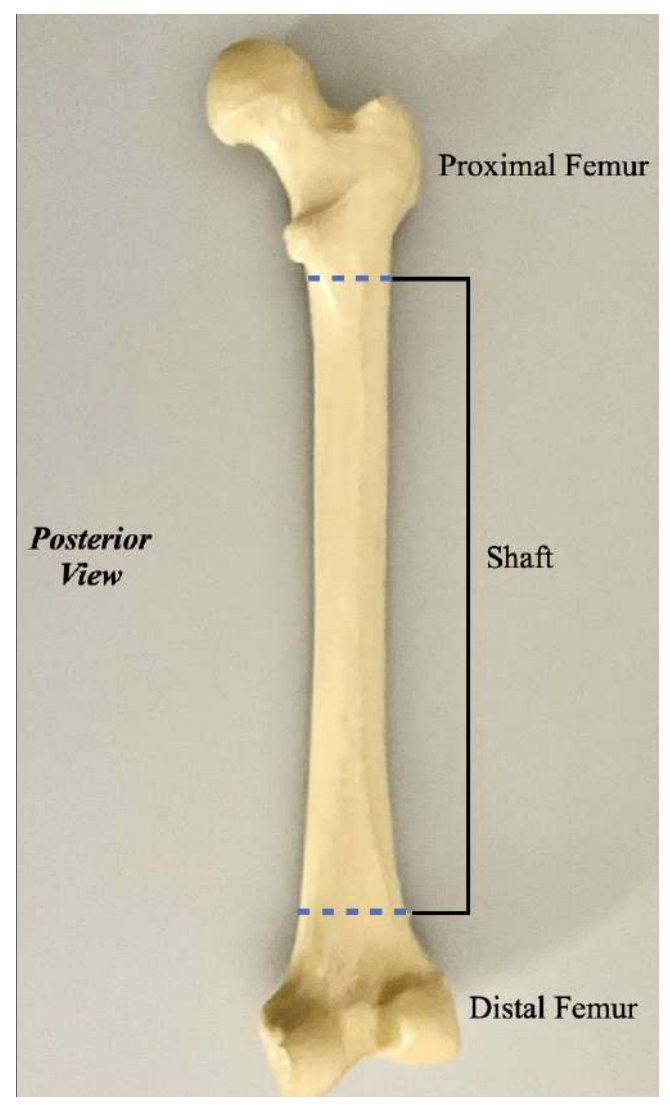
Using the obtained measurements, the dimensions, including the width, height and depth of a 3D femur, are determined by the deduction of maximum coordinate and minimum coordinate as shown in the flowchart of Fig. 6.5b, resulting the dimension array (dimension[0], dimension[1], dimension[2]). Moreover, the centre of the dimensions is calculated to allow the appropriate transformation of a 3D femur such as translation, to be fitted on the display. Fig. 6.8 illustrates the outcomes of this process.

This phase also involves measuring and recognising the distinctive features of the 3D femur. It examines every vertex to determine the position of the distal femur (the area of the leg just above the knee joint [37]) and proximal femur (including the femoral head, neck and the region 5-cm distal to the lesser trochanter [252]) as illustrated in Fig. 6.7.

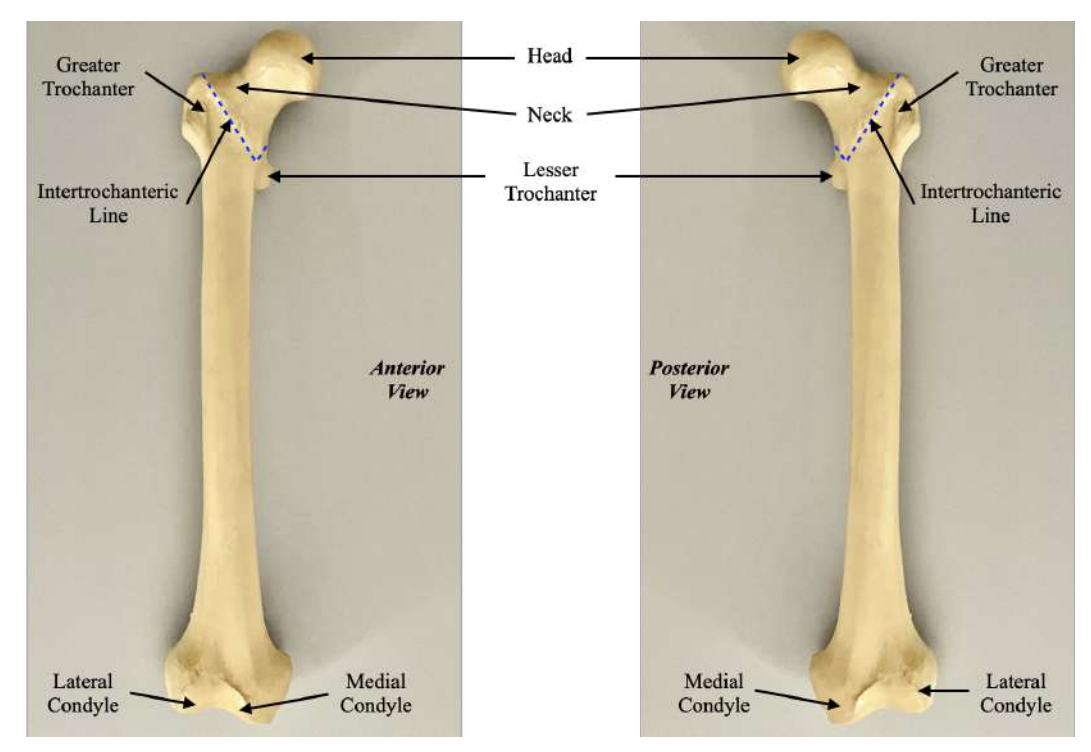
In addition, we create the method of RefreshDisplay() for managing all the drawings to the screen as illustrated in Fig. 6.6. The first step is to setup our camera with the appropriate parameters. Then, the RenderReferences() is called to draw the axes of (x,y,z).

Followed by the *DrawBoundary()* method which manages a pair of bounding boxes that are drawn as rectangles and *pink* in colour, as shown in Fig. 6.8. These bounding boxes are based on the obtained measurements of the dimensions of a 3D femur and served as the indicators of the beginning (the distal femur) and ending (the proximal femur) bases for a 3D femur.

Besides that, this phase involves recognising the distinctive features of a 3D femur. It examines every vertices to determine the position of the distal femur (the area of the leg just above the knee joint [37]) and proximal femur



(a) (Posterior View) The femur is divided into three parts: proximal, shaft and distal.



(b) The anatomy of the femur for proximal and distal parts in anterior view and posterior view respectively.

Figure 6.7: The anatomy of a right femur.

(including the femoral head, neck and the region 5-cm distal to the lesser trochanter [252]) as illustrated in Fig. 6.7. The flowchart in Fig. 6.6 also shows three (3) different methods that are used to manage the drawing of these distinctive features of a 3D femur which consists of RenderPoints(), RenderEdges() and RenderFaces().

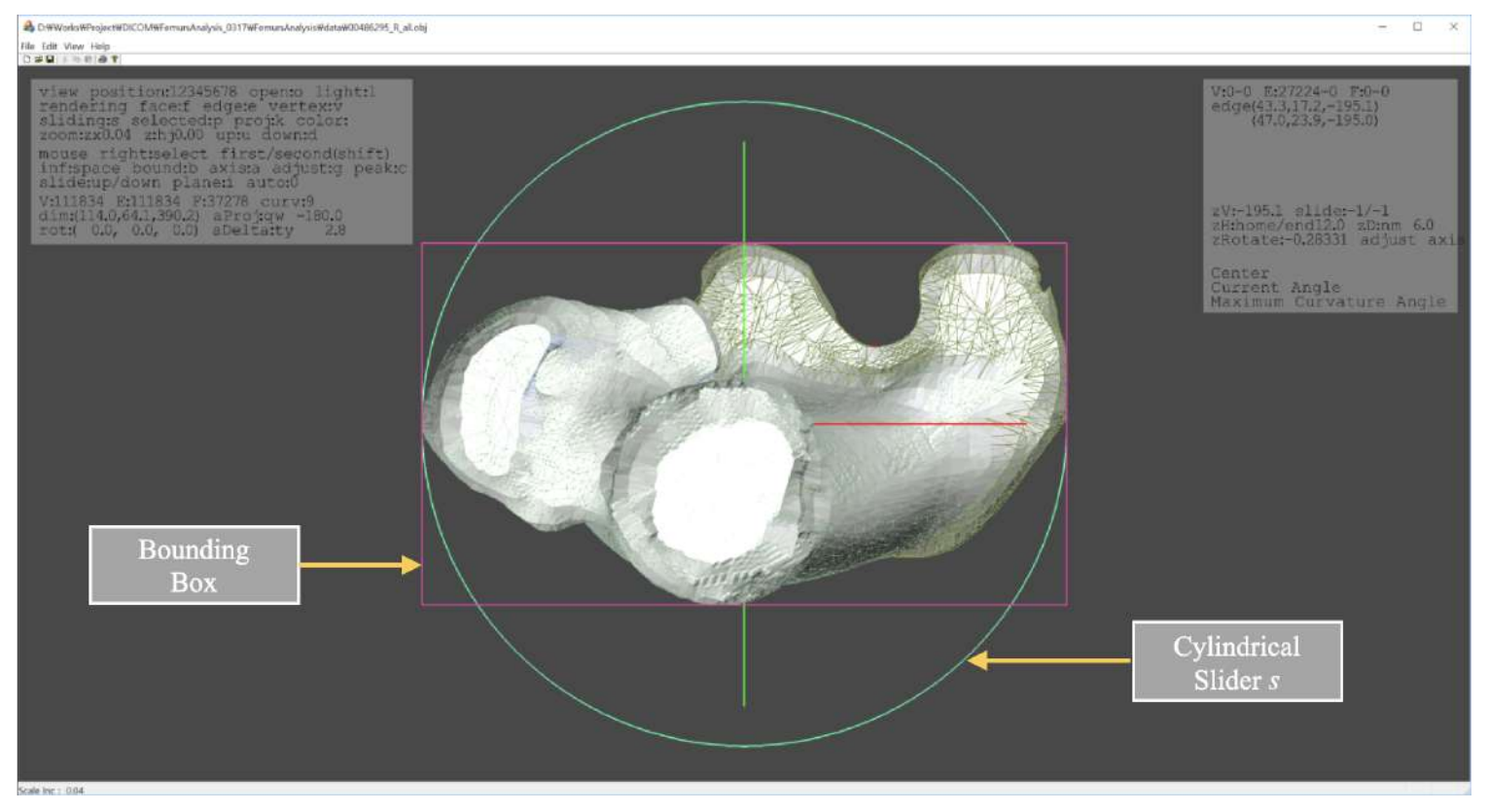
The green cylindrical shape that is made of two (2) separate circles with the defined distance or thickness h, decided by the user in the program is drawn by the method of RenderSliding(). The result is depicted in Fig. 6.9 and we called it the cylindrical slider s. The purpose of this cylindrical slider s is to slide over the entire 3D femur from the beginning to the end to capture and slice different portions.

Each slice that is captured by the cylindrical slider s is used to collect the adjacent faces (triangles) within that portion, as shown in brown in Fig.

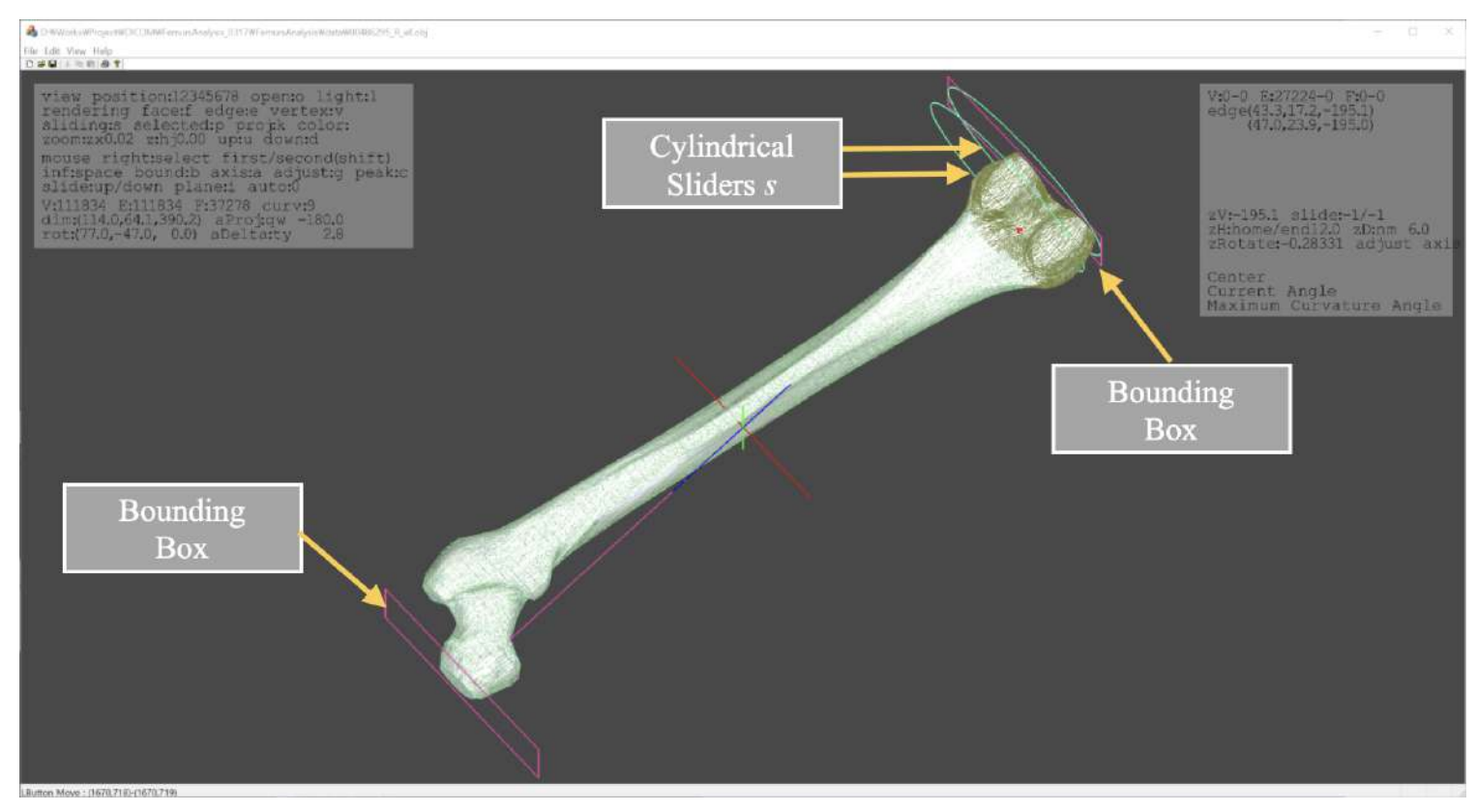
6.9, and perform the 3D skeletonization which will be explained in Section 6.4.2 and 6.4.3.

Another method that is written in this module is the *RenderCurvature()* method as shown in the flowchart of Fig. 6.6. This method is used to draw the calculated ROC which will be explained in Section 6.4.4.

Finally, the glFlush() command is to empty all commands in the buffers, causing all issued commands to be executed as quickly as they are accepted by the actual rendering engine. Though this execution may not be completed in any particular time period, it does complete in finite time. Thus, all programs should call this command whenever they count on having all of their previously issued commands completed [253].



(a) Left femur: The (x,y) – axis adjustment, bounding box $(pink\ in\ colour)$ and the cylindrical slider $s\ (green\ in\ colour)$ is calculated by the width and height of the left femur.



(b) Left femur: The z-axis adjustment extracted from the length of the left femur.

Figure 6.8: The calculation of the dimensions and adjustment for the axes in 3D based on the size of the 3D femur in the method of *glmDimensions*.

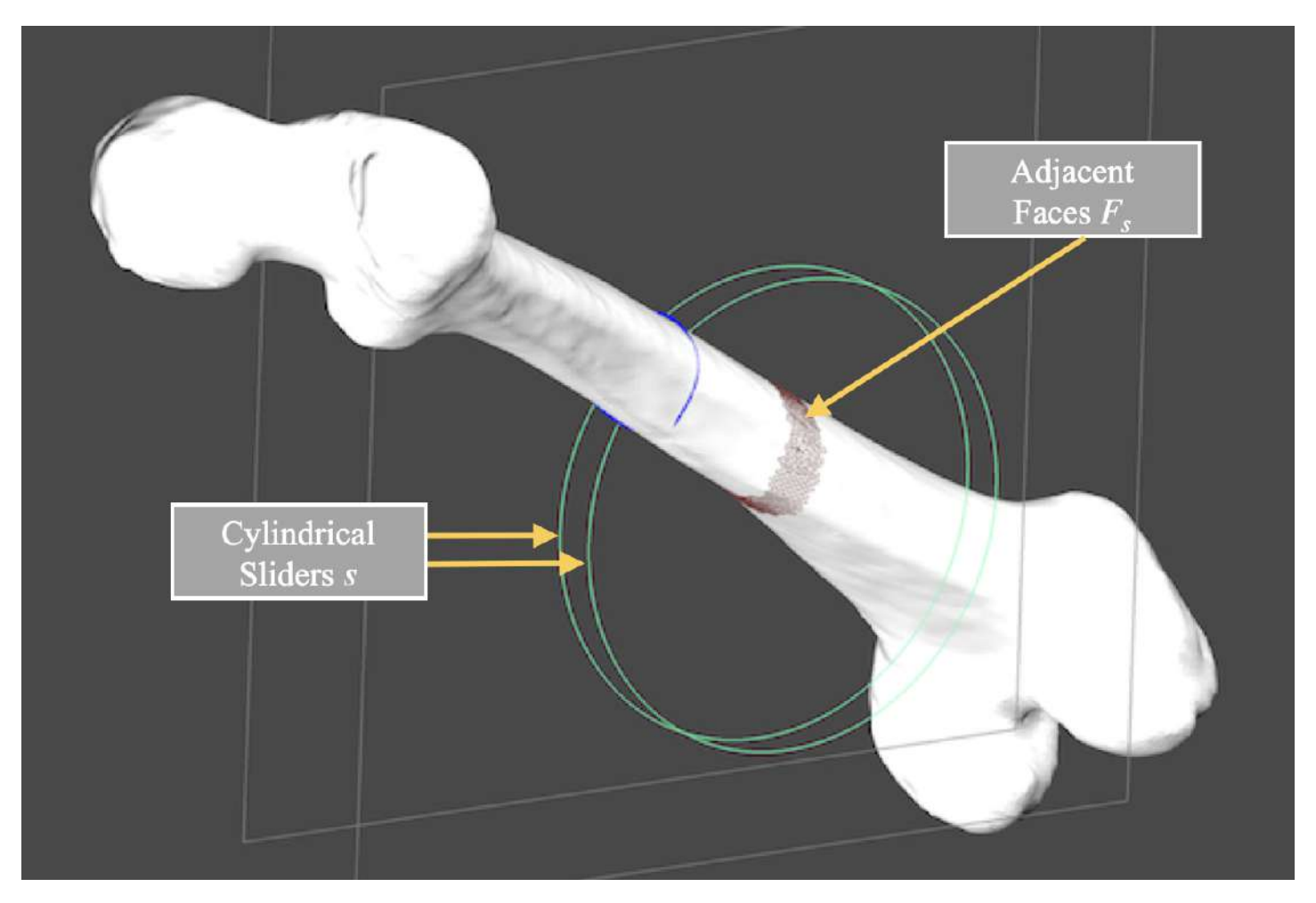


Figure 6.9: The cylindrical sliders s (The composition of two (2) green circles), adjacent faces F_s (brown faces (triangles)).

6.4.2 Maximum-Minimum Centre Approach

Prior to adjusting the axis and the feature detection of a 3D femur, we obtain the dimensions of the 3D femur by employing the strategy explained during Section 6.4.1, in order to obtain a set of significant parameters such as the boundary, the cylindrical slider s, and the proper display of the 3D femur to the screen. The results are then used in this Section for the computation of 3D skeletonization.

The MA is computed in this phase by simply applying our approach, namely the **maximum-minimum centre approach**. Once the MA is formed, the anatomical parameters of the femur, such as the diameter of the medullary canal and isthmus can be calculated. These parameters are significant in the preoperative measurements [10, 254, 52].

The medullary canal is the central cavity of the femur that contains the red or yellow bone marrow. These marrows are used to make blood cells and stores fat [255]. Whereas, isthmus of the femur is the region with the smallest IM diameter and the diameter of the isthmus affects the size of the IM nail that can be inserted into the femoral shaft [256].

Therefore, these scaled measurements can be obtained in this phase, by finding the maximum inscribed circle of the medullary canal as shown in the flowchart of Fig. 6.10. Moreover, the 3D femur is divided into several segments in sequence, by sliding the cylindrical sliders and the faces (triangles) within the specific segment are used in the computation. Each segment computes the centre vertex of the medullary canal and it is used to form the inscribed medial circles for the contour of the medullary canal.

It begins with the sliding process at position z-coordinate, together with

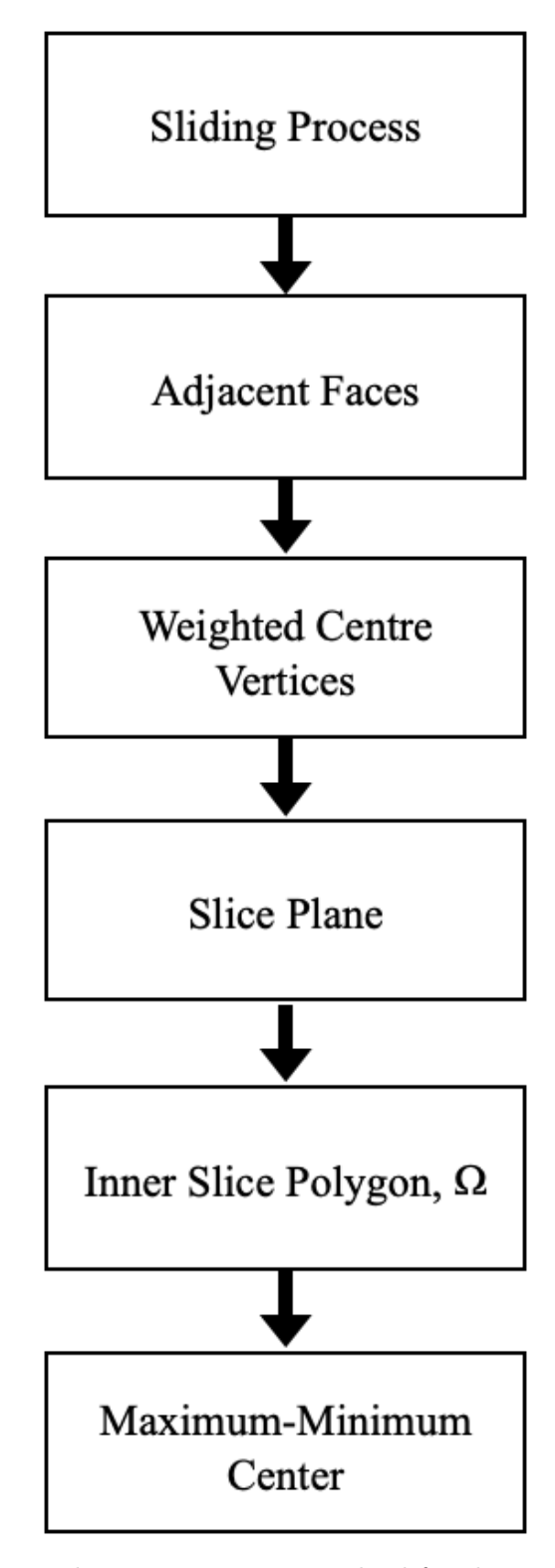


Figure 6.10: The implementation steps involved for the maximum-minimum centre approach in Section 6.4.2.

the defined cylindrical slider s, and the computed distance h. During this process, the vertices v_z within this selected portion from z to z + h are collected and added to V_s (refer to Eq. (6.3)).

Then, the faces (triangles) adjacent to each vertex in V_s are captured and stored in F_s with a total number of m faces (triangles). Thus, F_s consists of a collection of all the adjacent faces (triangles) within the cylindrical slider s.

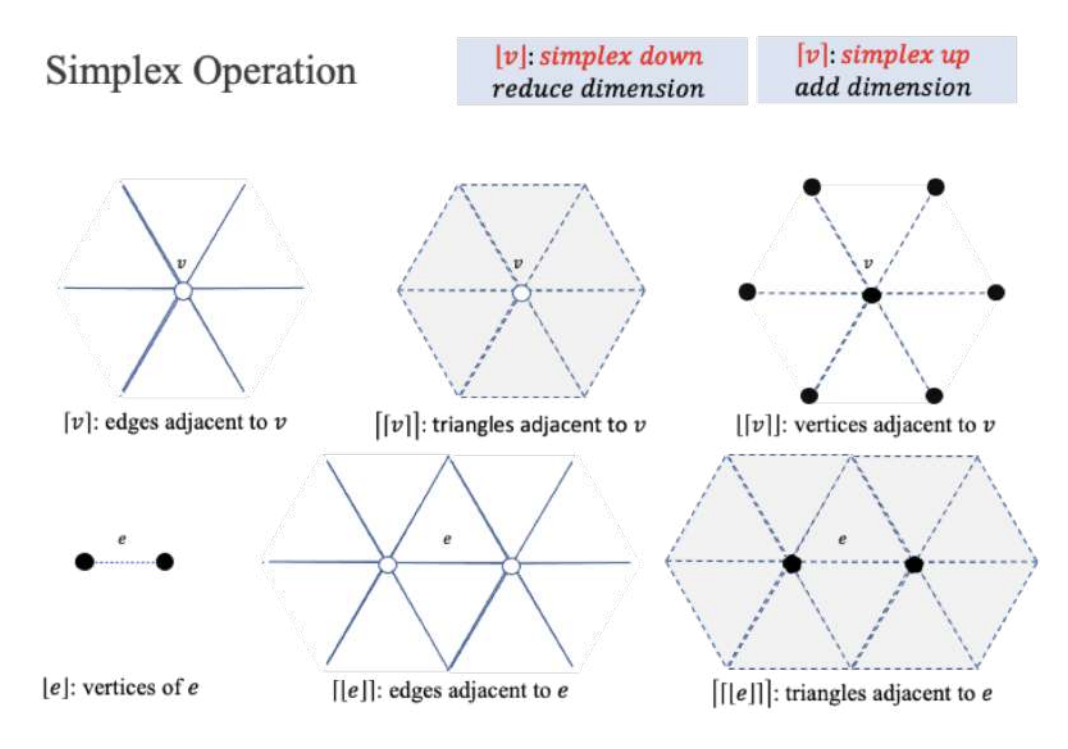


Figure 6.11: The simplex operators $\lfloor v \rfloor$ and $\lfloor v \rfloor$.

We take the advantage of the Lindstrom and Turk approach [257] for selecting the vertices, adjacent edges and the adjacent faces (triangles), by using the simplex operators as illustrated in Fig. 6.11. This approach was originally used for fast and memory-efficient 3D mesh simplification. The equation is denoted in Eq. (6.4) to acquire these adjacent faces (triangles). Fig. 6.9 illustrates the cylindrical slider and the adjacent faces (triangle) within the selected portion (highlighted faces (triangles) in brown).

$$V_s = \{v : v_z \in (z, z+h)\}$$
(6.3)

where $v = (v_x, v_y, v_z) \in R^3$, s = (z, z + h).

$$F_s = [[V_s]] = \{f_i\}_{i=0}^m. \tag{6.4}$$

With the acquired adjacent faces (triangles) in F_s , the following parameters (P) have to be computed for each face:

P. (1) The area $A(f_i)$ for each face (triangle) f_i in F_s is defined below:

According to [258], to find the area $A(f_i)$ for each face (triangle) f_i in F_s , we first find the vector of $\vec{e_i} = (v_0, v_2)$ and $\vec{e_{i+1}} = (v_1, v_2)$. Then, the cross product $\vec{e_i} \times \vec{e_{i+1}}$ is computed. The magnitude of this cross product will be calculated to obtain the area of the parallelogram enclosed by the two (2) vectors. Let assume that the cross product of $\vec{e_i} \times \vec{e_{i+1}}$ is \vec{n} . Taking the magnitude of this product yields to:

Area of parallelogram = $\|\vec{e_i} \times \vec{e_{i+1}}\| = \vec{n} (Refer to Fig. 6.12a)$ (6.5)

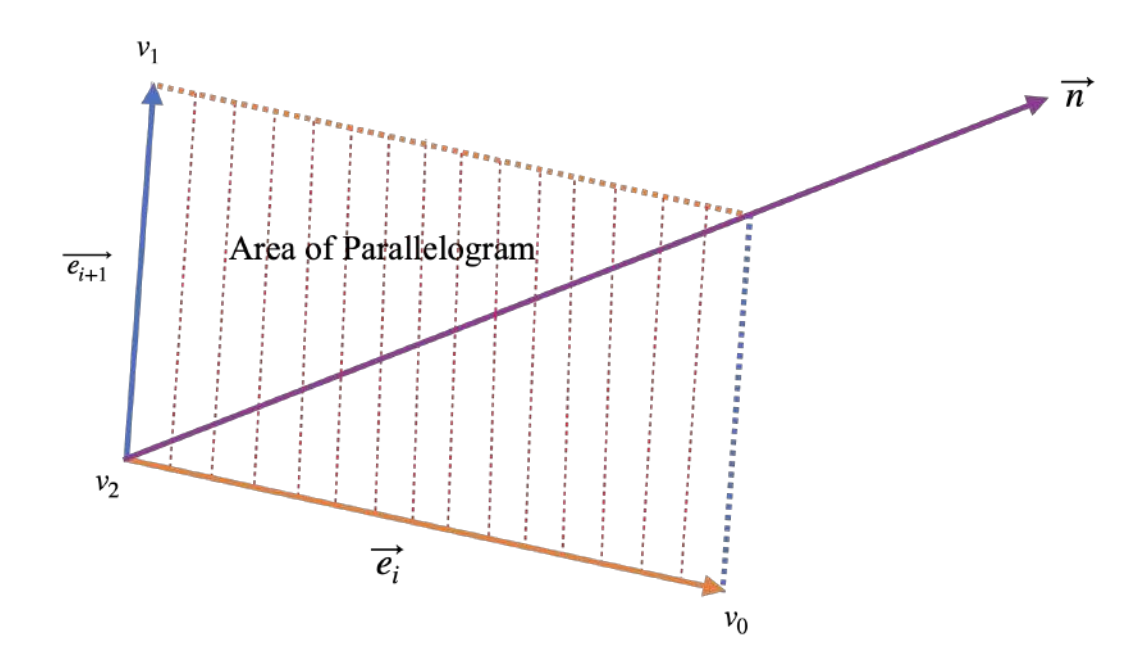
$$= \sqrt{n(x)^2 + n(y)^2 + n(z)^2}$$

The area of a face (triangle) is half the norm of the cross product. It computes to:

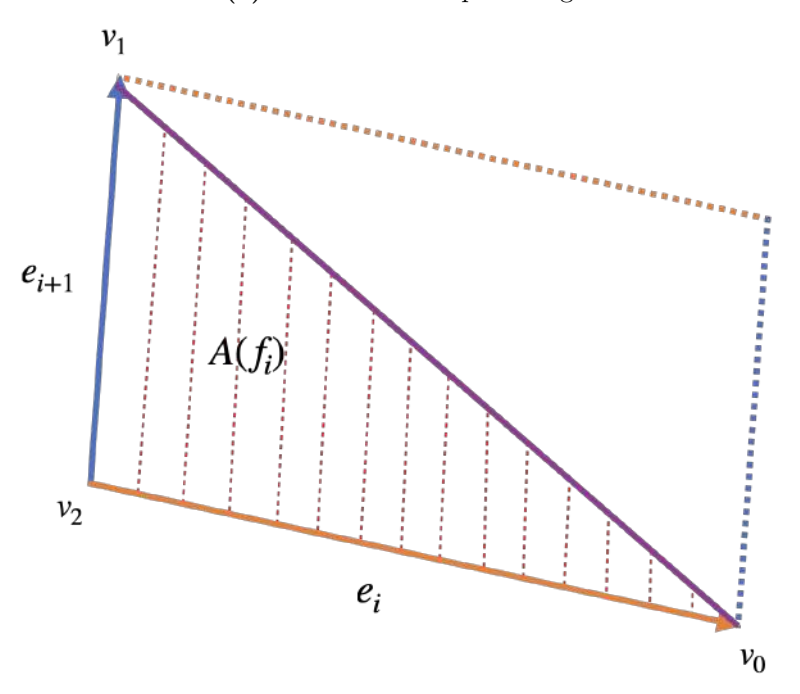
$$A(f_i) = \frac{1}{2} \times \sqrt{n(x)^2 + n(y)^2 + n(z)^2} (Refer to Fig. 6.12b)$$
 (6.6)

Therefore, the area $A(f_i)$ for each face (triangle) f_i in F_s is defined using the Eq. (6.6).

- **P.** (2) The centroid \bar{f}_i is shown in Fig. 6.13a which is calculated using the formula in Eq. (6.8).
- **P.** (3) The multiplication of area $A(f_i)$ and the centroid \bar{f}_i as denoted in Eq. (6.9) for each face (triangle) as shown in Fig. 6.13c.
- **P.** (4) The multiplication of area $A(f_i)$ and the unit normal vector \hat{N} (Refer to Eq. (4.7)), as denoted in Eq. (6.11) for each face (triangle) f_i as illustrated in Fig. 6.13d.

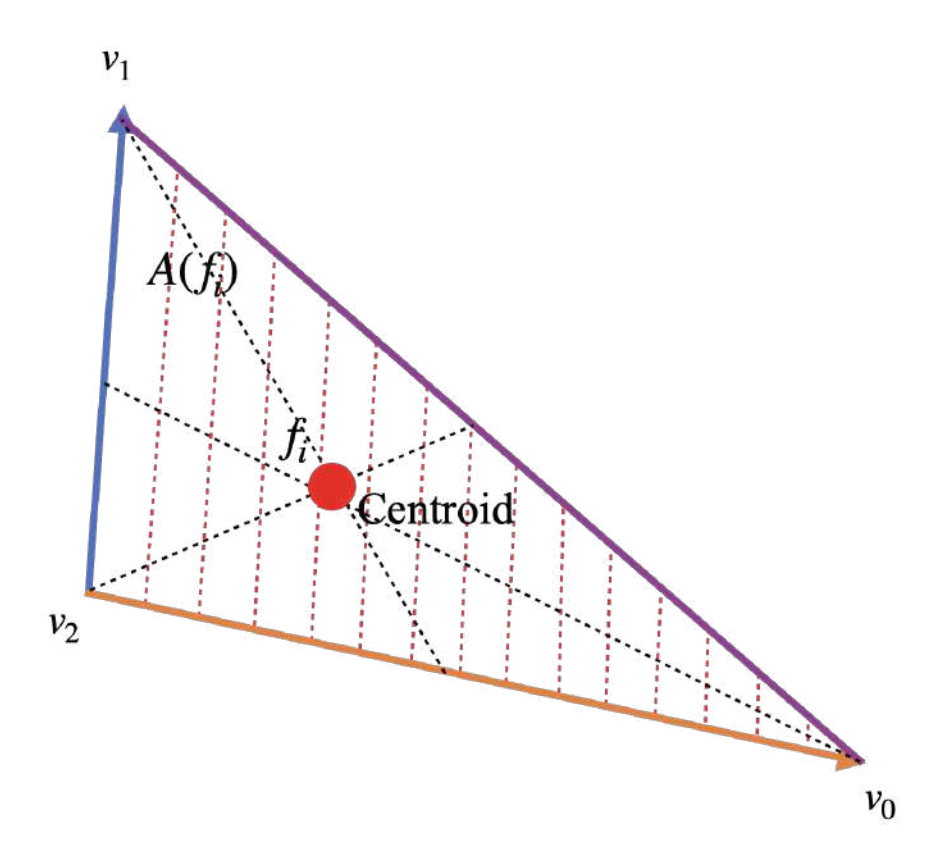


(a) The area of the parallelogram.

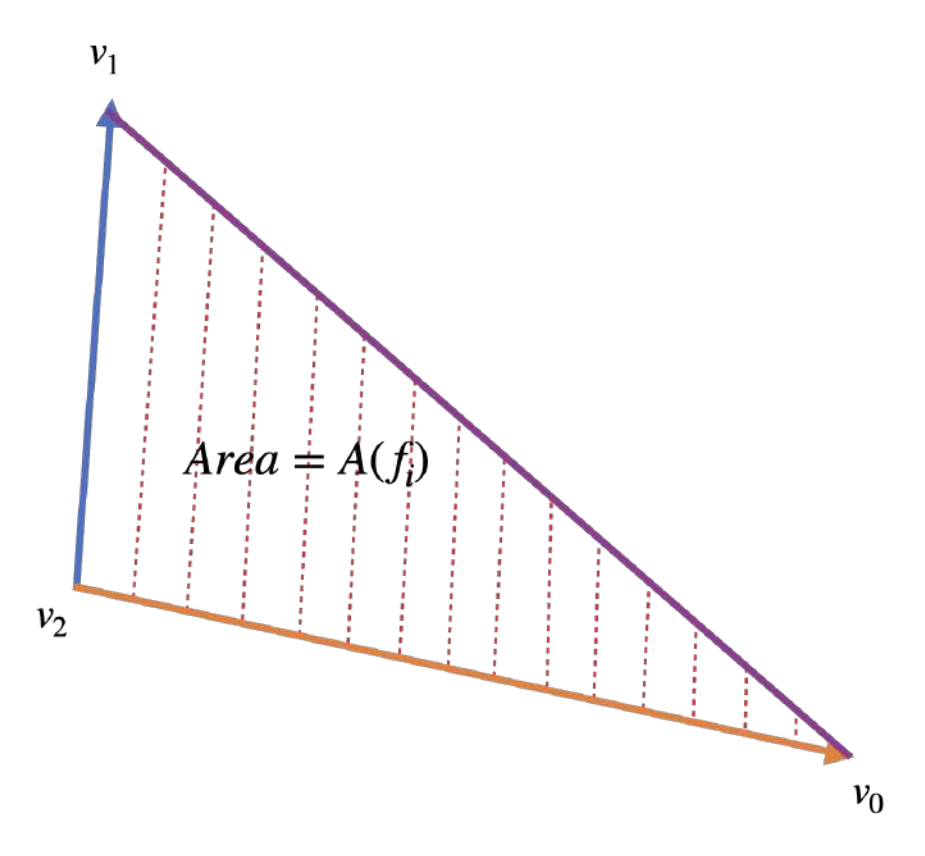


(b) The area of the triangle which follows from the fact that the parallelogram formed by u and v is being cut into half.

Figure 6.12: The relationship between the area of parallelogram and the area of the triangle enclosed by the two (2) vectors using the cross product.

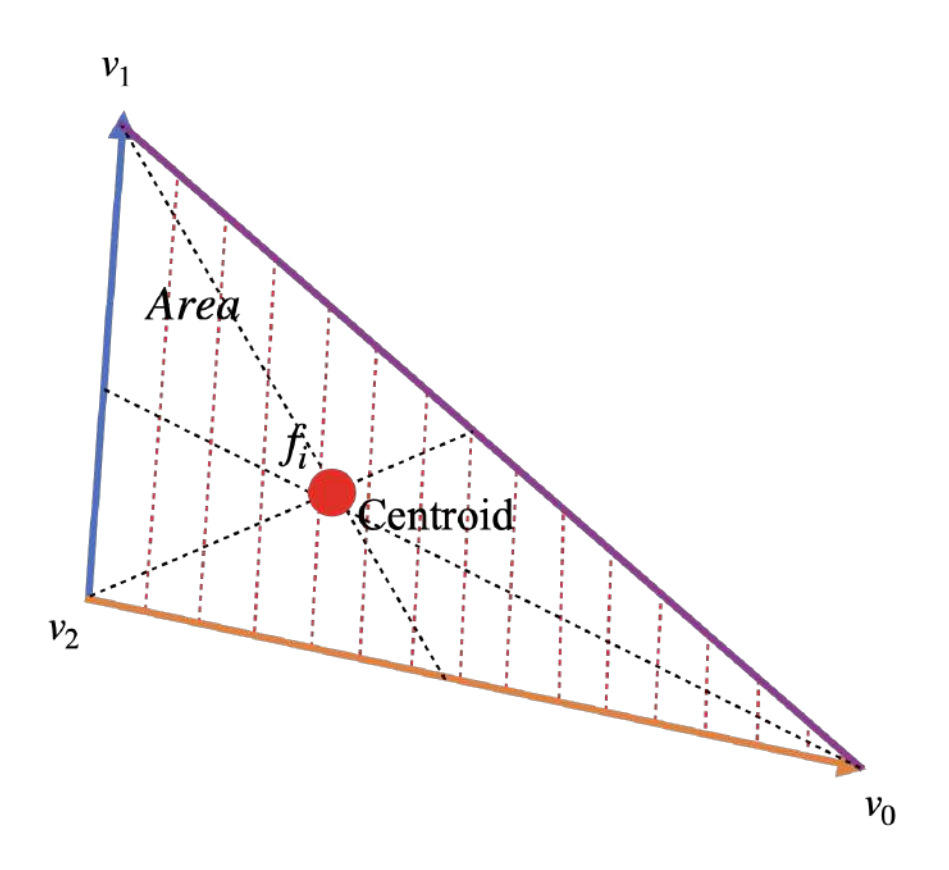


(a) The centroid \bar{f}_i of each face (triangle).

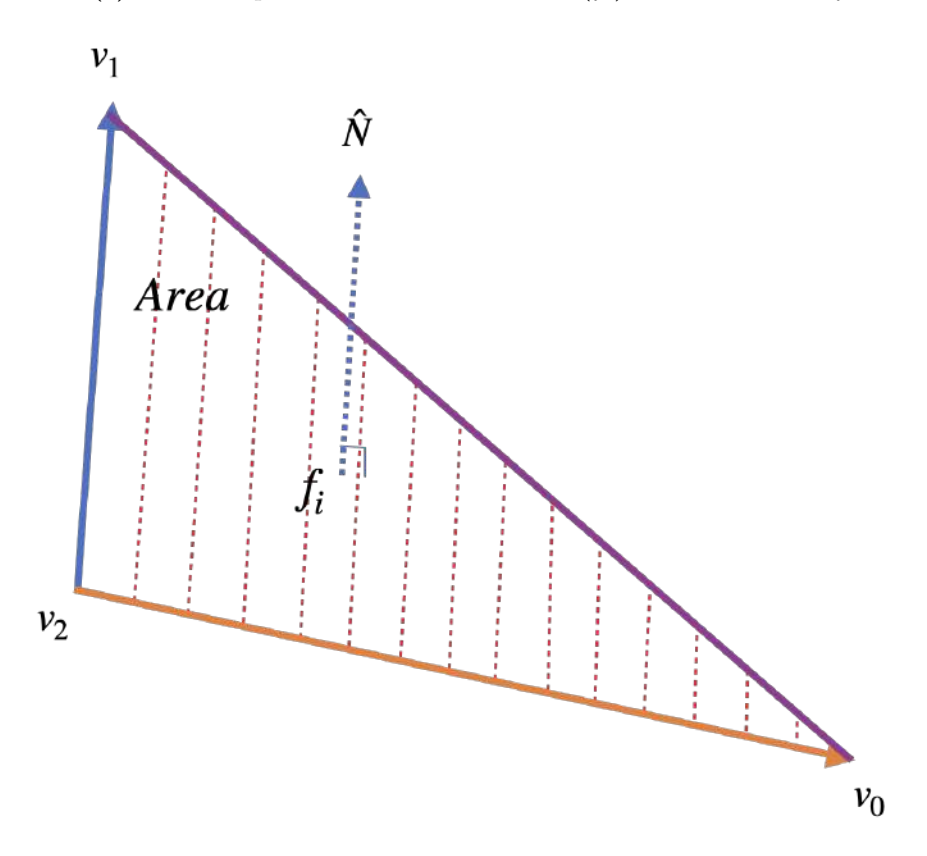


(b) The area $A(f_i)$ for each face (triangle) i in F_s .

Figure 6.13: The examples of the calculations for each face i in F_s .



(c) The multiplication of both the area $A(f_i)$ and the centroid \bar{f}_i .



(d) The weighted normal of a face (triangle) f_i as denoted in Eq. (6.11).

Figure 6.13: The examples of the calculations for each face i in F_s .

Once the above parameters are calculated for every face (triangle) f_i , **P.** (1) and **P.** (3) are accumulated for all the faces (triangles) in F_s as denoted in Eq. (6.10) and Eq. (6.12).

$$A_s = \sum_{i=0}^{m} A(f_i)$$
 (6.7)

 $A(f_i)$ = area of a face (triangle) f_i ,

m = the total number of faces (triangles) in F_s .

$$\bar{f}_i = \frac{1}{3} \sum_{i=0}^{2} v_i \tag{6.8}$$

$$A(f_i)\bar{f}_i \tag{6.9}$$

where $A(f_i)$ = area of a face (triangle) f_i , and $\bar{f_i}$ = centroid of a face f_i .

$$\sum_{i=0}^{m} A(f_i)\bar{f}_i \tag{6.10}$$

 $A(f_i)$ = area of a face (triangle) f_i , $\bar{f_i}$ = centroid of a face (triangle) f_i , m = the total number of faces (triangles) in F_s .

Weighted Normal of a Face (Triangle) =
$$A(f_i)\hat{N}(f_i)$$
 (6.11)

where $A(f_i)$ = area of a face (triangle) f_i , $\hat{N}(f_i)$ = unit normal of a face (triangle) f_i .

Weighted Normal of Faces (Triangles) =
$$\sum_{i=0}^{m} A(f_i)\hat{N}(f_i)$$
 (6.12)

where $A(f_i)$ = area of a face (triangle) f_i , $\hat{N}(f_i)$ = unit normal of a face (triangle) f_i , m = the total number of faces (triangles) in F_s .

Then, dividing the results of Eq. (6.10) and the accumulation of the areas A_s in Eq. (6.7) determines a weighted average \bar{F}_s of F_s , as denoted in Eq. (6.13). The result derived from this equation is to define the medial centre within the cylindrical slider, s.

$$\bar{F}_s = \frac{1}{A_s} \sum_{i=0}^m A(f_i) \bar{f}_i$$
 (6.13)

where $A_s = Eq.(6.7)$, $A(f_i) = area of a triangle <math>f_i$, and $\bar{f}_i = centroid of a triangle <math>f_i$.

$$\bar{M}_s = \frac{1}{m} \sum_{i=0}^{m} A(f_i) \hat{N}(f_i)$$
 (6.14)

where $A(f_i)$ = area of a face (triangle) f_i , $\hat{N}(f_i)$ = unit normal of a face (triangle) f_i , m = the total number of faces in f_i .

Besides that, the results of Eq. (6.12) are used to determine the mean for the weighted normal of faces \bar{M}_s , by dividing with the total number of faces (triangles) m in F_s , as denoted in Eq. (6.14).

The obtained value from Eq. (6.14) is then used to compute the residual error rates for every face (triangle) f_i in F_s , as denoted in Eq. (6.15). These values are used to derive the equation for the least squares plane fitting, which is then used to render the projection plane in the centre, as illustrated in Fig. 6.14 (peach in colour) and the projection of the face centre onto the plane.

$$R_s = A(f_i)\hat{N}(f_i) - \bar{M}_s \tag{6.15}$$

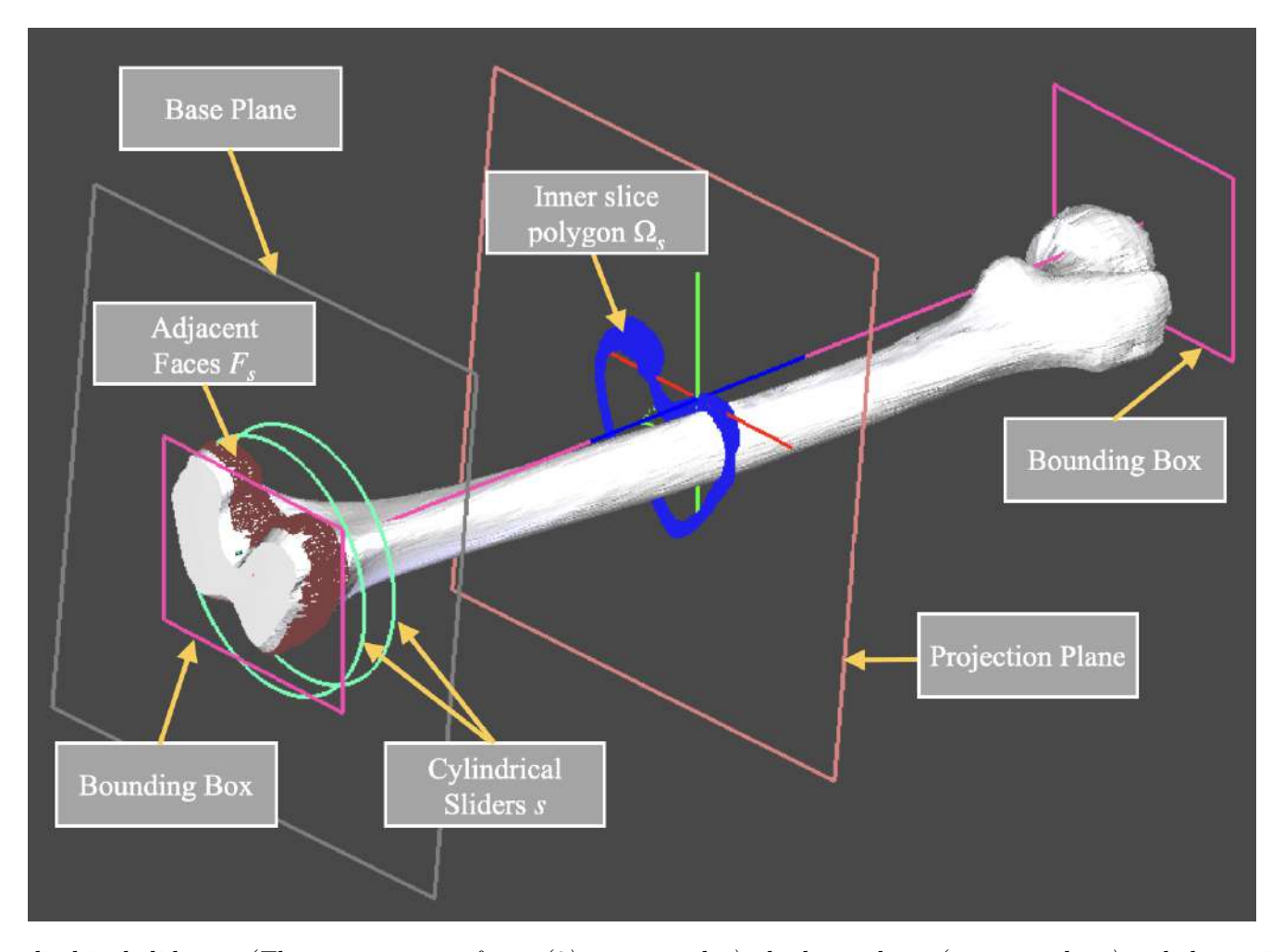


Figure 6.14: The cylindrical sliders s (The composition of two (2) green circles), the base plane (grey in colour) and the projection plane (peach in colour).

On the other hand, the results of Eq. (6.13) define the centre vertex for each segment of the medullary canal. When linking these centre vertices together, that are obtained from the segments that have been divided by the cylindrical sliders, a MA of the 3D femur is formed, as plotted using small and green spheres in Fig. 6.15. It defines the loci of all maximal inscribed disks that meet the inner contour of the medullary canal without any overlap, that is, the skeleton.

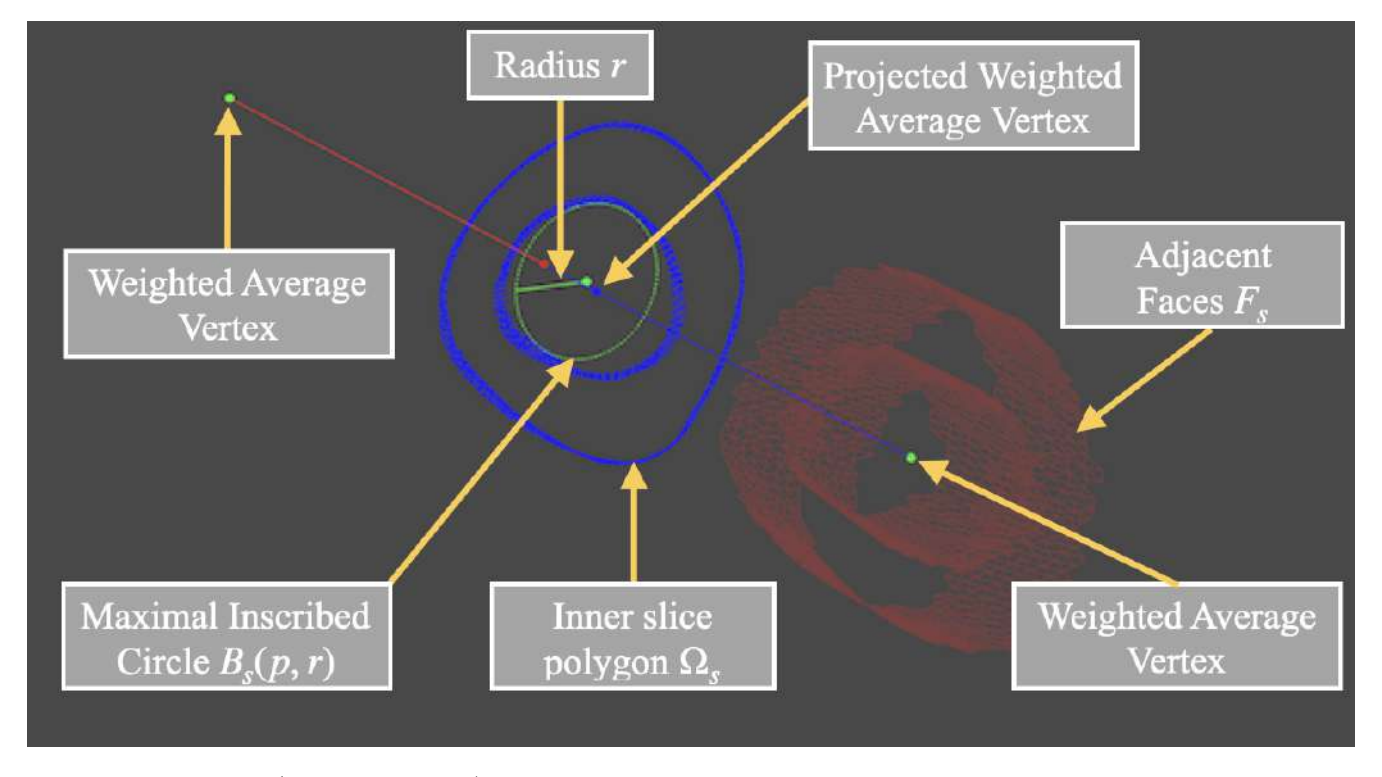


Figure 6.15: Weighted average vertex (green in colour), inner slice polygon Ω_s which consists of the projected centroids of the faces (triangles) in F_s (blue in colour), maximal inscribed circle $B_s(p,r)$ with radius r (green circle and radius).

During the sliding process, the cylindrical slider serves as a slice plane, which divides the 3D femur into several segments, from the beginning until the end, with a thickness of h, as shown in Fig. 6.14. The centroid of the faces in F_s within this cylindrical slider are projected onto the projection plane, as represented in blue vertices shown in Fig. 6.15. We also refer these projected vertices as the inner slice polygon Ω_s .

Apart from that, radii r as illustrated in Fig. 6.15 is calculated using Algorithm 1. We begin with generating a set of sample points that form a square shape. Then, starting from a sample point c_1 , we compare the distance from c_2 with the projected vertices in Ω_s .

In each comparison, only the minimum distance during the comparison is acquired and is saved in minDist. This process is repeated until all the projected vertices in Ω_s is compared. Then we change to another sample point c_2 to do the same comparisons, but this time, the maximum value maxDist is selected among the minDist when they completed the comparisons with all the projected vertices in Ω_s .

In the end of the process, the maxDist is obtained from the sample points and it is the optimal distance from the projected weighted average vertex to the boundary of medullary canal. Since the generated sample points form a square shape, the radius of this square refers to the distance from the centre of the polygon to any of its vertices [259].

The distance from the centre of a square to any one of its four (4) corners can be calculated by taking half the length of one side of the square, squaring that value, doubling the result, then taking the square root of the value of maxDist as denoted in Eq. (6.16), radius r_s is obtained.

Algorithm 1 Maximum-Minimum Centre Approach to find the MA and the Maximum Inscribed Circle.

the Maximum Inscribed Circle. Input:

```
Projected Plane P;
    Projected Weighted Centre Vertices P(\bar{F}_s);
             Maximal\ Circle\ B_s(p,r);
 1: [ax := a_i(x), ay := a_i(y), az := a_i(z)] \in A, maxDist := 0.0
 2: if (size(\bar{F}_s) < MaxCount_{radial}) then
      for i = -totalLoop to totalLoop do
         for j = -totalLoop to totalLoop do
 4:
            The sampling range: [bx := b_i(x), by := b_i(y), bz := b_i(z)] \in B
 5:
           minDist \coloneqq 1.0 \times 10^{10}
 6:
            for k = 0 to size(\bar{F}_s) do
 7:
              Calculate dist = Distance(ax, ay, az, bx, by, bz)
 8:
              if (dist < minDist)) then
 9:
10:
                 minDist := dist
              end if
11:
           end for
12:
           if (maxDist < minDist)) then
13:
              Assign to Optimal Indices:
14:
15:
16:
                 c_i \coloneqq j \; maxDist \coloneqq minDist
17:
           end if
         end for
18:
      end for
19:
20: end if
21: \mathbf{return} P
```

This obtained r_s is used to render the medial circle (maximum inscribed circle $B_s(p,r)$) within the selected portion of the cylindrical slider s (Refer to Fig. 6.15). We named this approach as maximum-minimum centre approach for finding the maximum inscribed circle for the contour of the medullary contour.

$$radius, r_s = \sqrt{maxDist}$$
 (6.16)

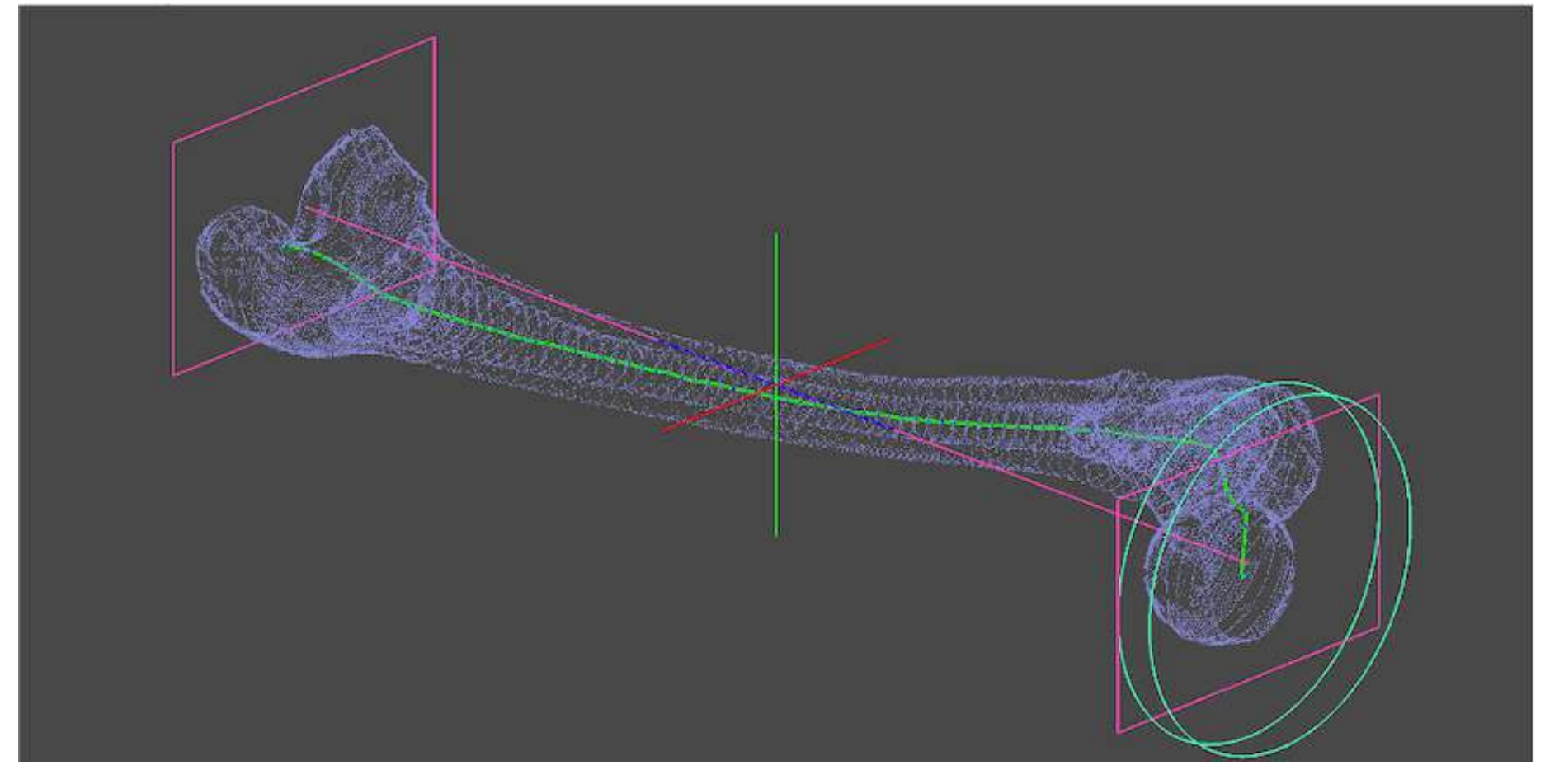


Figure 6.16: The 3D femur skeletonization result with the connected edges between the weighted average vertices (green in colour).

Fig. 6.15 illustrates the results obtained in this step which consists of the followings:

A. Cylindrical Sliders sB. m Faces (Triangles) F_s in the Cylindrical Sliders sC. Areas (Refer to Eq. (6.7)) D. Centroids (Refer to Eq. (6.8)) E. The Multiplication of Areas and Centroids (Refer to Eq. (6.9)) F. The Accumulation of E (Refer to Eq. (6.10)) G. The Weighted Normal of a Face (Triangle) (Refer to Eq. (6.11)) H. The Accumulation of G (Refer to Eq. (6.12)) I. Weighted Average Vertices \bar{F}_s (Medial Centre) (Refer to Eq. (6.13)) J. Projection Plane (Refer to Eq. (6.14) and Eq. (6.15); Fig. 6.14) K. Inner Slice Polygon Ω_s (Refer to Fig. 6.14)

L. Projected Weighted Average Vertices (Refer to Fig. 6.15)

M. Radii r (Refer to Fig. 6.15)

N. Maximum Inscribed Circle with M (Refer to Fig. 6.15)

O. The skeleton (Refer to Fig. 6.16)

6.4.3 Maximum-Minimum Thickness Calculation

Provided all the parameters obtained in Section 6.4.2, the outer diameter of the medullary canal or it is also called the compact bone plays an important role in the anatomical analysis.

The outer diameter of the medullary canal (Compact bone), also known as cortical bone forms the hard, dense outer layer of bones throughout the human body as shown in Fig. 6.17. It is primarily to give rigidity, strength and resistance to the femur.

In order to find this diameter, the contours [24] boundary information for the inner slice polygon Ω_s as shown in Fig. 6.18 are required.

The inner slice polygon Ω_s as shown in Fig. 6.18 is the projected centroids onto the 2D plane and the outer diameter of the medullary canal (compact bone) is measured from the outer curve of the inner boundary of contour 2, to the inner curve of the outer boundary of contour 1 as illustrated in Fig. 6.19b.

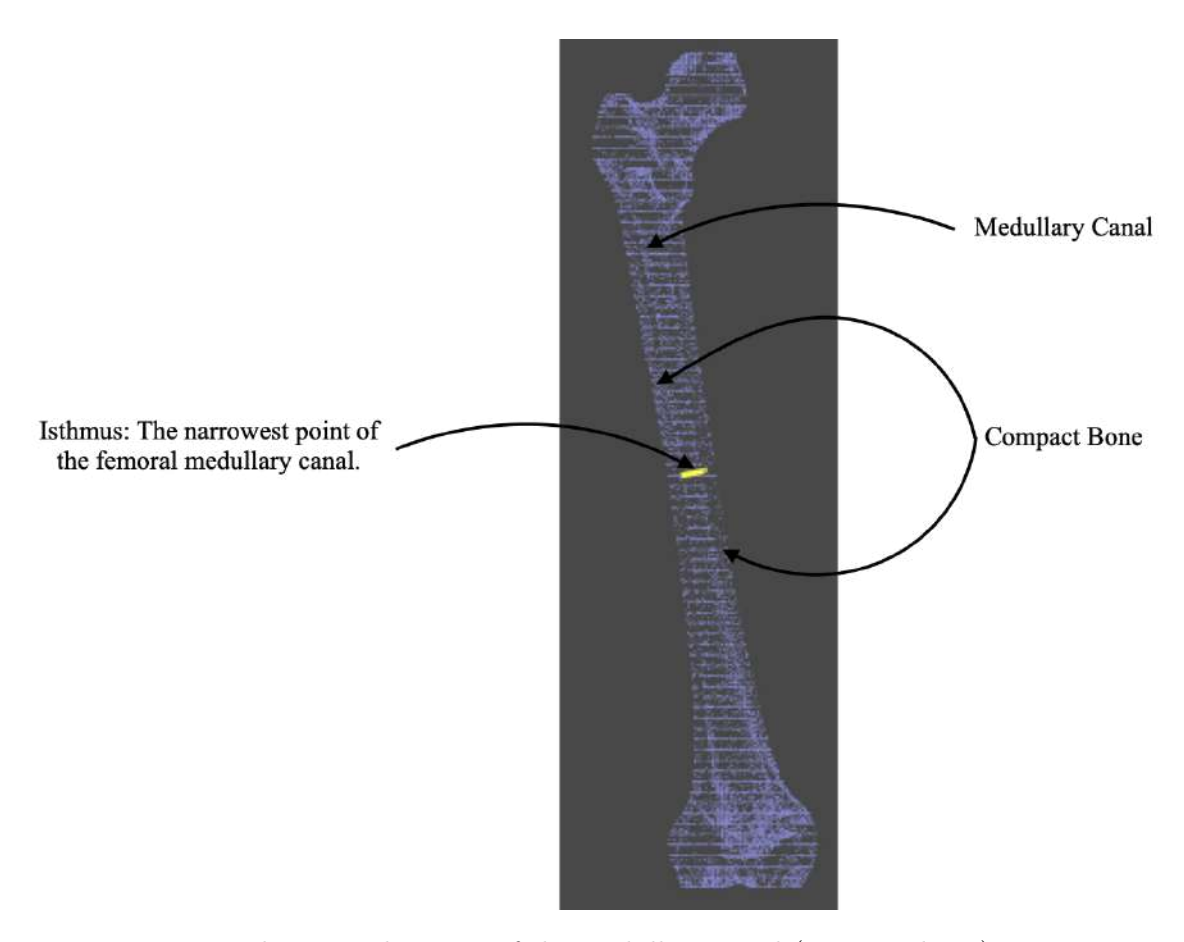


Figure 6.17: The outer diameter of the medullary canal (compact bone).

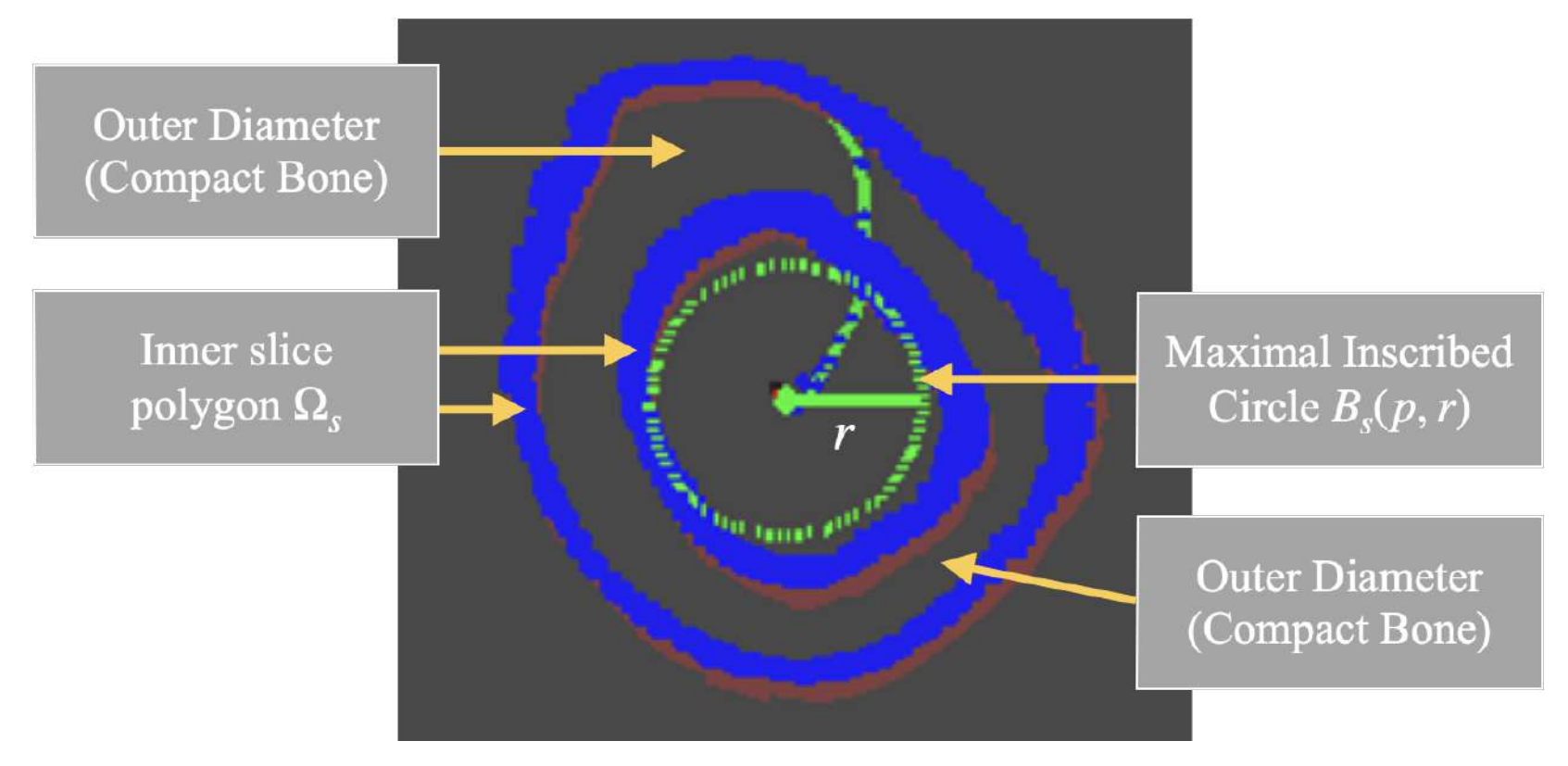


Figure 6.18: The inner slice polygon Ω_s obtained from Section 6.4.2. It consists of the projected centroids (blue in colour) of the faces (triangles) in F_s and it is used to determine the outer diameter of the medullary canal (compact bone).

Therefore, contour detection on Ω_s is important for the diameter measurement. OpenCV makes it really easy to find and draw contours in images. It provides two (2) simple functions:

```
A. findContours()
```

B. drawContours()

Steps for Detecting and Drawing Contours in OpenCV

OpenCV makes this a fairly simple task with the following steps [260]:

- A. Read an image and convert it to grayscale format.
- B. Apply binary thresholding (Refer to Fig. 6.19a).
- C. Find the contours [261] (Refer to Fig. 6.19b).
- D. Draw contours on the Red, Green and Blue (RGB) colour model for an original image.

We also utilised the contour hierarchies to denote the parent-child relationship between contours due to the following conditions:

• Single objects scattered around in an image, or

• Objects and shapes inside one another.

In most cases, especially in our case, where a shape contains more shapes, we can safely conclude that the outer shape is a parent of the inner shape. Thus, the findContours() method returns two (2) outputs:

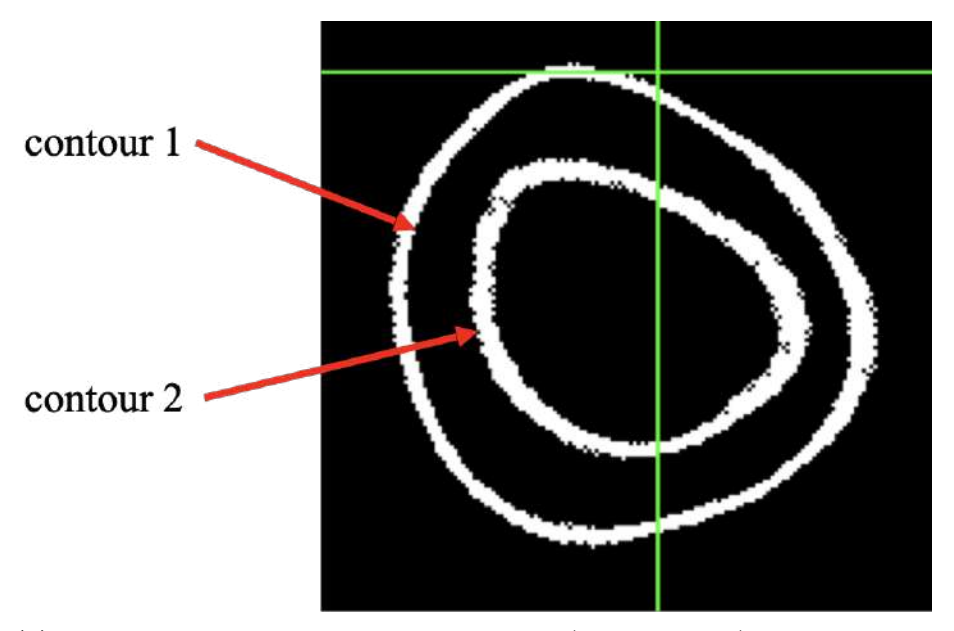
- A. Contours: It is the detected contours. Each contour is stored as a vector of points.
- B. Hierarchy: It is the optional output vector containing information about the image topology.

At this point, the inner curve of the inner boundary of *contour* 1 and the outer curve of the inner boundary of *contour* 2 are identified as shown in Fig. 6.19b.

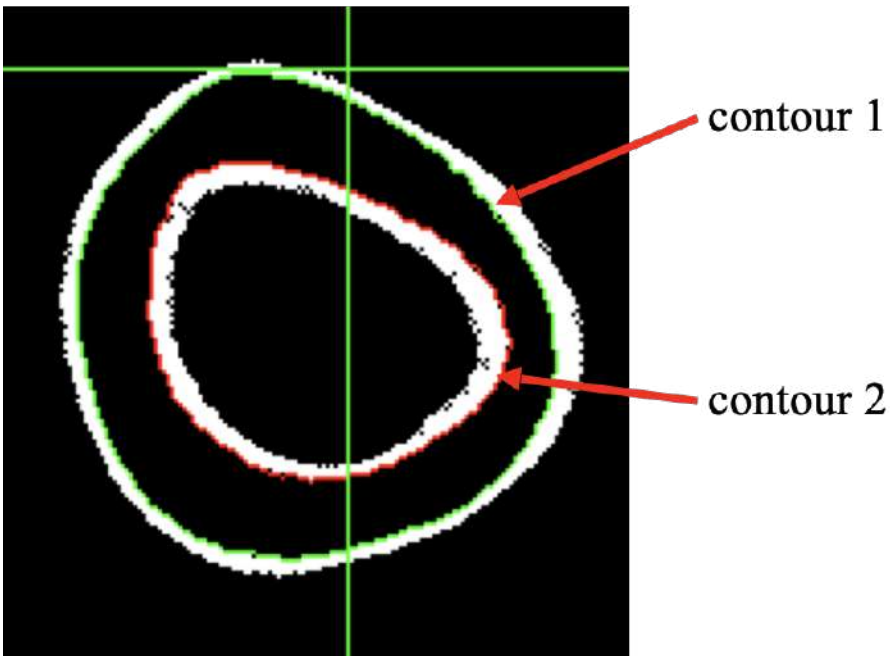
We adapted a popular contour matching technique to find the distance between these two (2) images (Fig. 6.19), namely the CD.

CD in Image Processing

CD is proposed by Borgefors and Gunilla [262]. There are many applications in computer vision (e.g.: 3D mesh reconstruction [263, 264, 265, 266], object detection and classification [267, 268, 269, 269]) and in medical image analysis. Besides that, CD is commonly used to perform the Chamfer Matching which basically calculates the distance (dissimilarity) between two (2) images.



(a) The outer diameter of the medullary canal (compact bone) is measured from the outer curve of the inner boundary of *contour* 2, to the inner curve of the outer boundary of *contour* 1.



(b) After the execution of Algorithm 2, contour 1 (green in colour) and contour 2 (tangerine in colour) are found and coloured.

Figure 6.19: Contours detection.

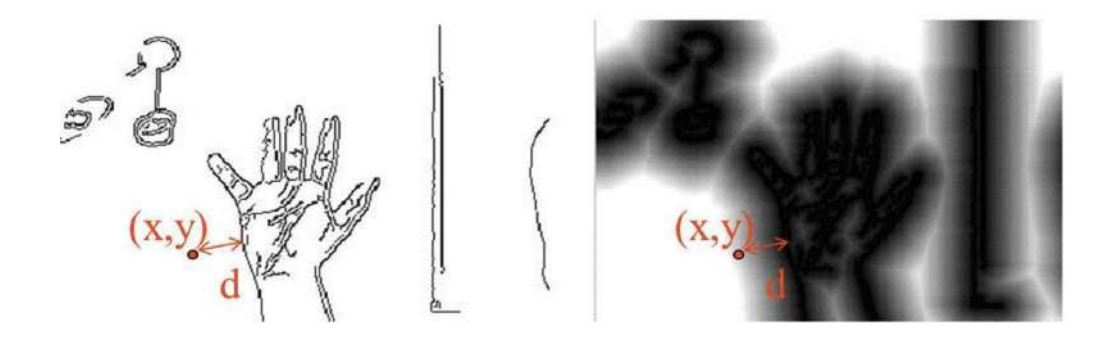
In order to enhance the understanding, let's take a look at one example of usage in image processing. Refer to Eq. (6.17), assume that A and B be the sets containing the contour points $\{u_i\}$ and $\{v_j\}$ from template image I_{te} and target image I_{ta} respectively. The CD is given by the average distance between the points in sets A and B. The CD between A and B is calculated using the distance-transform [270].

Distance-transform is derived by taking an average distance between each point $\{u_i\} \in B$ and its nearest point $\{v_j\} \in A$, where n is the number of contour points in the template image I_{te} . This transformation takes a binary image as input, and assigns to each pixel in the image the distance to its nearest contour point. The CD for matching a template to an edge map can then be computed as the average of the distance - transform values at the template contour points [21]. An example of the CD computation is illustrated in Fig. 6.20.

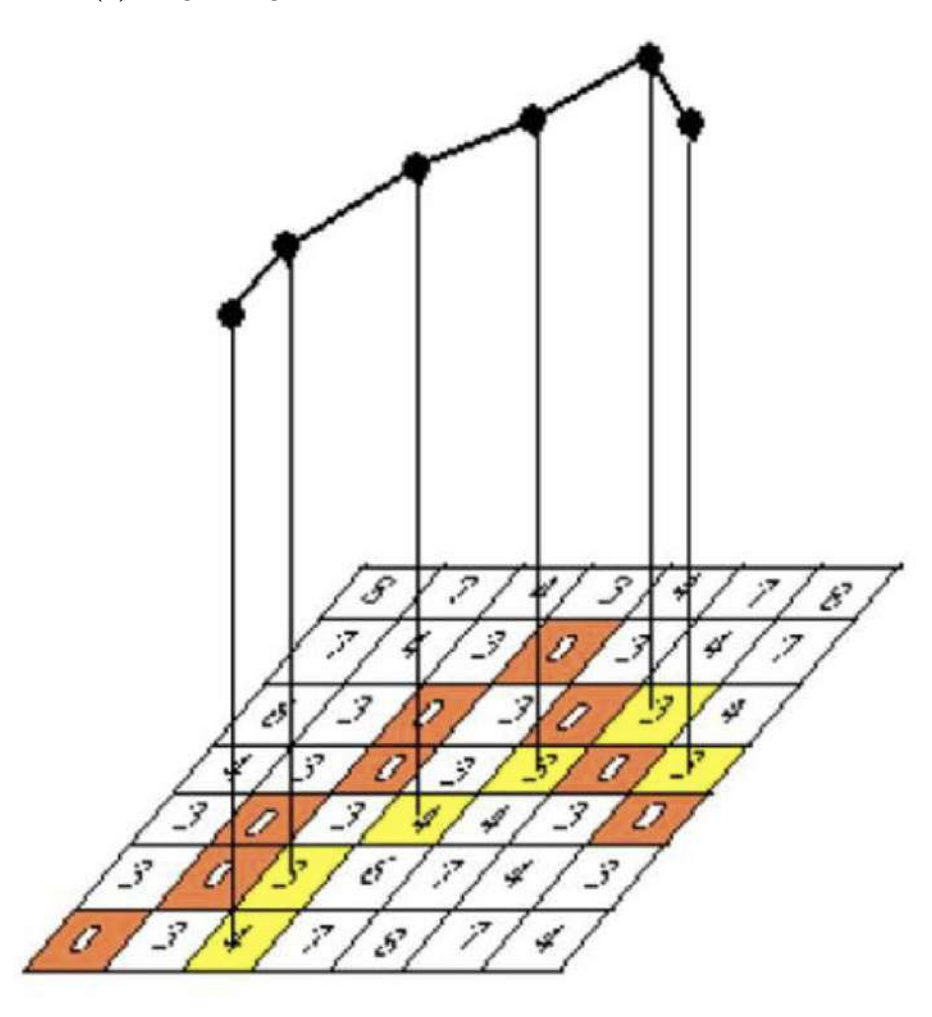
$$d_{CD}(A,B) = \frac{1}{n} \sum_{u_i \in A} \min_{v_j \in B} ||u_i - v_j||$$
 (6.17)

Chamfer Distance in Point Cloud

Apart from that, CD is also used in designing a loss function for comparing the distance between predicted point cloud and the the ground truth that is used in 3D object reconstruction [271]. The authors defined the following equation for the CD:

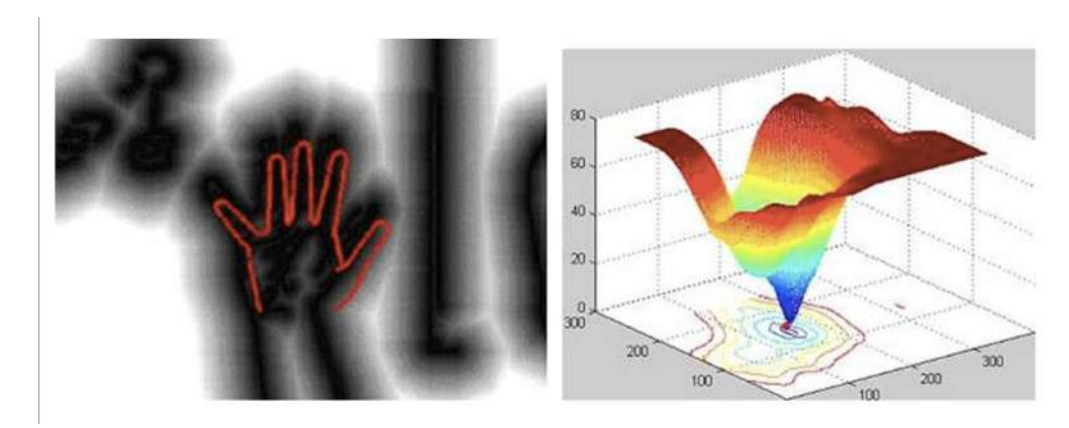


(a) Target image and the distance-transform's version.



(b) Computation of the CD.

Figure 6.20: An example of the CD computation in image processing. These figures are sourced from [21].



(c) Best match of template image in target image.

Figure 6.20: An example of the CD computation in image processing. These figures are sourced from [21].

$$d_{CD}(S_1, S_2) = \sum_{x \in S_1} \min_{y \in S_2} \|x - y\|_2^2 + \sum_{y \in S_2} \min_{x \in S_1} \|x - y\|_2^2$$
 (6.18)

Fan et al. [271] defined the term distance as any non-negative function defined on point set pairs. For each point, the algorithm of CD finds the nearest neighbour in the other set and sums the squared distances up. Viewed as a function of point locations in S_1 and S_2 . Moreover, CD is continuous and piecewise smooth. The range search for each point is independent and it produces reasonable high quality results in practice.

They first take two (2) sets of points: S_1 and S_2 . For each point in S_1 , find the nearest point in S_2 , and the same comparison process is repeated for points in S_2 . Based on the Eq. (6.18), the algorithm will sum the squares of each minimum distance found in S_1 and S_2 . Finally, they added all these sums to determine the dispersion of data points. A visual representation of their proposed method can be seen in [272].

Modified Chamfer Distance in this Phase

Based on the above mentioned mechanisms, we modified the CD algorithm to be used in our thickness calculation, and we named it as **maximum-minimum thickness approach** due to a part of the codes defined in Algorithm 1 is reused.

Let A and B be the sets containing the contour points $\{a_i\}$ and $\{b_j\}$ from template image I_{te} (Fig. 6.19a) and target image I_{ta} (Fig. 6.19b) respectively. These points are produced during the contour detection described previously.

Each set A and B consists of $contour\ 1$ and $contour\ 2$ which satisfy the Eq. (6.19). $Contour\ 1$ consists of contour points of P, whereas $contour\ 2$ consists of contour points of Q. The union of two sets P and Q consists of all the contour points in N, whereas the intersection of two sets P and Q consists of no common contour points. Fig. 6.19a illustrates these conditions.

Contour
$$1: P \in N$$

Contour $2: Q \in N$

$$P \cup Q = N$$

$$P \cap Q = \emptyset$$
(6.19)

For each contour point in the template image I_{te} $\{a_i \in A\}$, we compute the distance for all the contour points in the target image I_{ta} $\{b_j \in B\}$, then the nearest distance between these points are selected $min(A) = \{mn_{a_i}, mn_{a_{i+1}}, ..., mn_{a_{n_A}}\}$ with n_A is equals to the total number contour points in A. Once all the comparisons are done for all the points in A, the

computation is repeated for the points $b_j \in B$ with all the points in $a_i \in A$ and produce the minimum sets of $min(B) = \{mi_{b_j}, mi_{b_{j+1}}, ..., mi_{b_{n_B}}\}$ with n_B is equals to the total number contour points in B. Refer to Eq. (6.20) and Eq. (6.21) for these calculations.

Thus, with both minimum sets of min(A) and min(B), the maximum value in each set is then retrieved and forms max(A) and max(B) as derived in Eq. (6.22) and Eq. (6.23). By summing this pair of maximum values (Eq. (6.24)), the outer diameter (thickness) of the medullary canal (compact bone) of that particular contour point is derived as shown in Fig. 6.21.

Algorithm 2 presents the sequence to execute our maximum-minimum thickness calculation and Fig. 6.22 illustrates the final results after the all the phases mentioned above.

$$min(A) = \left[\min_{b_{j \in B}} ||a_i - b_j||_{j=0}^{j=n_B} \right]_{i=0}^{i=n_A}$$
(6.20)

$$min(B) = \left[\min_{a_{i \in A}} ||a_i - b_j||_{i=0}^{i=n_A} \right]_{j=0}^{j=n_B}$$
(6.21)

, where n_A is equals to the total number of contour points in set A, whereas n_B is equals to the total number of contour points in set B.

$$max(A) = \left[\max_{mn_i \in min(A)} \{mn_i, mn_{i+1}, ..., mn_m\} \right]_{i=0}^{i=m}$$
 (6.22)

$$max(B) = \left[\max_{mn_i \in min(B)} \{ mi_i, mi_{i+1}, ..., mi_n \} \right]_{i=0}^{i=n}$$
 (6.23)

, where m is equals to the total number of minimum distances obtained in min(A), whereas n is equals to the total number of minimum distances obtained in min(B).

$$d_{thickness} = \sum_{\substack{x \in max(A) \\ y \in max(B)}} \{x + y\}$$
(6.24)

Algorithm 2 Maximum-Minimum Thickness Approach.

Input:

Inner Slice Polygon $\Omega_s \equiv N \equiv A \cup B$;

Non – empty set $A \subseteq \mathbb{R}^3$ for I_{te}

 $Non-empty\ set\ B\subseteq\mathbb{R}^3\ for\ I_{ta}$

Output: Thickness Between Contour 1 and Contour 2: $d_{thickness}$;

1: $[a_i \subseteq A, b_j \subseteq B]$

2: for i = 0 to no_of_points , $n_A \in A$ do

3: $minDistance := 1.0 \times 10^{10}$

4: **for** j = 0 to no_of_points , $n_B \in B$ **do**

5: Calculate distance = $Distance(a_i, b_i)$

6: **if** (distance < minDistance) **then**

7: Assign to:

8: $min(A) := Add_to_List\{distance\}$

```
9:
              minDistance \coloneqq distance
         end if
10:
      end for
11:
      min(A) = \{mn_i, mn_{i+1}, ..., mn_m\}
12:
13: end for
14: for i = 0 to no\_of\_points, n_B \in B do
      minDistance \coloneqq 1.0 \times 10^{10}
15:
      for j = 0 to no\_of\_points, n_A \in A do
16:
17:
         Calculate distance = Distance(a_i, b_i)
         if (distance < minDistance) then
18:
           Assign to:
19:
              min(B) \coloneqq Add\_to\_List\{distance\}
20:
21:
              minDistance \coloneqq distance
         end if
22:
      end for
23:
      min(B) = \{mi_i, mi_{i+1}, ..., mi_n\}
24:
25: end for
26: maxDistance := 0
27: distance := mn_0)
28: for i = 1 to no\_of\_minimum\_points \in min(A) do
      if (distance > maxDistance) then
29:
30:
         Assign to:
            max(A) := distance
31:
            maxDistance \coloneqq distance
32:
            distance := mn_i
33:
      end if
34:
35: end for
36: maxDistance = 0
37: distance := mi_0)
```

```
38: for i = 1 to no\_of\_minimum\_points \in min(B) do
      if (distance > maxDistance) then
39:
         Assign to:
40:
           max(B) \coloneqq distance
41:
            maxDistance \coloneqq distance
42:
43:
            distance \coloneqq mn_i
      end if
44:
45: end for
46: d_{thickness} := max(A) + max(B)
47: return d_{thickness}
```

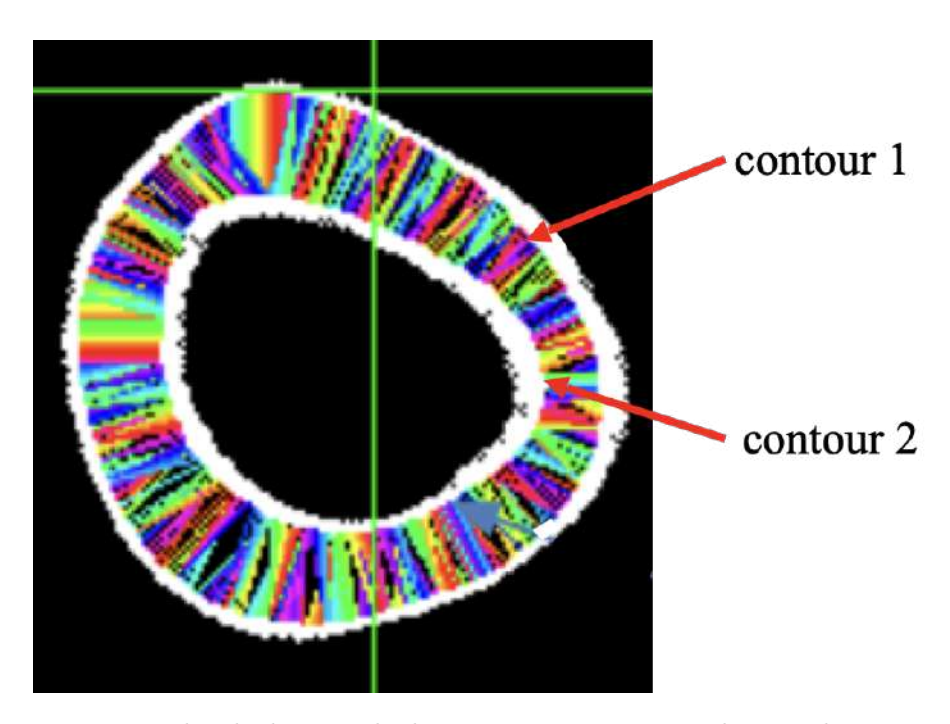


Figure 6.21: The thickness calculation using our approach, namely maximum-minimum thickness approach.

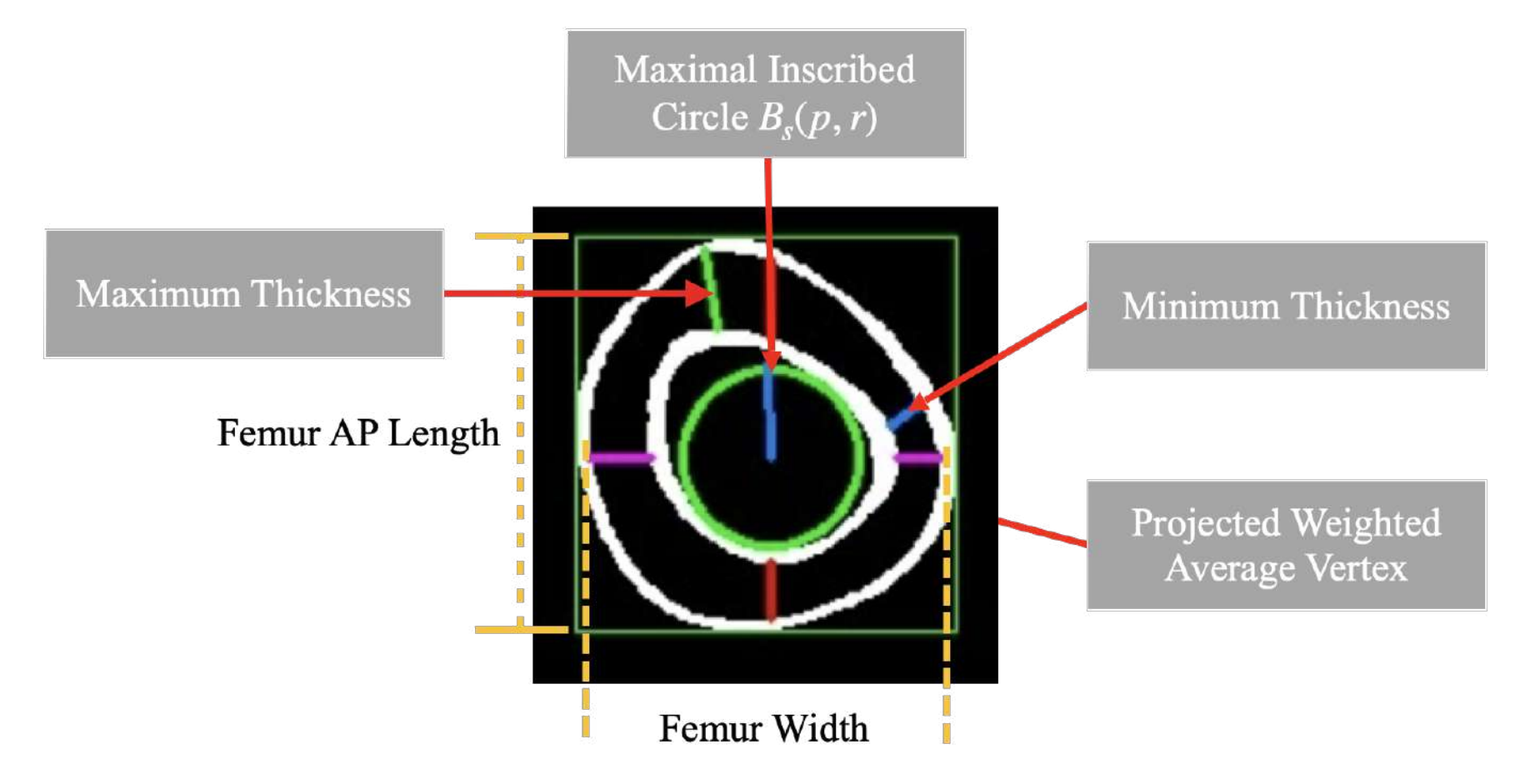


Figure 6.22: The maximum inscribed circle $B_s(p,r)$ (green circle) and the radius r, with the diameter (thickness) of the compact bone = 2r. These parameters are computed using the approaches described in Section 6.4.2 and Section 6.4.3.

6.4.4 Minimum Radius Angle Calculation

Despite decreases in nail ROC over the last decades, recent studies [273, 274, 10, 60, 1, 14, 67, 275, 276, 52, 15, 277, 52, 39, 68, 278, 16] still report the existence of mismatch between the curve of the natural femoral anatomy of some patients and the contemporary femoral nails [279].

This mismatch can lead to distal cortical impingement, which may occur in up to 25% of hip fracture repair cases [280, 10, 190]. This complication may lead to a fracture at the distal nail tip called anterior perforation, which requires revision surgery [280, 281, 186].

ROC is defined as, any approximate circular radius at any particular point. As we move along the curve, the ROC changes [282]. Whereas, in differential geometry, the ROC is denoted by R. The maximal circle $B_s(p,r)$ to determine the amount by which the curve derivates itself from being flat to a curve and from a curve back to a line. The ROC is the reciprocal of the curvature.

Therefore, 3D-FSA provides the computation for finding the curvature of the curve for the 3D Femur as written in Algorithm 3.

The projected weighted average vertices of the 3D femur is rotated for every 2°, between 0° and 180° on the longitudinal axis.

In each projected weighted average vertices, the ROC was calculated using circle fitting method. The minimum ROC among the angles was chosen as the representative of the 3D femur.

As presented in [283], the Least Square Fitting (LSF) is based on min-

imising the mean square distance from the fitting curve to the data points. Thus, given m points (x_i, y_i, z_i) , $1 \le i \le m$, the objective function is defined by:

$$\sum_{n=0}^{m} d_i^2 = 1 \tag{6.25}$$

where d is the Euclidean (geometric) distance from the point (x_i, y_i, z_i) to the curve.

When fitting the circles, one parametrises those by the equation:

$$(x-a)^2 + (y-b)^2 = r^2 (6.26)$$

where (a,b) is the centre and r is the radius.

The basic concept behind this computation is as follows:

"The circle defined by centre (a, b) and radius r will yield the least mean square value for the expression $(x - a)^2 + (y - b)^2 - r^2$ and the circle's curvature will be $\frac{1}{r}$ ".

The computation is followed by Eq. (6.27) to obtain the value of d_i .

$$d_i = \sqrt{(x_i - a)^2 + (y_i - b)^2} - r \tag{6.27}$$

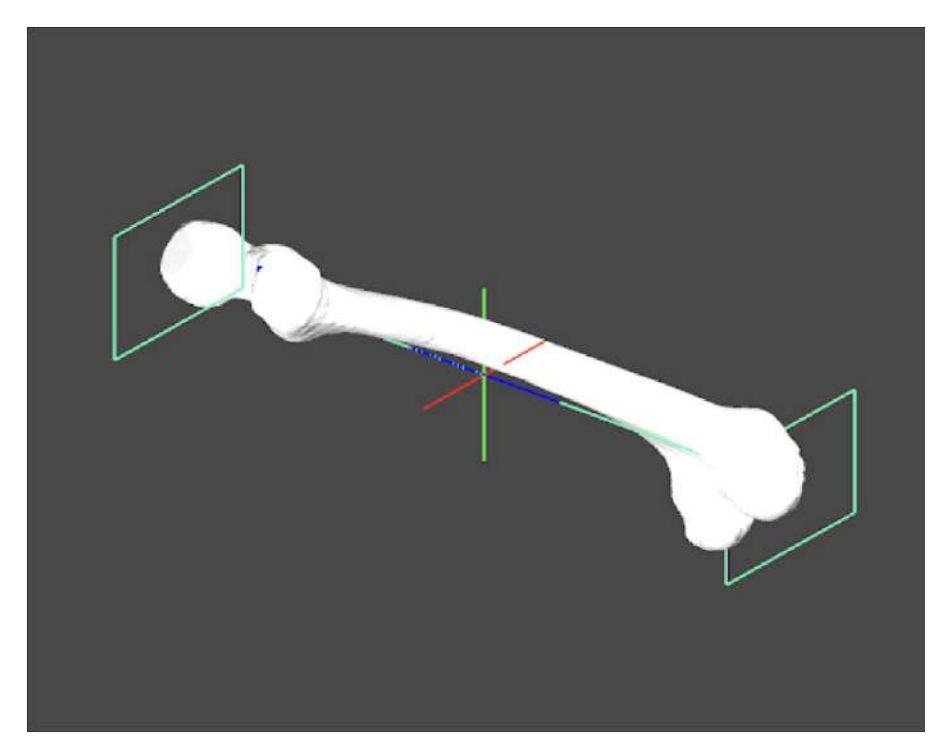
Fig. 6.23 demonstrates two (2) examples for the involved range of this calculation with various starting indices but similar ending indices. Additionally, Fig. 6.24 shows the projected vertices used for the calculation of

the minimum ROC, together with the projected angle and projected plane in the faces view and vertices view.

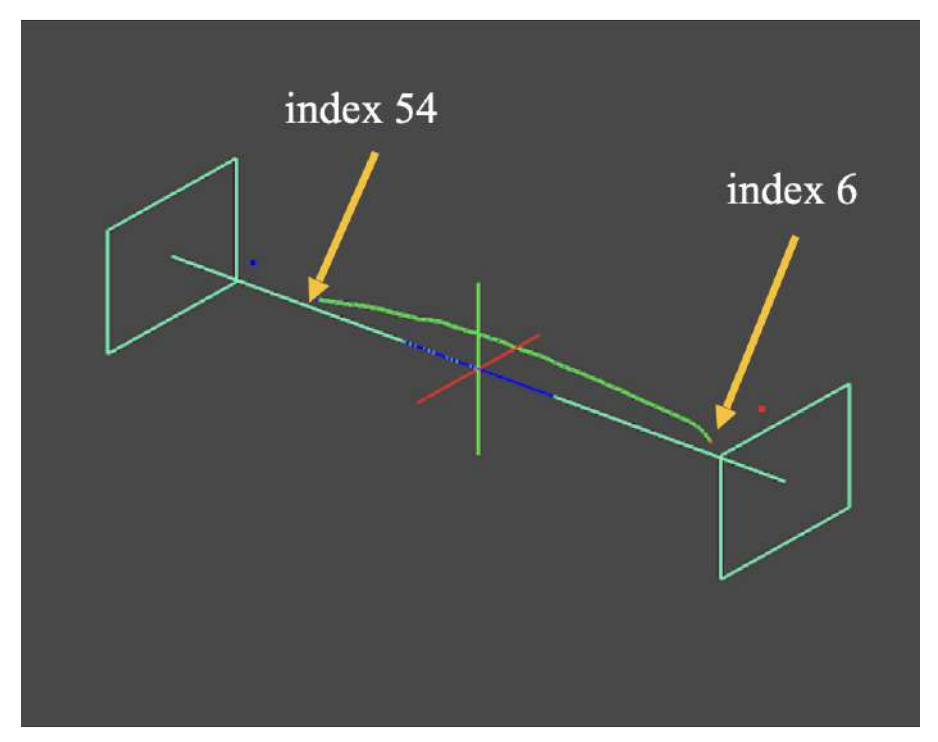
Algorithm 3 Algorithm for the LSF of the Circles.

```
Input:
               Projected Weighted Centre Vertices P(F_s);
     Reprojected Weighted Centre Vertices R[P(F_s)];
Output:
                Curvature(\kappa);
 1: Reprojected Vertices (px, py, pz) \in R[P(F_s)]
 2: total = size(F_s)
 3: for i = 0 to total do
        mx = \sum_{i=0}^{total} p_i x
mz = \sum_{i=0}^{total} p_i z
 5:
 6: end for
 7: Find the Mean for Both mx and my:
        mx = \frac{mx}{size(\bar{F}_s)},

mz = \frac{mz}{size(\bar{F}_s)}
 9:
10: for i = 0 to size(\bar{F}_s) do
        tx_i = p_i x - mx
        tz_i = p_i z - mz
13: end for
14: for i = 0 to total do
       x2 = (tx_i)^2; dx2 = \sum_{i=0}^{total} x2;dxz = \sum_{i=0}^{total} (tx_i \times tz_i)
15:
16:
        z2 = (tz_i)^2; dz2 = \sum_{i=0}^{total} z2
17:
18: end for
19:
       Reassign the Matrix Array
            A[0] = dx2; A[1] = A[2] = dxz; A[2] = dz2
20:
21:
        Compute the Determinant -> det
22:
        Division with the Matrix Array A:
            iA[0], iA[1], iA[2], iA[3]
23:
24: for i = 0 to size(\bar{F}_s) do
        ix_i = iA[0] \times tx_i + iA[1] \times tz_i
        iz_i = iA[2] \times tx_i + iA[3] \times tz_i
26:
        iy_i = -\sum_{i=0}^{total} (dx^2 + dz^2)
28: end for
29: for i = 0 to size(\bar{F}_s) do
        a0 = \sum_{i=0}^{total} ix_i \times iy_i; \ b0 = \sum_{i=0}^{total} iz_i \times iy_i
31: end for
32: a0 = \frac{a0}{2}; b0 = \frac{b0}{2}
33: Calculate the Center: x_i = a0 + mx; z_i = b0 + mz
34: Calculate the Radius:
        radius = \sqrt{dx^2 + dz^2 + a0^2 + b0^2}
36: Calculate the Curvature (\kappa): \frac{1}{radius}
37: return FILE
```

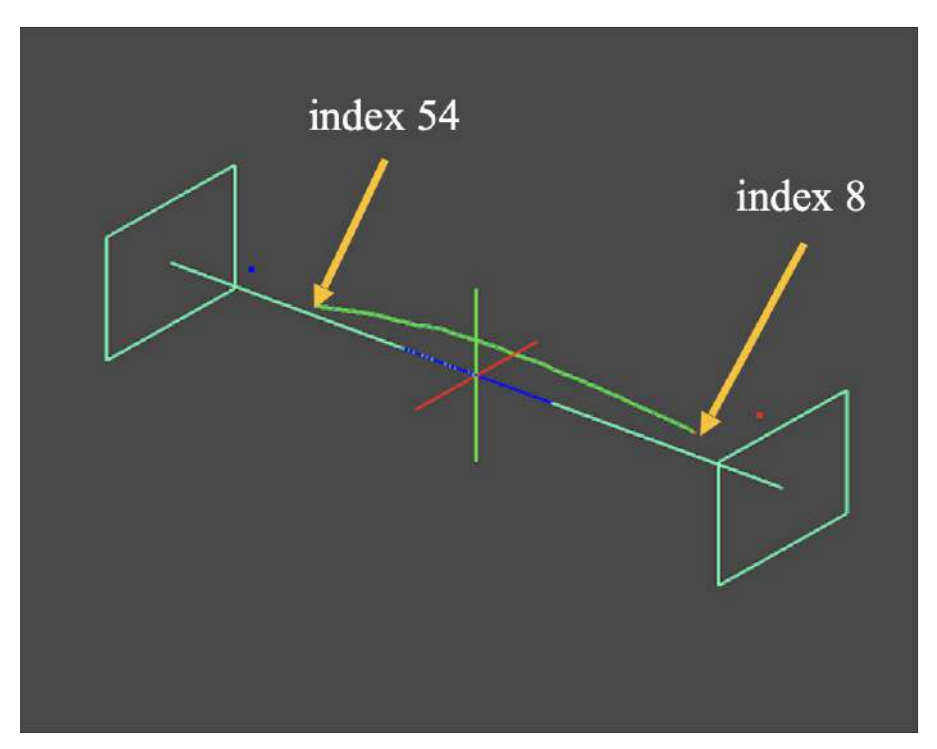


(a) After the calculation in Section 6.4.2, the results of sixty-eight (68) cylindrical sliders are generated and displayed in faces view.



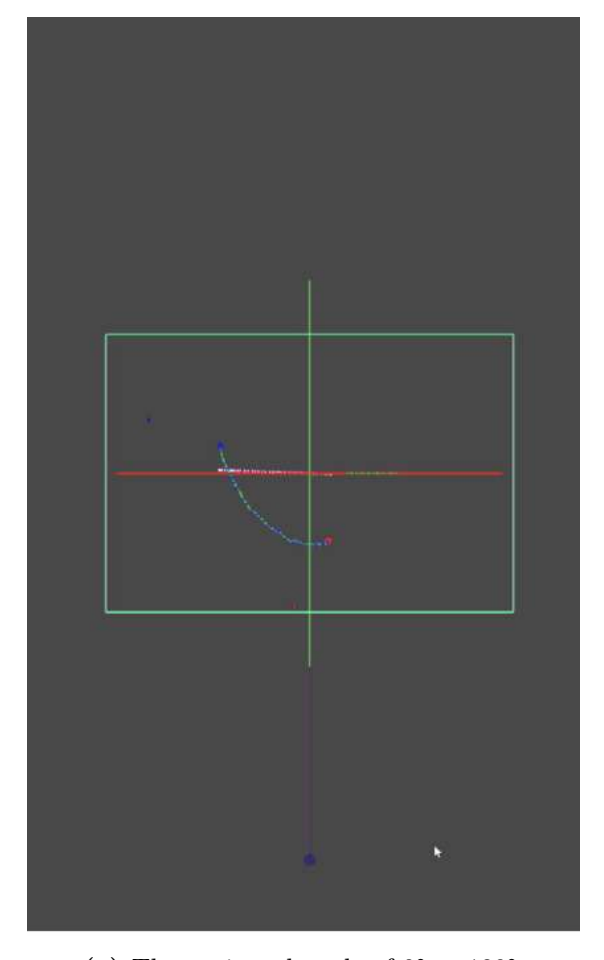
(b) The results from Section 6.4.2 are displayed in vertices view after the 'F' or 'f' key is pressed. Although sixty-eight (68) cylindrical sliders are generated, only the indices from six (6) (bottom margin is equal to 0.08%) to fifty-four (54) (top margin is equal to 0.18%) are used to calculate the minimum ROC.

Figure 6.23: The involved range for the calculation of the minimum ROC.

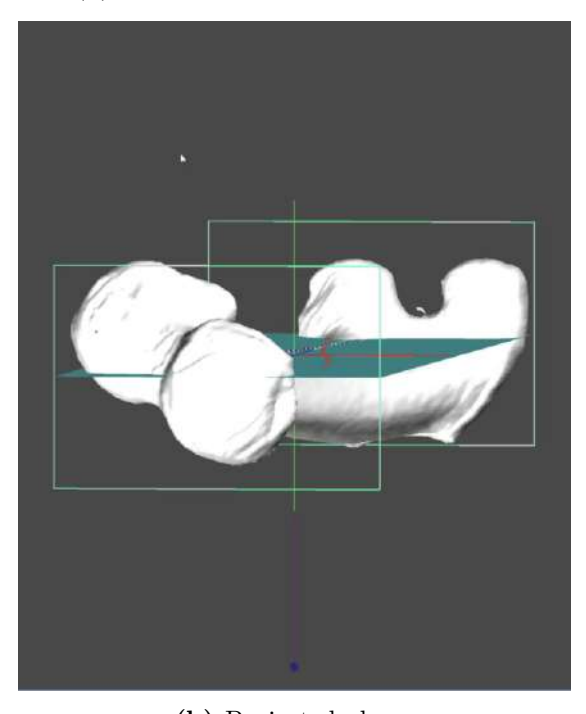


(c) Another example from the indices from eight (8) (bottom margin is equal to 0.11%) to 54 (top margin is equal to 0.18%) are used to calculate the minimum ROC.

Figure 6.23: The involved range for the calculation of the minimum ROC.

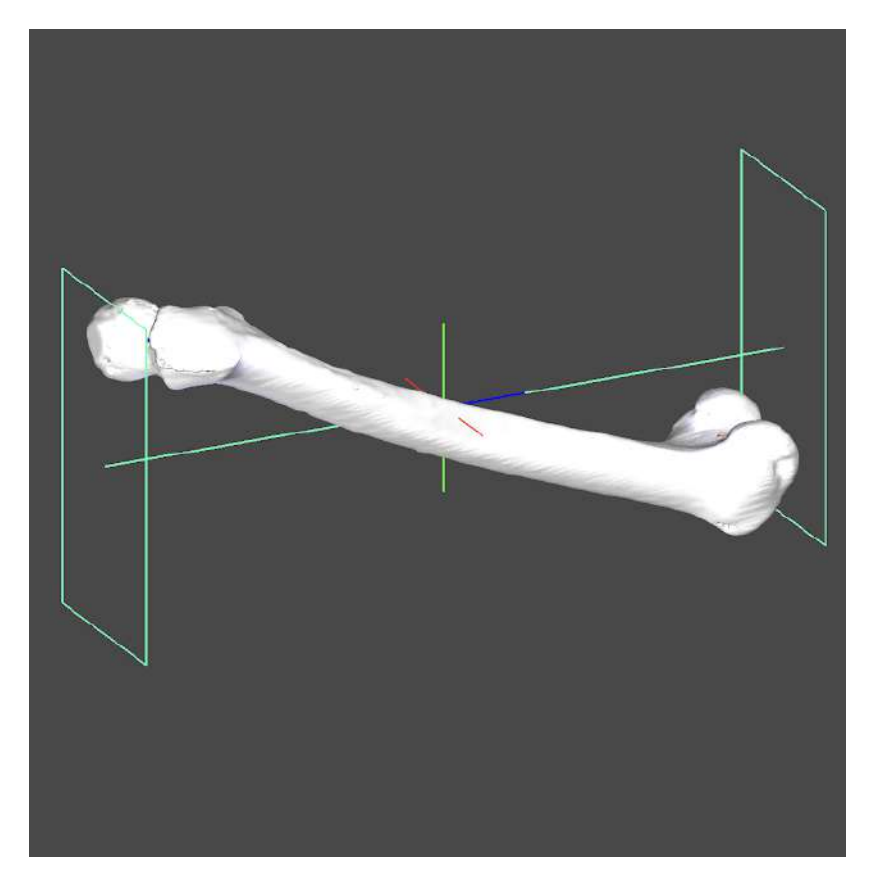


(a) The projected angle of 0° to 180° .

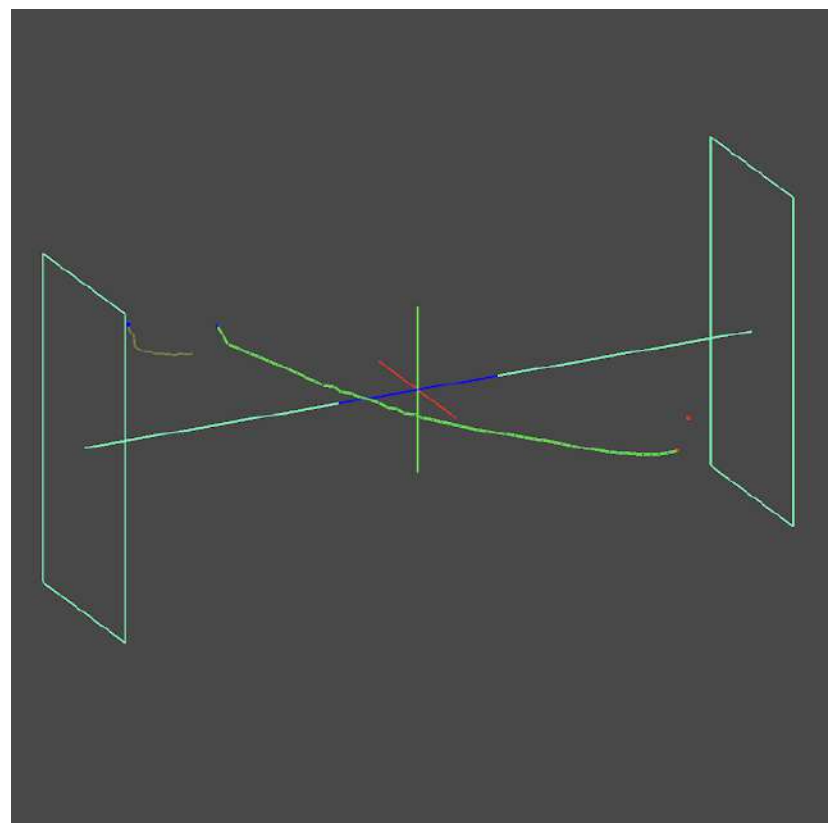


(b) Projected plane.

Figure 6.24: The projected vertices for the calculation of the minimum ROC.



 (\mathbf{c}) Resulting projection in faces view.



(d) The weighted normal of a face (triangle) f_i as denoted in Eq. (6.11).

Figure 6.24: The projected vertices for the calculation of the minimum ROC.

Chapter 7

RESULTS & DISCUSSIONS

There are mainly two (2) research questions in this research.

- A. How to perform 3D skeletonization on the given femur 3D mesh data?
- B. How is the resulting skeleton be used as an analysis study for the anatomical and geometrical parameters of the femur shaft?

The first research question has been answered in Chapter 6. Whereas the second research question is answered in this Chapter. We have divided it into four (4) sections:

- A. Results (Section 7.1)
- B. Verification and validation (Section 7.2)
- C. Comparative results (Section 7.3)

D. Future work (Section 8.2)

7.1 Results

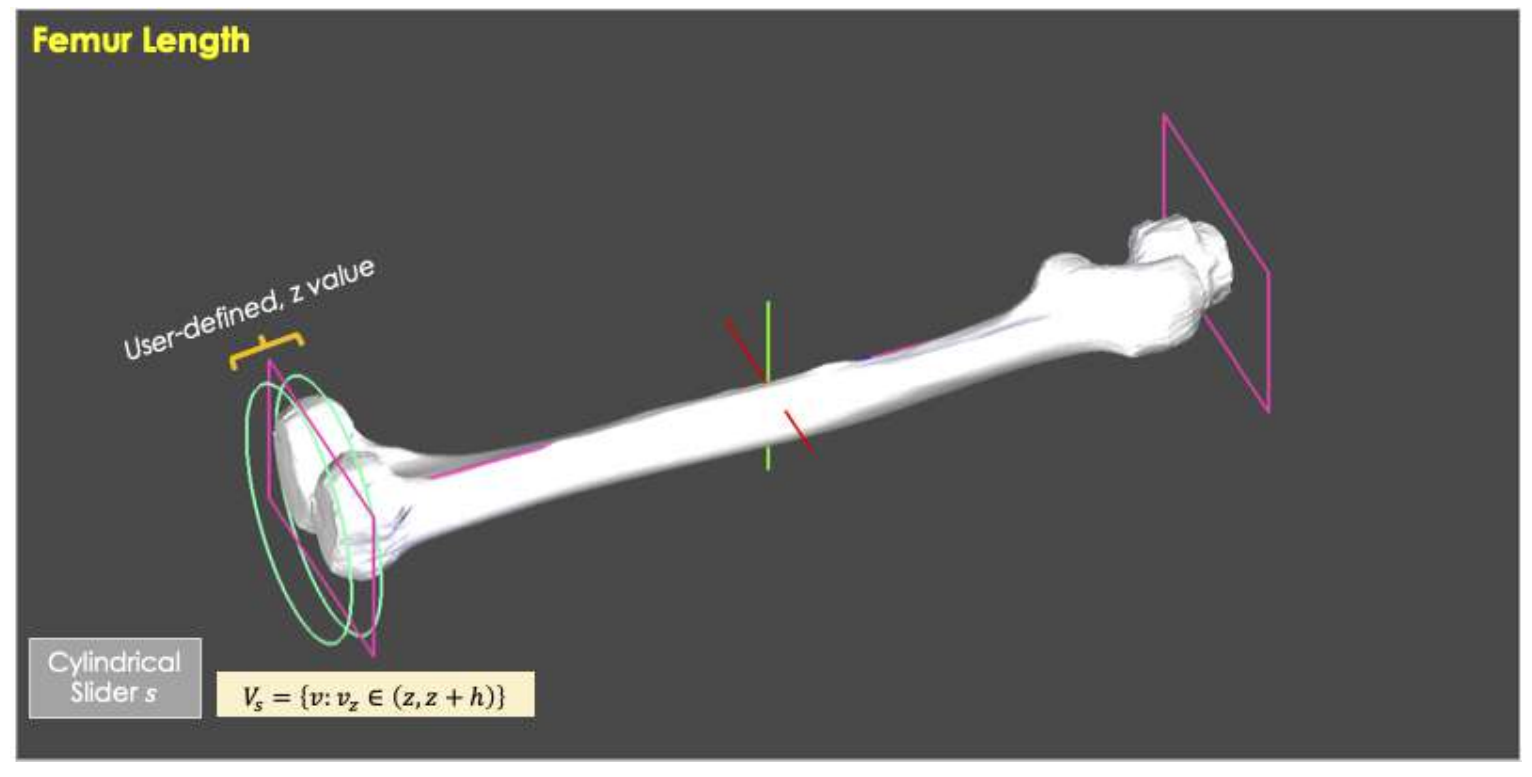
The results generated by 3D-FSA can be viewed in Table 7.1. Fig. 7.1a shows the femur length from the upper pole of the femoral head to the bicondylar baseline. Besides that, the femur shaft length from the tip of the greater trochanter to the bicondylar line is obtained from 3D-FSA as illustrated in Fig. 7.1b.

3D-FSA has also successfully compute the medial axis of the 3D femur as shown in Fig. 7.1c, by using the concept of cylindrical sliders. The base plane and the projection plane as denoted in Fig. 7.1d are used to determine the femur width and the AP length as shown in Fig. 7.1i. From the projection plane, we are able to derive the radius function for the MAT of the 3D femur as illustrated in Fig. 7.1e.

Based on the obtained result, the location and the diameter of the medullary canal are calculated as shown in Fig. 7.1f and Fig. 7.1g. The thickness of the compact bone and the ROC as shown in Fig. 7.1h and Fig. 7.1j respectively are also provided in 3D-FSA.

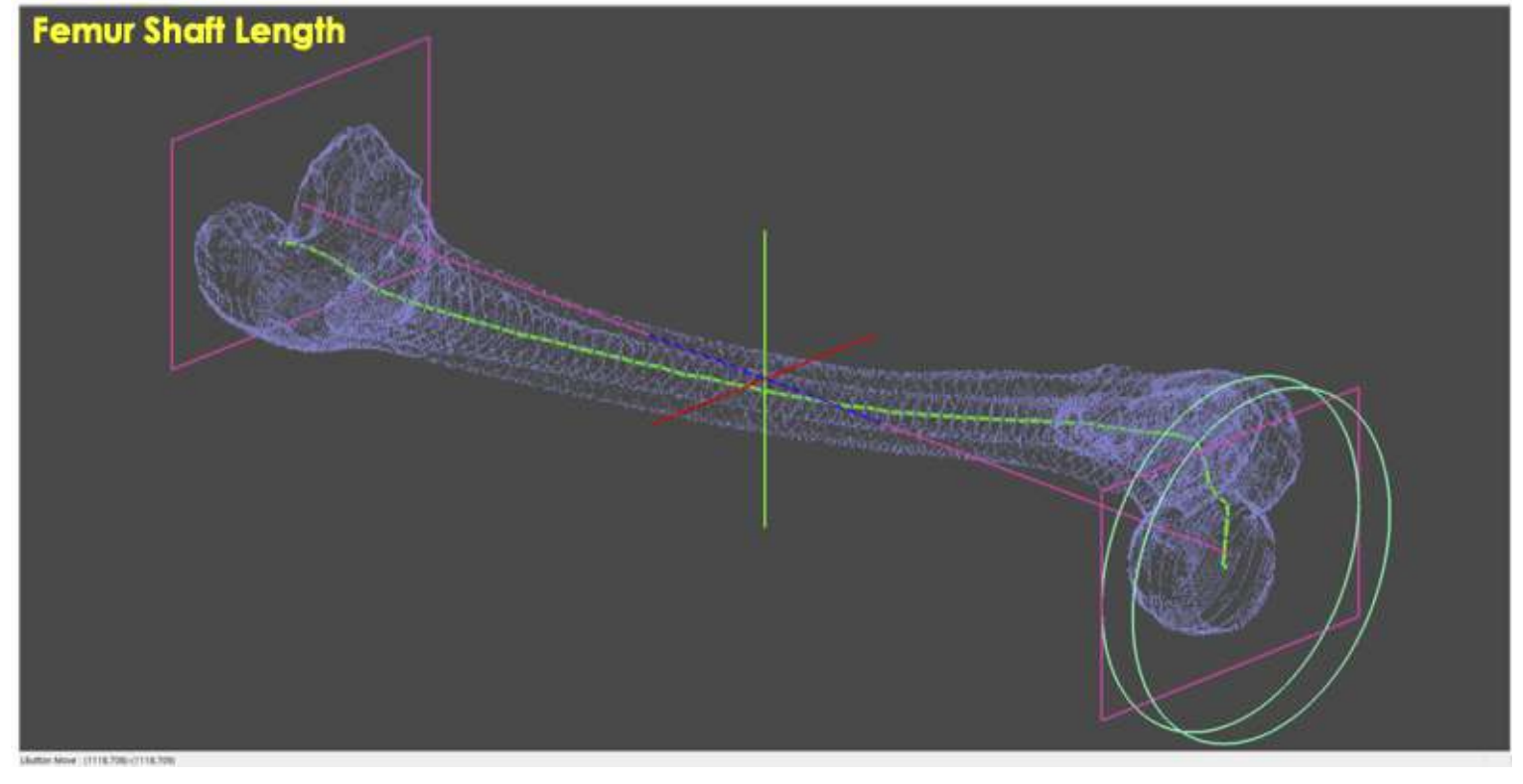
Table 7.1: Generated geometric parameters and the respective figures.

Generated Geometric Parameters	Figure No.
Femur Length	Fig. 1.24a
Femur Shaft Length	Fig. 1.24b
Femur Width	Fig. 1.24i
Femur AP Length	Fig. 1.24i
Diameter of medullary canal	Fig. 1.24f and Fig. 1.24g
Thickness of the Compact Bone	Fig. 1.24h
ROC	Fig. 1.24e and Fig. 1.24j



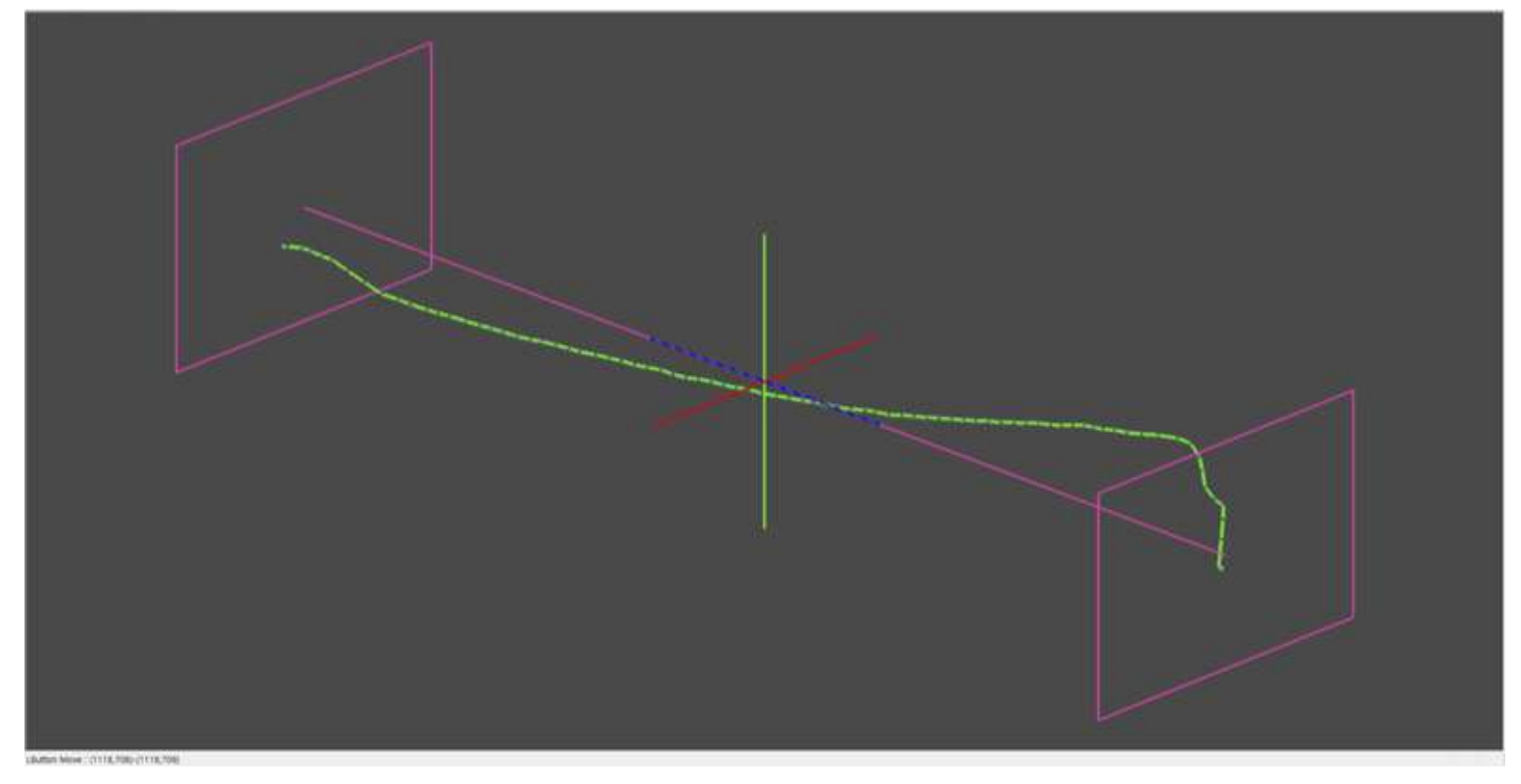
(a) The femur length.

Figure 7.1: The results generated by 3D-FSA.



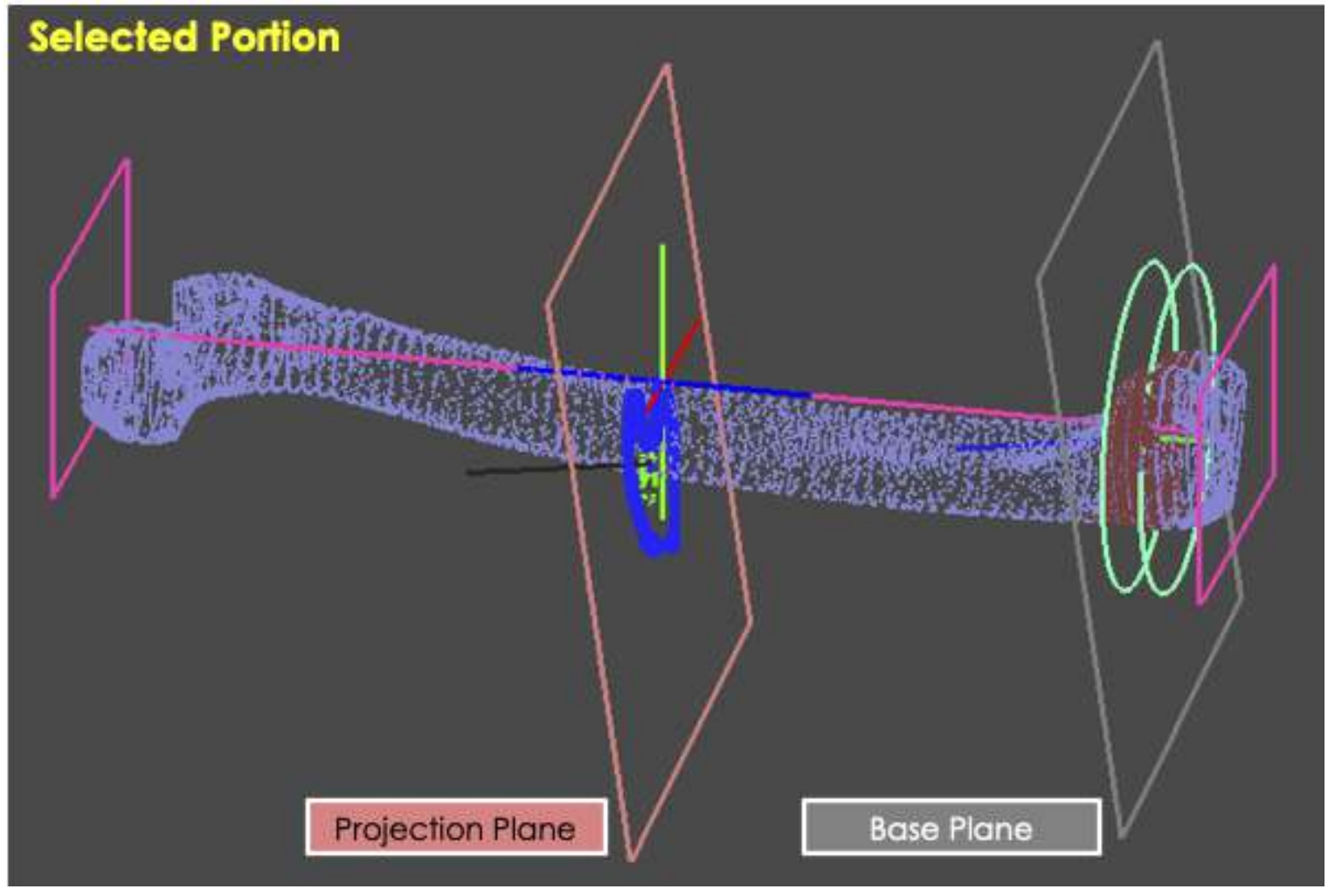
(b) The femur shaft length.

Figure 7.1: The results generated by 3D-FSA.



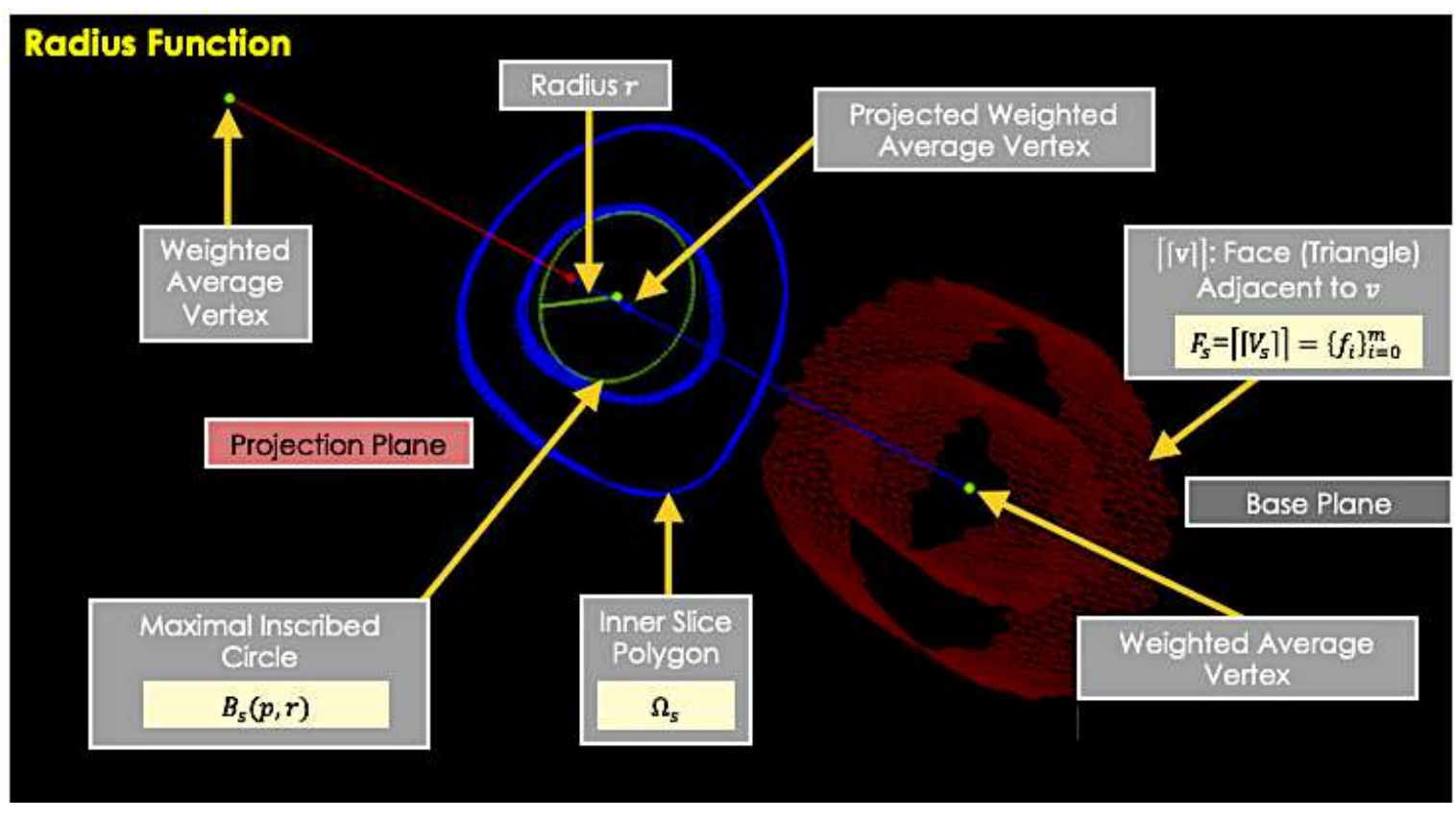
(c) The generated MA.

Figure 7.1: The results generated by 3D-FSA.



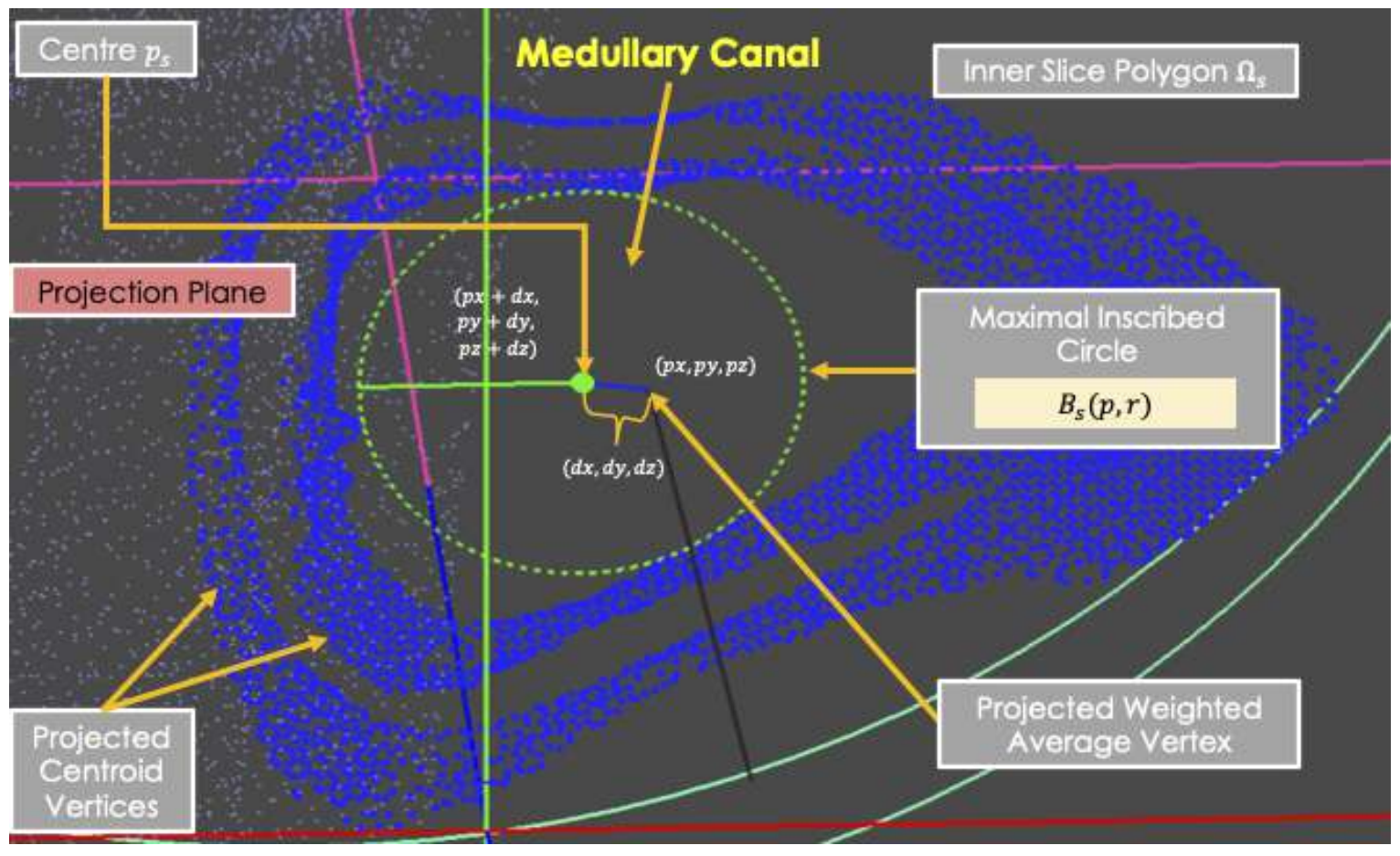
(d) The medial centres are generated by the selected portion of the cylindrical slider s on the base plane.

Figure 7.1: The results generated by 3D-FSA.



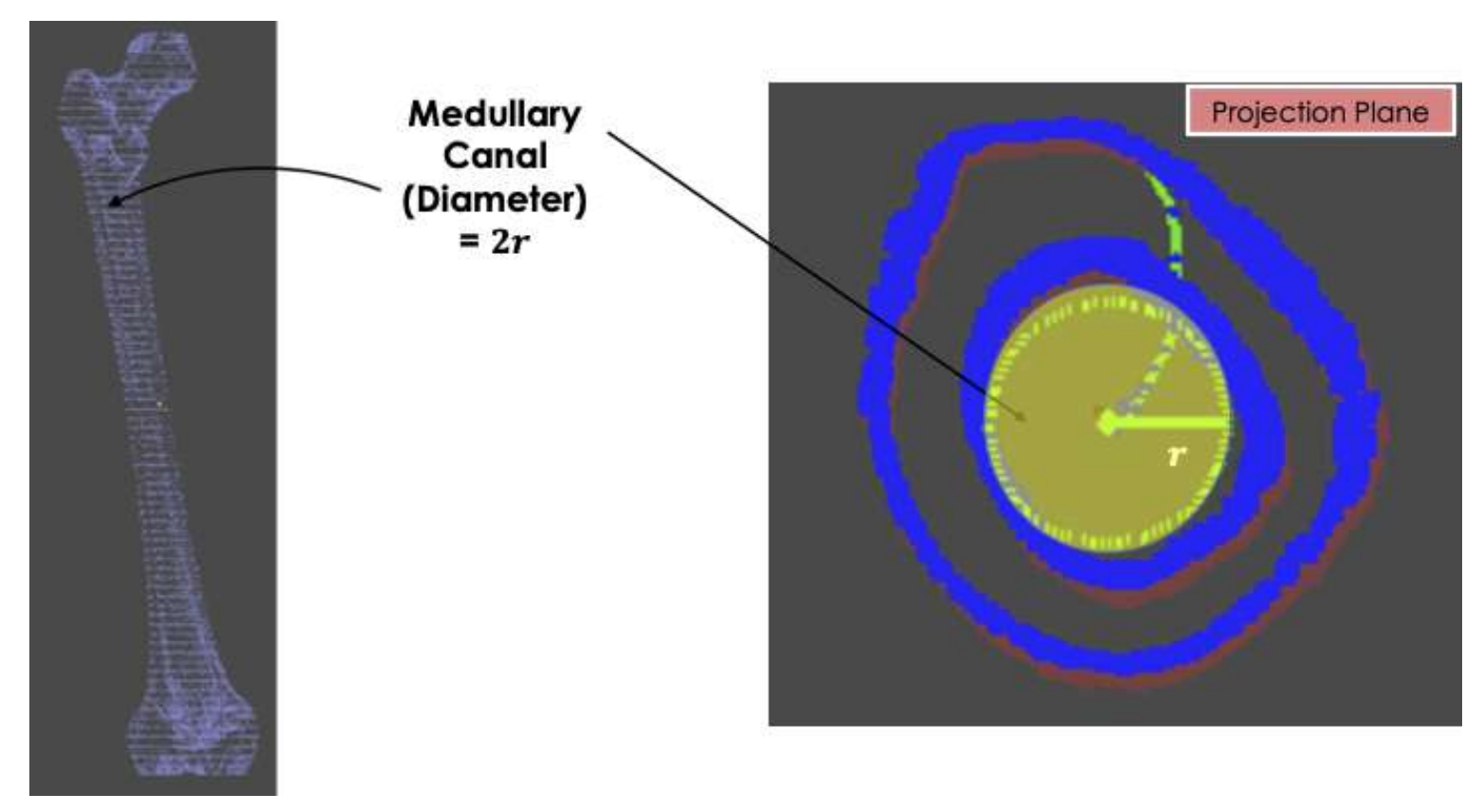
(e) The computed radius function for the MAT.

Figure 7.1: The results generated by 3D-FSA.



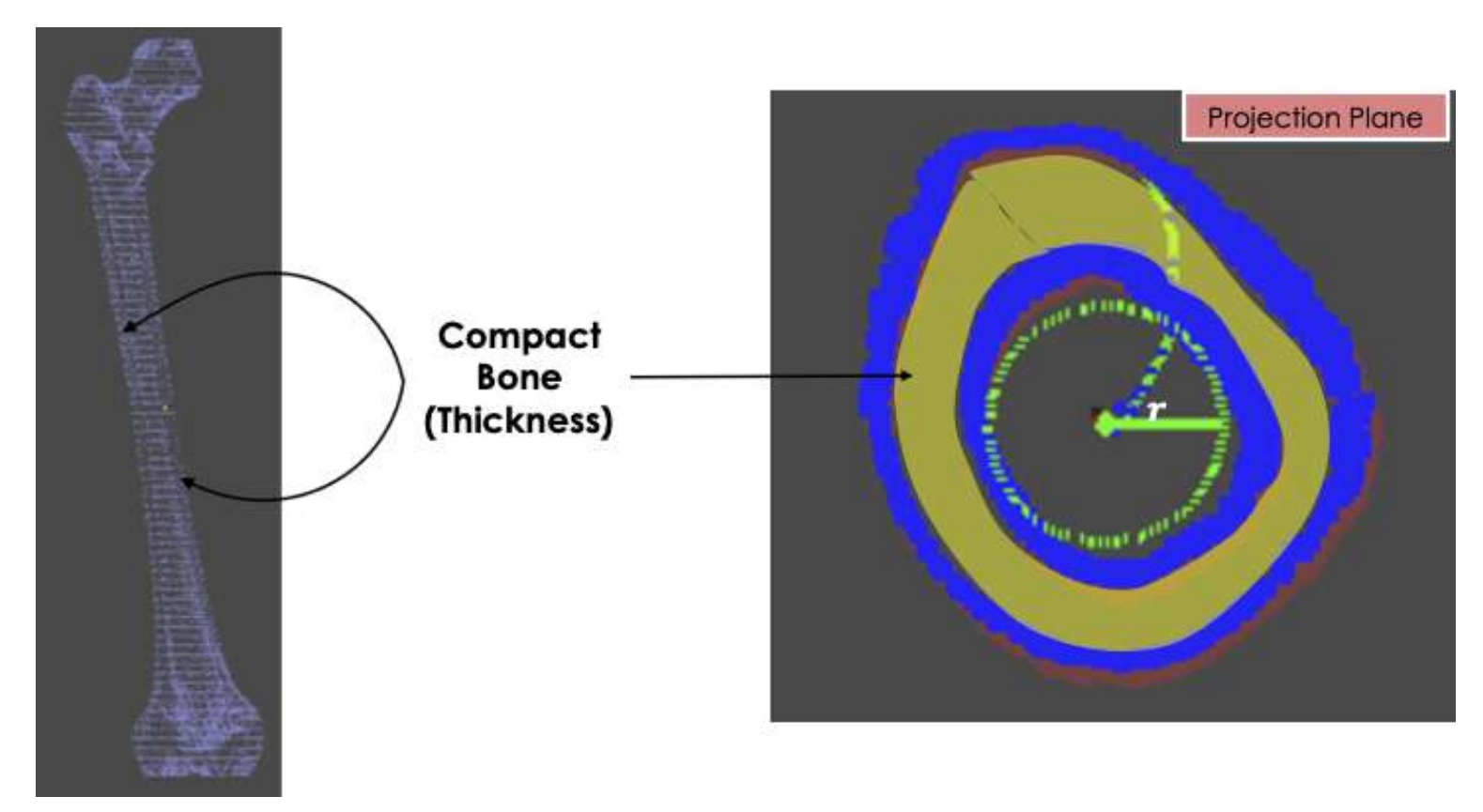
(f) The location of the medullary canal.

Figure 7.1: The results generated by 3D-FSA.



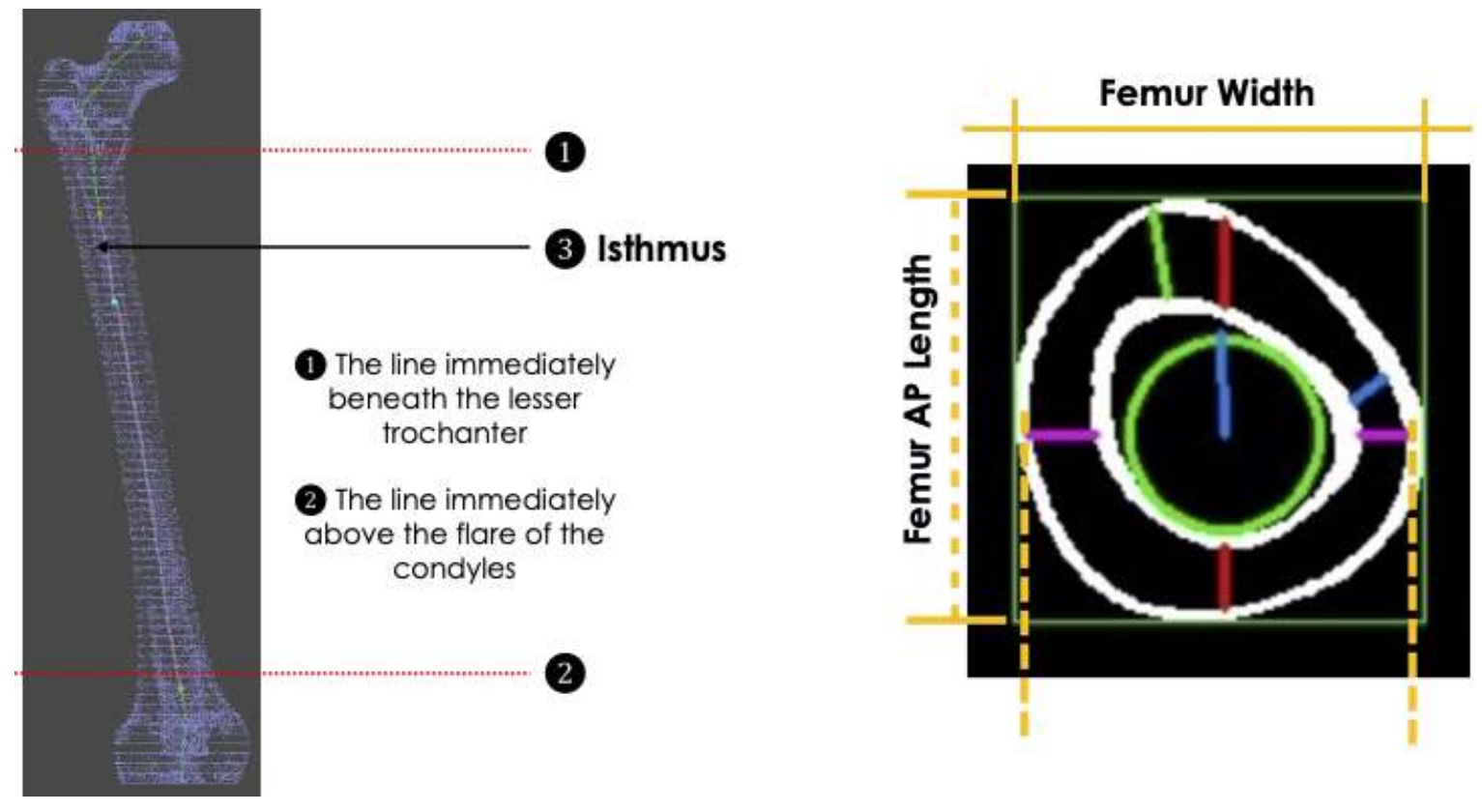
(g) The diameter of the medullary canal is obtained in the projection plane.

Figure 7.1: The results generated by 3D-FSA.



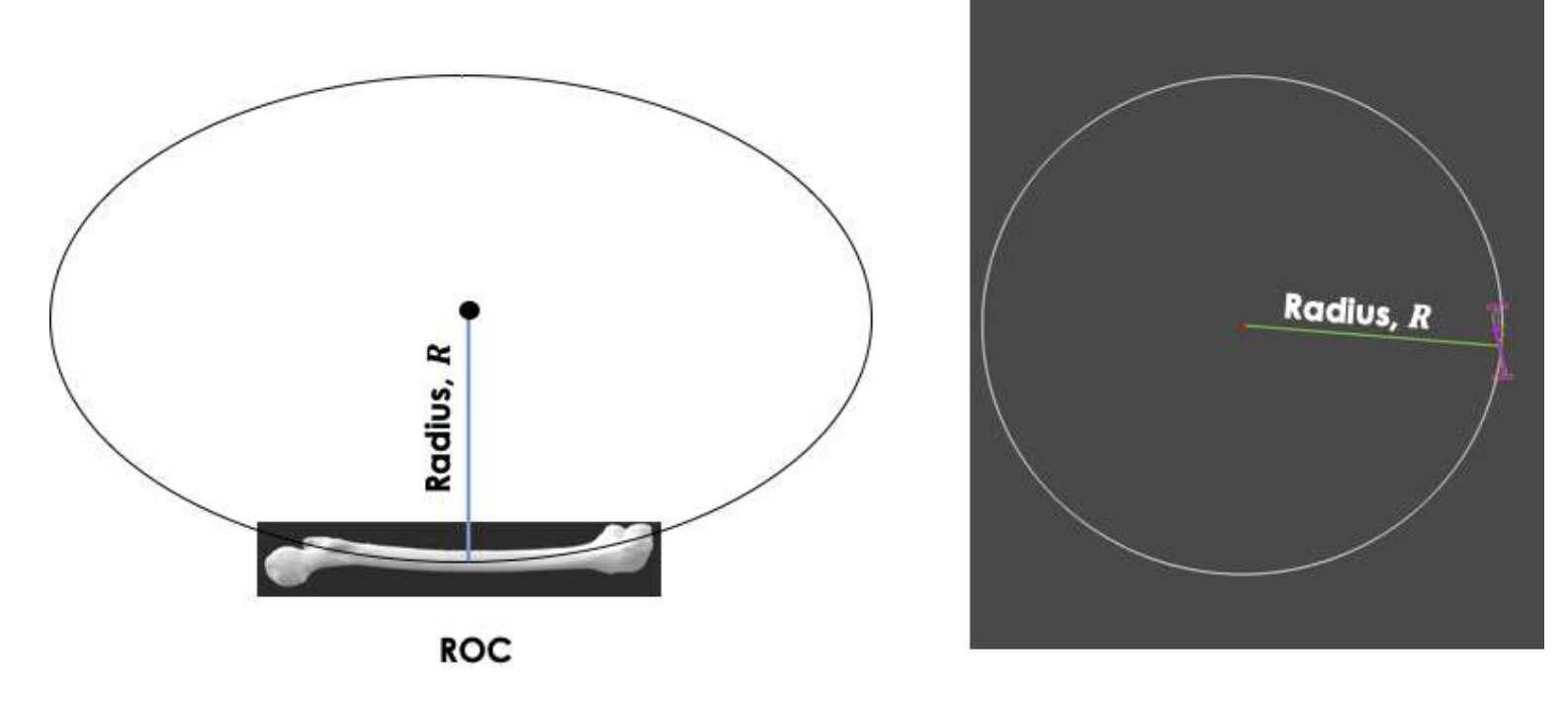
(h) The thickness of the compact bone is also calculated.

Figure 7.1: The results generated by 3D-FSA.



(i) The location of the isthmus and its diameter, the femur width and the AP length.

Figure 7.1: The results generated by 3D-FSA.



(j) The ROC together with the minimum radius angle.

Figure 7.1: The results generated by 3D-FSA.

7.2 Verification and Validation

These obtained parameters from 3D-FSA have been utilised by the researchers from South Korea [16] in their morphological study of the femoral geometry that focuses on the bowing and width among the Korean ethnicity for the age range between twenty (20) and eighty-nine (89) years old, without the concern of any implant, deformity, or surgical history of the femur. The researchers consists of the following:

- A. I. J. Jung from the University of Ulsan College of Medicine, Seoul (First Author).
- B. E. J. Choi from the Department of Orthopaedics, Asan Medical Centre, Seoul.
- C. B. G. Lee from the Division of Computer Engineering, Dongseo University, Busan.
- D. J. W. Kim from the Department of Orthopedic Surgery, University of Ulsan College of Medicine, Asam Medical Centre, Seoul (Corresponding Author).

In this study, a total of thousand and four hundred (1400) age and sex-stratified participants were enrolled and were divided into subgroups according to age (by decade) and sex. The collected CT images of both femurs from the participants were fully scanned, and the conversion to 3D file formats was completed using the commercial 3D modelling software.

The 3D-FSA is then reads the converted 3D file format in order to construct a 3D femur. Followed by applying the proposed 3D skeletonization method, a compact representation of the femur is obtained, resulting a skeleton for the 3D femur. Several significant parameters are captured from the obtained skeleton for the analysis of the femur shaft geometry from various age and sex related groups as shown in Table 7.1.

Apart from that, they have conducted the verification and validation of the measurements provided by 3D-FSA, by collecting fifty (50) participants who were evenly distributed by age and sex groups. A descriptive statistics were used to determine the group means and standard deviations for numerical data. [16] has compared each parameter between the left and right femur in the same patient using a paired t test or Wilcoxon signed-rank test.

Correlation with age was calculated using Pearson's correlation coefficients in women, men, and both sexes respectively. They have divided the participants by age group with the cutoff age of fifty (50) years old and compared them using a t test in women and men. Linear regression was used to compare the trend of change between age groups in each sex. Statistical significance was defined as a P value less than 0.05. Statistical analysis was performed using R version 3.0.2 [284].

Besides that, the ICC of each parameter were calculated, and the results were larger than 0.75, which has revealed the intra-observer reliability and accuracy of our system, 3D-FSA [16]. This result also indicates an excellent agreement according to Cicchetti [139], and 3D-FSA has been validated.

They have presented the age and sex related factors affect the femoral bowing and the diameter of the medullary canal. The results concluded that women had more bowed femurs than men. Moreover, as the age increases, the femur becomes more curved, and this tendency is more apparent in women. As a result, these patients are more vulnerable to insufficiency fractures. Several studies [55, 10, 52, 15, 285, 286] have shown that Asians have a smaller ROC than Caucasians, especially in women, and that femur bowing is correlated with race.

[39, 16] presumed that if seven-hundred (700) mm is the minimum ROC possible with the current nails, the current intramedullary nail would result in a mismatch problem in 11.5% of the Korean population because of their severely bowed femur. Their analysis demonstrated that during the ageing process, both the outer diameter and the diameter of the internal medullary canal were increased among women older than fifty (50) years. Moreover, the linear regression analysis showed that femoral bowing was not related to medullary canal widening but was related to ageing rather than osteo-porosis.

You may refer to this paper [16] for further information. Although I am not part of the author for this paper [16] due to some rules and regulations, I have submitted a poster proceeding to International Geometry Summit (IGS2019) about this research and presented in Simon Fraser University's Vancouver campus, Canada on 19th June 2019. This poster was a joint research with my main supervisor, Ir. Prof. Dato' Dr. Ewe Hong Tat, my co-supervisor Lee Byung-Gook (B. G. Lee: *The third author of [16]*) and Professor Dr. Kim Ji Wan (J. W. Kim *The corresponding author of [16]*).

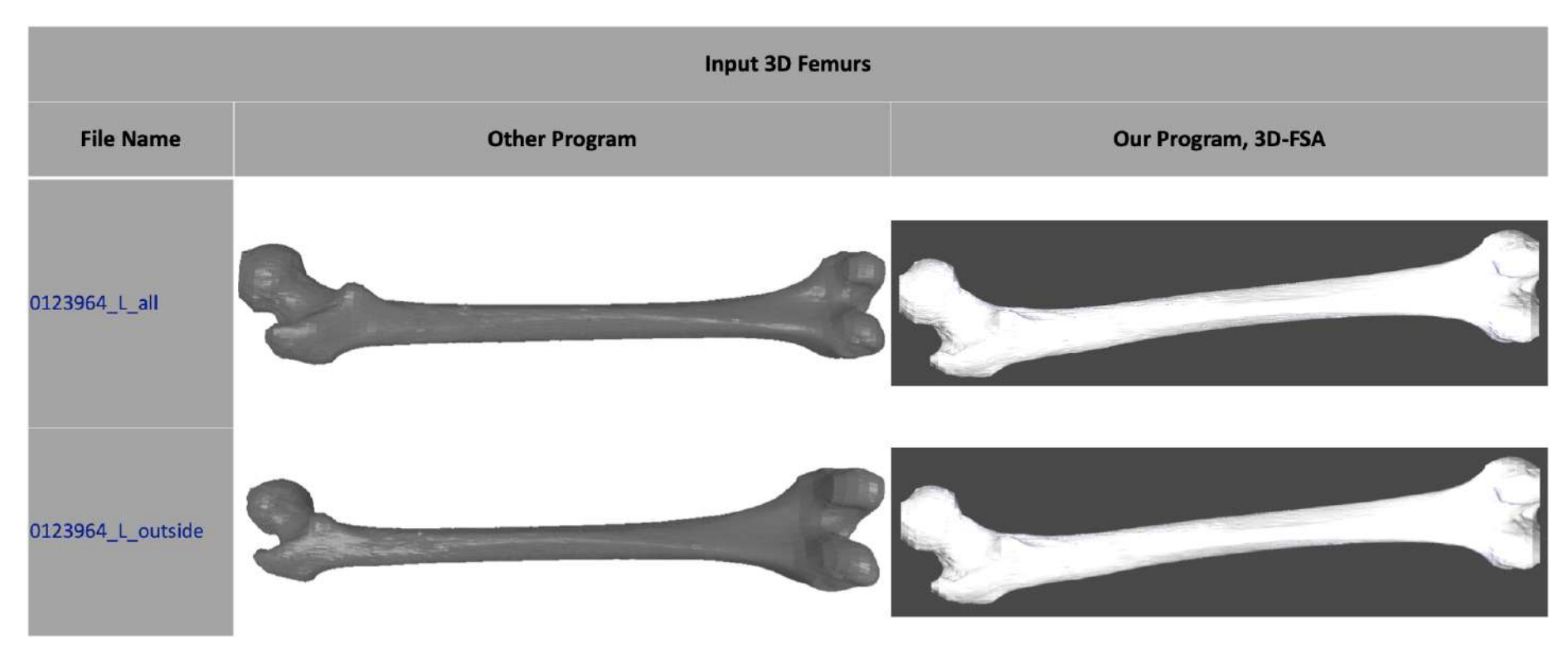
7.3 Comparative Results

It is important to produce a high-fidelity 3D femur from the input 3D data files of .obj format. Hence, we included the comparison results to show the quality of the constructed 3D femurs using the other program and using our program, 3D-FSA. The other program that we used as comparisons was downloaded from github [22].

7.3.1 Constructed 3D Femurs

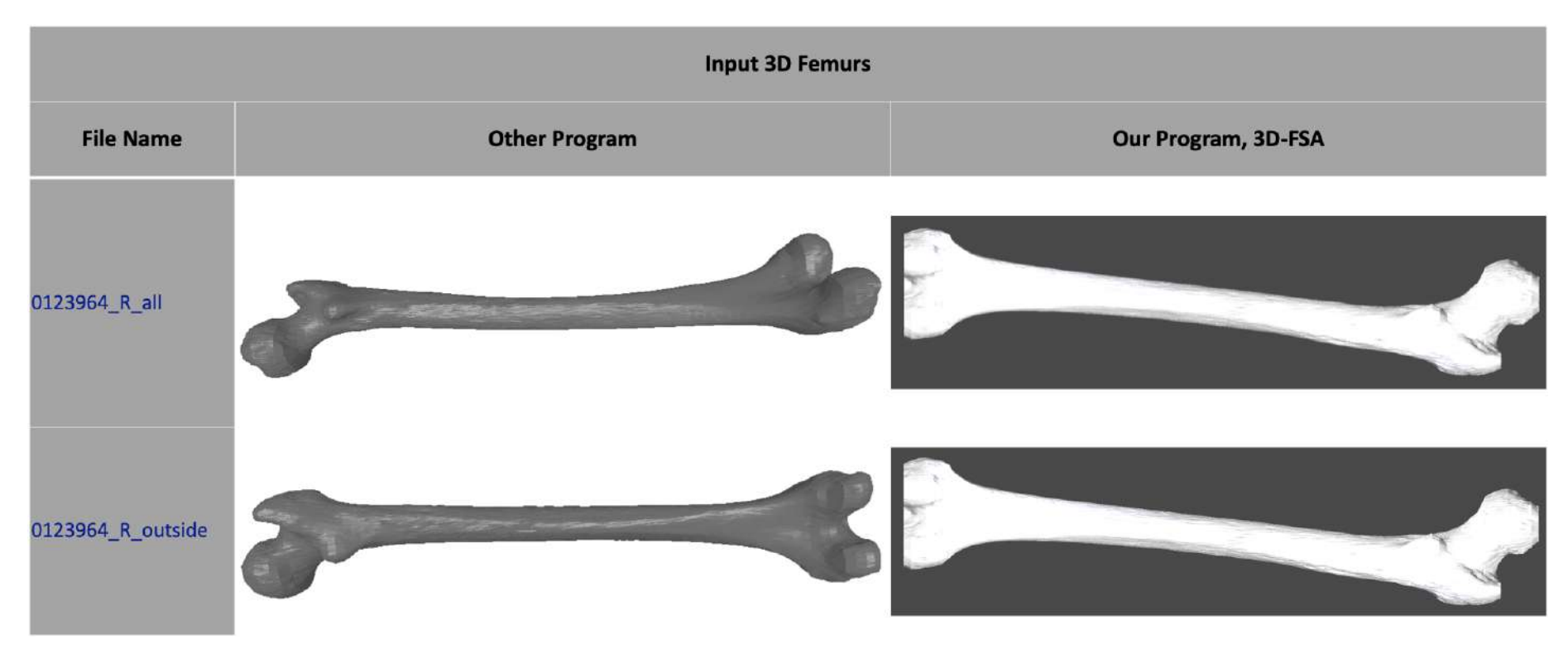
Schlegel et al., uses Python 3 library to construct the 3D femurs, together with the help of *trimesh*. As illustrated in Fig. 7.2, the constructed 3D femurs by [22] tends to have jagged edges.

On the other hand, the constructed 3D femurs by our program, 3D-FSA tends to be smoother and less jagged edges. Therefore, our program is more reliable and higher accuracy.



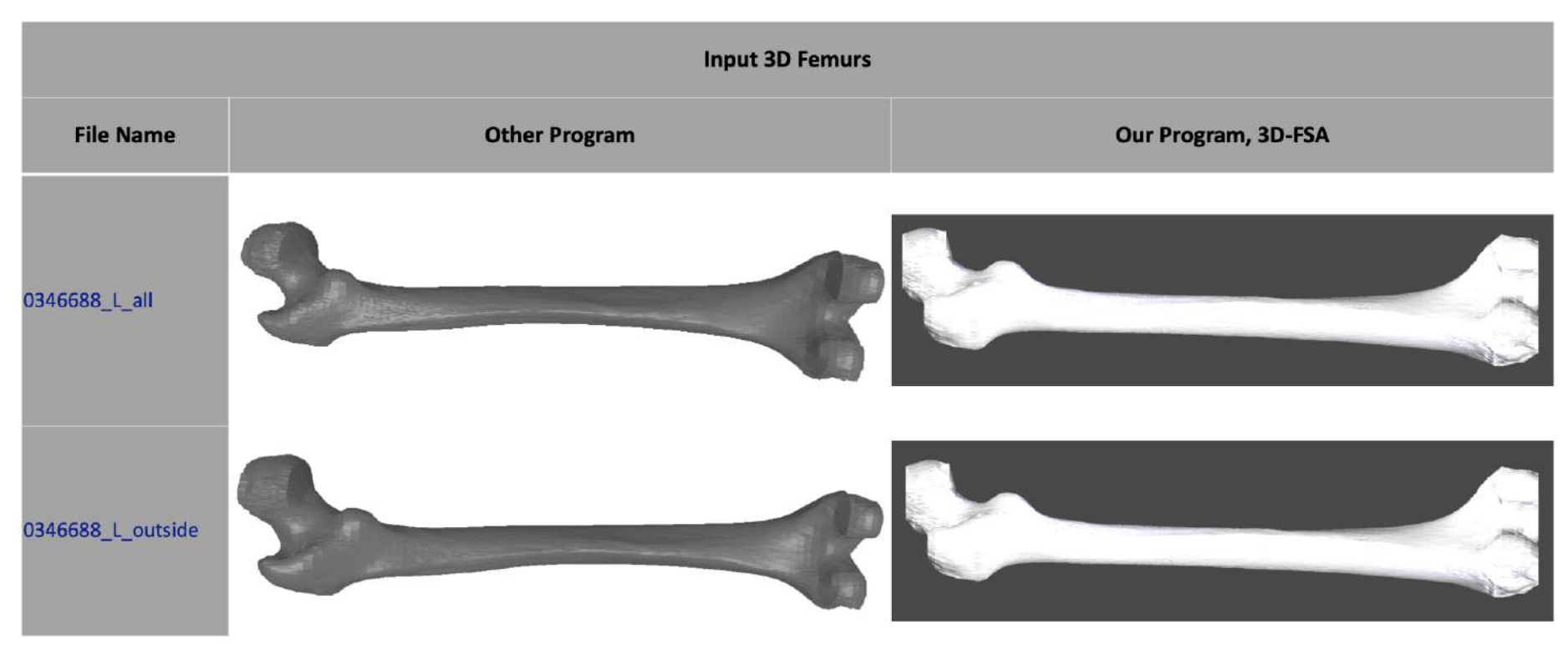
(a) Constructed 3D femurs of 0123964 (Left femur) using the other program [22] and our program.

Figure 7.2: The comparison results between using the other program [22] and our program to construct 3D femurs.



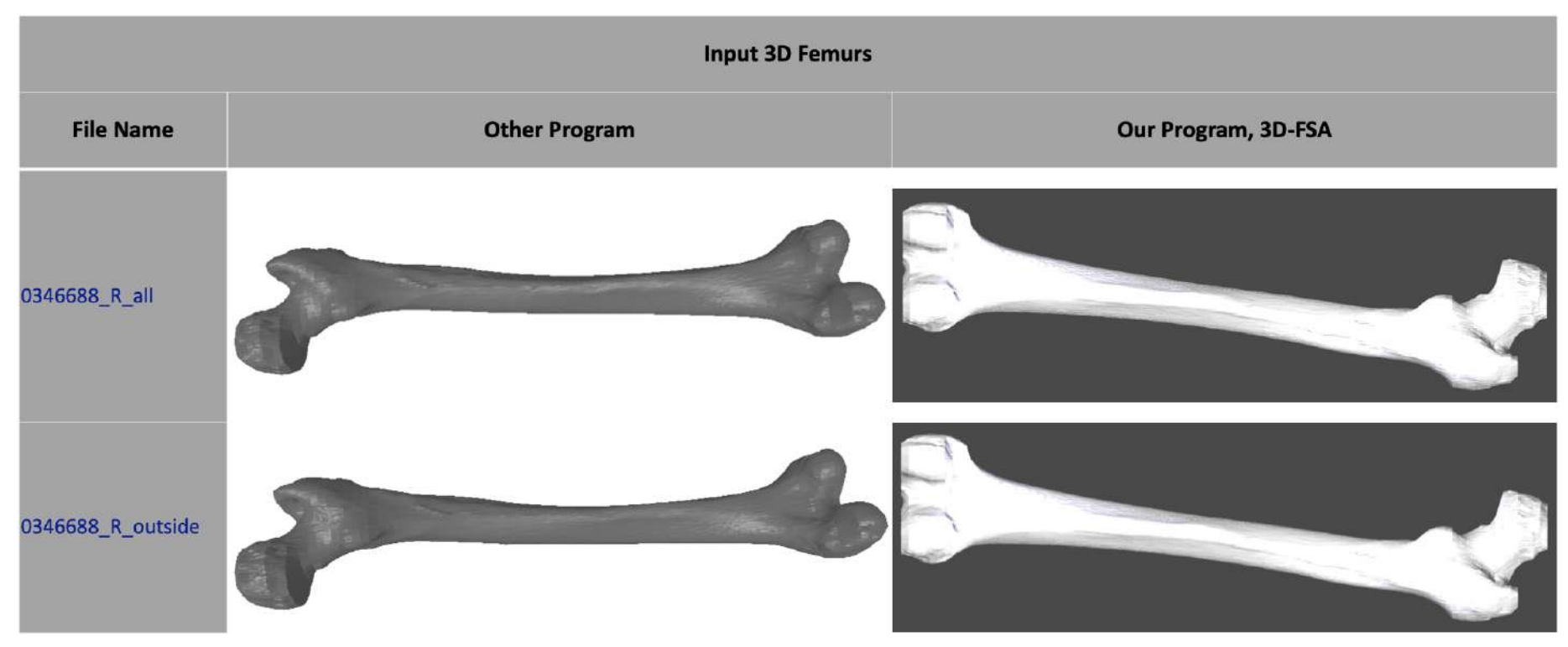
(b) Constructed 3D femurs of 0123964 (Right femur) using the other program [22] and our program.

Figure 7.2: The comparison results between using the other program [22] and our program to construct 3D femurs.



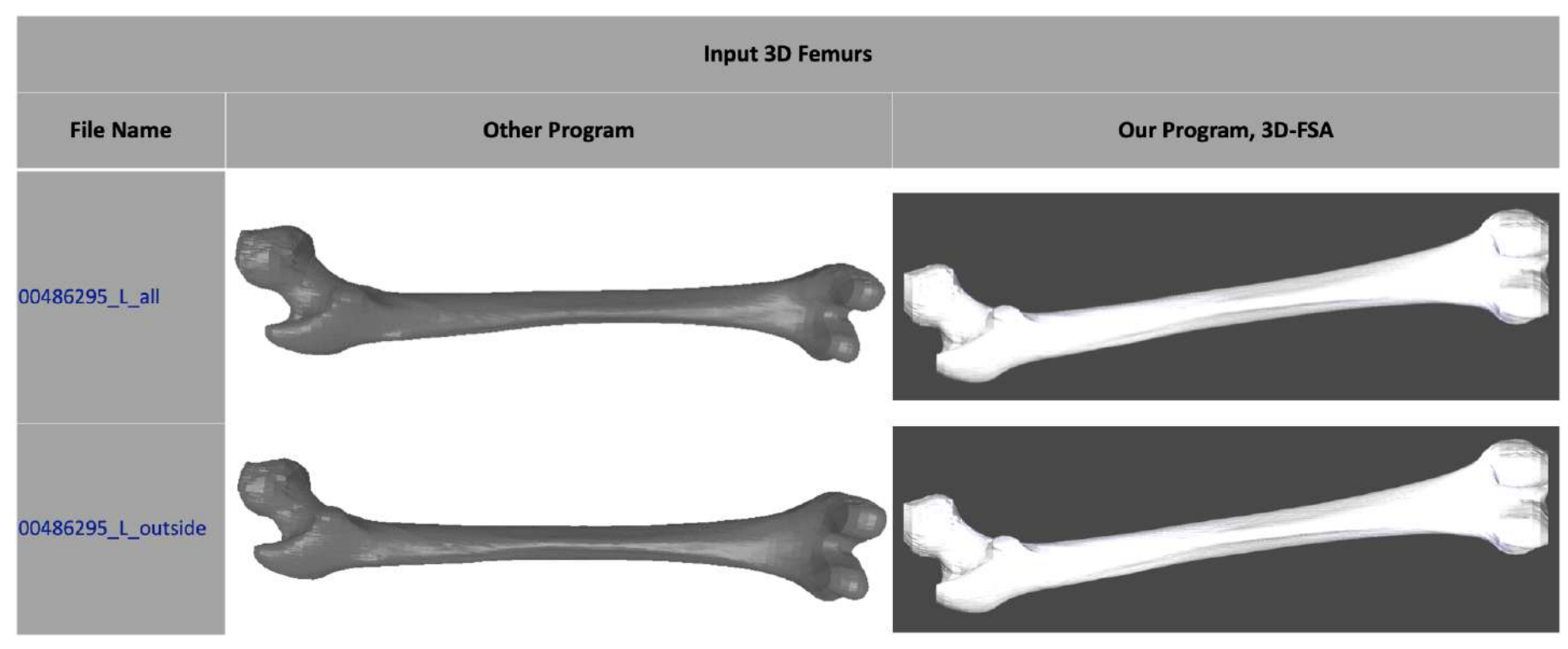
(c) Constructed 3D femurs of 0346688 (Left femur) using the other program [22] and our program.

Figure 7.2: The comparison results between using the other program [22] and our program to construct 3D femurs.



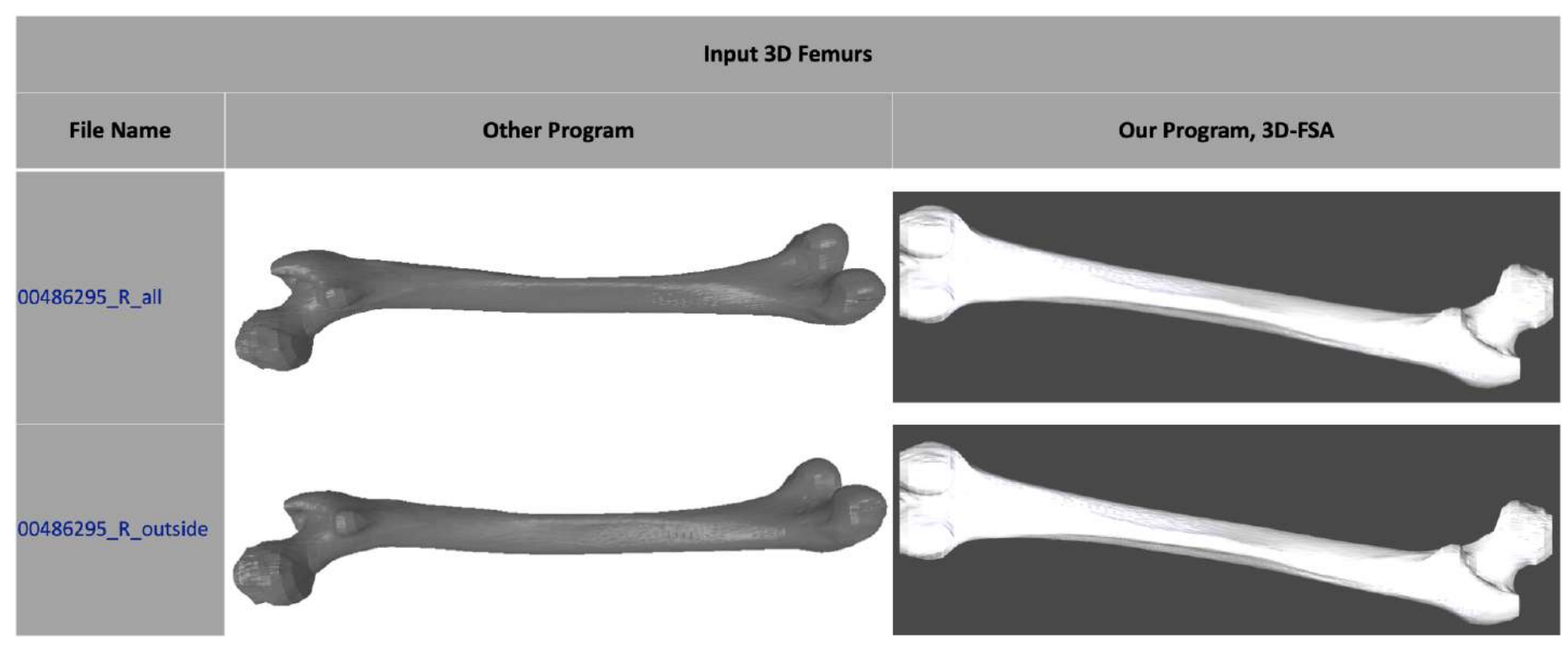
(d) Constructed 3D femurs of 0346688 (Right femur) using the other program [22] and our program.

Figure 7.2: The comparison results between using the other program [22] and our program to construct 3D femurs.



(e) Constructed 3D femurs of 00486295 (Left femur) using the other program [22] and our program.

Figure 7.2: The comparison results between using the other program [22] and our program to construct 3D femurs.



(f) Constructed 3D femurs of 00486295 (Left femur) using the other program [22] and our program.

Figure 7.2: The comparison results between using the other program [22] and our program to construct 3D femurs.

7.3.2 Computed Medial Axis (Skeleton)

For 3D femur shapes, we compared our 3D skeletonization method, maximum-minimum centre approach [140, 141] with the Thinning-based 3D skeletonization method [87] against the selected properties as delineated in Table 7.2.

Table 7.2: Skeletonization properties that are used in our comparative results.

No.	Properties				
1	Homotopy				
2	Thinness				
3	Centredness				
4	Computational Scalability				

There is only one (1) existing method to be included in this discussion due to this program that is shared by [22, 223] are the only program workable and it is able to read our 3D femur file formats.

Thinning-based methods iteratively smoothen and collapse the 3D mesh geometry in a constrained manner. It peels off the boundary voxels whose deletion sometimes alter the 3D mesh topology [86, 87, 88, 89]. The disadvantage of these methods are the extracted skeletons tends to be spurious and consists of a great number of noises as shown in Fig. 7.3. The detailed comparison are described next.

Homotopy

Both methods shown in Fig. 7.3a until Fig. 7.3f captured well the input shape topology, and delivered connected skeletons. The Thinning-based

methods also captured the protrusions and tunnels of the femure but not in our method.

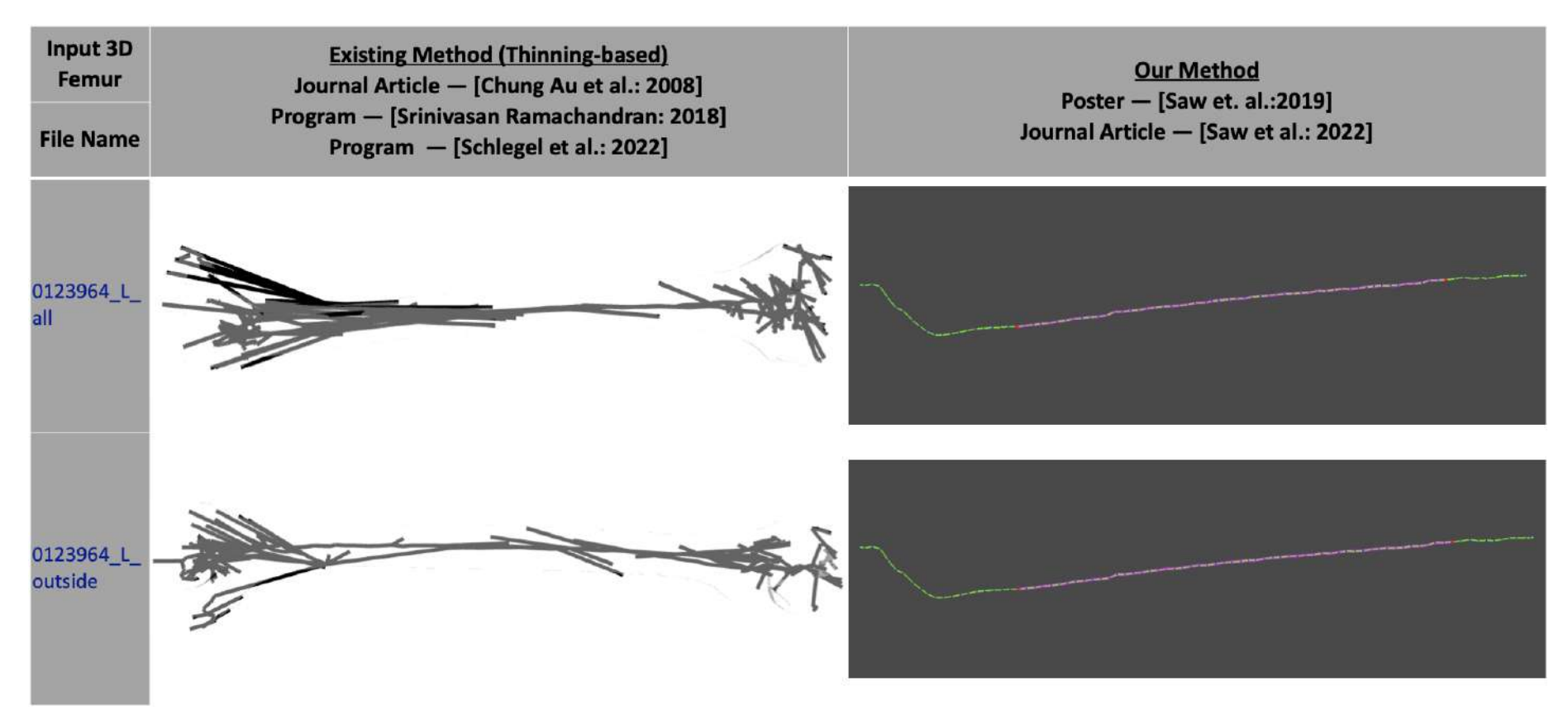
However, the obtained skeleton by the Thinning-based methods exhibits a great number of small spurious in all region especially in the proximal and distal femurs, but our method produces clean skeletons which match the human femur's topology. Besides that, the number of medial centres are equivalent to the number of the cylindrical sliders.

Thinness

For our method, this criterion implies one-thin curve skeletons by using visual inspection as illustrated in Fig. 7.3a until Fig. 7.3f. As for the Thinning-based methods create spurious thick fragments as illustrated in same figures at the third column. In fact, they do not have an explicit thinning step or similar post-processing to guarantee the thin skeletons.

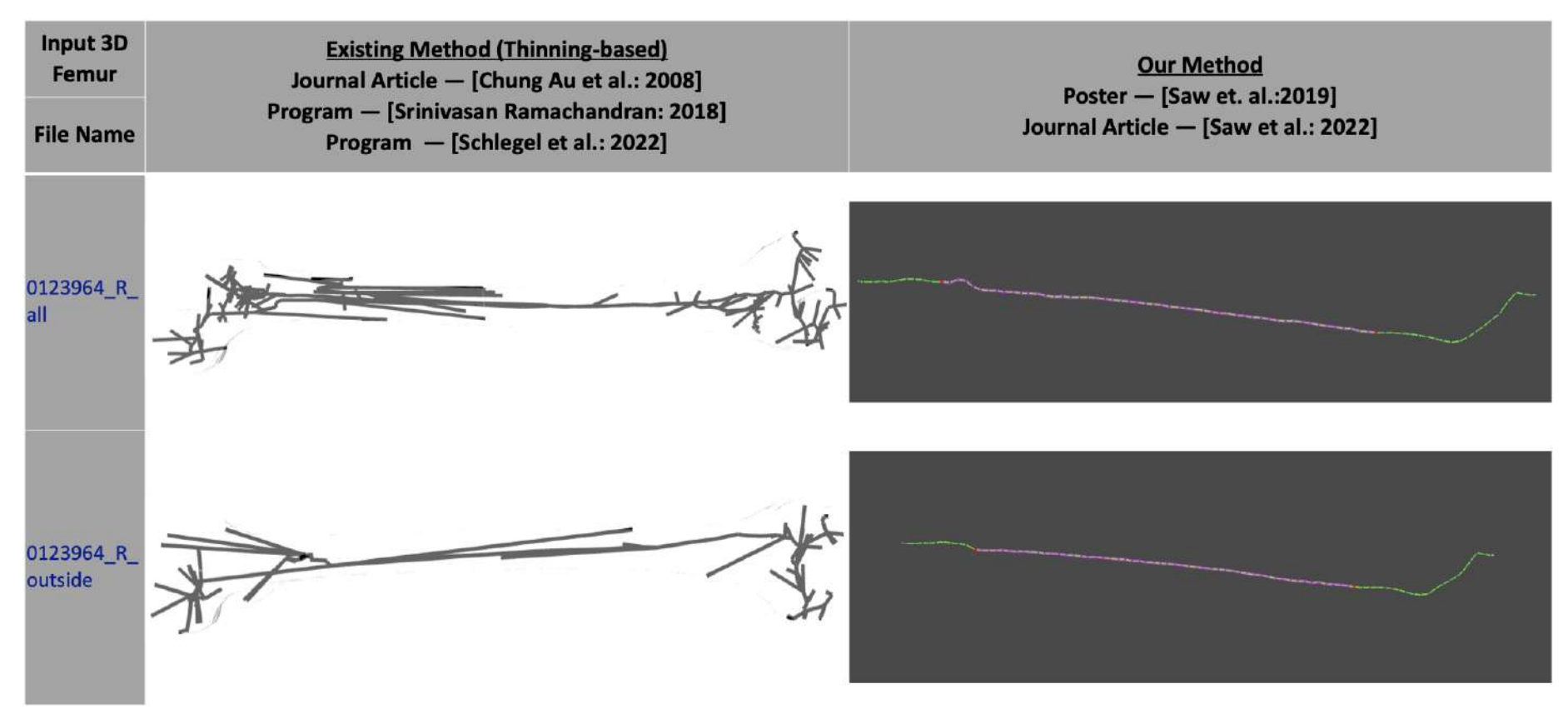
Centredness

Visual comparison of the computed skeletons by using our method appear well centred within the 3D femurs as illustrated in Fig 7.3. But not for the skeletons produced by the Thinning-based methods which arguably not in the centre, due to a great number of spurious branches in all region (Refer to Fig. 7.3).



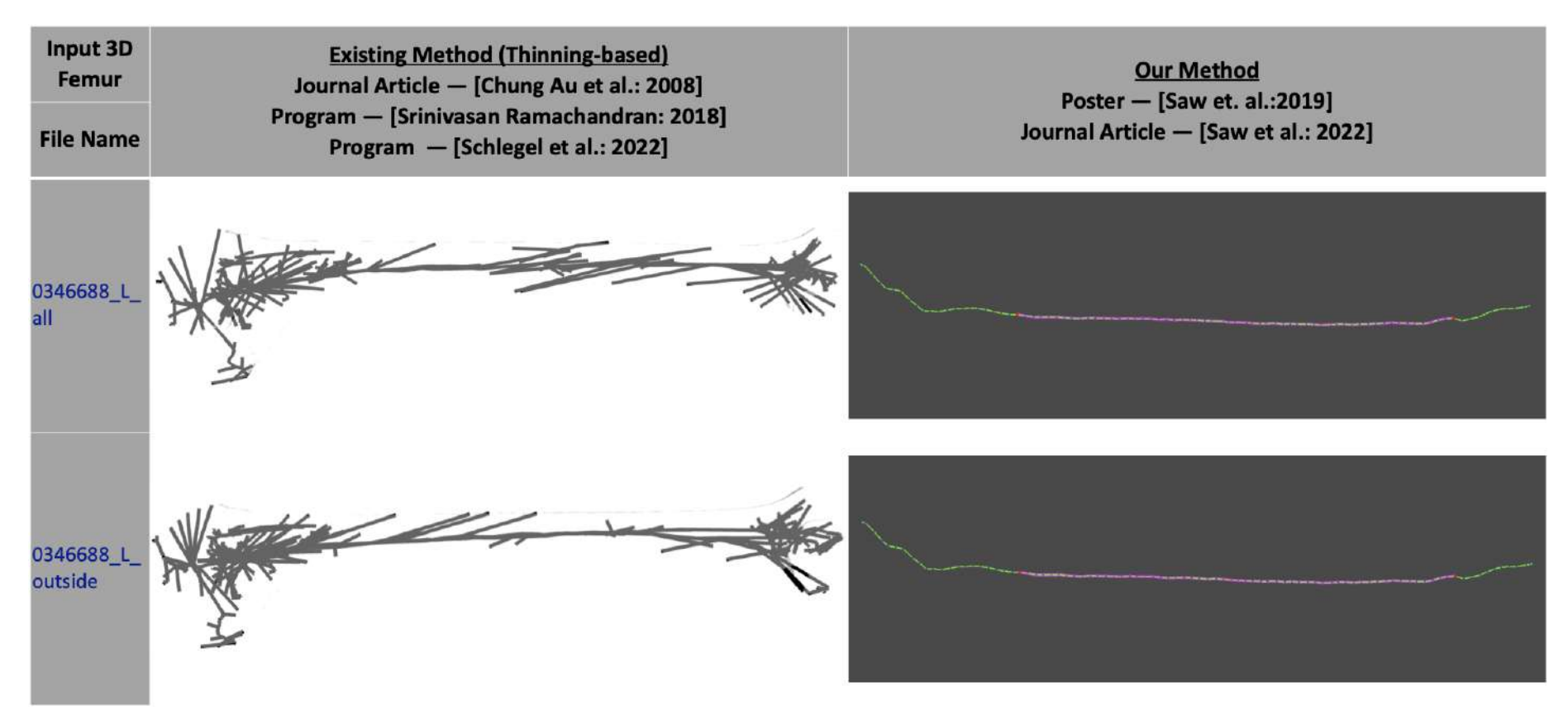
(a) 3D femurs obtained from a patient with the code number of 0123964 (Left femur), and the constructed skeletons using the existing method and our method.

Figure 7.3: The comparison results between using the existing method of Thinning-based 3D skeletonization and our method on the 3D femurs.



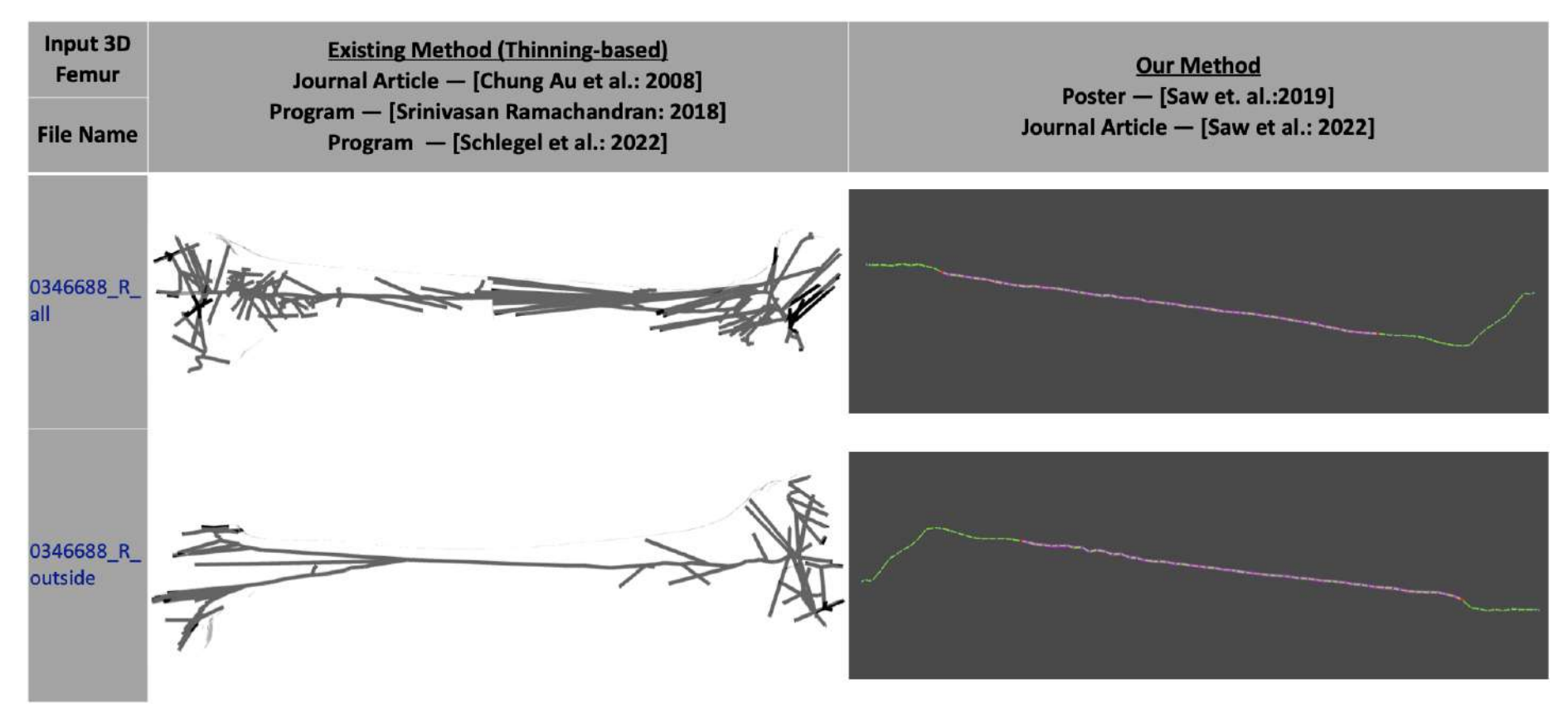
(b) 3D femure obtained from a patient with the code number of 0123964 (Right femur), and the constructed skeletons using the existing method and our method.

Figure 7.3: The comparison results between using the existing method of Thinning-based 3D skeletonization and our method on the 3D femurs.



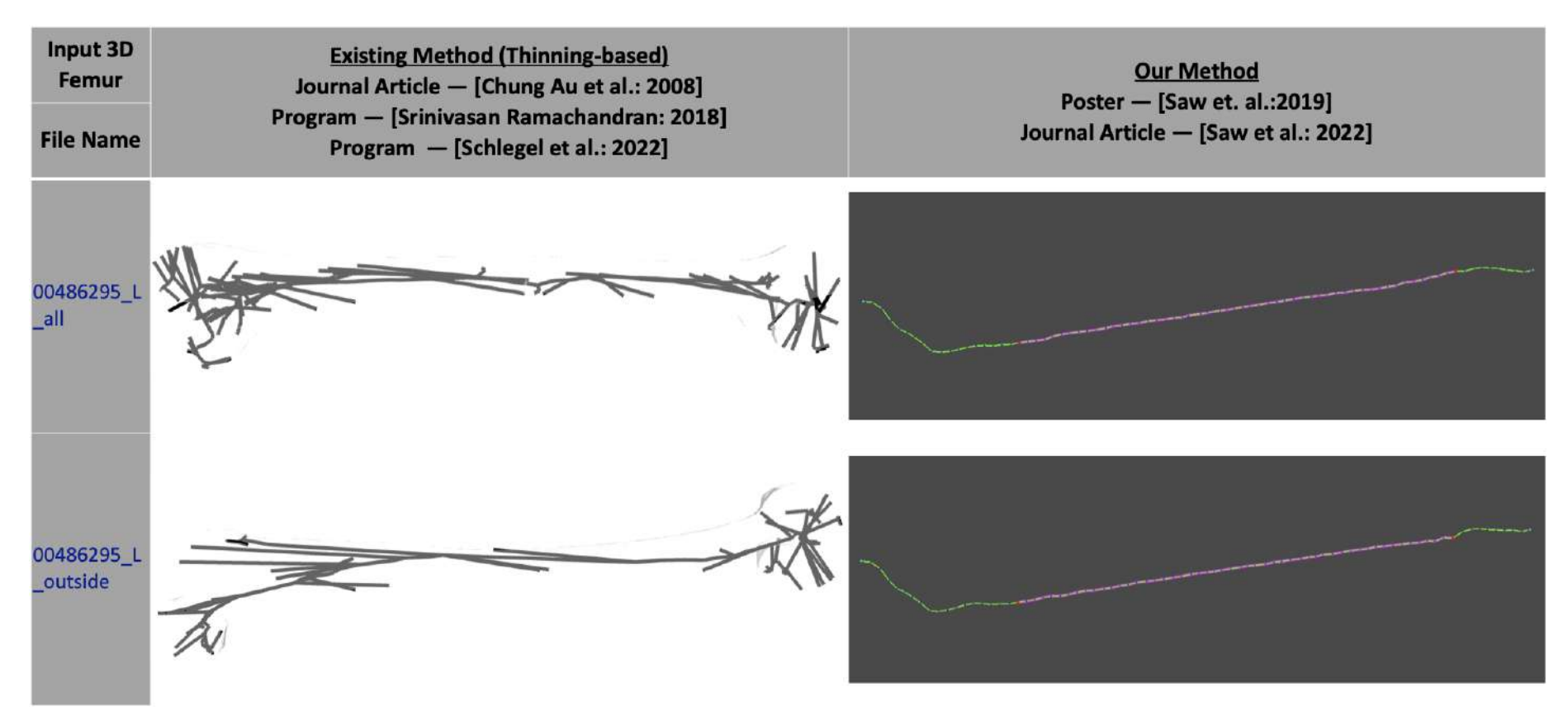
(c) 3D femurs obtained from a patient with the code number of 0346688 (Left femur), and the constructed skeletons using the existing method and our method.

Figure 7.3: The comparison results between using the existing method of Thinning-based 3D skeletonization and our method on the 3D femurs.



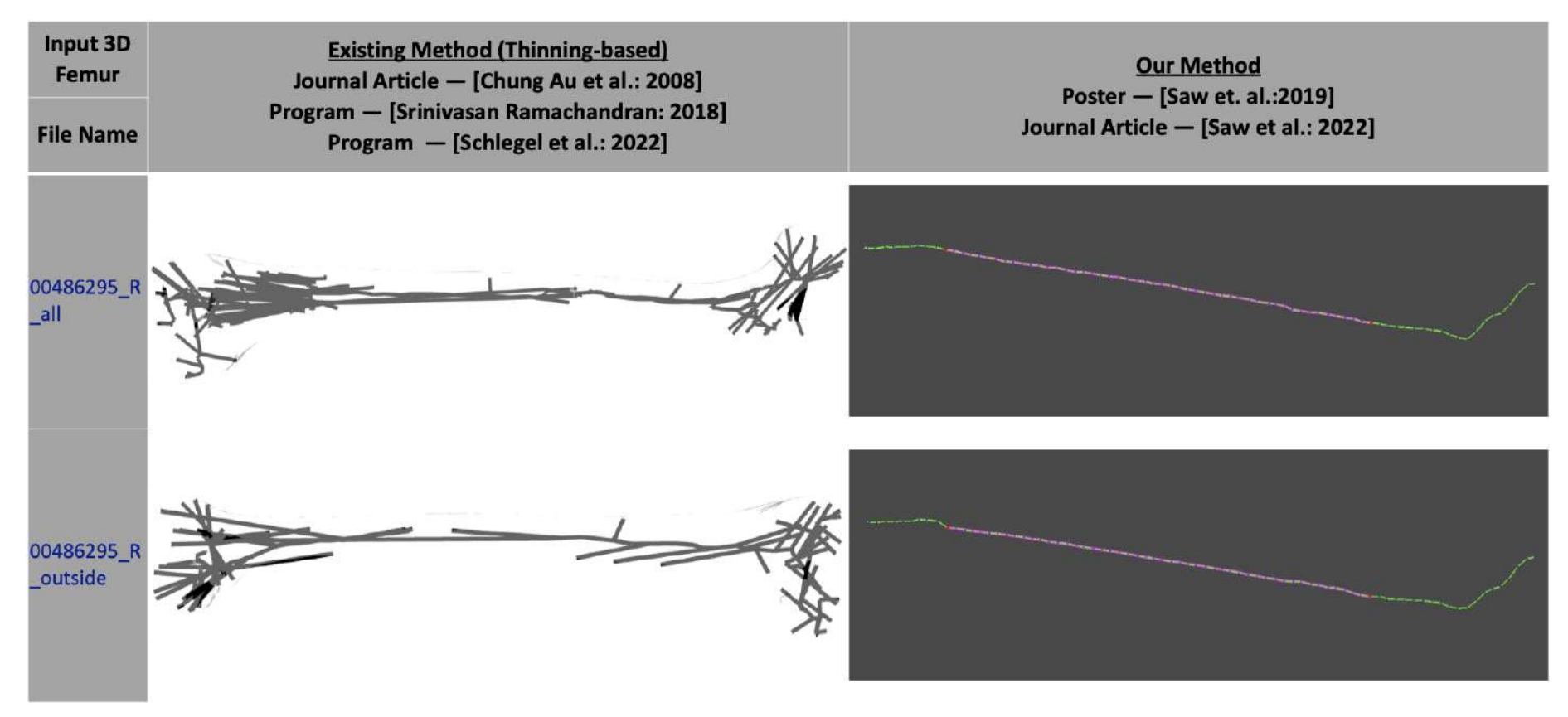
(d) 3D femurs obtained from a patient with the code number of 0346688 (Right femur), and the constructed skeletons using the existing method and our method.

Figure 7.3: The comparison results between using the existing method of Thinning-based 3D skeletonization and our method on the 3D femurs.



(e) 3D femurs obtained from a patient with the code number of 00486295 (Left femur), and the constructed skeletons using the existing method and our method.

Figure 7.3: The comparison results between using the existing method of Thinning-based 3D skeletonization and our method on the 3D femurs.



(f) 3D femurs obtained from a patient with the code number of 00486295 (Right femur), and the constructed skeletons using the existing method and our method.

Figure 7.3: The comparison results between using the existing method of Thinning-based 3D skeletonization and our method on the 3D femurs.

Computational Scalability

Table 7.3 presents computational aspects of the two (2) tested methods for the twelve (12) 3D femure as shown in Fig. 7.3. To make results consistent and unbiased, both algorithms were executed on the same platform with the following specifications:

- Windows Edition: Windows 10 Pro
- Processor: Intel(R) Core(TM) i5-6300U Central Processing Unit (CPU)
 2.40GHz 2.50 GHz
- Installed RAM: 8.00 GB
- System Type: 64-bit Operating System

However, there are differences in the usage of IDE for the algorithm implementation:

- A. Our Approach: Visual Studio Community 2019 C++ [140, 141].
- B. Thinning-based Approach: PyCharm 2022.3.1 (An IDE used for programming in Python) [87, 22, 223].

Intuitively, speed is computed in seconds, which can be seen as the throughput of a given method. The tested 3D meshes range between 10^5 and 20^5 vertices and were used in both approaches to compute skeletons.

The average of ten (10) computation times are retrieved from each 3D skeletonization algorithms as exhibited in Table 7.3. Although the Thinning-based approach takes faster time to compute the skeletons, the

resulting consists of a great number of spurious branches and boundary noises as shown in Fig. 7.3.

On the other hand, our approach produces straight, simple and meaningful skeletons, but consume more computation time than the Thinning-based approach. However, the degrees of dispersion of the computation speed in seconds relative to its mean are higher in Thinning-based approach compare to our approach. We have lower standard deviation which indicates that our data is closely clustered around the average. While the Thinning-based approach has higher standard deviation which indicates that the data is dispersed over a wider range of values.

3D skeletonization constraint can be understood as a selective tradeoff between the level of accuracy obtained and the computation speed. Both are the two (2) essential parameters any developer should consider while developing the algorithms. When our approach increases the accuracy by making more frames, we will lose speed (Table 7.3), and likewise, if we want to increase speed by reducing the frames, we have to pay for accuracy (Refer to Fig. 7.3 for the accuracy, and Table 7.3 for the speed). In other words, both parameters are in inverse relation, and one reduces the other.

Therefore, it is significant to always find the balance between the accuracy and the computation speed during the algorithm development.

Table 7.3: The computational scalability comparison between our algorithm and the Thinning-based algorithm.

	Our Approach		Thinning-based Approach	
Index Number (in seconds)	Average	Standard Deviation	Average	Standard Deviation
0123964_L_all.obj	29.3906	0.1735	27.2127	1.2687
0123964_L_outside.obj	29.0145	0.1158	25.0652	1.1958
0123964_R_all.obj	30.1109	0.1170	23.1925	2.5623
0123964_R_outside.obj	22.2549	0.4943	14.1036	2.4842

continued on next page

Table 7.3 - Continued from previous page

	Our Approach		Thinning-based Approach	
Index Number (in seconds)	Average	Standard Deviation	Average	Standard Deviation
0346688_L_all.obj	35.1529	0.0605	33.9437	1.3987
0346688_L_outside.obj	34.7671	0.1182	32.9737	0.9171
0346688_R_all.obj	35.8458	0.0945	24.4864	1.1518
0346688_R_outside.obj	23.2922	0.0866	9.9173	1.1124
00486295_L_all.obj	24.6316	0.0648	16.7393	1.0815

continued on next page

Table 7.3 - Continued from previous page

	Our Approach		Thinning-based Approach	
Index Number (in seconds)	Average	Standard Deviation	Average	Standard Deviation
00486295_L_outside.obj	16.9865	0.0781	9.7848	1.7777
00486295_R_all.obj	27.2248	0.0884	17.9034	2.0511
00486295_R_outside.obj	16.7553	0.0448	8.5080	1.7873

continued on next page

Chapter 8

CONCLUSION

8.1 Summary of the Thesis

In conclusion, this research marks a significant stride in automatic orthopaedics analysis with the introduction of the state-of-the-art system, 3D-FSA. The quantitative comparison between our approach and the Thinningbased method, conducted on a dataset comprising twelve (12) femurs collected from South Korean researchers, reveals compelling advancements.

The skeletons generated by the Thinning-based method, as observed through rigorous quantitative analysis, exhibit a notable deficiency in preserving both connectivity and topological information. They tend to manifest numerous spurious branches, undermining the fidelity of the skeletal structures. In contrast, our 3D-FSA approach produces skeletons charaterised by straight, simple, and clean structures, showcasing a marked improvement in connectivity preservation and topological information.

Quantitatively, our approach outperforms the Thinning-based method, demonstrating statistically significant enhancements in the preservation of femoral geometry. The observed outcomes not only validate the efficacy of 3D-FSA but also position it as a superior method for its ability to deliver precise 3D preoperative simulations.

Moreover, the substantial dataset of 2800 femurs employed in this study by the South Korean researchers provides a robust foundation for insightful findings. The results underscore a gradual increase in femoral bowing and the width of the medullary canal over time, with a distinct impact among women. The accuracy and reproducibility of the 3D analyses generated by 3D-FSA contribute to reinforcing the reliability of our approach.

The implications of these remarkable 3D analyses are substantial, serving as a valuable reference for surgical preparation and implant designs. The accurate preoperative simulations and in-depth morphological studies facilitated by 3D-FSA offer unprecedented insights into femoral characteristics, guiding personalised medical interventions and advancing the field of orthopaedics. In essence, this research not only introduces a cutting-edge analysis system but also quantitatively establishes the superiority of 3D-FSA in terms of connectivity preservation, topological information, and implementation simplicity.

8.2 Future Work

This research however, consists of several limitations as follows:

- A. The 3D-FSA system is only able to read one (1) 3D data format which is the .obj file format.
- B. The computation speed for our approach is yet higher than the Thinning-based method.

- C. The 3D-FSA system is only limited to the human femur and not the rest of the human body, such as the lower limb.
- D. The generated parameters are useful as the measurements analysis in some countries like South Korea, Japan, China and India but unfortunately not in Malaysia. This is because the morphometric parameters analysis can be obtained through the researches conducted in Asian countries.
- E. No studies or measurements have been conducted to assess the criteria for data loss in conjunction with our approach.

Therefore, there is always a great room for improvement. The followings are the proposed solutions in the future.

- A. To add an additional feature in 3D-FSA, that is able to read other 3D data format, e.g.: *stl* files.
- B. To find some point where the accuracy and computation speed should be fair enough to consider, Artificial Intelligence (AI) techniques should be deployed with a sufficient amount of data. As created AI has globally-attributed to mostly one goal, it obtains a higher level of accuracy and surpasses the existing benchmarks. Thus, more data will be required to produce a better, accurate and faster models.

- C. To extend the 3D skeletonization scope from just human femur to the other part of the human body, e.g.: lower limb.
- D. To ensure a comprehensive solution, we propose implementing additional measures to address data loss criteria in our forthcoming work, detailed in Chapter 8.2.1.
- E. To be used in 3D mesh segmentation which is explained in Chapter 8.2.2.

8.2.1 Data Loss Criteria: Measurement Approaches

In our study, we recognise the significance of evaluating measurement reliability through ICA. Future iterations of our research plan to conduct a comprehensive ICA to assess the agreement of all parameters. This process will include the validation of our analysis program, ensuring alignment with the standards of excellence outlined by Cichhetti [139].

To further refine the precision of our method, we propose the incorporation of a 3D printing approach for femur model generation. This involves utilising Polylactic acid to construct 3D models of femurs with the generated skeleton. By directly comparing and measuring errors against real human femurs, this method offers a tangible and practical assessment of our model's accuracy.

Considering the pivotal role of data accuracy in femur model generation, we advocate for an extensive comparison of scanning systems. This investigation, as presented by [287], will encompass quantitative, qualitative, femoral feature, skeleton properties, and deviation analyses for 3D models obtained from diverse scanning systems. Our aim is to identify and endorse the most accurate scanning method, with a particular emphasis on X-rays CT systems, recognised for providing superior data accuracy with minimal error.

8.2.2 3D Mesh Segmentation

3D mesh segmentation is generally meant by a process of partitioning a 3D mesh into disjoint yet connected components based on desirable constraints for the cut edges. Since a plain 3D mesh doesn't imply a high-level information, direct interpretation by either computer or human being can be difficult. Therefore, it is always straightforward to segment the 3D mesh into parts based on particular criteria.

3D skeletonization is commonly used before or after 3D mesh segmentation on a complex 3D mesh. Since the skeleton is extracted from the 3D human femur, we can extend the results by performing 3D mesh segmentation.

Several weight functions have have been proposed to be used in the max-flow min-cut algorithm to partition the obtained skeleton from 3D-FSA into source nodes and sink nodes respectively as shown in Table 8.1. The max-flow min-cut theorem is a network flow theorem. This theorem states that the maximum flows through any network from a given source to a given sink is exactly the sum of the edge weights that, if removed, would totally disconnect the source from the sink. In other words, for any network graph and a selected source and sink node, the max-flow from source to sink is equals to the min-cut necessary to separate source from sink [288].

The proposed weight functions in Equation No. 1, Equation No. 2, and Equation No. 3 are not able to partition the skeleton into two (2) partitions as shown in Fig. 8.1a, Fig. 8.1b and Fig. 8.1c respectively. However, the proposed weight function in Equation No. 4 is effectively partition the skeleton into two (2) partitions: the source nodes and the sink nodes as illustrated in Fig. 8.1.

Most of these ideas presented here was previously presented and published in [289].

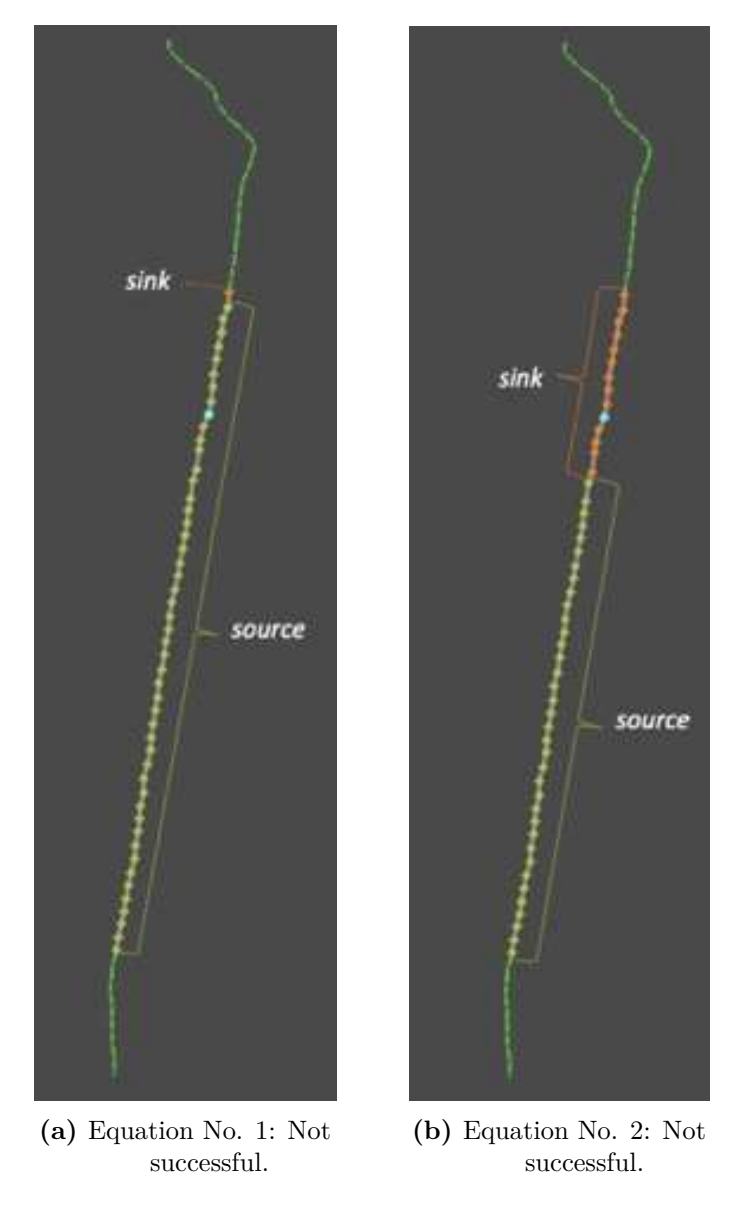


Figure 8.1: The 3D mesh segmentation results on the obtained skeleton using various proposed weight functions in max-flow min-cut algorithm.

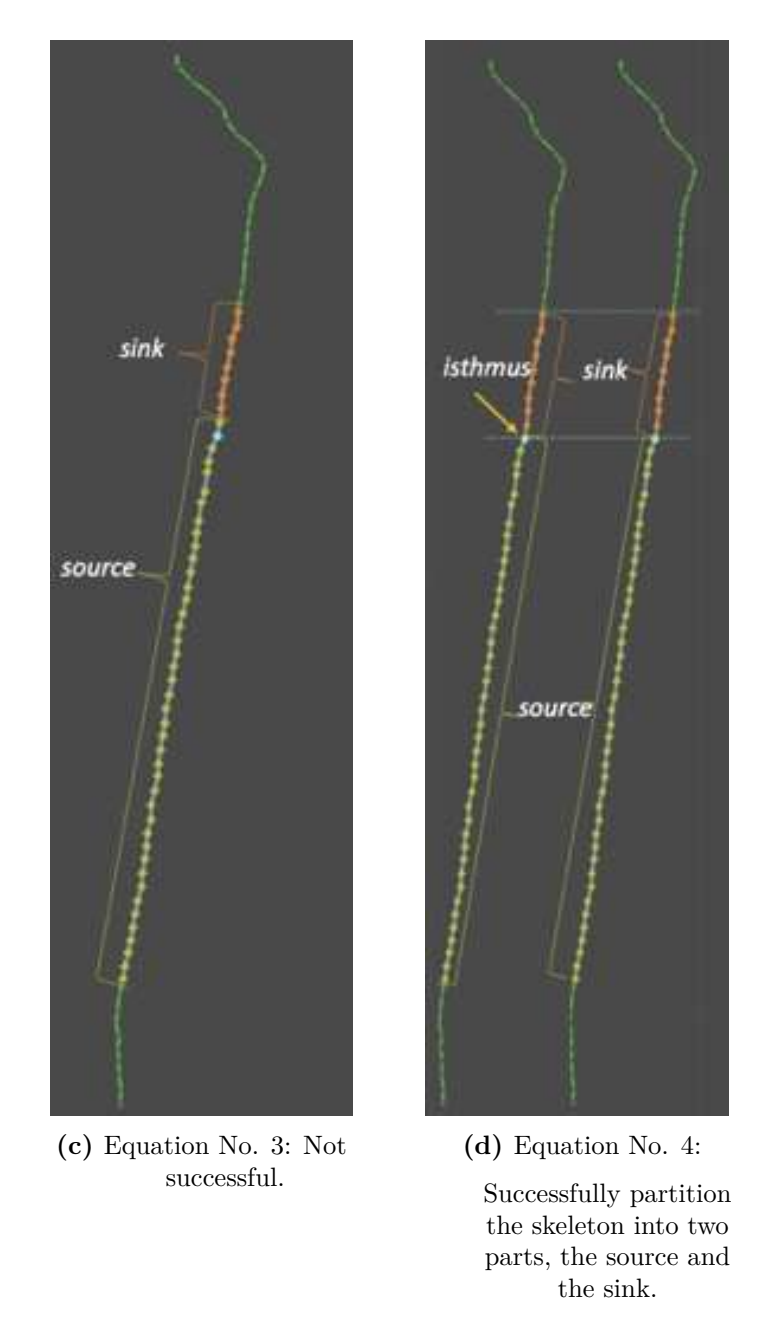


Figure 8.1: The 3D mesh segmentation results on the obtained skeleton using various proposed weight functions in max-flow min-cut algorithm.

Table 8.1: The tested equations of the length term and curvature term for max-flow and min-cut algorithm.

Approaches	Equation	Successfully Partition
1	$w(e) = \frac{1.0}{\ u-v\ \times \max_{f \in Tu} \{\min_{n \in Tuv} \{(1-f.normal \cdot n.normal)\}\}}$	×
2	$w(e) = u - v \times (radius_u + radius_v)$	×
3	$w(e) = u - u \times radius_u \times \left(\frac{slice_u - slice_i sthmus}{slice_s ource - slice_s ink}\right)$	×
4	$w(e) = u - u \times diameter_u \times (\frac{slice_u - slice_i sthmus}{slice_s ource - slice_s ink})$	~

Although we have finally found a proper weight function to successfully partition the skeleton into two (2) parts: the source and the sink, are these results useful? Hence, I have consulted several professionals and orthopaedics as follows:

- A. Professor Dato' Dr. Oh Kim Soon (Adjunct Clinical Professor, M. Kandiah Faculty of Medicine and Health Sciences, UTAR).
- B. Dr. Simerjit Singh (Clinical Associate Professor, Department of Surgery, M. Kandiah Faculty of Medicine and Health Sciences, UTAR).
- C. Dr. Yan Naing Soe (Clinical Associate Professor, Department of Surgery, M. Kandiah Faculty of Medicine and Health Sciences, UTAR).
- D. Dr. Din Xin Jet (Clinical Associate Professor, Department of Population Medicine, M. Kandiah Faculty of Medicine and Health Sciences, UTAR).
- E. Dr. Rajesh Singh (Orthopaedic Specialist, REGEN Healthcare).
- F. Professor Dr. David Ngo (Director of Research and Enterprise, Heriot-Watt University, Malaysia).

During the discussion with Dr. Rajesh, he asked me the following questions:

"What are the characteristic of the femur I can identify using the proposed technique?"

Therefore, the labelling of the significant parts of the femur can be achieved by using both techniques of 3D skeletonization and 3D mesh segmentation. For example, the entry point of the femur, the neck shaft angle, the rotation of curvature of the bone which is difficult to estimate the angle, etc. These are very challenging research in the future.

Finally, this research can be extended to other fields with a lot of point clouds or any complicated shape, and employ 3D skeletonization to simplify the visual and the data.

Bibliography

- [1] K. Subburaj, B. Ravi, and M. Agarwal, "Computer-aided Methods for Assessing Lower Limb Deformities in Orthopaedic Surgery Planning," Computerized Medical Imaging and Graphics, vol. 34, no. 4, pp. 277– 288, 2010.
- [2] M. Gharenazifam and E. Arbabi, "Anatomy-based 3D Skeleton Extraction from Femur Model," *Journal of Medical Engineering & Technology*, vol. 38, no. 8, pp. 402–410, 2014, pMID: 25340717. [Online]. Available: https://doi.org/10.3109/03091902.2014.963257
- [3] M. Laura Marie Fayad, M.D., "CT Scan Versus What Versus X-Ray: Type of Imaging Do Need." Accessed: August 5, 2022. [Online]. Available: https://www.hopkinsmedicine.org/health/treatment-tests-andtherapies/ct-vs-mri-vs-xray.
- [4] E. Radiology, "X-Ray vs. CT vs. MRI," Accessed: August 5, 2022.
 [Online]. Available: https://www.envrad.com/difference-between-x-ray-ct-scan-and-mri/.
- [5] InsideView, "Different Imaging Tests, Explained," Accessed: August 5, 2022. [Online]. Available: https://blog.radiology.virginia.edu/different-imaging-tests-explained/.

- [6] K. GmbH, "Femur," Accessed: August 20, 2022. [Online]. Available: https://www.kenhub.com/en/library/anatomy/femur/.
- [7] M. L. Richardson, "Genu Varum," Accessed: December 13, 2022. [Online]. Available: https://commons.wikimedia.org/w/index.php?curid=59299/.
- [8] S. Labs, "What is MAR?? Explaining the Medial Axis," Accessed: September 20, 2021. [Online]. Available: https://www.youtube.com/watch?v=tdVHKzYt5TM/.
- [9] P. Mazengenya and M. D. Fasemore, "Morphometric Studies of the Nutrient Foramen in Lower Limb Long Bones of Adult Bblack and White South Africans," Eur J Anat, vol. 19, no. 2, pp. 155–163, 2015.
- [10] K. A. Egol, E. Y. Chang, J. Cvitkovic, F. J. Kummer, and K. J. Koval, "Mismatch of Current Intramedullary Nails with the Anterior Bow of the Femur," *Journal of orthopaedic trauma*, vol. 18, no. 7, pp. 410–415, 2004.
- [11] M. A. Er A. (2023) Femur (Lateral View). https://radiopaedia.org/articles/femur-lateral-view?lang=us/. Accessed: 23 May 2023.
- [12] C. M. 2023, "Materialise Mimics," Accessed: May 23, 2023., 1990.
 [Online]. Available: https://www.materialise.com/en/.
- [13] S. K. Coreline, "AVIEW Modeler; Coreline Soft," Accessed: Mar. 28, 2022., 2022. [Online]. Available: https://www.corelinesoft.com/homeeng-2/.
- [14] B. Yang, J.-K. Yu, Z.-Z. Zheng, Z.-H. Lu, and J.-Y. Zhang, "Comparative Study of Sex Differences in Distal Femur Morphology in Osteoarthritic Knees in a Chinese Population," *PloS one*, vol. 9, no. 2, p. e89394, 2014.

- [15] A. H. K. Abdelaal, N. Yamamoto, K. Hayashi, A. Takeuchi, A. F. Morsy, S. Miwa, Y. Kajino, D. A. Rubio, and H. Tsuchiya, "Radiological Assessment of the Femoral Bowing in Japanese Population," SICOT-J, vol. 2, Jan. 2016, doi: 10.1051/sicotj/2015037.
- [16] I. Jung, E. Choi, B.-G. Lee, and J.-W. Kim, "Population-based, Three-dimensional Analysis of Age-and Sex-Related Femur Shaft Geometry Differences," Osteoporosis International, pp. 1631–1638, Jan. 2021, doi: https://doi.org/10.1007/s00198-021-05841-6.
- [17] H. Autodesk, "Polygon Normals," Accessed: August 2, 2022., August 2018. [Online]. Available: https://help.autodesk.com/view/MAYAUL/2018/ENU/?guid=GUID-9C257D44-924D-4B3F-ADEF-C71FAA98EAB1.
- "What of Face?" [18] stackoverflow, is the Normal a Accessed: September 8, 2022. [Online]. Available: https://stackoverflow.com/questions/16441498/what-is-thenormal-of-a-face.
- [19] B. Corporation, "Blender," Accessed: December 13, 2022. [Online]. Available: https://www.blender.org/.
- [20] Nate Robins, "Wavefront OBJ Model File Format Reader," Accessed: June 30, 2023., 1997. [Online]. Available: https://www.pobox.com/nate.
- [21] S. Marvaniya, "Simultaneous Part-Decomposition and Contour Matching using Dynamic Programming," Ph.D. dissertation, Indian Institute of Technology Madras, 06 2013.
- [22] A. G. Philipp Schlegel, Tom Kazimiers, "Skeletor: 3D Skeleton Extraction from Meshes." Accessed: December 30, 2022., 2022.
 [Online]. Available: https://github.com/navis-org/skeletor/.

- [23] Q. Wang, X. Liao, Y. Qian, and P. Liu, "Haptics and Virtual Reality for Oral and Maxillofacial Surgery," in Computer-Aided Oral and Maxillofacial Surgery. Elsevier, 2021, pp. 141–159.
- [24] R. Jain, R. Kasturi, and B. G. Schunk, Machine Vision. Indo American Books, 2016.
- [25] M. "Microsoft Foundation Class Lib-Corporation, Accessed: January 31, 2023. [Online]. rary," Availhttps://learn.microsoft.com/en-us/cpp/mfc/mfc-desktopable: applications?view=msvc-170/.
- [26] Microsoft Corporation, "OpenGL Mathematics," Accessed: January 31, 2023. [Online]. Available: https://g.co/kgs/xEXYGB/.
- [27] K. Hormann, B. Lévy, and A. Sheffer, "Mesh Parameterization: Theory and Practice," SIGGRAPH Asia 2008 Course Notes, 2008.
- [28] Scratchapixel, "Introduction to Shading," Accessed: August 30, 2022.

 [Online]. Available: https://www.scratchapixel.com/lessons/3d-basic-rendering/introduction-to-shading/what-is-shading-light-matter-interaction.
- [29] O. Jones, "The Femur," Accessed: August 4, 2022., November 2020. [Online]. Available: https://teachmeanatomy.info/lower-limb/bones/femur/.
- [30] P. Contributors, "Femoral Fractures," Accessed: December 2, 2022. [Online]. Available: https://www.physio-pedia.com/index.php/.
- [31] K. J. Agarwal-Harding, J. G. Meara, S. L. Greenberg, L. E. Hagander, D. Zurakowski, and G. S. Dyer, "Estimating the Global Incidence of Femoral Fracture from Road Traffic Collisions: A Literature Review," JBJS, vol. 97, no. 6, p. e31, 2015.

- [32] Fact Sheet for Patients and Families, "Open Reduction and Internal Fixation (ORIF)," Intermountain Healthcare, Jul. 2012. [Online]. Available: https://intermountainhealthcare.org/ckrext/Dcmnt?ncid=521402750.
- [33] Y.-B. Gao, S.-L. Tong, J.-H. Yu, and W.-J. Lu, "Case Control Study on Open Reduction Internal Fixation (ORIF) and Minimally Invasive Percutaneous Plate Osteosynthesis (MIPPO) for the Treatment of Proximal Humerus Fractures in Aged," Zhongguo Gu Shang (China Journal of Orthopaedics and Traumatology), vol. 28, no. 4, pp. 335–339, Apr. 2015. [Online]. Available: https://pubmed.ncbi.nlm.nih.gov/26072616/.
- [34] K. Nunez, "Repairing Major Bone Breaks with Open Reduction Internal Fixation Surgery," Accessed: Mar. 24, 2022., January 2019.
 [Online]. Available: https://www.healthline.com/health/orif-surgery.
- [35] WebMD, "What Is ORIF Surgery?" Accessed: Mar. 24, 2022., 2005. [Online]. Available: https://www.webmd.com.
- [36] M. R. Bong, F. J. Kummer, K. J. Koval, and K. A. Egol, "Intramedullary Nailing of the Lower Extremity: Biomechanics and Biology," *JAAOS-Journal of the American Academy of Orthopaedic Surgeons*, vol. 15, no. 2, pp. 97–106, 2007.
- [37] OrthoInfo, "Femur Shaft Fractures (Broken Thighbone)," Accessed: Mar. 24, 2022., May 2018. [Online]. Available: https://orthoinfo.aaos.org/en/diseases-conditions/femur-shaft-fractures-broken-thighbone/.
- [38] W. Chan, C. Yen, K. Wong, P. Tse, and K. Mak, "Breakage of Intramedullary Femoral Guide Rod during Total Knee Arthroplasty:

- A Case Report," Journal of Orthopaedic Surgery, vol. 14, no. 1, pp. 96–98, Apr. 2006, doi: https://doi.org/10.1177/230949900601400121.
- [39] J. H. Park, Y. Lee, O.-J. Shon, H. C. Shon, and J. W. Kim, "Surgical Tips of Intramedullary Nailing in Severely Bowed Femurs in Atypical Femur Fractures: Simulation with 3D Printed Model," *Injury*, vol. 47, no. 6, pp. 1318–1324, Jun. 2016, doi: https://doi.org/10.1016/j.injury.2016.02.026.
- [40] J. W. Kim, H. Kim, C.-w. Oh, J.-W. Kim, O.-J. Shon, Y.-S. Byun, J. J. Kim, H. K. Oh, H. Minehara, K.-T. Hwang et al., "Surgical Outcomes of Intramedullary Nailing for Diaphyseal Atypical Femur Fractures: Is It Safe to Modify a Aail Entry in Bowed Femur?" Archives of Orthopaedic and Trauma Surgery, vol. 137, no. 11, pp. 1515–1522, Aug. 2017, doi: https://doi.org/10.1007/s00402-017-2764-1.
- [41] J.-W. Kim, C.-W. Oh, J.-K. Oh, K.-H. Park, H.-J. Kim, T.-S. Kim, I. Seo, and E.-K. Park, "Treatment of Infra-isthmal Femoral Fracture with an Intramedullary Nail: Is Retrograde Nailing a Better Option than Antegrade Nailing?" Archives of orthopaedic and trauma surgery, vol. 138, no. 9, pp. 1241–1247, May. 2018, doi: https://doi.org/10.1007/s00402-018-2961-6.
- [42] K.-L. Hsu, F.-C. Kuan, W.-L. Chang, Y.-F. Liu, C.-K. Hong, M.-L. Yeh, and W.-R. Su, "Interlocking Nailing of Femoral Shaft Fractures with an Extremely Narrow Medullary Canal is Associated with Introgenic Fractures," *Injury*, vol. 50, no. 12, pp. 2306–2311, 2019.
- [43] I. Hudson, K. Mauch, M. Schuurman, M. T. Padela, P. Gheraibeh, and R. Vaidya, "Effect of Inherent Tibial Asymmetry on Leg Length Discrepancy Measurements After Intramedullary Nailing of Comminuted Femoral Shaft Fractures," SICOT-J, vol. 5, Jan. 2019, doi: 10.1051/sicotj/2018053.

- [44] S. Sabharwal, C. Zhao, J. J. McKeon, E. McClemens, M. Edgar, and F. Behrens, "Computed Radiographic Measurement of Limb-Length Discrepancy: Full-Length Standing Anteroposterior Radiograph Compared with Scanogram," JBJS, vol. 88, no. 10, pp. 2243—2251, Oct. 2006, doi: 10.2106/JBJS.E.01179.
- [45] S. Sabharwal, C. Zhao, J. McKeon, T. Melaghari, M. Blacksin, and C. Wenekor, "Reliability Analysis for Radiographic Measurement of Limb Length Discrepancy: Full-Length Standing Anteroposterior Radiograph Versus Scanogram," *Journal of Pediatric Orthopaedics*, vol. 27, no. 1, pp. 46–50, Jan. 2007, doi: 10.1097/01.bpo.0000242444.26929.9f.
- [46] S. Sabharwal and A. Kumar, "Methods for Assessing Leg Length Discrepancy," Clinical Orthopaedics and Related Research, vol. 466, no. 12, pp. 2910–2922, Oct. 2008, doi: https://doi.org/10.1007/s11999-008-0524-9.
- [47] A. Aaron, D. Weinstein, D. Thickman, and R. Eilert, "Comparison of Orthoroentgenography and Computed Tomography in the Measurement of Limb-length Discrepancy." The Journal of bone and joint surgery. American volume, vol. 74, no. 6, pp. 897–902, Jul. 1992.
- [48] R. Vaidya, B. Anderson, A. Elbanna, R. Colen, D. Hoard, and A. Sethi, "CT Scanogram for Limb Length Discrepancy in Comminuted Femoral Shaft Fractures following IM Nailing," Injury, vol. 43, no. 7, pp. 1176–1181, Jul. 2012, doi: https://doi.org/10.1016/j.injury.2012.03.022.
- [49] D. Herscovici and J. M. Scaduto, "Assessing Leg Length After Fixation of Comminuted Femur Fractures," *Clinical Orthopaedics and Related Research*, vol. 472, no. 9, pp. 2745–2750, Sept. 2014, doi: https://doi.org/10.1007/s11999-013-3292-0.

- [50] D.-I. Kim, D.-S. Kwak, and S.-H. Han, "Sex Determination using Discriminant Analysis of the Medial and Lateral Condyles of the Femur in Koreans," Forensic science international, vol. 233, no. 1-3, pp. 121–125, Dec. 2013, doi: https://doi.org/10.1016/j.forsciint.2013.08.028.
- [51] H.-J. Cho, D.-S. Kwak, and I.-B. Kim, "Morphometric Evaluation of Korean Femurs by Geometric Computation: Comparisons of the Sex and the Population," *BioMed Research International*, vol. 2015, 2015.
- [52] X.-Y. Su, Z. Zhao, J.-X. Zhao, L.-C. Zhang, A.-H. Long, L.-H. Zhang, and P.-F. Tang, "Three-dimensional Analysis of the Curvature of the Femoral Canal in 426 Chinese Femurs," *BioMed research interna*tional, vol. 2015, 2015.
- [53] J. N. Insall, R. Binazzi, M. Soudry, and L. A. Mestriner, "Total Knee Arthroplasty." Clinical Orthopaedics and Related Research, no. 192, pp. 13–22, 1985.
- [54] M. A. Ritter, P. M. Faris, E. M. Keating, and J. B. Meding, "Postoperative Alignment of Total Knee Replacement. Its Effect on Survival." *Clinical Orthopaedics and Related Research*, no. 299, pp. 153–156, Feb. 1994.
- [55] M. B. Trudell, "Anterior Femoral Curvature Revisited: Race Assessment from the Femur," Journal of Forensic Science, vol. 44, no. 4, pp. 700–707, 1999.
- [56] I. Papaioannou, G. Pantazidou, A. Baikousis, and P. Korovessis, "Femoral Bowing and Femoral Neck-Shaft Angle Evaluation Can Reduce Atypical Femoral Fractures in Osteoporotic Patients: A Scientific Report," Cureus, vol. 12, no. 10, pp. 1–5, Oct. 2020, doi: 10.7759/cureus.10771.

- [57] W. Bruns, M. Bruce, G. Prescott, and N. Maffulli, "Temporal Trends in Femoral Curvature and Length in Medieval and Modern Scotland," American Journal of Physical Anthropology: The Official Publication of the American Association of Physical Anthropologists, vol. 119, no. 3, pp. 224–230, 2002.
- [58] I. De Groote, "Femoral Curvature in Neanderthals and Modern Humans: A 3D Geometric Morphometric Analysis," Journal of Human Evolution, vol. 60, no. 5, pp. 540–548, 2011.
- [59] P. C. Noble, J. W. Alexander, L. J. Lindahl, D. T. Yew, W. M. Granberry, and H. S. Tullos, "The Anatomic Basis of Femoral Component Design." Clinical Orthopaedics and Related Research, no. 235, pp. 148–165, Oct. 1988.
- [60] A. Harma, B. Germen, H. M. Karakas, N. Elmali, and M. Inan, "The Comparison of Femoral Curves and Curves of Contemporary Intramedullary Nails," *Surgical and Radiologic Anatomy*, vol. 27, no. 6, pp. 502–506, Aug. 2005, doi: https://doi.org/10.1007/s00276-005-0019-2.
- [61] K. P. Walsh, J. R. Fowler, O. Chen, J. P. Gaughan, S. Ali, M. Rehman, and S. Rehman, "The Validity and Reliability of Preoperative Radiographic Canal Diameter Measurements of the Femur," HSS Journal®, vol. 9, no. 2, pp. 150–156, Jul. 2013, doi: https://doi.org/10.1007/s11420-013-9334-z.
- [62] P. Rubin, P. Leyvraz, J. Aubaniac, J. Argenson, P. d. Estève, and B. De Roguin, "The Morphology of the Proximal Femur. A Threedimensional Radiographic Analysis," *The Journal of bone and joint* surgery. British volume, vol. 74, no. 1, pp. 28–32, Jan. 1992, doi: https://doi.org/10.1302/0301-620X.74B1.1732260.

- [63] H. Laine, K. Kontola, M. Lehto, M. Pitkänen, P. Jarske, and T. Lindholm, "Image Processing for Femoral Endosteal Anatomy Detection: Description and Testing of a Computed Tomography Based Program," Physics in Medicine & Biology, vol. 42, no. 4, p. 673, 1997.
- [64] M. Y. Baharuddin, S.-H. Salleh, A. H. Zulkifly, M. H. Lee, and A. Mohd Noor, "Morphological Study of the Newly Designed Cementless Femoral Stem," *Biomed Research International*, vol. 2014, Jun. 2014, doi: https://doi.org/10.1155/2014/692328.
- [65] M. Masjedi, C. Tay, S. J. Harris, and J. P. Cobb, "A Local Rreference Frame for Describing the Proximal Human Femur: Application in Clinical Settings," *Skeletal radiology*, vol. 43, no. 3, pp. 323–329, Mar. 2014, doi: https://doi.org/10.1007/s00256-013-1782-5.
- [66] J.-x. Zhao, X.-y. Su, Z. Zhao, L.-c. Zhang, Z. Mao, H. Zhang, L.-h. Zhang, and P.-f. Tang, "Predicting the Optimal Entry Point for Femoral Antegrade Nailing using a New Measurement Approach," International Journal of Computer Assisted Radiology and Surgery, vol. 10, no. 10, pp. 1557–1565, Oct. 2015, doi: https://doi.org/10.1007/s11548-015-1182-5.
- [67] L.-P. Chen, T.-K. Chang, T.-Y. Huang, T.-G. Kwok, and Y.-C. Lu, "The Correlation Between Lateral Bowing Angle of the Femur and the Location of Atypical Femur Fractures," Calcified Tissue International, vol. 95, no. 3, pp. 240–247, Jul. 2014, doi: https://doi.org/10.1007/s00223-014-9887-y.
- [68] H. Yoo, Y. Cho, Y. Park, and S. Ha, "Lateral Femoral Bowing and the Location of Atypical Femoral Fractures," *Hip & Pelvis*, vol. 29, no. 2, pp. 127–132, Jun. 2017, doi: https://doi.org/10.5371/hp.2017.29.2.127.

- [69] K. Atesok, D. Galos, L. M. Jazrawi, and K. A. Egol, "Preoperative Planning in Orthopaedic Surgery: Current Practice and Evolving Applications," *Bulletin of the NYU Hospital for Joint Diseases*, vol. 73, no. 4, pp. 257–257, Oct. 2015.
- [70] A. M. Ghanem, A. H. Hamimi, J. R. Matta, A. Carass, R. M. Elgarf, A. M. Gharib, and K. Z. Abd-Elmoniem, "Automatic Coronary Wall and Atherosclerotic Plaque Segmentation from 3D Coronary CT Angiography," *Scientific Reports*, vol. 9, no. 1, pp. 1–13, Jan. 2019, doi: https://doi.org/10.1038/s41598-018-37168-4.
- [71] J. Li, J. Weng, H. Xu, C. Zhou, D. Zhang, and G. Lu, "Design of Robotic Mannequin Formed by Flexible Belt Net," Computer-Aided Design, vol. 110, pp. 1–10, May. 2019, doi: https://doi.org/10.1016/j.cad.2018.12.010.
- [72] F. Buonamici, R. Furferi, L. Governi, S. Lazzeri, K. S. McGreevy, M. Servi, E. Talanti, F. Uccheddu, and Y. Volpe, "A CAD-based Procedure for Designing 3D Printable Arm-Wrist-Hand Cast," Computer Aided Design and Application, vol. 16, no. 1, pp. 25–34, 2019.
- [73] C. Patruno, R. Marani, G. Cicirelli, E. Stella, and T. D'Orazio, "People Re-identification using Skeleton Standard Posture and Color Descriptors from RGB-D Data," *Pattern Recognition*, vol. 89, pp. 77–90, May. 2019, doi: https://doi.org/10.1016/j.patcog.2019.01.003.
- [74] Blum and Harry, "A Transformation for Extracting New Descriptors of Shape," Models for Perception of Speech and Visual Form, vol. 19, no. 5, pp. 362–380, 1967.
- [75] A. Tagliasacchi, T. Delame, M. Spagnuolo, N. Amenta, and A. Telea, "3D Skeletons: A State-of-the-art Report," in *Computer Graphics Forum*, vol. 35, no. 2. Wiley Online Library, 2016, pp. 573–597.

- [76] A. Sobiecki, A. Jalba, and A. Telea, "Comparison of Curve and Surface Skeletonization Methods for Voxel Shapes," Pattern Recognition Letters, vol. 47, pp. 147–156, 2014.
- [77] C. Arcelli, G. S. di Baja, and L. Serino, "Distance-driven Skeletonization in Voxel Images," *IEEE Transactions on Pattern Analysis and Machine Intelligence*, vol. 33, no. 4, pp. 709–720, 2011.
- [78] A. C. Jalba, J. Kustra, and A. C. Telea, "Surface and Curve Skeletonization of Large 3D Models on the GPU," *IEEE transactions on* pattern analysis and machine intelligence, vol. 35, no. 6, pp. 1495– 1508, 2012.
- [79] N. D. Cornea, D. Silver, and P. Min, "Curve-skeleton Properties, Applications, and Algorithms," *IEEE Transactions on Visualization & Computer Graphics*, no. 3, pp. 530–548, 2007.
- [80] M. Näf, G. Székely, R. Kikinis, M. E. Shenton, and O. Kübler, "3D Voronoi Skeletons and Their Usage for the Characterization and Recognition of 3D Organ Shape," Computer Vision and Image Understanding, vol. 66, no. 2, pp. 147–161, 1997.
- [81] N. Amenta, S. Choi, and R. K. Kolluri, "The Power Crust, Unions of Balls, and the Medial Axis Transform," Computational Geometry, vol. 19, no. 2-3, pp. 127–153, Jul. 2001, doi: https://doi.org/10.1016/S0925-7721(01)00017-7.
- [82] J. Ma, S. W. Bae, and S. Choi, "3D Medial Axis Point Approximation Using Nearest Neighbors and the Normal Field," *The Visual Computer*, vol. 28, no. 1, pp. 7–19, 2012.
- [83] J. Cheng, X. Zheng, S. Chen, G. Liu, S. Xin, L. Lu, Y. Zhou, and C. Tu, "Skeletonization Via Dual of Shape Segmentation," *Com-*

- puter Aided Geometric Design, vol. 80, p. 101856, Jun. 2020, doi: https://doi.org/10.1016/j.cagd.2020.101856.
- [84] K. Siddiqi, S. Bouix, A. Tannenbaum, and S. W. Zucker, "Hamilton-Jacobi Skeletons," *International Journal of Computer Vision*, vol. 48, no. 3, pp. 215–231, Jul. 2002, doi: https://doi.org/10.1023/A:1016376116653.
- [85] A. Tabb and H. Medeiros, "Fast and Robust Curve Skeletonization for Real-World Elongated Objects," in 2018 IEEE Winter Conference on Applications of Computer Vision (WACV), May. 2018, pp. 1935–1943, doi: 10.1109/WACV.2018.00214.
- [86] A. Telea and A. Vilanova, "A Robust Level-set Algorithm for Centerline Extraction," in *Proceedings of the symposium on Data visualisa*tion 2003, 2003, pp. 185–194.
- [87] O. K.-C. Au, C.-L. Tai, H.-K. Chu, D. Cohen-Or, and T.-Y. Lee, "Skeleton Extraction by Mesh Contraction," ACM transactions on graphics (TOG), vol. 27, no. 3, pp. 1–10, 2008.
- [88] X. Jin and J. Kim, "A 3D Skeletonization Algorithm for 3D Mesh Models Using A Partial Parallel 3D Thinning Algorithm and 3D Skeleton Correcting Algorithm," Applied Sciences, vol. 7, no. 2, p. 139, 2017.
- [89] C. Lin, L. Liu, C. Li, L. Kobbelt, B. Wang, S. Xin, and W. Wang, "SEG-MAT: 3D Shape Segmentation Using Medial Axis Transform," IEEE Transactions on Visualization and Computer Graphics, vol. 28, no. 6, pp. 2430–2444, Oct. 2020, doi: 10.1109/TVCG.2020.3032566.
- [90] R. Van Uitert and I. Bitter, "Subvoxel Precise Skeletons of Volumetric Data Based on Fast Marching Methods," *Medical physics*, vol. 34, no. 2, pp. 627–638, 2007.

- [91] J. Tierny, J.-P. Vandeborre, and M. Daoudi, "Topology Driven 3D Mesh Hierarchical Segmentation," in Proc. IEEE International Conference on Shape Modeling and Applications 2007 (SMI'07), Jul. 2007, pp. 215–220, doi: 10.1109/SMI.2007.38.
- [92] K. B. Deborah Silver, "3D Skeletonization/ Volume Thinning," Accessed: September 26, 2022., Unknown Unknown. [Online]. Available: https://vizlab.rutgers.edu/vol_thin/.
- [93] S. Katz and A. Tal, "Hierarchical Mesh Decomposition using Fuzzy Clustering and Cuts," in ACM Transactions on Graphics TOG, vol. 22, no. 3. ACM, 2003, pp. 954–961.
- [94] D. Brunner and G. Brunnett, "Mesh Segmentation Using the Object Skeleton Graph," in Proc. IASTED International Conf. on Computer Graphics and Imaging, 2004, pp. 48–55.
- [95] A. Shamir, "Segmentation and Shape Extraction of 3D Boundary Meshes." in Eurographics (State of the Art Reports), 2006, pp. 137– 149.
- [96] L. Shapira, A. Shamir, and D. Cohen-Or, "Consistent Mesh Partitioning and Skeletonisation Using the Shape Diameter Function," The Visual Computer, vol. 24, no. 4, pp. 249–259, 2008.
- [97] J.-M. Lien and N. M. Amato, "Approximate Convex Decomposition of Polyhedra and Its Applications," Computer Aided Geometric Design, vol. 25, no. 7, pp. 503–522, 2008.
- [98] X. Qin, X. Sang, S. Zhu, and S. Cheng, "Line-skeleton Extraction of 3D Meshes Based on Geometry Segmentation," in 2010 First ACIS International Symposium on Cryptography, and Network Security, Data Mining and Knowledge Discovery, E-Commerce and Its Applications, and Embedded Systems. IEEE, 2010, pp. 354–357.

- [99] X. Sun, J. Pan, and X. Wei, "3D Mesh Skeleton Extraction Using Prominent Segmentation," Computer Science and Information Systems, vol. 7, no. 1, pp. 63–74, 2010.
- [100] X. Zhang, Y. Xia, J. Wang, Z. Yang, C. Tu, and W. Wang, "Medial Axis Tree-An Internal Supporting Structure for 3D Printing," Computer Aided Geometric Design, vol. 35, pp. 149–162, 2015.
- [101] Y. Zhang, F. Tan, S. Wang, D. Kong, and B. Yin, "3D Human Body Skeleton Extraction from Consecutive Surfaces." in PG (Short Papers), 2019, pp. 53–57.
- [102] Y. Zhang, F. Tan, S. Wang, and B. Yin, "3D Human Body Skeleton Extraction From Consecutive Surfaces Using A Spatial—temporal Consistency Model," *The Visual Computer*, vol. 37, no. 5, pp. 1045–1059, 2021.
- [103] N. Amenta, M. Bern, and M. Kamvysselis, "A New Voronoi-based Surface Reconstruction Algorithm," in Proceedings of the 25th annual conference on Computer graphics and interactive techniques, 1998, pp. 415–421.
- [104] M. Berger, A. Tagliasacchi, L. Seversky, P. Alliez, J. Levine, A. Sharf, and C. Silva, "State of the Art in Surface Reconstruction from Point Clouds," *Eurographics 2014-State of the Art Reports*, vol. 1, no. 1, pp. 161–185, 2014.
- [105] J. Kustra, A. Jalba, and A. Telea, "Robust Segmentation of Multiple Intersecting Manifolds from Unoriented Noisy Point Clouds," in Computer Graphics Forum, vol. 33, no. 1. Wiley Online Library, 2014, pp. 73–87.

- [106] A. Chaudhury and C. Godin, "Skeletonization of Plant Point Cloud Data Using Stochastic Optimization Framework," Frontiers in Plant Science, vol. 11, p. 773, 2020.
- [107] Q. Ke, M. Bennamoun, S. An, F. Sohel, and F. Boussaid, "A New Representation of Skeleton Sequences for 3D Action Recognition," in *Proceedings of the IEEE conference on computer vision and pattern recognition*, 2017, pp. 3288–3297.
- [108] S. Win and T. L. L. Thein, "Real-Time Human Motion Detection, Tracking and Activity Recognition with Skeletal Model," in 2020 IEEE Conference on Computer Applications (ICCA), 2020, pp. 1–5.
- [109] A. Chaturvedi and Z. Lee, "Three-dimensional Segmentation and Skeletonization to Build an Airway Tree Data Structure for Small Animals," *Physics in Medicine & Biology*, vol. 50, no. 7, p. 1405, 2005.
- [110] J. Kvam, L. E. Gangsei, J. Kongsro, and A. H. Schistad Solberg, "The Use of Deep Learning to Automate the Segmentation of the Skeleton from CT Volumes of Pigs," *Translational Animal Science*, vol. 2, no. 3, pp. 324–335, 2018.
- [111] S. Capell, S. Green, B. Curless, T. Duchamp, and Z. Popović, "Interactive Skeleton-driven Dynamic Deformations," ACM transactions on graphics (TOG), vol. 21, no. 3, pp. 586–593, 2002.
- [112] C. Ma, S. Zhang, A. Wang, Y. Qi, and G. Chen, "Skeleton-based Dynamic Hand Gesture Recognition Using An Enhanced Network with One-shot Learning," *Applied Sciences*, vol. 10, no. 11, p. 3680, 2020.
- [113] M. Wan, F. Dachille, and A. Kaufman, "Distance-field Based Skeletons for Virtual Navigation," in *Proceedings Visualization*, 2001. VISÓ1. IEEE, 2001, pp. 239–560.

- [114] T. Becker, C. Nagel, and T. H. Kolbe, A Multilayered Space-Event Model for Navigation in Indoor Spaces. Berlin, Heidelberg: Springer Berlin Heidelberg, 2009, pp. 61–77. [Online]. Available: https://doi.org/10.1007/978-3-540-87395-2_5.
- [115] L. Hong, S. Muraki, A. Kaufman, D. Bartz, and T. He, "Virtual Voyage: Interactive Navigation in the Human Colon," in *Proceedings* of the 24th annual conference on Computer graphics and interactive techniques, 1997, pp. 27–34.
- [116] I. Nystrom, G. S. di Baja, and S. Svensson, "Representing Volumetric Vascular Structures Using Curve Skeletons," in *Proceedings 11th International Conference on Image Analysis and Processing*. IEEE, 2001, pp. 495–500.
- [117] E. Sorantin, C. Halmai, B. Erdohelyi, K. Palágyi, L. G. Nyúl, K. Ollé, B. Geiger, F. Lindbichler, G. Friedrich, and K. Kiesler, "Spiral-CT-based Assessment of Tracheal Stenoses Using 3-D-skeletonization," IEEE transactions on Medical Imaging, vol. 21, no. 3, pp. 263–273, 2002.
- [118] D. M. Cooper, A. L. Turinsky, C. W. Sensen, and B. Hallgrímsson, "Quantitative 3D Analysis of the Canal Network in Cortical Bone By Micro-computed Tomography," The Anatomical Record Part B: The New Anatomist: An Official Publication of the American Association of Anatomists, vol. 274, no. 1, pp. 169–179, 2003.
- [119] S. R. Aylward, J. Jomier, S. Weeks, and E. Bullitt, "Registration and Analysis of Vascular Images," *International journal of computer* vision, vol. 55, no. 2, pp. 123–138, 2003.
- [120] G. Hamarneh, R. ABU-GHARBIEH, and T. McInerney, "Medial Profiles for Modeling Deformation and Statistical Analysis of Shape and

- Their Use in Medical Image Segmentation," *International Journal of Shape Modeling*, vol. 10, no. 02, pp. 187–209, 2004.
- [121] Y. Fridman, S. M. Pizer, S. Aylward, and E. Bullitt, "Extracting Branching Tubular Object Geometry Via Cores," *Medical Image Analysis*, vol. 8, no. 3, pp. 169–176, 2004.
- [122] D. Perchet, C. I. Fetita, and F. J. Preteux, "Advanced Navigation Tools for Virtual Bronchoscopy," in *Image Processing: Algorithms* and Systems III, vol. 5298. SPIE, 2004, pp. 147–158.
- [123] S. Tran and L. Shih, "Efficient 3D Binary Image Skeletonization," in 2005 IEEE Computational Systems Bioinformatics Conference-Workshops (CSBW'05). IEEE, 2005, pp. 364–372.
- [124] W. H. Hesselink and J. B. Roerdink, "Euclidean Skeletons of Digital Image and Volume Data in Linear Time By the Integer Medial Axis Transform," *IEEE Transactions on Pattern Analysis and Machine Intelligence*, vol. 30, no. 12, pp. 2204–2217, 2008.
- [125] A. D. Ward and G. Hamarneh, "The Groupwise Medial Axis Transform for Fuzzy Skeletonization and Pruning," *IEEE Transactions on pattern analysis and machine intelligence*, vol. 32, no. 6, pp. 1084–1096, 2009.
- [126] N. Mann and P. Singh, "Medial Axis Transformation based Skeletonzation of Image Patterns using Image Processing Techniques," International Journal of Science and Research (IJSR), India Online ISSN, pp. 2319–7064, 2012.
- [127] W. Abu-Ain, S. N. H. S. Abdullah, B. Bataineh, T. Abu-Ain, and K. Omar, "Skeletonization Algorithm for Binary Images," *Procedia Technology*, vol. 11, pp. 704–709, 2013.

- [128] J. Kustra, A. Jalba, and A. Telea, "Shape Segmentation Using Medial Point Clouds With Applications to Dental Cast Analysis," in 2014 International Conference on Computer Vision Theory and Applications (VISAPP), vol. 3. IEEE, 2014, pp. 162–170.
- [129] R. Plantefève, S. Kadoury, A. Tang, and I. Peterlik, "Robust Automatic Graph-Based Skeletonization of Hepatic Vascular Trees," in Intravascular Imaging and Computer Assisted Stenting, and Large-Scale Annotation of Biomedical Data and Expert Label Synthesis, M. J. Cardoso, T. Arbel, S.-L. Lee, V. Cheplygina, S. Balocco, D. Mateus, G. Zahnd, L. Maier-Hein, S. Demirci, E. Granger, L. Duong, M.-A. Carbonneau, S. Albarqouni, and G. Carneiro, Eds. Cham: Springer International Publishing, 2017, pp. 20–28.
- [130] J. Lee, D.-W. Kim, C. S. Won, and S.-W. Jung, "Graph Cut-based Human Body Segmentation in Color Images Using Skeleton Information from the Depth Sensor," Sensors, vol. 19, no. 2, p. 393, 2019.
- [131] M. Gaillard, C. Miao, J. Schnable, and B. Benes, "Sorghum Segmentation By Skeleton Extraction," in *European Conference on Computer Vision*. Springer, 2020, pp. 296–311.
- [132] K. Huebner, S. Ruthotto, and D. Kragic, "Minimum Volume Bounding Box Decomposition for Shape Approximation in Robot Grasping," in 2008 IEEE International Conference on Robotics and Automation. IEEE, 2008, pp. 1628–1633.
- [133] J. Aleotti and S. Caselli, "A 3D Shape Segmentation Approach for Robot Grasping By Parts," *Robotics and Autonomous Systems*, vol. 60, no. 3, pp. 358–366, 2012.
- [134] O. M. d. S. Contente, J. N. P. N. Lau, J. F. M. Morgado, and R. M. Pereira Morais Dos Santos, "Vineyard Skeletonization for Autonom-

- ous Robot Navigation," in 2015 IEEE International Conference on Autonomous Robot Systems and Competitions, 2015, pp. 50–55.
- [135] W. R. Quadros, B. Gurumoorthy, K. Ramaswami, and F. B. Prinz, "Skeletons for Representation and Reasoning in Engineering Applications," *Engineering with Computers*, vol. 17, no. 2, pp. 186–198, 2001.
- [136] H. Sundar, D. Silver, N. Gagvani, and S. Dickinson, "Skeleton Based Shape Matching and Retrieval," in 2003 Shape Modeling International. IEEE, 2003, pp. 130–139.
- [137] M. Gharenazifam and E. Arbabi, "Anatomy-based 3D Skeleton Extraction From Femur Model," Journal of Medical Engineering & Technology, vol. 38, no. 8, pp. 402–410, 2014, pMID: 25340717. [Online]. Available: https://doi.org/10.3109/03091902.2014.963257
- [138] Z. Bobbitt, "Intraclass Correlation Coefficient: Definition + Example," Accessed: September 28, 2022., 2021. [Online]. Available: https://www.statology.org/intraclass-correlation-coefficient/.
- [139] D. V. Cicchetti, "Guidelines, Criteria, and Rules of Thumb for Evaluating Normed and Standardized Assessment Instruments in Psychology." Psychological Assessment, vol. 6, no. 4, p. 284?290, Jan. 1994, https://doi.org/info:doi/.
- [140] S. H. Saw, H. T. Ewe, J.-W. Kim, and B.-G. Lee, "3D Femur Skeletonization Using Maximum-Minimum Centre Approach," 6 2019, poster Presented in International Geometry Summit (IGS 2019).
- [141] S. H. Saw, B.-G. Lee, and H. T. Ewe, "Skeleton-Based 3D Femur Shape Analysis System Using Maximum-Minimum Centre Approach," *IEEE Access*, vol. 10, pp. 53533-53545, 2022.
- [142] T. D. Stewart, "Anterior Femoral Curvature: Its Utility for Race Identification," *Human Biology*, vol. 34, no. 1, pp. 49–62, 1962.

- [143] N. A. Walensky, "A Study of Anterior Femoral Curvature in Man," The Anatomical Record, vol. 151, no. 4, pp. 559–570, 1965.
- [144] L. L. Shackelford and E. Trinkaus, "Late Pleistocene Human Femoral Diaphyseal Curvature," American Journal of Physical Anthropology: The Official Publication of the American Association of Physical Anthropologists, vol. 118, no. 4, pp. 359–370, 2002.
- [145] S. Singh and S. Singh, "A Study of Anterior Femoral Curvature in Indian Subjects," *Acta Anatomica*, vol. 83, no. 3, pp. 416–425, 1972.
- [146] B. M. Gilbert, "Anterior Femoral Curvature: Its Probable Basis and Utility as a Criterion of Racial Assessment," American Journal of Physical Anthropology, vol. 45, no. 3, pp. 601–604, 1976.
- [147] M. B. Trudell, Anterior Femoral Curvature Revisited: Race Assessment from the Femur. University of Florida, 1996.
- [148] K. A. Murshed, A. E. Çiçekcibaşi, A. Karabacakoğlu, M. Şeker, and T. Ziylan, "Distal Femur Morphometry: A Gender and Bilateral Comparative Study using Magnetic Resonance Imaging," Surgical and radiologic anatomy, vol. 27, pp. 108–112, 2005.
- [149] A. Harma and H. M. Karakas, "Determination of Sex from the Femur in Anatolian Caucasians: A Digital Radiological Study," *Journal of forensic and legal medicine*, vol. 14, no. 4, pp. 190–194, 2007.
- [150] H. M. Karakaş, A. Harma et al., "Femoral Shaft Bowing with Age: A Digital Radiological Study of Anatolian Caucasian Adults," Diagn Interv Radiol, vol. 14, no. 1, pp. 29–32, 2008.
- [151] B. Ferris, C. Kennedy, M. Bhamra, and W. Muirhead-Allwood, "Morphology of the Femur in Proximal Femoral Fractures," The Journal of Bone and Joint Surgery. British volume, vol. 71, no. 3, pp. 475–477, 1989.

- [152] G. S. Lausten, F. Jorgensen, and J. Boesen, "Measurement of Anteversion of the Femoral Neck. Ultrasound and Computerised Tomography Compared," *The Journal of Bone and Joint Surgery. British volume*, vol. 71, no. 2, pp. 237–239, 1989.
- [153] K. L. Hermann and N. Egund, "CT Measurement of Anteversion in the Femoral Neck: The Influence of Femur Positioning," Acta radiologica, vol. 38, no. 4, pp. 527–532, 1997.
- [154] O. Husmann, P. J. Rubin, P.-F. Leyvraz, B. de Roguin, and J.-N. Argenson, "Three-dimensional Morphology of the Proximal Femur," The Journal of arthroplasty, vol. 12, no. 4, pp. 444–450, 1997.
- [155] N. Sugano, P. C. Noble, and E. Kamaric, "A Comparison of Alternative Methods of Measuring Femoral Anteversion," *Journal of Computer Assisted Tomography*, vol. 22, no. 4, 1998. [Online]. Available: https://journals.lww.com/jcat/Fulltext/1998/07000/
 A_Comparison_of_Alternative_Methods_of_Measuring.19.aspx
- [156] A. Kaneuji, T. Matsumoto, M. Nishino, T. Miura, T. Sugimori, and K. Tomita, "Three-dimensional Morphological Analysis of the Proximal Femoral Canal, Using Computer-aided Design System, in Japanese Patients with Osteoarthrosis of the Hip," *Journal of orthopaedic* science, vol. 5, pp. 361–368, 2000.
- [157] H.-J. Laine, M. Lehto, and T. Moilanen, "Diversity of Proximal Femoral Medullary Canal," The Journal of arthroplasty, vol. 15, no. 1, pp. 86–92, 2000.
- [158] P. Massin, L. Geais, E. Astoin, M. Simondi, and F. Lavaste, "The Anatomic Basis for the Concept of Lateralized Femoral Stems: A Frontal Plane Radiographic Study of the Proximal Femur," The Journal of arthroplasty, vol. 15, no. 1, pp. 93–101, 2000.

- [159] K. Haraguchi, N. Sugano, T. Nishii, T. Koyama, S. Nishihara, H. Yoshikawa, and T. Ochi, "Comparison of Fit and Fill Between Anatomic Stem and Straight Tapered Stem Using Virtual Implantation on the ORTHODOC Workstation," Computer aided surgery, vol. 6, no. 5, pp. 290–296, 2001.
- [160] B. Mahaisavariya, K. Sitthiseripratip, T. Tongdee, E. L. Bohez, J. Vander Sloten, and P. Oris, "Morphological Study of the Proximal Femur: A New Method of Geometrical Assessment using 3-dimensional Reverse Engineering," *Medical Engineering & Physics*, vol. 24, no. 9, pp. 617–622, 2002. [Online]. Available: https://www.sciencedirect.com/science/article/pii/S1350453302001133
- [161] G. Khang, K. Choi, C.-S. Kim, J. S. Yang, and T.-S. Bae, "A Study of Korean Femoral Geometry," Clinical Orthopaedics and Related Research®, vol. 406, no. 1, pp. 116–122, 2003.
- [162] B. Atilla, A. Oznur, O. Caglar, M. Tokgözoglu, and M. Alpaslan, "Osteometry of the Femora in Turkish Individuals: A Morphometric Study in 114 Cadaveric Femora as an Anatomic Basis of Femoral Component Design," Acta Orthop Traumatol Turc, vol. 41, no. 1, pp. 64–8, 2007.
- [163] X. Cheng, J. Li, Y. Lu, J. Keyak, and T. Lang, "Proximal Femoral Density and Geometry Measurements by Quantitative Computed Tomography: Association with Hip Fracture," *Bone*, vol. 40, no. 1, pp. 169–174, 2007.
- [164] E. Khmelnitskaya, P. Mohandas, P. Walker, and S. Muirhead-Allwood, "Optimizing for Head Height, Head Offset, and Canal Fit in a Set of Uncemented Stemmed Femoral Components," *Hip International*, vol. 18, no. 4, pp. 286–293, 2008.

- [165] G. Lecerf, M. Fessy, R. Philippot, P. Massin, F. Giraud, X. Flecher, J. Girard, P. Mertl, E. Marchetti, and E. Stindel, "Femoral Offset: Anatomical Concept, Definition, Assessment, Implications for Preoperative Templating and Hip Arthroplasty," Orthopaedics & traumatology: surgery & research, vol. 95, no. 3, pp. 210–219, 2009.
- [166] S. Schumann, M. Tannast, L.-P. Nolte, and G. Zheng, "Validation of Statistical Shape Model Based Reconstruction of the Proximal Femu— A Morphology Study," *Medical engineering & physics*, vol. 32, no. 6, pp. 638–644, 2010.
- [167] M. Ito, N. Wakao, T. Hida, Y. Matsui, Y. Abe, K. Aoyagi, M. Uetani, and A. Harada, "Analysis of Hip Geometry by Clinical CT for the Assessment of Hip Fracture Risk in Elderly Japanese Women," *Bone*, vol. 46, no. 2, pp. 453–457, 2010.
- [168] A. Unnanuntana, P. Toogood, D. Hart, D. Cooperman, and R. E. Grant, "Evaluation of Proximal Femoral Geometry Using Digital Photographs," *Journal of orthopaedic research*, vol. 28, no. 11, pp. 1399–1404, 2010.
- [169] M. Umer, Y. J. Sepah, A. Khan, A. Wazir, M. Ahmed, and M. U. Jawad, "Morphology of the Proximal Femur in a Pakistani Population," *Journal of orthopaedic surgery*, vol. 18, no. 3, pp. 279–281, 2010.
- [170] K. Kim, J. Brown, K. Kim, H. Choi, H. Kim, Y. Rhee, and S.-K. Lim, "Differences in Femoral Neck Geometry Associated with Age and Ethnicity," Osteoporosis international, vol. 22, pp. 2165–2174, 2011.
- [171] D. S. Casper, G. K. Kim, J. Parvizi, and T. A. Freeman, "Morphology of the Proximal Femur Differs Widely with Age and Sex: Relevance to

- Design and Selection of Femoral Prostheses," *Journal of Orthopaedic Research*, vol. 30, no. 7, pp. 1162–1166, 2012. [Online]. Available: https://onlinelibrary.wiley.com/doi/abs/10.1002/jor.22052.
- [172] P. L. Poilvache, J. N. Insall, G. R. Scuderi, and D. E. Font-Rodriguez, "Rotational Landmarks and Sizing of the Distal Femur in Total Knee Arthroplasty." *Clinical Orthopaedics and Related Research* (1976-2007), vol. 331, pp. 35–46, 1996.
- [173] M. D. Tillman, K. R. Smith, J. A. Bauer, J. H. Cauraugh, A. B. Falsetti, and J. L. Pattishall, "Differences in Three Intercondylar Notch Geometry Indices Between Males and Females: A Cadaver Study," The Knee, vol. 9, no. 1, pp. 41–46, 2002.
- [174] W. P. Charlton, T. A. S. John, M. G. Ciccotti, N. Harrison, and M. Schweitzer, "Differences in Femoral Notch Anatomy Between Men and Women: A Magnetic Resonance Imaging Study," *The American Journal of Sports Medicine*, vol. 30, no. 3, pp. 329–333, 2002.
- [175] K. Hitt, J. R. Shurman, K. Greene, J. McCarthy, J. Moskal, T. Hoeman, M. A. Mont et al., "Anthropometric Measurements of the Human Knee: Correlation to the Sizing of Current Knee Arthroplasty Systems," JBJS, vol. 85, no. suppl_4, pp. 115–122, 2003.
- [176] K. Urabe, H. Miura, T. Kuwano, S. Matsuda, R. Nagamine, S. Sakai, K. Masuda, and Y. Iwamoto, "Comparison Between the Shape of Resected Femoral Sections and Femoral Prostheses Used in Total Knee Arthroplasty in Japanese Patients: Simulation Using Three-dimensional Computed Tomography." The journal of knee surgery, vol. 16, no. 1, pp. 27–33, 2003.
- [177] W.-P. Ho, C.-K. Cheng, and J.-J. Liau, "Morphometrical Measurements of Resected Surface of Femurs in Chinese Knees: Correlation

- to the Sizing of Current Femoral Implants," *The Knee*, vol. 13, no. 1, pp. 12–14, 2006.
- [178] J. Victor, "Rotational Alignment of the Distal Femur: A Literature Review," Orthopaedics & traumatology: surgery & research, vol. 95, no. 5, pp. 365–372, 2009.
- [179] F. B. Cheng, X. F. Ji, Y. Lai, J. C. Feng, W. X. Zheng, Y. F. Sun, Y. W. Fu, and Y. Q. Li, "Three-dimensional Morphometry of the Knee to Design the Total Knee Arthroplasty for Chinese Population," *The Knee*, vol. 16, no. 5, pp. 341–347, 2009.
- [180] D.-S. Kwak, S. Han, C. W. Han, and S.-H. Han, "Resected Femoral Anthropometry for Design of the Femoral Component of the Total Knee Prosthesis in a Korean Population," *Anatomy & Cell Biology*, vol. 43, no. 3, pp. 252–259, 2010.
- [181] C. Chaichankul, A. Tanavalee, and P. Itiravivong, "Anthropometric Measurements of Knee Joints in Thai Population: Correlation to the Sizing of Current Knee Prostheses," *The Knee*, vol. 18, no. 1, pp. 5–10, 2011.
- [182] J. Dargel, J. W. Michael, J. Feiser, R. Ivo, and J. Koebke, "Human Knee Joint Anatomy Revisited: Morphometry in the Light of Sex-specific Total Knee Arthroplasty," *The Journal of arthroplasty*, vol. 26, no. 3, pp. 346–353, 2011.
- [183] D. S. Kwak, Q. B. Tao, M. Todo, and I. Jeon, "Determination of Representative Dimension Parameter Values of Korean Knee Joints for Knee Joint Implant Design," Proceedings of the Institution of Mechanical Engineers, Part H: Journal of Engineering in Medicine, vol. 226, no. 5, pp. 368–376, 2012.

- [184] H.-C. Lim, J.-H. Bae, J.-Y. Yoon, S.-J. Kim, J.-G. Kim, and J.-M. Lee, "Gender Differences of the Morphology of the Distal Femur and Proximal Tibia in a Korean Population," *The Knee*, vol. 20, no. 1, pp. 26–30, 2013.
- [185] K. Leung, P. Procter, B. Robioneck, and K. Behrens, "Geometric Mismatch of the Gamma Nail to the Chinese Femur," Clinical Orthopaedics and Related Research®, vol. 323, pp. 42–48, 1996.
- [186] R. Miedel, S. Ponzer, H. Törnkvist, A. Söderqvist, and J. Tidermark, "The Standard Gamma Nail or the Medoff Sliding Plate for Unstable Trochanteric and Subtrochanteric Fractures: A Randomised, Controlled Trial," *The Journal of Bone and Joint Surgery. British volume*, vol. 87, no. 1, pp. 68–75, 2005.
- [187] J. H. Hwang, J. K. Oh, S. H. Han, W. Y. Shon, and C. W. Oh, "Mismatch between PFNa and Medullary Canal Causing Difficulty in Nailing of the Pertrochanteric Fractures," *Archives of orthopaedic* and trauma surgery, vol. 128, no. 12, pp. 1443–1446, 2008.
- [188] R. F. Ostrum and M. S. Levy, "Penetration of the Distal Femoral Anterior Cortex during Intramedullary Nailing for Subtrochanteric Fractures: A Report of Three Cases," *Journal of orthopaedic trauma*, vol. 19, no. 9, pp. 656–660, 2005.
- [189] D. B. Bazylewicz, K. A. Egol, and K. J. Koval, "Cortical Encroachment after Cephalomedullary Nailing of the Proximal Femur: Evaluation of a More Anatomic Radius of Curvature," *Journal of Orthopaedic Trauma*, vol. 27, no. 6, pp. 303–307, 2013.
- [190] C. A. Collinge and C. M. J. Beltran, "Does Modern Nail Geometry Affect Positioning in the Distal Femur of Elderly Patients with Hip Fractures? A Comparison of Otherwise Identical Intramedullary Nails

- with a 200 Versus 150 cm Radius of Curvature," *Journal of Ortho*paedic Trauma, vol. 27, no. 6, pp. 299–302, 2013.
- [191] A. J. Kanawati, B. Jang, R. McGee, and J. Sungaran, "The Influence of Entry Point and Radius of Curvature on Femoral Intramedullary Nail Position in the Distal Femur," *Journal of Orthopaedics*, vol. 11, no. 2, pp. 68–71, 2014.
- [192] W. Tang, K. Chiu, M. Kwan, T. Ng, and W. Yau, "Sagittal Bowing of the Distal Femur in Chinese Patients Who Require Total Knee Arthroplasty," *Journal of Orthopaedic Research*, vol. 23, no. 1, pp. 41–45, 2005.
- [193] Y. Onoue, Y. Sunami, H. Fujiwara, T. Sadakane, and S. Yasuda, "Treatment of the Femoral Shaft Fracture with a Curved Heat-treated COP Clover-leaf Nail," *International Orthopaedics*, vol. 3, pp. 203–210, 1979.
- [194] M. C. HARPER and W. L. Carson, "Curvature of the Femur and the Proximal Entry Point for an Intramedullary Rod," *Clinical Orthopaedics and Related Research*, vol. 220, pp. 155–161, 1987.
- [195] A. R. MacLeod, H. Rose, and H. S. Gill, "A Validated Open-source Multisolver Fourth-generation Composite Femur Model," *Journal of biomechanical engineering*, vol. 138, no. 12, 2016.
- [196] A. U. Abd Aziz, H. S. Gan, A. K. Nasution, M. R. A. Kadir, and M. H. Ramlee, "Development and Verification of Three-dimensional Model of Femoral Bone: Finite Element Analysis," in *Journal of Physics: Conference Series*, vol. 1372, no. 1. IOP Publishing, 2019, p. 012014.
- [197] N. Sugano, P. C. Noble, and E. Kamaric, "A Comparison of Alternative Methods of Measuring Femoral Anteversion," *Journal of computer assisted tomography*, vol. 22, no. 4, pp. 610–614, 1998.

- [198] J. Kim, T. Park, S. Park, J. Kim, and S. Kim, "Measurement of Femoral Neck Anteversion in 3D. Part 2: 3D Modelling Method," Medical and Biological Engineering and Computing, vol. 38, pp. 610– 616, 2000.
- [199] B. Mahaisavariya, K. Sitthiseripratip, T. Tongdee, E. L. Bohez, J. Vander Sloten, and P. Oris, "Morphological Study of the Proximal Femur: A New Method of Geometrical Assessment using 3dimensional Reverse Engineering," Medical engineering & physics, vol. 24, no. 9, pp. 617–622, 2002.
- [200] Z.-H. Lu, J.-K. Yu, L.-X. Chen, X. Gong, Y.-J. Wang, and K. K. M. Leung, "Computed Tomographic Measurement of Gender Differences in Bowing of the Sagittal Femoral Shaft in Persons Older Than 50 Years," The Journal of Arthroplasty, vol. 27, no. 6, pp. 1216–1220, 2012.
- [201] J. Maratt, P. L. Schilling, S. Holcombe, R. Dougherty, R. Murphy, S. C. Wang, and J. A. Goulet, "Variation in the Femoral Bow: A Novel High-Throughput Analysis of 3922 Femurs on Cross-sectional Imaging," *Journal of Orthopaedic Trauma*, vol. 28, no. 1, pp. 6–9, 2014.
- [202] W. L. Buford Jr, B. J. Turnbow, Z. Gugala, and R. W. Lindsey, "Three-dimensional Computed Tomography-based Modeling of Sagittal Cadaveric Femoral Bowing and Implications for Intramedullary Nailing," *Journal of orthopaedic trauma*, vol. 28, no. 1, pp. 10–16, 2014.
- [203] J.-x. Z. Xiu-yun Su, Z. Zhao, L. cheng Zhang, C. Li, J. tao Li, J. feng Zhou, L. hai Zhang, and P. fu Tang, "Three-dimensional Analysis of the Characteristics of the Femoral Canal Isthmus: An Anatomical Study." BioMed Research International, 2015.

- [204] T. A. C. Company, "Aquariusnet Viewer," Accessed: June 02, 2023., 1997. [Online]. Available: https://www.terarecon.com/.
- [205] B. Schmutz, J. Amarathunga, S. Kmiec, P. Yarlagadda, and M. Schuetz, "Quantification of Cephalomedullary Nail Fit in the Femur using 3D Computer Modelling: A Comparison between 1.0 and 1.5 m Bow Designs," *Journal of Orthopaedic Surgery and Re*search, vol. 11, no. 1, pp. 1–7, 2016.
- [206] T. Scientific, "Amira Software: Visualize and Analyse Life Sciences Imaging Data," Accessed: June 02, 2023., 1998. [Online]. Available: https://www.thermofisher.com/my/en/home/electron-microscopy/products/software-em-3d-vis/amira-software.html/.
- [207] K. Rathnayaka, T. Sahama, M. A. Schuetz, and B. Schmutz, "Effects of CT Image Segmentation Methods on the Accuracy of Long Bone 3D Reconstructions," *Medical engineering & physics*, vol. 33, no. 2, pp. 226–233, 2011.
- [208] Y. Wu, Z. Chen, K. He, and W. Geng, "Rapid Generation of Human Femur Models based on Morphological Parameters and Mesh Deformation," *Biotechnology & Biotechnological Equipment*, vol. 31, no. 1, pp. 162–174, 2017.
- [209] M. Corporation, "GitHub Copilot and Visual Studio 2022,"

 Accessed: June 3, 2023. [Online]. Available: https://visualstudio.microsoft.com/.
- [210] M. . SIMULINK, "MATLAB," Accessed: June 3, 2023. [Online]. Available: https://www.mathworks.com/products/matlab.html/.
- [211] M. A. S. M. Aspar, N. A. Abd Razak, M. R. A. Kadir, and H. Manap, "Development of 3-dimensional Model of Femur Bone Considering

- Cortical and Cancellous Structures," *International journal of engineering technology and sciences*, vol. 4, no. 1, pp. 109–116, 2017.
- [212] J.-K. Park, S.-M. Choi, S.-W. Kang, K.-J. Kim, and K.-T. Min, "Three-dimensional Measurement of the Course of the Radial Nerve at the Posterior Humeral Shaft: An In Vivo Anatomical Study," *Journal* of Orthopaedic Surgery, vol. 28, no. 2, p. 2309499020930828, 2020.
- [213] I. J. Jung and J. W. Kim, "Differences in Femur Geometry and Bone Markers in Atypical Femur Fractures and the General Population," *Scientific Reports*, vol. 11, no. 1, p. 24149, 2021.
- [214] H.-K. Lim, S.-K. Jung, S.-H. Kim, Y. Cho, and I.-S. Song, "Deep Semi-supervised Learning for Automatic Segmentation of Inferior Alveolar Nerve Using a Convolutional Neural Network," BMC Oral Health, vol. 21, no. 1, pp. 1–9, 2021.
- [215] J. H. Choi and W. Baek, "Late Reconstruction of Post-traumatic Enophthalmos and Hypoglobus using Three-dimensional Implants: A Case Series," Archives of Craniofacial Surgery, vol. 23, no. 5, pp. 232– 236, 2022.
- [216] F. M. Milian, F. Garcia, M. V. M. Guevara, I. K. Correia, and N. G. Meira, "Development of Voxel Models from 3D Surfaces. Optimized Methodology," Associacao Brasileira de Física Médica, 2010.
- [217] G. Vega, R. Paz, A. Gleadall, M. Monzón, and M. E. Alemán-Domínguez, "Comparison of CAD and Voxel-based Modelling Methodologies for the Mechanical Simulation of Extrusion-based 3D Printed Scaffolds," *Materials*, vol. 14, no. 19, p. 5670, 2021.
- [218] N. Roussopoulos, S. Kelley, and F. Vincent, "Nearest Neighbor Queries," in Proceedings of the 1995 ACM SIGMOD international conference on Management of data, 1995, pp. 71–79.

- [219] P. Li, B. Wang, F. Sun, X. Guo, C. Zhang, and W. Wang, "Q-mat: Computing Medial Axis Transform By Quadratic Error Minimization," ACM Transactions on Graphics (TOG), vol. 35, no. 1, pp. 1–16, 2015.
- [220] A. C. Jalba, J. Kustra, and A. C. Telea, "Surface and Curve Skeletonization of Large 3D Models on the GPU," *IEEE transactions on* pattern analysis and machine intelligence, vol. 35, no. 6, pp. 1495– 1508, 2013.
- [221] K. Subburaj, S. Patil, and B. Ravi, "Voxel-based Thickness Analysis of Intricate Objects," *International Journal of CAD/CAM*, vol. 6, no. 1, pp. 105–115, 2006.
- [222] O. K.-C. Au, C.-L. Tai, H.-K. Chu, D. Cohen-Or, and T.-Y. Lee, "Skeleton Extraction by Mesh Contraction," *ACM Trans. Graph.* (*Proc. SIGGRAPH*), vol. 27, no. 3, pp. 44:1–44:10, 2008.
- [223] S. Ramachandran, "Mesh Skeletonization," Accessed: December 30, 2022., 2018. [Online]. Available: https://github.com/aalavandhaann/.
- [224] B. M. C. (BMC), "Femur Shaft Fracture Diagnosis," Accessed: August 17, 2022. [Online]. Available: https://www.bmc.org/trauma-and-fracture-surgery/femur-shaft/diagnosis.
- [225] M. Avci and N. Kozaci, "Comparison of X-Ray Imaging and Computed Tomography Scan in the Evaluation of Knee Trauma," *Medicina*, vol. 55, no. 10, p. 623, 2019.
- [226] N. I. of Biomedical Imaging and B. (NIH), "Computed Tomography (CT)," Accessed: August 18, 2022. [Online].

 Available: https://www.nibib.nih.gov/science-education/science-topics/computed-tomography-ct.

- [227] T. Zamora, I. Klaber, J. Ananias, F. Bengoa, E. Botello, P. Amenabar, and D. Schweitzer, "The Influence of the CT Scan in the Evaluation and Treatment of Nondisplaced Femoral Neck Fractures in the Elderly," *Journal of Orthopaedic Surgery*, vol. 27, no. 2, p. 2309499019836160, 2019.
- [228] T. T. Kellock, B. Khurana, and J. C. Mandell, "Diagnostic Performance of CT for Occult Proximal Femoral Fractures: A Systematic Review and Meta-Analysis," *American Journal of Roentgenology*, vol. 213, no. 6, pp. 1324–1330, 2019.
- [229] T. Gatt, D. Cutajar, L. Borg, and R. Giordmaina, "The Necessity of CT Hip Scans in the Investigation of Occult Hip Fractures and Their Effect on Patient Management," Advances in Orthopedics, vol. 2021, 2021.
- [230] S. Heikal, P. Riou, and L. Jones, "The Use of Computed Tomography in Identifying Radiologically Occult Hip Fractures in the Elderly," The Annals of The Royal College of Surgeons of England, vol. 96, no. 3, pp. 234–237, 2014.
- [231] E. Eggenberger, G. Hildebrand, S. Vang, A. Ly, and C. Ward, "Use of CT vs. MRI for Diagnosis of Hip or Pelvic Fractures in Elderly Patients After Low Energy Trauma," *The Iowa orthopaedic journal*, vol. 39, no. 1, p. 179, 2019.
- [232] M. H. Tran, H. M. Q. Vu et al., "A Research on 3D Model Construction from 2D DICOM," in 2016 International Conference on Advanced Computing and Applications (ACOMP). IEEE, 2016, pp. 158–163.
- [233] Scratchapixel, "Geometry," Accessed: September 5, 2022. [Online].

 Available: https://www.scratchapixel.com/lessons/mathematics-

- physics-for-computer-graphics/geometry/points-vectors-and-normals.
- [234] Clemson, "Vector Magnitude & Normalization," Accessed: September 4, 2022. [Online]. Available: https://people.cs.clemson.edu/dhouse/courses/404/notes/barycentric.pdf.
- Triangles," [235] K. Academy, "Barycentric Coordinates for Accessed: September 4, 2022. [Online]. Available: https://www.khanacademy.org/computing/computerprogramming/programming-natural-simulations/programmingvectors/a/vector-magnitude-normalization.
- [236] GeeksforGeeks, "Interpolation Methods in Computer Graphics," Accessed: September 4, 2022. [Online]. Available: https://www.geeksforgeeks.org/interpolation-methods-incomputer-graphics/.
- [237] D. Chakravorty, "OBJ File Format All You Need to Know," Accessed: Jan. 20, 2019, 2021. [Online]. Available: https://all3dp.com/1/obj-file-format-3d-printing-cad/.
- [238] S. Schechter, "Everything You Need to Know About Using OBJ Files," Accessed: August 27, 2022. [Online]. Available: https://www.marxentlabs.com/obj-files/.
- [239] D. H. House, "Alias/ Wavefront Object (.obj) File Format," Accessed: August 27, 2022. [Online]. Available: https://people.cs.clemson.edu/ dhouse/courses/405/docs/brief-obj-file-format.html.
- [240] H. Gouraud, "Continuous Shading of Curved Surfaces," *IEEE transactions on computers*, vol. 100, no. 6, pp. 623–629, 1971.

- [241] B. T. Phong, "Illumination for Computer Generated Pictures," Commun. ACM, vol. 18, no. 6, p. 311?317, jun 1975. [Online]. Available: https://doi.org/10.1145/360825.360839
- [242] N. Robins, "Wavefront OBJ Model File Format Reader,"
 Accessed: October 26, 2022. [Online]. Available:
 https://github.com/joyeecheung/obj-loader/tree/master/src.
- [243] M. Sanver, L. Yang, and E. Gillispie, "A Webware for Computer Graphics Education," in 2003 Annual Conference, 2003, pp. 8–10.
- [244] E. Velázquez-Armendáriz and E. Millán, "Integrating Advanced GLSL Shading and XML Agents into a Learning-Oriented 3D Engine," in 16th International Conference on Electronics, Communications and Computers (CONIELECOMP'06). IEEE, 2006, pp. 43–43.
- [245] C. Manrique-Juan, Z. V. Grostieta-Dominguez, R. Rojas-Ruiz, M. Alencastre-Miranda, L. Muñoz-Gómez, and C. Silva-Muñoz, "A Portable Augmented-reality Anatomy Learning System Using a Depth Camera in Real Time," *The American Biology Teacher*, vol. 79, no. 3, pp. 176–183, 2017.
- [246] S. Mena, M. Visentin, C. E. Witt, L. E. Honan, N. Robins, and P. Hashemi, "Novel, User-Friendly Experimental and Analysis Strategies for Fast Voltammetry: Next Generation FSCAV with Artificial Neural Networks," ACS Measurement Science Au, vol. 2, no. 3, pp. 241–250, 2022.
- [247] S. G. Khronos Group, "OpenGL," Accessed: February 2, 2023. [Online]. Available: https://g.co/kgs/xpTAWp/.
- [248] Microsoft, "CFileDialog Class," Accessed: February 7, 2023. [Online]. Available: https://learn.microsoft.com/en-us/cpp/mfc/reference/cfiledialog-class?view=msvc-170/.

- [249] J.-M. Lien, J. Keyser, and N. M. Amato, "Simultaneous Shape Decomposition and Skeletonization," in *Proceedings of the 2006 ACM symposium on Solid and physical modeling*, 2006, pp. 219–228.
- [250] M. Livesu, F. Guggeri, and R. Scateni, "Reconstructing the Curveskeletons of 3D Shapes Using the Visual Hull," *IEEE transactions on* visualization and computer graphics, vol. 18, no. 11, pp. 1891–1901, 2012.
- [251] H. I. Choi, S. W. Choi, and H. P. Moon, "Mathematical Theory of Medial Axis Transform," *Pacific Journal of Mathematics*, vol. 181, no. 1, pp. 57–88, Nov. 1997, doi: 10.2140/pjm.1997.181.57.
- [252] F. Eyübo?lu, Çetin Sayaca, M. Çalik, D. Korkem, L. N. Tascilar, and D. Kaya, "Chapter 21 kinesiology of the Hip," in *Comparative Kinesiology of the Human Body*, S. Angin and I. E. ÅžimÅŸek, Eds. Academic Press, 2020, pp. 375–392.
- [253] S. G. Khronos Group, "glFlush," Accessed: February 10, 2023. [Online]. Available: https://registry.khronos.org/OpenGL-Refpages/gl2.1/xhtml/glFlush.xml/.
- [254] J.-y. Ru, L.-x. Chen, F.-y. Hu, D. Shi, R. Xu, J.-w. Du, and Y.-f. Niu, "Factors Associated with Development of Re-nonunion After Primary Revision in Femoral Shaft Nonunion Subsequent to Failed Intramedullary Nailing," *Journal of Orthopaedic Surgery and Research*, vol. 13, no. 1, pp. 1–11, Jul. 2018, doi: https://doi.org/10.1186/s13018-018-0886-y.
- [255] C. Cancer Society, "The Bones," Accessed: September 23, 2022. [Online]. Available: https://cancer.ca/en/cancer-information/cancer-types/bone-childhood/what-is-childhood-bone-cancer/the-bones/.

- [256] M. Key, "Femoral Shaft," Accessed: September 23, 2022. [Online]. Available: https://musculoskeletalkey.com/femoral-shaft/.
- [257] P. Lindstrom and G. Turk, "Evaluation of Memoryless Simplification," IEEE Transactions on Visualization and Computer Graphics, vol. 5, no. 2, pp. 98–115, 1999, doi: 10.1109/2945.773803.
- [258] dkmathstats, "Area Parellelograms & of Triangles with Cross Products," Accessed: February 10, 2023. Online. Available: https://dk81.github.io/dkmathstats_site/linalgarea-paraellogram.html/.
- [259] L. G. Media, "How to Calculate the Radius of a Square," Accessed: February 10, 2023. [Online]. Available: https://sciencing.com/area-inscribed-square-7270647.html/.
- [260] S. Mallick, "Contour Detection using OpenCV," Accessed: February 11, 2023. [Online]. Available: https://learnopencv.com/contour-detection-using-opency-python-c/.
- [261] S. Suzuki and Κ. be. "Topological Structural Ana-Digitized Binary Images Followlysis of by Border Computer Vision, Graphics, and Image Processing, ing," vol. 30, 32-46, 1985. [Online]. Available: htno. pp. tps://www.sciencedirect.com/science/article/pii/0734189X85900167
- [262] G. Borgefors, "Distance Transformations in Arbitrary Dimensions," Computer vision, graphics, and image processing, vol. 27, no. 3, pp. 321–345, 1984.
- [263] H. Fan, H. Su, and L. J. Guibas, "A Point Set Generation Network for 3D Object Reconstruction from a Single Image," in *Proceedings* of the IEEE conference on computer vision and pattern recognition, 2017, pp. 605–613.

- [264] T. Groueix, M. Fisher, V. G. Kim, B. C. Russell, and M. Aubry, "A Papier-mâché Approach to Learning 3D Surface Generation," in Proceedings of the IEEE conference on computer vision and pattern recognition, 2018, pp. 216–224.
- [265] N. Wang, Y. Zhang, Z. Li, Y. Fu, W. Liu, and Y.-G. Jiang, "Pixel2mesh: Generating 3D Mesh Models from Single RGB Images," in *Proceedings of the European conference on computer vision* (ECCV), 2018, pp. 52–67.
- [266] N. Agarwal, S.-E. Yoon, and M. Gopi, "Learning Embedding of 3D Models with Quadric Loss," arXiv preprint arXiv:1907.10250, 2019.
- [267] T. Ma, X. Yang, and L. J. Latecki, "Boosting Chamfer Matching by Learning Chamfer Distance Normalization," in *European Conference* on Computer Vision. Springer, 2010, pp. 450–463.
- [268] M.-Y. Liu, O. Tuzel, A. Veeraraghavan, and R. Chellappa, "Fast Directional Chamfer Matching," in 2010 IEEE Computer Society Conference on Computer Vision and Pattern Recognition. IEEE, 2010, pp. 1696–1703.
- [269] H. G. Barrow, J. M. Tenenbaum, R. C. Bolles, and H. C. Wolf, "Parametric Correspondence and Chamfer Matching: Two New Techniques forImage Matching," SRI INTERNATIONAL MENLO PARK CA ARTIFICIAL INTELLIGENCE CENTER, Tech. Rep., 1977.
- [270] P. Felzenszwalb and D. Huttenlocher, "Distance Transforms of Sampled Functions. Technical Report TR2004–1963," Cornell Computing and Information Science, 2004.
- [271] H. Fan, H. Su, and L. J. Guibas, "A Point Set Generation Network for 3D Object Reconstruction from a Single

- image," CoRR, vol. abs/1612.00603, 2016. [Online]. Available: http://arxiv.org/abs/1612.00603
- [272] L. Hawkes, "A Visual Representation of the Chamfer Distance Function," Accessed: November 25, 2022. [Online]. Available: https://www.youtube.com/watch?v=P4IyrsWicfs/.
- [273] W. L. Jungers, L. R. Godfrey, E. L. Simons, and P. S. Chatrath, "Phalangeal Curvature and Positional Behavior in Extinct Sloth Lemurs (Primates, Palaeopropithecidae)," *Proceedings of the National Academy of Sciences*, vol. 94, no. 22, pp. 11998–12001, Oct. 1997, doi: https://doi.org/10.1073/pnas.94.22.11998.
- [274] T. Gausepohl, D. Pennig, J. Koebke, and S. Harnoss, "Antegrade Femoral Nailing: An Anatomical Determination of the Correct Entry Point," *Injury*, vol. 33, no. 8, pp. 701–705, Oct. 2002, doi: https://doi.org/10.1016/S0020-1383(02)00158-4.
- [275] Y. Oh, Y. Wakabayashi, Y. Kurosa, M. Ishizuki, and A. Okawa, "Stress Fracture of the Bowed Femoral Shaft is Another Cause of Atypical Femoral Fracture in Elderly Japanese: A Case Series," Journal of Orthopaedic Science, vol. 19, no. 4, pp. 579–586, May. 2014, doi: 10.1007/s00776-014-0572-9.
- [276] J. Maratt, P. L. Schilling, S. Holcombe, R. Dougherty, R. Murphy, S. C. Wang, and J. A. Goulet, "Variation in the Femoral Bow: A Novel High-Throughput Analysis of 3922 Femurs on Cross-Sectional Imaging," *Journal of Orthopaedic Trauma*, vol. 28, no. 1, pp. 6–9, Jan. 2014, doi: 10.1097/BOT.0b013e31829ff3c9.
- [277] A. J. Fantry, G. Elia, B. G. Vopat, and A. H. Daniels, "Distal Femoral Complications Following Antegrade Intramedullary Nail

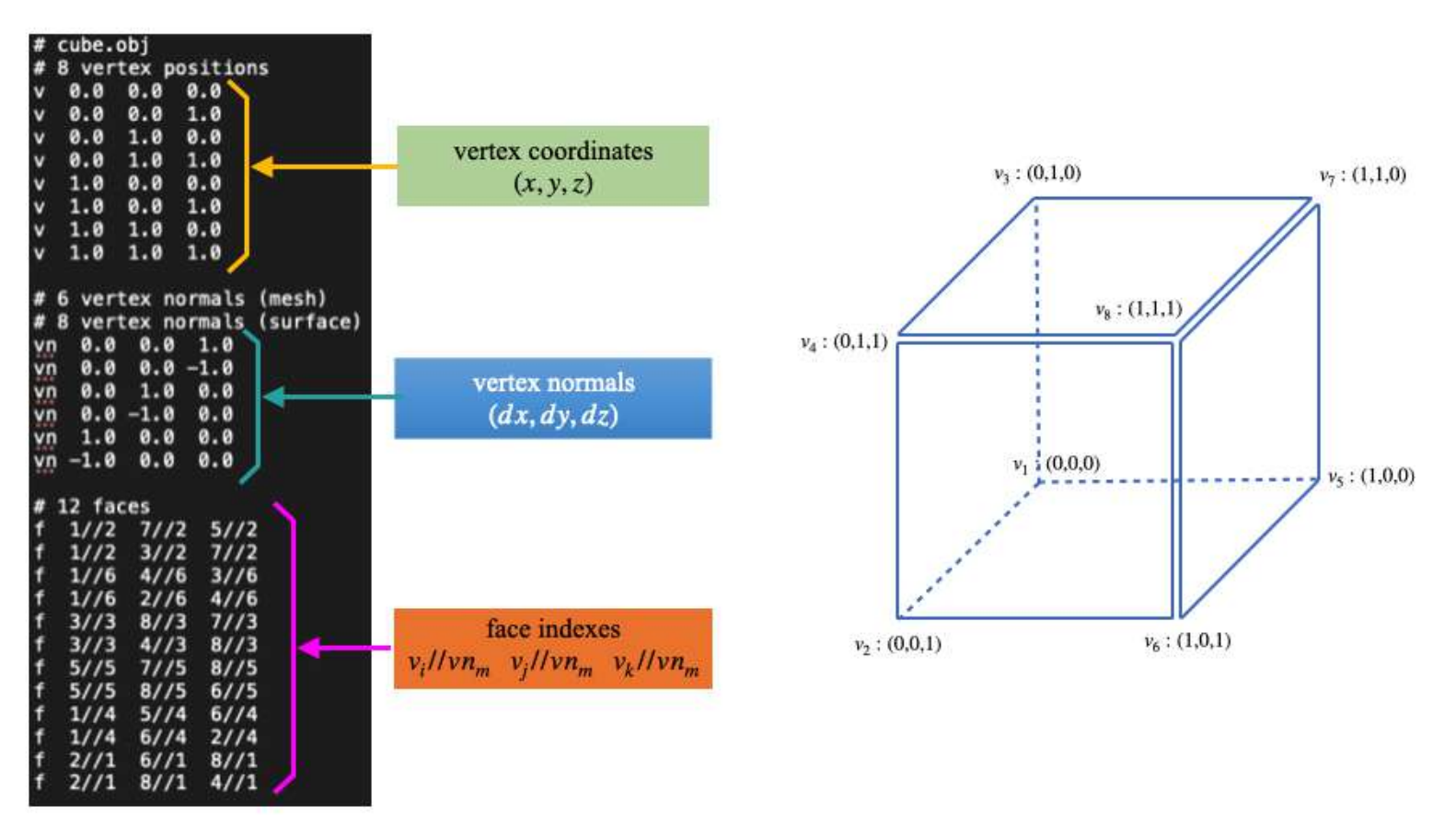
- Placement," *Orthopedic Reviews*, vol. 7, no. 1, pp. 12–14, Mar. 2015, doi: 10.4081/or.2015.5820.
- [278] A. Shetty, P. Shenoy, and R. Swaminathan, "Mismatch of Long Gamma Intramedullary Nail with Bow of the Femur: Does Radius of Curvature of the Nail Increase Risk of Distal Femoral Complications?" *Journal of Clinical Orthopaedics and Trauma*, vol. 10, no. 2, pp. 302–304, 2019, doi: https://doi.org/10.1016/j.jcot.2017.12.006.
- [279] B. Schmutz, S. Kmiec, M. E. Wullschleger, M. Altmann, and M. Schuetz, "3D Computer Graphical Anatomy Study of the Femur: A Basis For A New Nail Design," Archives of orthopaedic and trauma surgery, vol. 137, no. 3, pp. 321–331, 2017.
- [280] J. W. Roberts, L. A. Libet, and P. R. Wolinsky, "Who is in Danger? Impingement and Penetration of the Anterior Cortex of the Distal Femur During Intramedullary Nailing of Proximal Femur Fractures: Preoperatively Measurable Risk Factors," *Journal of Trauma and Acute Care Surgery*, vol. 73, no. 1, pp. 249–254, 2012.
- [281] M. Parker, T. Bowers, and G. Pryor, "Sliding Hip Screw Versus the Targon PF Nail in the Treatment of Trochanteric Fractures of the Hip: A Randomised Trial of 600 Fractures," The Journal of Bone and Joint Surgery. British volume, vol. 94, no. 3, pp. 391–397, 2012.
- [282] M. Khurma, "Radius of Curvature Formula," Accessed: Apr. 11, 2022., 2013. [Online]. Available: https://www.cuemath.com/radiusof-curvature-formula/.
- [283] N. Chernov and C. Lesort, "Least Squares Fitting of Circles," *Journal of Mathematical Imaging and Vision*, vol. 23, no. 3, pp. 239–252, 2005.

- [284] T. R. F. Membership, "The R Project for Statistical Computing," Accessed: December 30, 2022. [Online]. Available: https://www.r-project.org/foundation/members.html/.
- [285] H. Tsuchie, N. Miyakoshi, Y. Kasukawa, S. Senma, Y. Narita, S. Miyamoto, Y. Hatakeyama, K. Sasaki, and Y. Shimada, "Factors Related to Curved Femur in Elderly Japanese Women," *Upsala Journal of Medical Sciences*, vol. 121, no. 3, pp. 170–173, May. 2016, doi: https://doi.org/10.1080/03009734.2016.1185200.
- [286] D. M. Thiesen, F. Prange, J. Berger-Groch, D. Ntalos, A. Petersik, B. Hofstätter, J. M. Rueger, T. O. Klatte, and M. J. Hartel, "Femoral Antecurvation—A 3D CT Analysis of 1232 Adult Femurs," PLoS One, vol. 13, no. 10, p. e0204961, Oct. 2018, doi: https://doi.org/10.1371/journal.pone.0204961.
- [287] V. Sindhu and S. Soundarapandian, "Three-dimensional modelling of femur bone using various scanning systems for modelling of knee implant and virtual aid of surgical planning," *Measurement*, vol. 141, pp. 190–208, 2019.
- [288] Y. Boykov and V. Kolmogorov, "An Experimental Comparison of Min-cut/Max-flow Algorithms for Energy Minimization in Vision," IEEE transactions on pattern analysis and machine intelligence, vol. 26, no. 9, pp. 1124–1137, 2004.
- [289] S. H. Saw, Y.-D. Han, B.-G. Lee, and H.-T. Ewe, "A Weighted Mincut Max-flow Approach for 3D Mesh Segmentation," China Academic Journal Electronic Publishing House, pp. 574–577, June 2015.

Appendix A

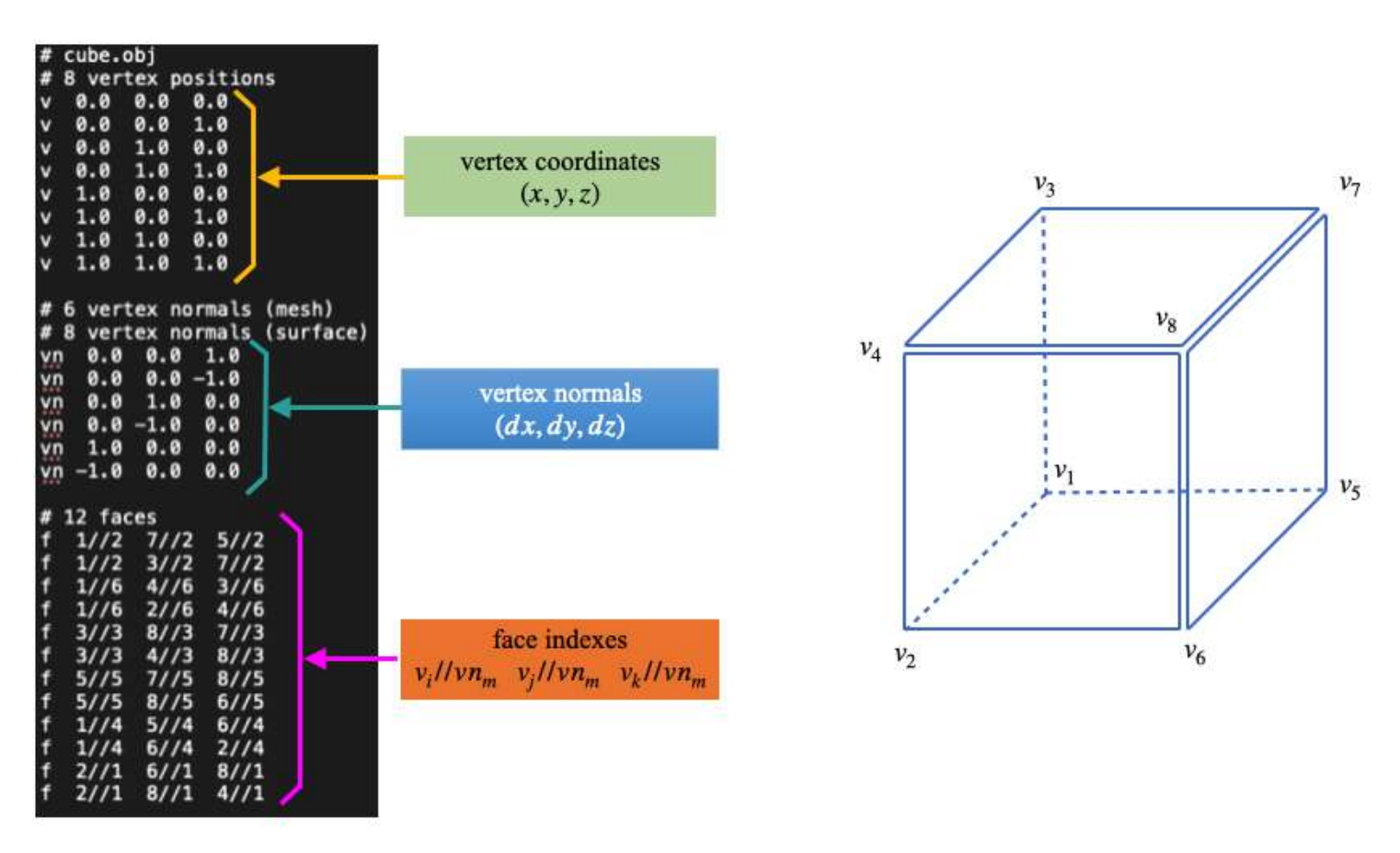
Cube.obj 3D File

In this appendix, we provide the illustrations of how the 3D mesh (A cube in this example) is constructed based on the structure in .obj file.



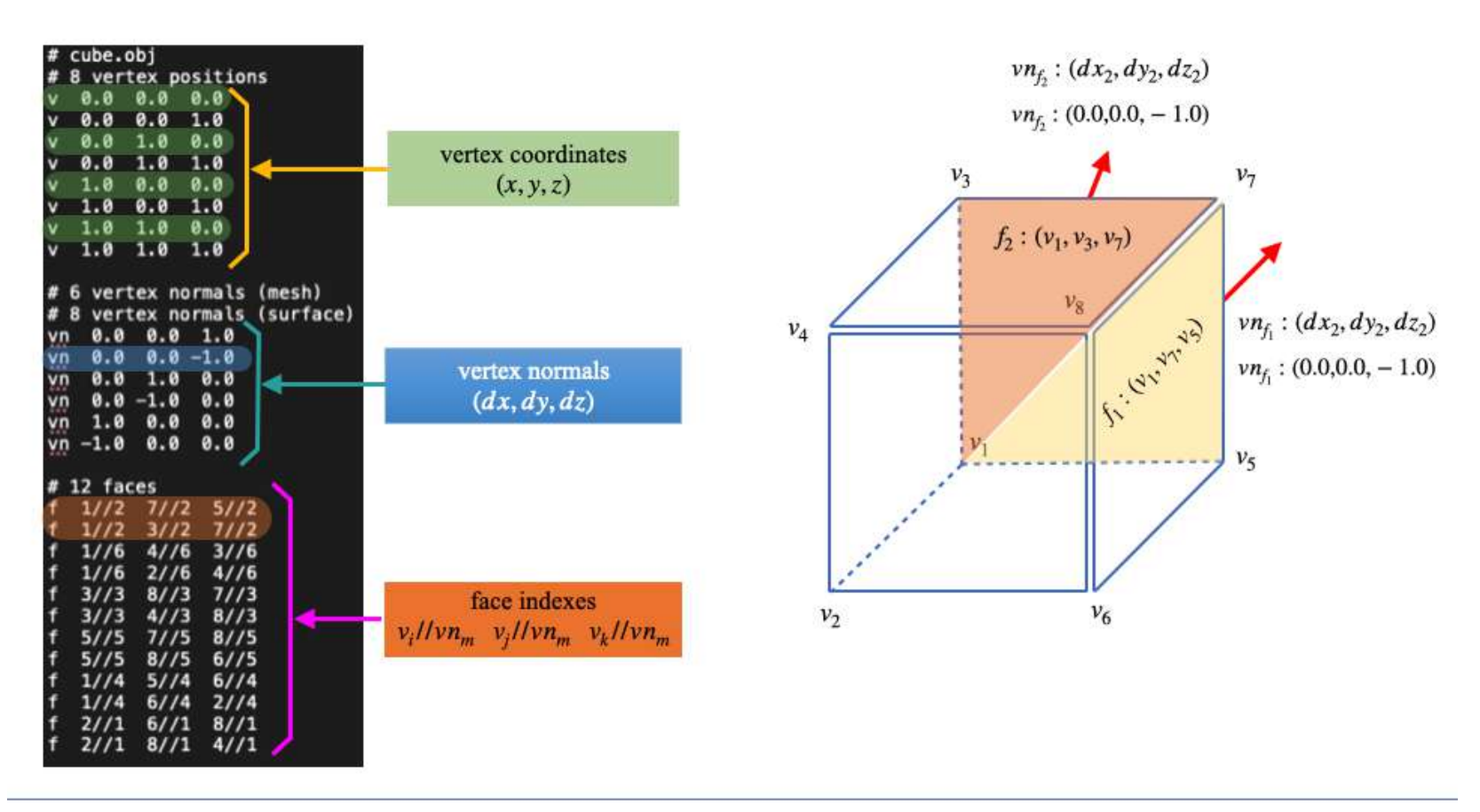
(a) The constructed 3D cube based on the definition in *cube.obj*. There are three (3) types of information: vertex coordinates, vertex normals and face indexes that are used to construct this 3D cube.

Figure A.1: An example *cube.obj* to illustrate the definition for the keywords in .obj that are used in 3D-FSA.



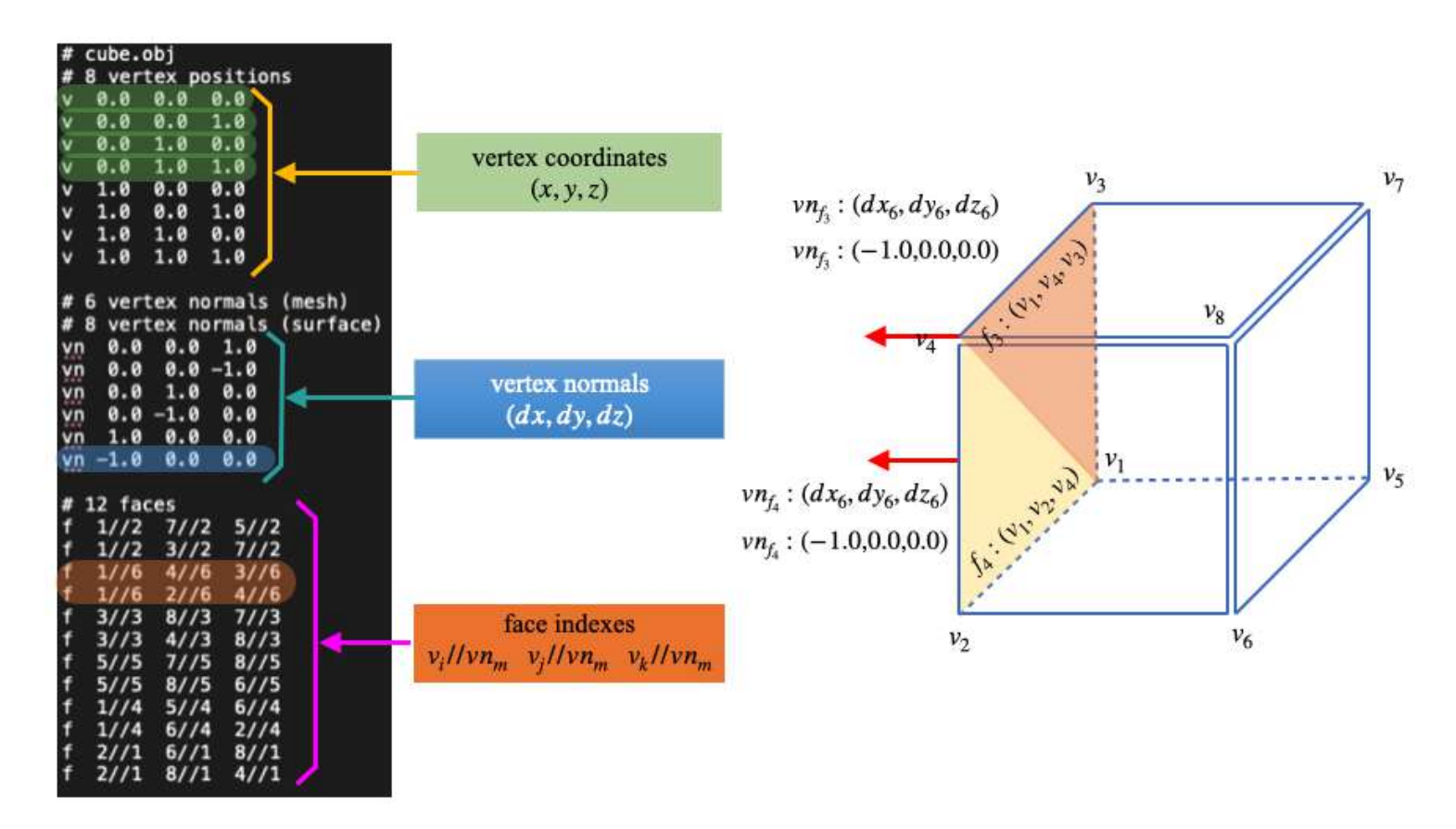
(b) The vertices of the cube are arranged according to the specified vertex coordinates. It begins with the first row of vertex coordinates: $v_1: (0.0, 0.0, 0.0)$, then followed by $v_2: (0.0, 0.0, 1.0)$, $v_3: (0.0, 1.0, 1.0)$, $v_4: (0.0, 1.0, 1.0)$, $v_5: (1.0, 0.0, 1.0)$, $v_6: (1.0, 0.0, 1.0)$, $v_7: (1.0, 1.0, 0.0)$ and $v_8: (1.0, 1.0, 1.0)$. There are total of eight (8) vertices used to construct the 3D cube.

Figure A.1: An example *cube.obj* to illustrate the definition for the keywords in .obj that are used in 3D-FSA.



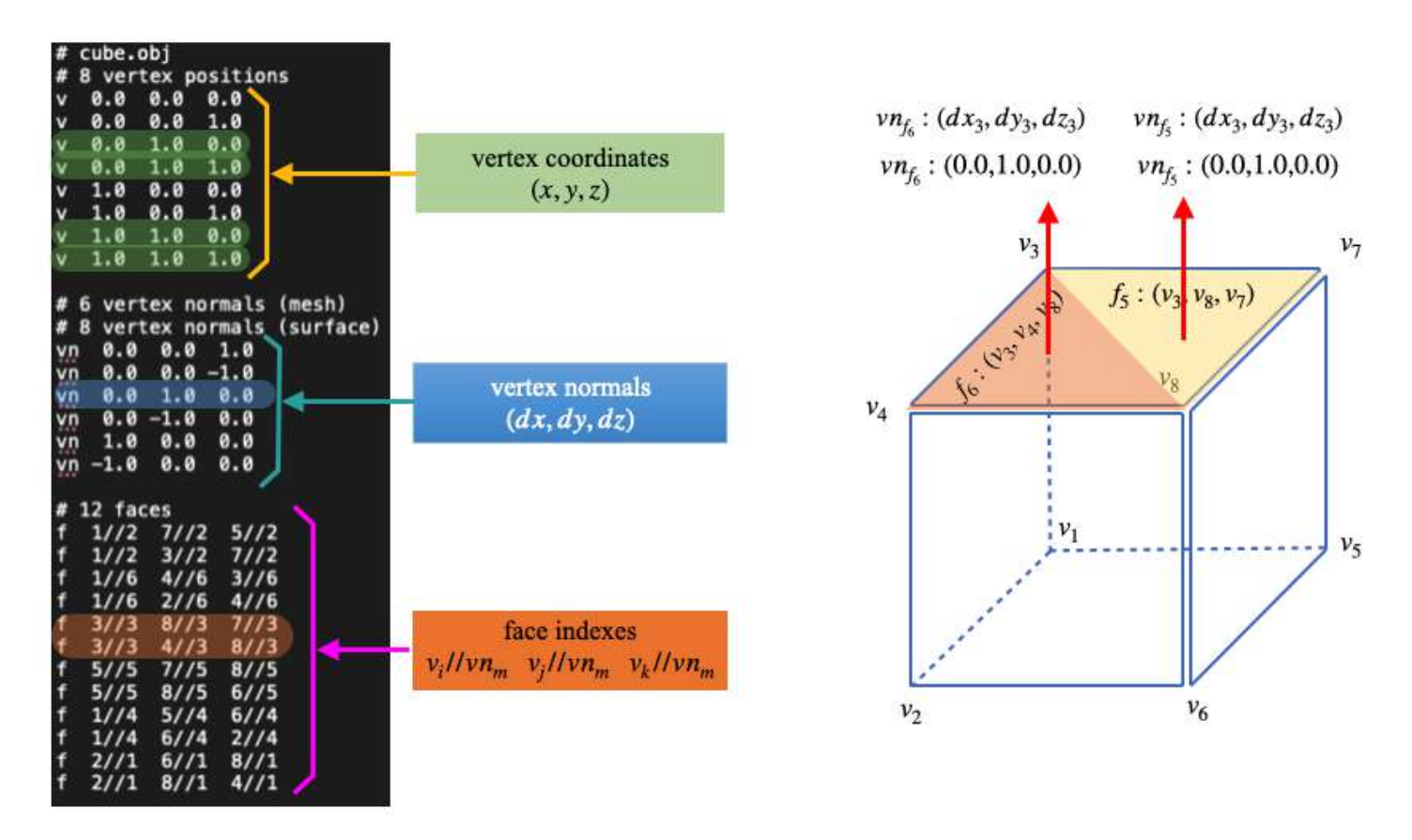
(c) The face indexes define the three vertices that are used to form the triangle face, and its vertex normal. The first row indicates the first triangle face, f_1 that is formed by (v_1, v_7, v_5) . The vertex normal for this face is (vn_2, vn_2, vn_2) , which is equals to (0.0, 0.0, -1.0) that is located at the second row in the vertex normals part. Same goes to the second triangle face, f_2 that is formed by (v_1, v_3, v_7) with the same vertex normals as f_1 .

Figure A.1: An example *cube.obj* to illustrate the definition for the keywords in .obj that are used in 3D-FSA.



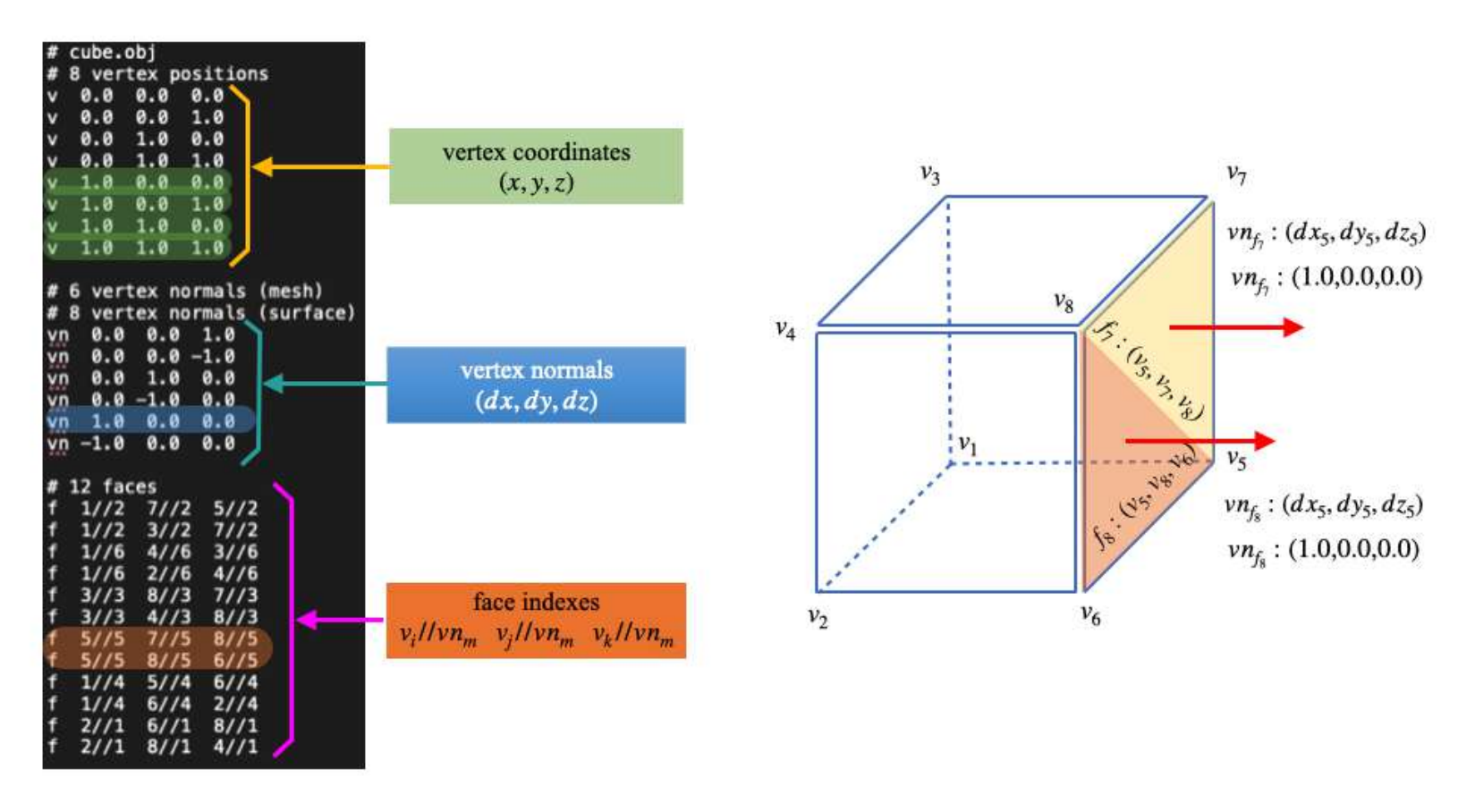
(d) Triangle face f_3 is formed by (v_1, v_4, v_3) , with the (vn_6, vn_6, vn_6) that is equals to (-1.0, 0.0, 0.0). Triangle face f_4 is formed by (v_1, v_2, v_4) , with the same vertex normals as f_3 .

Figure A.1: An example *cube.obj* to illustrate the definition for the keywords in .obj that are used in 3D-FSA.



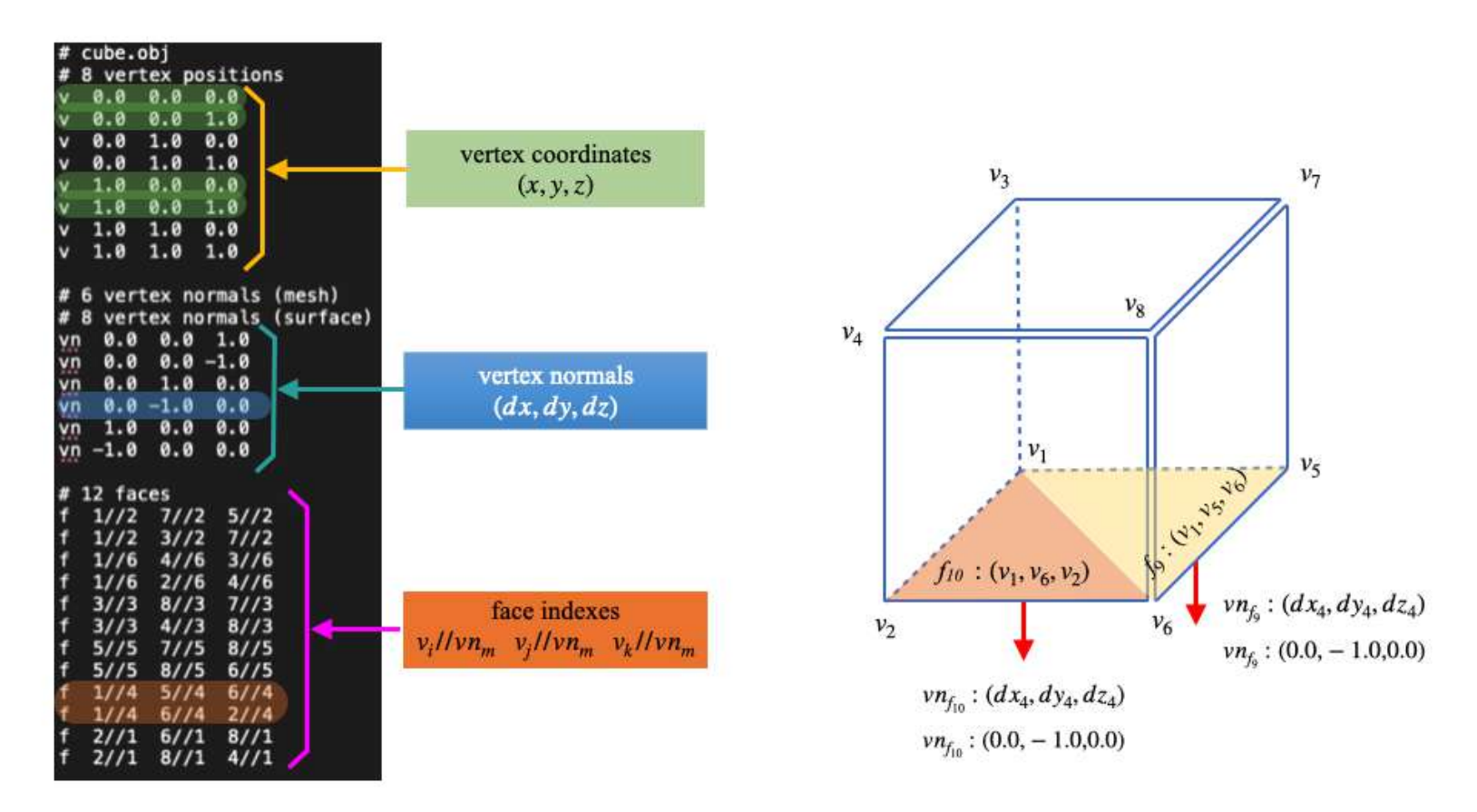
(e) Triangle face f_5 is formed by (v_3, v_8, v_7) , with the (vn_3, vn_3, vn_3) that is equals to (0.0, 1.0, 0.0). Triangle face f_6 is formed by (v_3, v_4, v_8) , with the same vertex normals as f_5 .

Figure A.1: An example *cube.obj* to illustrate the definition for the keywords in .obj that are used in 3D-FSA.



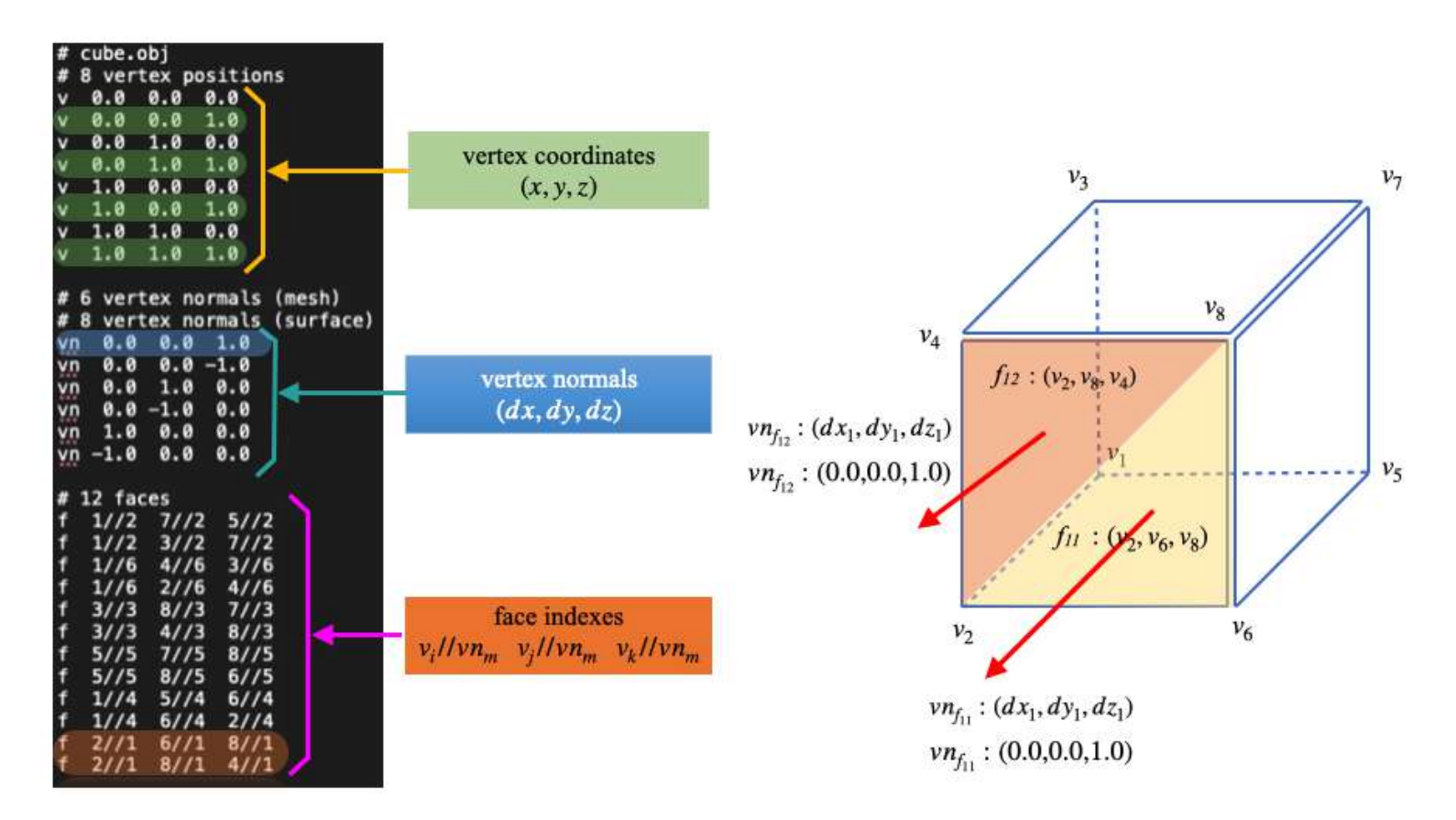
(f) Triangle face f_7 is formed by (v_5, v_7, v_8) , with the (vn_5, vn_5, vn_5) that is equals to (1.0, 0.0, 0.0). Triangle face f_8 is formed by (v_5, v_8, v_6) , with the same vertex normals as f_7 .

Figure A.1: An example *cube.obj* to illustrate the definition for the keywords in .obj that are used in 3D-FSA.



(g) Triangle face f_9 is formed by (v_1, v_5, v_6) , with the (vn_4, vn_4, vn_4) that is equals to (0.0, -1.0, 0.0). Triangle face f_{10} is formed by (v_1, v_6, v_2) , with the same vertex normals as f_9 .

Figure A.1: An example *cube.obj* to illustrate the definition for the keywords in .obj that are used in 3D-FSA.



(h) Triangle face f_{11} is formed by (v_2, v_6, v_8) , with the (vn_1, vn_1, vn_1) that is equals to (0.0, 0.0, 1.0). Triangle face f_{12} is formed by (v_2, v_8, v_4) , with the same vertex normals as f_{11} .

Figure A.1: An example *cube.obj* to illustrate the meaning for the keywords in .obj that are used in 3D-FSA.

Appendix B

Experimental Results

In this appendix, the computational scalability results are shown using our maximum-minimum centre approach for skeleton construction.

Table B.1: Time complexity measurements for ten (10) times of the 3D femur meshes using **our algorithm**. The average and the standard deviation are calculated based on these measurements.

Patient's Code No.	1	2	3	4	5	6	7	8	9	10	Average	Standard Deviation
0123964_L_all.obj	29.5730	29.2059	29.3423	29.7055	29.2336	29.4151	29.2498	29.6107	29.1942	29.3762	29.3906	0.1735
0123964_L_outside.obj	28.9740	28.8724	28.8977	29.2840	29.0126	29.0198	29.0754	29.0302	29.0914	28.8876	29.0145	0.1158
0123964_R_all.obj	30.0571	30.2059	29.7858	30.1201	30.2095	30.1662	30.1182	30.1609	30.1116	30.1735	30.1109	0.1170
0123964_R_outside.obj	22.1696	21.9392	22.0701	22.2274	22.1061	22.0239	22.1551	22.1194	22.0196	23.7185	22.2549	0.4943
0346688_L_all.obj	35.2641	35.1607	35.1145	35.0939	35.1603	35.0774	35.1176	35.1080	35.1836	35.2491	35.1529	0.0605
0346688_L_outside.obj	34.7590	34.5607	35.0499	34.7361	34.6956	34.8339	34.8018	34.7815	34.6964	34.7558	34.7671	0.1182
0346688_R_all.obj	35.8335	35.9495	35.6840	35.8921	35.8487	35.7722	35.8554	35.7442	36.0308	35.8479	35.8458	0.0945

continued on next page

Table B.1 – Continued from previous page

Patient's Code No.	1	2	3	4	5	6	7	8	9	10	Average	Standard Deviation
0946600 B 4:1 1:	00 0055	09 5101	02.0076	09.0776	00.0465	09 9051	00 0401	22 2000	09 0710	22 2000	02 0000	0.0000
0346688_R_outside.obj	23.2355	23.5191	23.2076	23.2776	23.2465	23.3251	23.3431	23.2860	23.2718	23.2099	23.2922	0.0866
00486295_L_all.obj	24.5964	24.6765	24.6651	24.6341	24.7032	24.5540	24.5750	24.7234	24.5164	24.6718	24.6316	0.0648
00486295_L_outside.obj	16.8737	17.0152	17.0285	17.0499	17.0796	17.0927	17.0076	16.9339	16.8744	16.9096	16.9865	0.0781
00486295_R_all.obj	27.1442	27.1960	27.2787	27.1806	27.1599	27.3119	27.3516	27.0800	27.3517	27.1936	27.2248	0.0884
00486295_R_outside.obj	16.7667	16.6939	16.7296	16.8256	16.7900	16.6674	16.7870	16.7797	16.7514	16.7613	16.7553	0.0448

continued on next page